FERDINAND RISSNER

Collective Effects in Self-Assembled Monolayers of Polar Organic Molecules

DOCTORAL THESIS

For obtaining the academic degree of
Doktor der technischen Wissenschaften

Doctoral Programme of Technical Sciences
Technical Physics

Graz University of Technology

Graz University of Technology

Supervisor:

Ao.Univ.-Prof. Dipl.-Ing. Dr.techn. Egbert Zojer
Institute of Solid State Physics

Graz, February 2012

Deutsche Fassung:
Beschluss der Curricula-Kommission für Bachelor-, Master- und Diplomstudien vom 10.11.2008
Genehmigung des Senates am 1.12.2008

EIDESSTATTLICHE ERKLÄRUNG

Ich erkläre an Eides statt, dass ich die vorliegende Arbeit selbstständig verfasst, andere als die angegebenen Quellen/Hilfsmittel nicht benutzt, und die den benutzten Quellen wörtlich und inhaltlich entnommene Stellen als solche kenntlich gemacht habe.

Graz, am ……………………………   ………………………………………………..
(Unterschrift)

Englische Fassung:

STATUTORY DECLARATION

I declare that I have authored this thesis independently, that I have not used other than the declared sources / resources, and that I have explicitly marked all material which has been quoted either literally or by content from the used sources.

……………………………   ………………………………………………..
date   (signature)

To Samuel T.,
† fall 2010.

Acknowledgements

My special thanks go to my supervisor Egbert Zojer. First of all, he made this PhD thesis possible financially:. There was a salary to pay and the many conferences I have attended and two research visits I have enjoyed have not been cheap either. He was available to answer my many questions patiently and whenever possible he was willing to drop everything else for a discussion. Beyond that, he spent a lot of time improving the sometimes-not-so-good manuscripts I have written, and made possible our annual barbeque and Christmas party.

I also wish to thank all former and present members of the group I got to know, especially: The ‘old gang’ Anna Track, Oliver Hofmann and Gerold Rangger, for making work in the office so much fun (and, of course, for explaining to me all the details and pitfalls of the simulations), for thousands of coffee breaks and for having lunch together. Oliver for the many unanticipated discussions which sometimes lasted for hours. Georg Heimel for providing his competence via phone and e-mail whenever I got stuck. Piet Reuter for plenty of nice conversations about (among other topics) religion, and for staying in touch. The ‘new gang’ David Egger, Simon Ausserlechner and Martin Stolterfoht for spending so much time together, not just at work. For stimulating discussions about anything and everything on a regular basis. David and Martin for fixing all the little computer issues together, and David for the successful teamwork on some topics and for renewing my enthusiasm when I felt frustrated. Marco Marchl for a nice week at the MRS in San Francisco, and Lukas Ladinig, Hannes Brandner and Yao Shan for solving all those brainteasers together.

I am grateful to Leeor Kronik and Amir Natan for giving me such a warm welcome in Israel, for being there during working hours and on weekends, for showing me around and introducing me to topics I should have been familiar with before; and for doing their best in teaching me density functional theory. Natalia Kuritz, Ariel Biller and Adi Makmal for sharing their office with me and making me feel comfortable and welcome there. Thank you all for the hospitality.

I also want to thank Zhigang Shuai and ZhongYun Ma for hosting me in Beijing and going with me through all the trouble of visa prolongation. ZhongYun for the great teamwork and for showing me places together with Tian Zhang. Jianming Chen for our nice chats and Qinwen Chen, Xiao Deng and all of you who taught me the basics of how to use chopsticks.

Abstract

Self-assembled monolayers (SAMs) of polar organic molecules and their interfaces with metals or (organic) semiconductors are of interest in the research on organic and molecular electronics. Key to understanding the mechanisms which control the electronic properties of polar SAMs is (i) to explain the difference between a molecule in gas phase and when embedded in a monolayer and (ii) to account for the interfacial interaction between the SAM and the material it bonds to.

The purpose of the present thesis is to shed light on those topics in computer experiments employing density functional theory. Concerning (ii), it focuses on the microscopic details of how thermodynamic equilibrium is established in cases where pinning at the Fermi level is observed. Qualitatively different interfaces are studied: a SAM chemisorbed on a metal surface, a three-component system in which the SAM is physisorbed on another SAM (which is chemisorbed on a metal surface), and finally a SAM whose molecules turn into radicals upon adsorption. Regarding (i), the intra-molecular arrangement of dipoles is varied with respect to their position, number, and direction. Specifically, mixed SAMs are studied in which the dipoles of neighboring molecules point in opposite directions. These dipoles are attached to otherwise only weakly polar molecules in the form of polar terminal groups. Conceptually different systems are discussed in the two final chapters, where the investigated molecules consist of polar repeating units. The number of repeating units, the molecular orientation and the distance between the SAM-forming molecules are varied. In all cases, the impact of the dipoles on the electronic structure of the corresponding SAMs is then discussed.

Kurzfassung

Ein Schwerpunkt in der Forschung über organische und molekulare Elektronik sind selbstorganisierte Monolagen (SAMs) polarer organischer Moleküle und die Grenzflächen, die sie mit Metallen bzw. (organischen) Halbleitern bilden. Für ein tiefes Verständnis der elektronischen Eigenschaften von SAMs sind vor allem zwei Aspekte sind zentral: Es ist (i) dem Unterschied Rechnung zu tragen zwischen den Eigenschaften eines isolierten Moleküls im Vakuum und denen eines Moleküls, das in einer Monolage eingebettet ist - also von seinesgleichen umgeben ist. Nicht minder wichtig ist (ii) die Wechselwirkung zwischen der SAM und dem Material, an das sie gebunden ist.

Diese Arbeit versucht sich diesen Themen mit Hilfe von von Computerexperimenten auf Basis der Dichtefunktionaltheorie zu nähern. Thema (ii) betreffend diskutiert sie sogenanntes Fermi-Level-Pinning, welches in vielen Fällen die elektronische Struktur an der Grenzfläche bestimmt. In drei qualitativ unterschiedlichen Systemen wird untersucht, welche Mechanismen zur Herstellung des thermodynamischen Gleichgewichts an der Grenzschicht führen. Dies sind (a) auf Metall chemisorbierte Monolagen, (b) Dreischichtsysteme in welchen auf Systemen der Art (a) eine zusätzliche SAM physisorbiert ist, und schließlich (c) SAMs deren Moleküle durch die Adsorption radikalischen Charakter annehmen. Bezüglich (i) wird untersucht, inwiefern Position, Anzahl und Ausrichtung von intramolekularen Dipolen die elektronischen Eigenschaften einer Monolage determinieren, welche aus den entsprechenden Molekülen gebildet wird. Dabei werden zuerst gemischte Monolagen betrachtet, in denen die Dipole benachbarter Moleküle in entgegengesetzte Richtung zeigen. Die molekularen Dipole sind dabei in Form polarer Endgruppensubstituenten realisiert. Die beiden letzten Kapitel beschäftigen sich mit konzeptionell unterschiedlichen Molekülen, welche aus polaren Wiederholeinheiten bestehen. Die Verteilung der Dipole kann in diesem Fall über die Anzahl der Wiederholeinheiten, Orientierung der Moleküle und schießlich den intermolekularen Abstand eingestellt werden.

Contents

Chapter 1

Introduction

Amount and variety of research on self-assembled monolayers (SAMs) of organic molecules are impressive. The following lines give a few examples to illustrate this richness and, needless to say, it is an arbitrarily chosen selection. Recent review papers are cited and may be suitable starting points for further reading.

Self-assembly itself is fascinating.[1–4] A metallic or semiconducting surface serves as support for more or less strongly bonded molecules, where the orientation of the molecules with respect to the surface is to a great extent determined by the position of the chemical group facilitating bonding. In addition to the molecule-substrate interaction, particularly the more or less weak intermolecular interactions are responsible for the ordering of the molecules. Structuring techniques based on self-assembly processes (so-called "bottom-up" approaches) were used to fabricate supra-molecular assemblies which mechanically react to external stimuli and have thus been labeled molecular "motors" or "machines".[5,6] For instance, the structure of the monolayer can be switched (upright-standing *vs.* kinked,[7] chicken-wired *vs.* lamellar[8]) between two conformations. Suitable stimuli can be irradiation with light, changing the temperature or applying a voltage.[5]

Another example is based on rotaxanes.[6] These molecules are shaped like dumbbells which are threaded through a ring-like molecule (called "macrocyle"). Redox-reactions in bistable rotaxanes can push their ring along the dumbbell[9] over a distance of several nanometers. The molecules can form an upright-standing layer on a gold surface, and one can trigger the redox-reaction by applying a voltage.[10] The stored information is readable because the molecular conductance is different in the two states and a memory chip was fabricated based on this mechanism.[6,11]

In a completely different context, coating by organic monolayers is used to prevent fouling.[12] This is of great importance not only in medical equipment and implants, but also in food packaging, marine equipment, or sensor applications. The organic layers either degrade the biofoulants or prevent their attachment to the surface.

In electrochemical sensors, SAMs are used as sensing elements. Here, the interaction with an analyte (be it, for instance, metal ions, organic or biomolecules) is transduced into an electric signal.[13] SAMs can also be used to immobilize biomolecules via covalent or non-covalent interactions, which can then serve as sensors.[14] Besides electrochemical signals, also optical (change in thickness) and piezoelectric (change in mass) detection is used. In this context, mixed SAMs can be used to control the density (and, in principle, even the pattern) of the immobilized biomolecules when a proper terminal group is attached to only one of the mixed components and the other one remains inactive.

Research is further done on the magnetic properties of organic molecules,[15,16] where - for instance - applications like information storage, as magnetic switches and for spintronics are envisaged. Amongst others, metal-organic open-shell complexes, single-molecule magnets or organic radicals are studied, and self-assembly comes into play when those particles are to be structured.[15] Using organic radicals, switches triggered by redox reactions were fabricated. They change simultaneously their magnetic and optical properties.[16]

Redox reactions also change the electronic properties of the monolayer.[17] Those are the focus of the present work. In the fields of organic and/or molecular electronics, SAMs are used as interface modification to improve the efficiency of devices such as light-emitting diodes, photovoltaic cells and transistors.[18–20] In another approach, the SAM itself acts as the functional component of the device[20,21] and the ultimate miniaturization of this approach then leads to the active material being a single molecule: the single-molecule diode, transistor, switch, memory.[22–25]

In single-molecule experiments, reproducibility is often a problem and one of the reasons is that it is difficult to tell if indeed only one molecule is sandwiched in the "single-molecule" junction. The processes at work in a single-molecule device and a SAM-device differ fundamentally. For instance, the measured current-voltage characteristics of a SAM (divided by the number of sandwiched molecules) does *not* equal that of a single molecule,[26] and in related contexts "opposite" behavior of single molecules and monolayers have been observed by several groups.[27–29] For instance, it was found that the dipole of a single molecule is *enhanced* by bonding to a cluster surface. When the corresponding monolayer binds to a (flat) surfaces, not only is such enhancement absent. In addition, the dipoles are *reduced* because of inter-molecular depolarization.[27] In another study, the work function of a metallic substrate was found to decrease when covered with a SAM of low packing density, but it increased when the SAM was closely packed.[29]

These observations are essentially of electrostatic origin. Molecules with permanent dipole moments interact with their environment electrostatically, and the relevant electric field depends on how the involved dipoles are arranged. For illustration it is useful to compare a single polar molecule to a monolayer

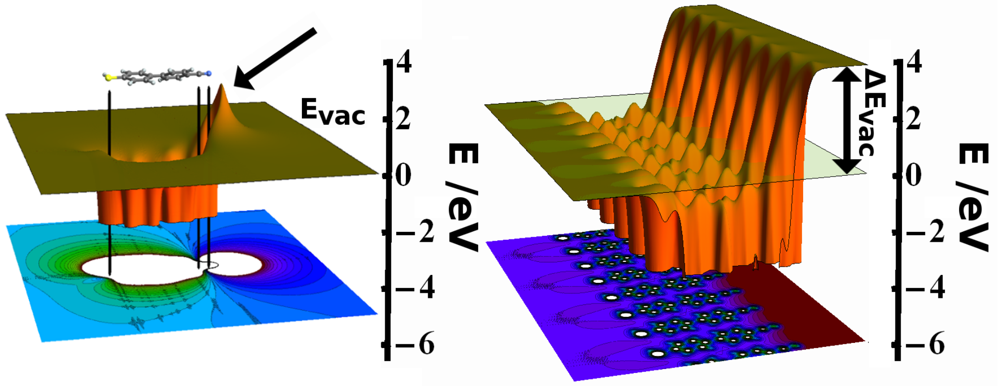

Figure 1.1: *Left: Electron potential energy in the plane of an isolated biphenylthiol molecule to which a polar cyano group is attached, and corresponding contour plot. The black vertical lines help locating the position of thiol and cyano group in both plots. The black arrow highlights the dipole potential. Right: Equivalent plots for an infinitely extended 2D monolayer of such molecules, averaged over one dimension. A semi-transparent plane at the energy of the "left-side" vacuum level helps spotting the step* ΔE_{vac} *in the electron potential energy across the monolayer. Reproduced with permission from ref. 31, ©2010 WILEY-VCH Verlag GmbH & Co. KGaA, Weinheim.*

formed from identical copies of that molecule (see Fig. 1.1): The field of a single molecular dipole is long-ranged whereas in a monolayer it is *de facto* eliminated everywhere outside the layer (with the important constraint, that the layer is defect-free and closely packed).[30,31] Furthermore, for a gas phase molecule a vacuum energy is always uniquely defined. The opposite is true for monolayers, as soon as the the net dipole perpendicular to the layer is nonzero (giving rise to ΔE_{vac}) and this property is exploited for the optimization of level-offsets at interfaces. All this is caused by well-known electrostatic dimensionality effects - often called *cooperative* or *collective* - acting on molecules as quantum-mechanical objects. Rationalizing the way in which the (quantum-mechanical) electronic structure of SAMs changes due to the electric fields of the molecular dipoles is the topic of the present thesis.

It is organized in two parts. Part I focuses on Fermi level pinning in three- (Chapter 4) and two-layer systems (Chapter 5). Here, one or two organic monolayers (on top of each other) are adsorbed onto a metal surface, and the dipoles incorporated in the respective layers shift the electronic states in the organic such that occupied (unoccupied) states would come to lie above (below) the metallic Fermi level. It is then investigated which processes drive the system to thermodynamic equilibrium, and the resulting alignment of the electronic states is discussed. The next set of *de facto* pinned systems, discussed in Chapter 6, is different from those in Chapters 4 & 5 in many respects, as the studied molecules become radicals during adsorption.

Having discussed the alignment of states at metal/organic(/organic) interfaces, the second part of the thesis focuses on the effect of the collectively induced electric fields on the electronic structure of the field-generating monolayer itself. It is well understood that electric fields change the electronic structure of molecules, and plenty studies exist which study the effect of external fields (see Chapter 9 for more details). Not so common is the focus on internal fields generated by the SAM-forming molecules. This part of the work could be subsumed also under the keyword *field engineering*, as it is studied how the position and direction of dipoles within a monolayer influence its electronic properties: Chapter 8 studies mixed SAMs, where neighboring molecules carry dipoles pointing in opposite direction, causing a strongly inhomogeneous electric field. Chapters 9 & 10 discuss monolayers in which the molecules consist of repeated polar units. This entails that the electric field penetrates the SAM. In the latter systems, dimensionality effects are discussed by calculating the transition from short to long molecule (0D→1D), from single molecule to densely-packed SAM (0D→2D), and from SAMs of short to SAMs of long molecules (2D→3D).

Chapter 2

Methodological prologue

The computer experiments presented throughout this work are based on simulations at the atomic length-scale. A quantum-mechanical approach is used to describe the electronic structure of the systems of interest. Describing many-particle systems is highly non-trivial and, consequently, approximations have to be used. In extended systems, one of these approximations are the chosen boundary conditions. Instead of treating the complete sample, *periodic boundary conditions* are applied as shown in Fig. 2.1: A unit cell is defined and repeated in space, and the potential is forced to be unit-cell periodic. This is appropriate for describing the bulk of a system; all surface effects are missed *a priori*, an issue to be discussed in Chapter 10. To calculate surfaces, a *repeated-slab approach* is often used. Here, the surface is modeled by "adding" a sufficient amount of vacuum to the unit cell (empty space in Fig. 2.1). This is necessary to separate neighboring surfaces with respect to quantum-mechanical interaction as standard band-structure codes apply periodic boundary conditions also in the direction perpendicular to the surface. Decoupling with respect to long-range (*i.e.*, Coulomb) forces is achieved by inserting a dipole layer in the vacuum region. It is sketched in the plot by a layer of red and blue charges. The dipole sheet compensates for the net dipole of the unit cell and thus suppresses the artificial electric field that would be generated by the forced periodicity of the electrostatic potential in that direction.[32] A more elegant way of calculating surfaces is applying periodic boundary conditions only in two directions, rendering dipole correction unnecessary.[33] This method will be used in Chapter 10.

Another implication of periodic boundary conditions is that only strictly periodic systems can be studied and that a unit cell must be defined *in advance* of the calculation. Even though the defining lattice vectors and the relative positions of the nuclei can be optimized with respect to the system's total energy, number and type of nuclei the cell comprises cannot. As a consequence, the unit of periodicity remains fixed and is an *input* of the calculation.

Finding the correct geometry is a complex problem. Often the large number of degrees of freedom render finding a global minimum in energy difficult and different optimization algorithms end up with different converged geometries.

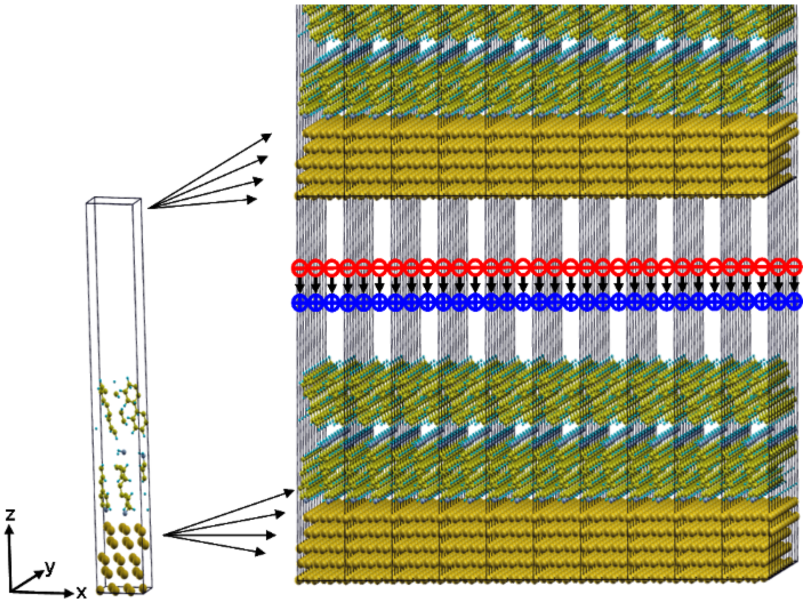

Figure 2.1: *Illustration of the repeated slab approach. A unit cell is repeated in the three Cartesian directions. To treat surfaces, a gap is added which is chosen wide enough to prevent the charge densities of neighboring surfaces to overlap. Electrostatic decoupling is guaranteed by a dipole layer, which compensates for the net dipole of the surface. Reproduced from ref. 34.*

Common optimizers stop as soon as a certain convergence criterion is reached (small enough forces). In general, however, small forces do not guarantee closeness to a minimum, let alone the global minimum. This is true especially for shallow potential wells. An instructive study in which the results of two optimization strategies for metal/organic interfaces are compared is presented in the Appendix.

The most important methodological problem, however, is for sure that finding the correct electronic structure has to be considered as "difficult" - even after having accepted the restrictions of modeling sketched above.

2.1 Density functional theory and self interaction

For many-electron systems with a significant number of electrons ($\approx 10^{23}$ atoms for macroscopic systems), the many-particle wave-function is an intractable object. The method of choice for electronic-structure calculations in systems of "many" electrons (like the one shown in Fig. 2.1) more often than not is density-functional theory (DFT). The reason for this is a drastic reduction of the computational cost compared to wave-function based methods, where *each electron* is described by 3 variables (4 if spin is included). DFT instead relies only on the density (3 (4) variables independent of the number of electrons) and Hohenberg and Kohn proved that this is sufficient to describe the ground state of a many-electron system.[35] Kohn and Sham have reintroduced one-electron wave-functions $\varphi_j(\mathbf{r})$ in DFT in the so-called Kohn-Sham equations

$$\left\{-\frac{1}{2}\nabla^2 + v_{\text{eff}}(\mathbf{r})\right\}\varphi_j(\mathbf{r}) = \epsilon_j\varphi_j(\mathbf{r}) \quad , \tag{2.1}$$

where each Kohn-Sham orbital φ_j is subject to the *same* effective potential

$$v_{\text{eff}}(\mathbf{r}) = v_{\text{ext}}(\mathbf{r}) + \int \frac{n(\mathbf{r}')}{|\mathbf{r}-\mathbf{r}'|}\mathrm{d}^3r' + v_{\text{xc}}(\mathbf{r}) \quad , \tag{2.2}$$

meaning that the Kohn-Sham electrons do *not* interact. v_{ext} is an external potential, usually the interaction with the positively charged nuclei, the second term describes the Coulomb potential of the electron density itself and v_{xc} is the potential due to exchange interaction and correlation. It was proven[35] that this approach gives the correct ground state electron density defined as

$$n(\mathbf{r}) = \int |\varphi_j(\mathbf{r})|^2\mathrm{d}^3r \quad . \tag{2.3}$$

Note that this holds true although the Kohn-Sham (KS) electrons do not strictly correspond to the electrons of the real system (which, of course, interact which each other). In fact, it is often stated that the φ_j are mere auxiliary quantities that can not be interpreted but are useful only to calculate the total density (given by eqn. (2.3)). To quote Walter Kohn's Nobel Lecture:[36]

> Neither the exact KS wave functions φ_j nor energies ϵ_j have any known, directly observable meaning [. . .]

and this is so because they describe only the fictitious, non-interacting particles ("Kohn-Sham orbitals") the real many-electron system is mapped onto. However, the situation is more complicated than that as (i) these quantities *are* interpreted frequently - also in the present work - and (ii) this is often done with great success. Part of the reason for this is given already by quoting the final part of above statement:

> [. . .] except for [eqn. (2.3) being the true density] and the fact that the magnitude of the highest occupied ϵ_j, relative to the vacuum equals the ionization energy [citing ref. 37].

One of the eigenvalues, at least, is meaningful. It is, however, not necessary to discard all the others.[i] Görling showed that the difference between Kohn-Sham eigenenergies "is a well-defined approximation to excitation energies of zeroth order in the electron-electron interaction"[39] and, interestingly, they have approximate meaning also as relaxed ionization energies.[40] The latter are defined as the energy needed to extract an electron from the system when the relaxations of the other electrons are taken into account (see below).

All this holds true as long as one uses the correct v_{xc} - which remains unknown ever since the introduction of Kohn-Sham theory itself. Much of the

---

[i] This reasoning follows ref. 38.

development of DFT focuses on improving approximations to $v_{\mathrm{xc}} = v_{\mathrm{x}} + v_{\mathrm{c}}$, where v_{x} denotes the truly quantum-mechanical exchange interaction and v_{c}, by definition, describes all effects whatsoever that are not described by the free-electron kinetic term $-\nabla^2/2$ or one of the other potentials. These are, by definition, the so-called many-body effects. For instance, if the eigenenergies are supposed to denote ionization energies, in a many electron system the remaining electrons will screen the hole (missing charge) generated by the ionization process and this reduces the eigenenergies compared to the non-screened situation.

As long as only approximations to v_{xc} are used, the reliability of the results depends on the quality of the approximation. Results have to be interpreted with care as, despite the great success of DFT, one has to be aware of some systematic errors it suffers from.[ii] One of these shortcomings will be discussed in Chapter 9: self interaction. Self interaction can be easily understood on the basis of eqn. (2.2), where the Coulomb potential to which (KS-)electron φ_j is exposed is calculated as being caused by n, the *total* electron density. This is, the electrostatic interaction of each electron not only with the other electrons is calculated, but - erroneously - also the interaction with itself. The same holds for common xc-functionals and for the exact density-functional the two contributions must cancel. Many of the failures of DFT have been attributed to the self-interaction error, and the one that will be discussed in this work (Chapter 9) is the interpretability of Kohn-Sham eigenvalues ϵ_j as ionization energies. The most important property of self-interaction with respect to the ϵ_j can be understood quite intuitively: because the Coulomb potential decays with $1/r$, the amount of self-repulsion a certain orbital φ_j is exposed to depends on its distribution in space. Self-interaction will, thus, affect localized and delocalized orbitals differently and this can severely distort the electronic structure.[42,43] Exactly this is the case for the molecules studied in Chapter 9.

It is further interesting to note that there is an analogy to classical electrostatics, where continuous charge densities carry self-energy and ideal point-like charge carriers do not.[iii] The electrostatic energy W of a continuous charge density is nonzero because it is subject to the field *generated by itself*. Mathematically,

$$W = \frac{\epsilon_0}{2} \int \mathrm{d}^3 r |\mathbf{E}(\mathbf{r})|^2 \qquad , \tag{2.4}$$

where $\mathbf{E}(\mathbf{r})$ is the field due to the charge density of interest. This expression diverges for a point charge q_i, for which $|\mathbf{E}(\mathbf{r})|^2 \propto q_i^2/|\mathbf{r} - \mathbf{r}_i|^4$ and in a picture of point-like charge carriers this "self-energy" is explicitly excluded in the expression of the electrostatic energy by setting $i \neq j$ in the summation

$$W = \frac{1}{8\pi\epsilon_0} \sum_{i \neq j}^{N} \frac{q_i q_j}{|\mathbf{r}_i - \mathbf{r}_j|} \qquad . \tag{2.5}$$

[ii] Some references are, for instance, given in the introduction of ref. 41.

[iii] This follows ref. 44.

This is, eqn. (2.5) sums up the energy of each charge in the potential of only all *other* charges.

These two notions of W are not consistent as can be deduced, for example, from the fact that eqn. (2.4) cannot evaluate to a negative number, and eqn. (2.5) can.

The most natural way[iv] of getting rid of self-interaction seems to be given immediately by its definition. If one identifies electrons with orbitals (as done above), and calculates the sum of Hartree- and *xc*-energy for each orbital, the result will usually not equal zero for a given approximate functional. One can, thus, try to modify the effective potential such that these contributions do cancel, *i.e.*, one can subtract self-interaction orbital by orbital. This approach is called self-interaction correction (SIC), and is discussed in detail in refs. 45 & 38.

Another approach derives from the knowledge that Hartree-Fock theory is self-interaction free as Hartree- and exchange contributions cancel exactly for each orbital.[v] The idea is to improve upon standard functionals by using a fraction of exact exchange also in DFT.

In both cases, one ends up with *orbital-dependent* functionals[38] instead of non-interacting electrons in a common, external potential. Such functionals are outside the Kohn-Sham framework and part of so-called *generalized* Kohn-Sham theory. Here, instead of mapping the real system to a non-interacting reference system it is mapped to an interacting system to which the theorem of Hohenberg and Kohn still applies.

The situation is further complicated by the fact that every orbital-dependent functional can be interpreted also as a Kohn-Sham functional (*i.e.*, not generalized). This is possible because as long as a functional depends explicitly on *Kohn-Sham* orbitals, it implicitly depends on the density, and this is true because in Kohn-Sham theory orbitals are uniquely defined by the density. One can thus for each orbital-dependent functional find an effective potential - the optimized effective potential (OEP) - which minimizes the total energy with respect to the density and is strictly within Kohn-Sham theory.

This classification is not only of theoretical interest as the results will differ depending on whether a certain orbital-dependent functional is implemented within Kohn-Sham or generalized Kohn-Sham theory.[46] A detailed discussion of all this is far beyond the scope of the present work and the competence of its author. The reader is referred to the pertinent literature (especially ref. 38 and references therein).

[iv] The remainder of this chapter again follows ref. 38.

[v] Unfortunately, though, it is also free from correlation and thus does not give better results than DFT *per se*.

Part I

Fermi Level Pinning.

Chapter 3

Preface

The content of the following chapters can be subsumed under the keyword "Fermi level pinning". They discuss various kinds of metal/organic interfaces at which states in the organic material are "pinned" at the Fermi level determined by the metallic substrate.

With respect to the electronic states, it is possible to distinguish between three qualitatively different situations when an interface between two materials is formed. These are shown in Fig. 3.1, where the electrostatic potential of two materials is shown before they are connected. Like in Chapter 4, one of them is a Au(111) surface (5 layers) covered with a certain self-assembled monolayer. The SAM determines the relative position of the Fermi energy (gray horizontal line) and the electrostatic potential above the SAM. When a material (a monolayer of biphenyl molecules in case of Chapter 4) approaches this surface, its highest occupied and lowest unoccupied states (indicated by red and blue horizontal lines, respectively) can align with the Fermi energy in three ways. This is indicated in panels (a)-(c). Which of these sketches applies depends on the specific system at hand. After binding, no occupied states can exist above and no unoccupied states below the Fermi energy by its very definition, at least as long thermodynamic equilibrium is established. (Strictly speaking,

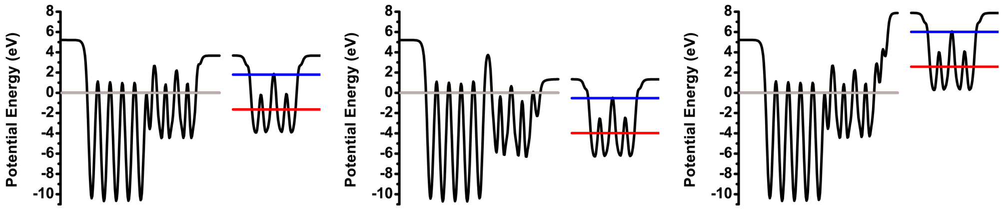

(a) *No pinning.* **(b)** *Pinning of unoccupied states.* **(c)** *Pinning of occupied states.*

Figure 3.1: *Plane-averaged electrostatic energy curves for different Au(111) surface modifications and a monolayer of 2P, isolated from the former. The gray, red and blue horizontal lines mark the Fermi level of the metal and HOPS and LUPS of 2P, respectively; reproduced from ref. 34.*

this is true only at $T = 0$ K, a common approximation made also in this work.) To establish equilibrium, certain processes must be induced in situations (b) and (c) which "push" ("pull") the unoccupied (occupied) states in the biphenyl layer to above (below) the Fermi level.

It is interesting to note that metal/organic interfaces can indeed be out of equilibrium, and that in such cases unoccupied states far below (or occupied above) the Fermi energy have been found experimentally.[47–49] Such special cases are not treated in the present work, where the self-consistent calculations always end up in equilibrium.

To establish equilibrium, the mechanism one intuitively expects is charge transfer between the subsystems as it can easily guarantee that all states below the Fermi level are filled and no states above. However, the situation seems to be more complicated and one of the results of the following chapters will be that hardly any charge transfer is found in many cases. Three qualitatively different interfaces are dealt with:

In Chapter 4, a layer of biphenyl is adsorbed onto a SAM-covered metal. This process is dominated by physisorption. Accordingly, in general no strong changes in the electronic structure of the subsystems are expected and for systems without Fermi level pinning this is indeed the case. This situation is referred to as vacuum level alignment. It renders such interfaces ideal to study Fermi level pinning as every strong response of the charge density to adsorption can exclusively be attributed to pinning effects.

Chapter 5, in contrast, deals with molecules which are chemisorbed (*via* pyridine groups) on a metal surface, *i.e.*, no spacer layer is present. Here vacuum level alignment is not common, as the formation of a chemical bond at the interface implies pronounced rearrangements of charge density, and they are usually confined to the very interface. This changes as soon as pinning effects occur, where significant rearrangements can also be found near the terminal groups pointing away from the surface. The focus of this chapter is on the details of these rearrangements and how they depend on the localization of the orbital which is pinned. This is studied by changing various substituents as well as the length of the backbone of the SAM-forming molecules.

Note that pinning phenomena are not collective *per se* and that above considerations most likely apply to any interface. However, in the systems discussed here pinning is caused by changes in the potential landscape specific to collective phenomena in periodic systems. In other words, the results described in the following chapters would differ completely for non-periodic systems (like clusters).

This does not necessarily hold for the data presented in Chapter 6, which deals with a different kind of systems. Here, the electronic structure of the adsorbed molecules is changed fundamentally during adsorption. The molecules are chosen such that bonding to the metal surface turns them into radicals. A radical is characterized by the presence of an unpaired electron and this implies a series of interesting consequences. They are not fully understood yet and the article presented in this chapter actually raises at least as many questions as it answers, see also Summary.

Chapter 4

Understanding the electronic structure of metal/SAM/organic-semiconductor heterojunctions (ref. 50)

The first kind of systems to be presented are heterointerfaces consisting of a metallic substrate, a SAM chemisorbed onto it, and a physisorbed layer of organic molecules on top of the SAM. The functional groups of the SAM interlayer are systematically varied in order to adjust the (effective) work function over a wide range. This way the SAM shifts the electronic states of the topmost layer from a situation with the highest occupied states above the metal Fermi level (E_F) to a situation with E_F in the gap of the organic, and finally also to a case with the unoccupied states below E_F. This was sketched in Fig. 3.1. It is then studied in which way thermodynamic equilibrium is established and to what extent the situation changes when the metal substrate, defining E_F, is removed. The work was published[50] and is reproduced below with minor modifications

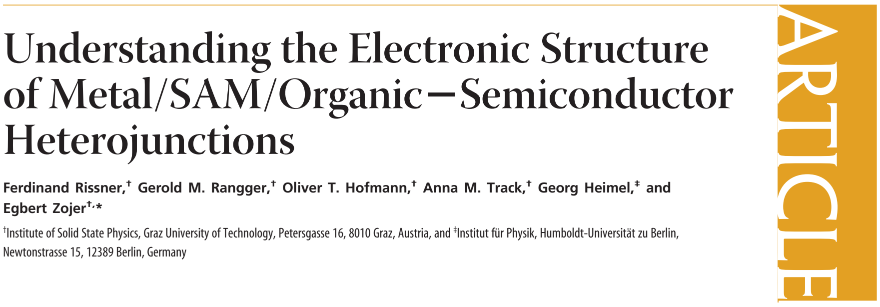

Understanding the Electronic Structure of Metal/SAM/Organic−Semiconductor Heterojunctions

Ferdinand Rissner,[†] Gerold M. Rangger,[†] Oliver T. Hofmann,[†] Anna M. Track,[†] Georg Heimel,[‡] and Egbert Zojer[†,*]

[†]Institute of Solid State Physics, Graz University of Technology, Petersgasse 16, 8010 Graz, Austria, and [‡]Institut für Physik, Humboldt-Universität zu Berlin, Newtonstrasse 15, 12389 Berlin, Germany

Figure 4.1: *Header of the article ref. 50 showing its title and all contributing authors. This chapter is essentially identical to the article.*

(Fig. 4.1).[i]

Author contributions. I started working on the topic already during my diploma thesis[34] where some additional details on the calculations can be found. In the course of my PhD thesis, I have (i) extended the set of studied interfaces to clarify our point, (ii) added a section on organic/organic interfaces (no metal included) and (iii) I have further added a discussion of two models for describing interfaces which are frequently used in literature: the ICT (integer charge transfer) and the IDIS (induced density of interface states) model. The latter discussion was presented as an appendix in the original article.[50] For the sake of the reader, the whole article is reproduced in the following (even if part of it stems from the diploma thesis); only minor adaptations have been made.

I have done all calculations of this work and have written the manuscript. The other authors have contributed by introducing me to the general methodology of the calculations and with many discussions about the interpretation of the results. Especially Georg Heimel and my supervisor Egbert Zojer contributed greatly also with improving the text and clarifying the presentation to make the manuscript suitable for publication. Last, definitely not least, all this was Egbert's idea.

Abstract. Computational modeling is used to describe the mechanisms governing energy level alignment between an organic semiconductor (OSC) and a metal covered by various self-assembled monolayers (SAMs). In particular, we address the question to what extent and under what circumstances SAM-induced work-function modifications lead to an actual change of the barriers for electron and hole injection from the metal into the OSC layer. Depending on the nature of the SAM, we observe clear transitions between Fermi level pinning and vacuum-level alignment regimes. Surprisingly, although in most cases the pinning occurs only when the metal is present, it is not related to charge transfer between the electrode and the organic layer. Instead, charge rearrangements at the interface between the SAM and the OSC are observed, accompanied by a polarization of the SAM.

4.1 Introduction

In organic (opto)electronics, the performance of devices strongly depends on the energy level alignment at interfaces between different functional materials and the electrodes. Deviations from optimum charge carrier injection barriers often imply a significant loss of efficiency.[51–53] A method of optimizing the device performance is to introduce self-assembled monolayers (SAMs) between electrodes and organic semiconductors (OSCs). They can be used to adjust the work function Φ of the electrode, and significant steps toward understanding the mechanisms that govern SAM-induced work-function modifications, $\Delta\Phi_{\mathrm{SAM}}$,

---

[i] Reproduced with permission from ACS Nano. Copyright 2009 American Chemical Society. The original article is available online at `http://dx.doi.org/10.1021/nn9010494`.

have been made.[54–63] SAMs have also been shown to reduce carrier injection barriers in devices.[54,64] However, to what extent and under which conditions $\Delta\Phi_{\mathrm{SAM}}$ actually translates into a change of the carrier injection barriers[65] and the crucial question what are the microscopic mechanisms responsible for deviations is not yet really understood. Resolving that matter is the purpose of the present study.

To achieve that we rely on density functional theory (DFT)-based slab-type band structure calculations to obtain an in-depth understanding of the electronic processes in metal/SAM/OSC systems. Depending on the actual magnitude of $\Delta\Phi_{\mathrm{SAM}}$, we observe clear-cut transitions between pinning of the metal Fermi level at the frontier orbitals of the OSC (and thus a SAM-independent carrier injection barrier) and vacuum-level alignment, where $\Delta\Phi_{\mathrm{SAM}}$ more or less directly translates into a modification of electron and hole injection properties. Interestingly, in spite of the fact that the presence of the metal is what causes the pinning, it is found to be not related to long-range charge transfer between the metal and the OSC, but rather results from a polarization of the SAM, accompanied by charge transfer between the SAM and the OSC layer. To further elucidate how the presence of the substrate affects the vacuum-level shift and charge rearrangements, we compare the full metal/SAM/OSC system to the SAM/OSC interface in the absence of the metal. Finally, in the appendix, it is discussed to what extent the integer charge transfer (ICT) model[66,67] and the unified IDIS (induced density of interface states) model[65] can provide a satisfactory rationale for the properties of the present structures, which is useful as both approaches have been applied to organic/organic interfaces and the ICT model is often used to describe pinning effects.

4.2 Results and discussion

4.2.1 The systems

The studied model interfaces consist of a Au(111) surface, a SAM interlayer, and on top of it an additional monolayer of biphenyl, 2P (regarding the choice of the semiconductor compare the discussion in the Methods section). The latter represents a computationally viable model system for the bulk of an OSC. The SAMs, used as "tools" to vary the metal work function are biphenyl derivatives assumed to pack in a herringbone patterned $p(3 \times \sqrt{3})$ surface unit cell (Fig. 4.2).[68] They are substituted at the two terminal positions (4 and 4′) by a docking group (directed toward the electrode) and a head group (pointed at the OSC). The net change in the metal work function induced by such a SAM, $\Delta\Phi_{\mathrm{SAM}}$, is determined, on the one hand, by the dipole moment and the electron-donating or -withdrawing character of the head group and, on the other hand, by the nature of the docking group and the resulting charge rearrangements at the interface induced by the bonding to the metal.[61,69] It has been shown that the net effect of head and docking groups is essentially additive.[70] Independently varying the docking groups and head group substituents, thus, provides a handle for tuning the work function of the metal/SAM system over

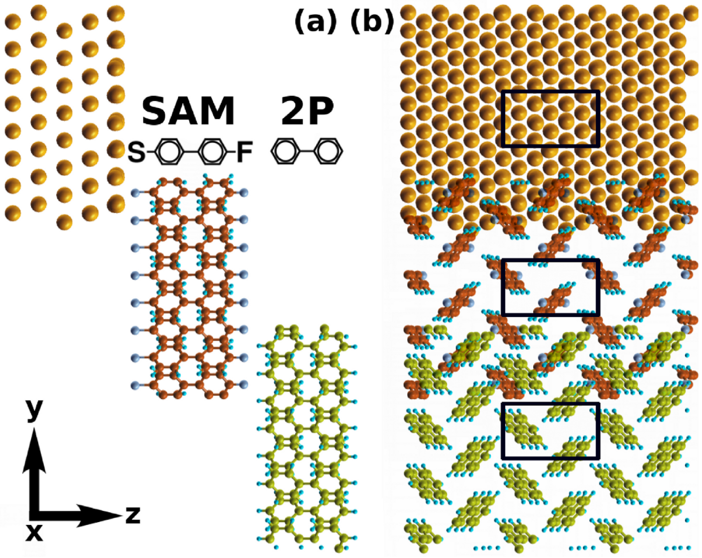

Figure 4.2: *Side (a) and top (b) view of the representative system Au|S|2P|F||2P. The two monolayers (S|2P|F and 2P) are shifted for the sake of clarity. The black rectangles mark the* $p(3 \times \sqrt{3})$ *surface unit cell.*

a wide range.

In the following, the systems are denoted as metal|docking group|number of rings|head group||2P. Here, 2P refers to the weakly bound monolayer of 2P on top of the SAM. They include (sorted by ascending $\Delta\Phi_{\mathrm{SAM}}$)

(**1**) Au| Pyr |2P| N(CH$_3$)$_2$ ||2P,
(**2**) Au| Pyr |2P| NH$_2$ ||2P,
(**3**) Au| CN |2P| NH$_2$ ||2P,
(**4**) Au| Pyr |2P| H ||2P,
(**5**) Au| S |2P| NH$_2$ ||2P,
(**6**) Au| CN |2P| H ||2P,
(**7**) Au| S |2P| H ||2P,
(**8**) Au| S |2P| F ||2P,
(**9**) Au| Pyr |2P| CN ||2P,
(**10**) Au| CN |2P| CN ||2P, and
(**11**) Au| S |2P| CN ||2P.

The pyridine docking group gives rise to the largest work function decrease, followed by the isocyanide (CN–) and the thiolate (S–).[70] As head groups, we studied the dimethylamine and amine group (–N(CH$_3$)$_2$ and –NH$_2$) as strong donors, hydrogen, the (weak) σ-acceptor –F and the cyano group (-CN) as a strong acceptor.[61] This allowed modifying the Au(111) work function over a huge range with a calculated $\Delta\Phi_{\mathrm{SAM}}$ ranging from -4.06 eV (**1**)[ii] to $+2.66$ eV

[ii] The analysis of the charge rearrangements resulting from the bond formation between systems **1** and **2** and the Au(111) surface (calculations performed in analogy, for example, to ref. 61) displays certain features related to electron accumulation located clearly above the

(**11**).[iii]

A challenge when setting up the model system is to determine the geometry of the SAM||2P interface. Its structure is primarily determined by van der Waals forces, which are not properly accounted for in DFT calculations based on state-of-the-art functionals such as the chosen PW91. Hence, the relative position of 2P with respect to the SAM had to be set "manually" starting from the experimentally determined bulk structure of 2P.[71] The 2P unit cell is, however, incommensurate with the dimensions of the $p(3 \times \sqrt{3})$ surface unit cell dictated by the periodicity of the SAM. We, therefore, assumed that at least the first monolayer of 2P at the SAM||2P interface adopts the same unit cell as the SAM with the 2P bulk unit cell stretched in x- and compressed it in y-direction ($+0.74/-0.52$ Å). The atomic positions within the distorted unit cell were then re-optimized (while fixing the z-coordinates of the lower-most hydrogens to keep the layer flat). This is reasonable, as (i) the distortion of the 2P unit cell leaves its volume virtually unchanged and (ii) the ability of organic thin films to act as templates for the heteroepitaxial growth of other organic layers has been observed experimentally.[72,73] The orientation of the substrate molecules was found to be the primary factor determining in organic/organic heteroepitaxial growth.[74] We, therefore, only studied upright standing 2P molecules and did not consider any geometries with 2P lying flat on the SAM. The distance between the SAM and the 2P layer was chosen to avoid overlapping van der Waals spheres, and its influence was carefully tested (for further details, see Methods section).

4.2.2 Level alignment

The key question to be addressed here is how the SAM-induced work-function change[61,70] affects the actual alignment of the electrode Fermi level relative to the energy levels of the subsequently deposited OSC, that is, the highest occupied and the lowest unoccupied π-states (HOPS/LUPS) of 2P. Three representative examples are shown in Fig. 4.3, where the Fermi energy (determined *de facto* by the metal) and the densities of states projected onto the SAM and the 2P regions are shown. HOPS and LUPS energies (E_{HOPS} and E_{LUPS}) are determined from the maxima of the corresponding peaks. The top horizontal lines in Fig. 4.3 denote the calculated vacuum-level energies above the respective surfaces (metal, metal|SAM, and complete system).

The system containing the biphenyl thiolate SAM (**7**) shown in Fig. 4.3a is an example for vacuum-level alignment at the SAM||2P interface. The work

---

head groups. At the time of publication, they were not understood but extensive tests had shown that they are not due to wrongly set parameters of the calculations. This issue has been resolved by now and is in detail described in Chapter 5.

[iii] These numbers represent fully self-consistent calculations; *i.e.*, effects like the mutual depolarization of neighboring molecules are fully taken into account. Moreover, in the computer experiments, SAM formation does not constitute a problem. In the real world, however, one can expect dipole-dipole repulsion to provide a significant experimental challenge for SAM formation especially for the systems implying the extreme values of $\Delta\Phi_{\text{SAM}}$.

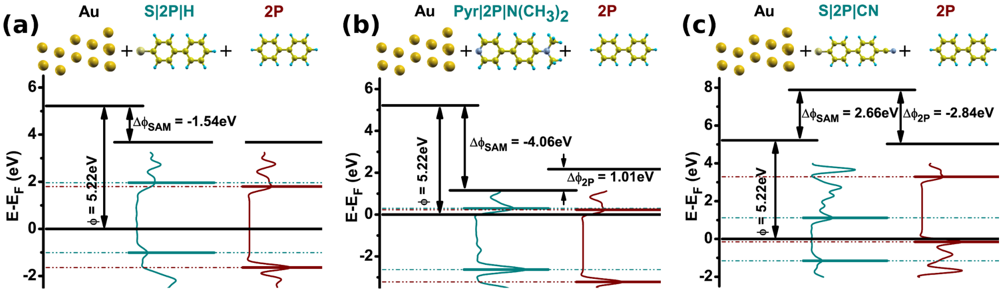

Figure 4.3: *Energy level schemes for three selected systems. The systems' Fermi level is shown together with the density of states projected onto the SAM and 2P atoms (cyan and red curves); the HOPS and LUPS are drawn as horizontal lines. The work-function Φ of gold and the work-function changes due to the SAM adsorption, $\Delta\Phi_{SAM}$, and the inclusion of the 2P layer, $\Delta\Phi_{2P}$, are also shown (when present). Vacuum-level alignment between the SAM and the OSC applies to system **7** (a). The Fermi level is pinned at the LUPS of 2P in system **1** (b) and at the HOPS of 2P in system **11** (c).*

function of gold is decreased by $\Delta\Phi_{\mathrm{SAM}}$ = -1.54 eV due to adsorption of the biphenylthiol SAM, and the addition of a monolayer of 2P on top of the SAM has no further effect on Φ. Here, the energetic distances of the Fermi level E_{F} to the HOPS and LUPS of 2P, $E_{\mathrm{F}} - E_{\mathrm{HOPS}}^{\mathrm{2P}}$ and $E_{\mathrm{LUPS}}^{\mathrm{2P}} - E_{\mathrm{F}}$, which can be taken as measures for the hole and electron injection barriers, are directly controlled by $\Delta\Phi_{\mathrm{SAM}}$.

The situation changes dramatically for metal electrodes covered by SAMs that induce particularly large work-function increases/decreases. If $\Delta\Phi_{\mathrm{SAM}}$ became negative (positive) enough, the LUPS (HOPS) of 2P would be shifted below (above) the Fermi level for vacuum-level alignment. In thermodynamic equilibrium, this is not possible. Instead, the Fermi level gets pinned close to the LUPS (HOPS) of the 2P layer (Fig. 4.3b,c). The consequence of this is a work function modification $\Delta\Phi_{\mathrm{2P}}$ that counteracts $\Delta\Phi_{\mathrm{SAM}}$. For the systems investigated here, pinning[66,75,76] of E_{F} close to the LUPS is seen in **1-3** and pinning close to the HOPS in systems **8-11**. The level diagrams for the case with the largest positive and negative $\Delta\Phi_{\mathrm{2P}}$, systems **1** and **11**, are shown in Fig. 4.3b,c, respectively.

The level alignments for all investigated SAM interlayers are summarized in Fig. 4.4 as a function of the work function of the SAM-covered Au(111) electrode, Φ_{mod}. The energetic difference between the Fermi level (characterizing the energy up to which the states in the metal are filled) and the 2P HOPS ($E_{\mathrm{F}} - E_{\mathrm{HOPS}}^{\mathrm{2P}}$, cyan diamonds) and 2P LUPS ($E_{\mathrm{LUPS}}^{\mathrm{2P}} - E_{\mathrm{F}}$, red circles) peaks is a measure for the electron and hole injection barriers. We find that the level alignments can be organized in three regimes: Fermi level pinning close to the LUPS of 2P, vacuum-level alignment (*i.e.*, the Schottky-Mott limit), and pinning close to the HOPS. Consequently, the SAM-induced work-function modification directly controls the charge carrier injection barriers only for a limited number of systems (**4-7**). In the other cases, the positions of the 2P

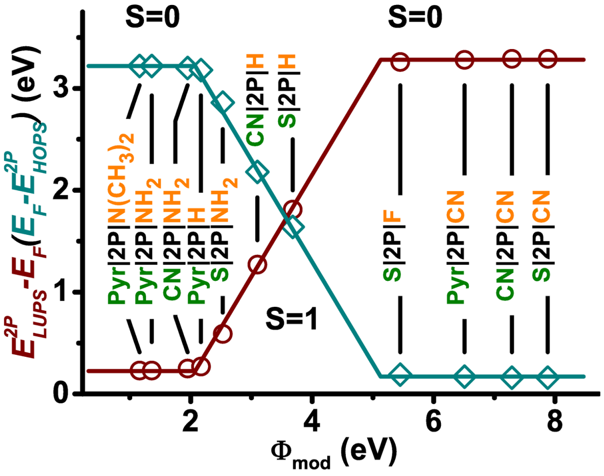

Figure 4.4: *$E^{2P}_{LUPS} - E_F$ (red circles) and $E_F - E^{2P}_{HOPS}$ (cyan diamonds) as a function of the work function of the SAM covered Au(111) electrode, Φ_{mod}. For the definition of the slope parameter S, see text. The values of E^{2P}_{LUPS} and E^{2P}_{HOPS} correspond to the peak positions in the respective molecular DOS. $E^{2P}_{LUPS} - E_F$ and $E_F - E^{2P}_{HOPS}$ are measures for the electron and hole injection barriers. The lines serve as guides to the eye.*

states are almost independent of $\Delta\Phi_{\mathrm{SAM}}$. The three regimes can also be distinguished on the basis of the slope parameter S:[60,75,77,78,iv]

$$S = -\frac{\mathrm{d}(E_{\mathrm{F}} - E^{\mathrm{2P}}_{\mathrm{HOPS}})}{\mathrm{d}\Phi_{\mathrm{mod}}} \qquad .$$

A value of S close to 1 is found when the vacuum levels align, and $S \approx 0$ when E_{F} is pinned close to the HOPS or LUPS of the 2P layer.

4.2.3 Organic-organic interfaces

In the absence of the metal, a completely different situation is encountered. In that case, pinning can occur only at the organic/organic interface to prevent the HOMO-derived band of one of the organic layers from lying above the LUMO-derived band of the other organic material. As examples, in Fig. 4.5, the situations for 2P on Pyr|2P|N(CH$_3$)$_2$ and HS|2P|CN are shown. In both cases, pinning of the Fermi level close to the LUPS and HOPS occurred in the full system (see Figures 4.3 and 4.4). In the absence of the metal, however, there is vacuum-level alignment at the Pyr|2P|N(CH$_3$)$_2$||2P interface, while pinning still occurs for HS|2P|CN||2P. Nevertheless, also in the latter case, the level alignment at the organic/organic interface is markedly different from the situation encountered when the metal is present; that is, $\Delta\Phi_{\mathrm{2P}}$ is reduced from −2.84 to −1.39 eV (*cf.* Figures 4.3 and 4.5).

[iv] In the article, because of a typo the denominator in the following formula reads d(Φ_{SAM}) instead of dΦ_{mod}.

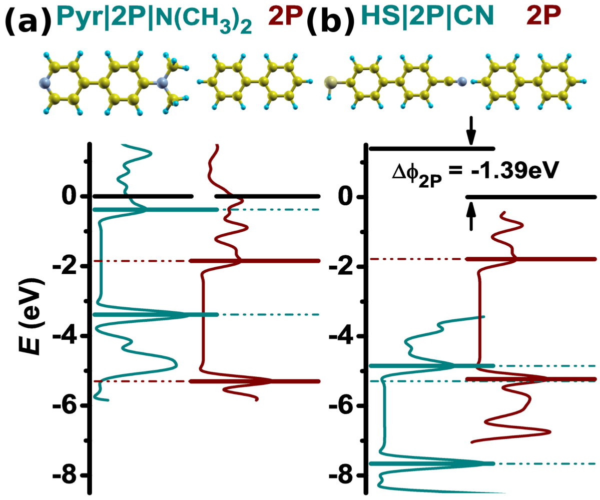

Figure 4.5: *Energy level schemes for the organic/organic interfaces Pyr|2P|N(CH_3)$_2$||2P (a) and HS|2P|CN||2P (b) in the absence of the substrate metal. The density of states projected onto the SAM and 2P atoms is shown around the band gap (cyan and red curves); the HOPS and LUPS are drawn as horizontal lines. The black horizontal lines show the vacuum levels at the substituent side of the SAM before 2P deposition (left part of each plot) and at the 2P side in the SAM||OSC system (right part). The latter is set as the origin of the energy axis.* $\Delta\Phi_{2P}$ *denotes the step in the electron electrostatic potential due to contact between the layers in analogy to the work-function changes in Fig. 4.3.*

A summary of the situation for all investigated systems is given in Fig. 4.6. There, the changes in the work function due to the presence of the OSC layer for the situations with and without metal substrate are compared. When the metal is present, $\Delta\Phi_{2P} \approx 0$ eV only for systems **4-7**, consistent with the vacuum-level alignment for these three systems shown in Fig. 4.4; for **1-3** and **8-11**, a linear dependence of $\Delta\Phi_{2P}$ on Φ_{mod} with a slope of approximately -1 is observed as expected for Fermi level pinning. In contrast, for the mere organic/organic interface, a significant deviation from vacuum-level alignment ($\Delta\Phi_{2P} \approx 0$ eV) is observed only for the three –CN substituted systems. There, if $\Delta\Phi_{2P}$ were also vanishingly small, the particularly large ionization potential on the –CN side of the SAM[61] would result in the HOPS of the 2P layer above the LUPS of the SAM inconsistent with thermodynamic equilibrium. The magnitude of $\Delta\Phi_{2P}$ in all three cases is independent of the docking group, in sharp contrast to the situation when the metal is present. This can be well understood by the fact that in the free-standing film only the head group modifies the ionization potential of the SAM on the side of the SAM where the OSC layer is deposited, which is the determining quantity for level alignment in that situation. The docking group impacts only the potential landscape at that respective side of the SAM[70] and, thus, has no impact on the level alignment between the SAM and the OSC (*cf.* the extensive discussion of SAM electrostatics in ref. 69).

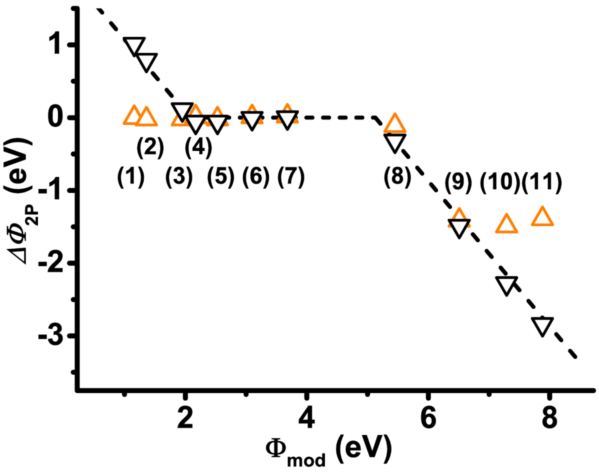

Figure 4.6: *Vacuum-level shift at the SAM||2P interface, $\Delta\Phi_{2P}$, as a function of the work function of the SAM-modified gold surface, Φ_{mod}. The downward triangles denote the situation for the three-component systems consisting of metal, SAM, and the organic semiconductor; the upward triangles represent the case when removing the metal (keeping Φ_{mod} unchanged). The dashed straight lines (with slopes of -1 and 0) serve as guides to the eye.*

4.2.4 Charge rearrangements

As the investigated systems including the metal substrate cover both vacuum-level alignment ($\Delta\Phi_{2P} \approx 0$ eV) as well as different degrees of Fermi level pinning ($\Delta\Phi_{2P} \neq 0$ eV), they allow a detailed analysis of the processes which lead to a nonvanishing $\Delta\Phi_{2P}$ in the latter case. The work-function modification $\Delta\Phi_{2P}$ is connected via the Poisson equation to a change in the charge density upon addition of 2P ($\Delta\rho = \rho_{\text{metal|SAM||2P}} - (\rho_{\text{metal|SAM}} + \rho_{\text{2P}})$; *cf.* Methods section).[61] As long as the charge transfer to/from the 2P layer remains small enough so that its eigenstates are not significantly modified, $\Delta\rho$ also directly affects the carrier injection barriers.[70]

For system **7**, which represents the vacuum-level alignment regime ($S = 1$), the charge rearrangements (integrated over the x, y-plane of the unit cell) are depicted as solid lines in the uppermost panel of Fig. 4.7a. Reminiscent of Pauli repulsion at metal/organic contacts, electron density is pushed back from the interface into the two monolayers in a close to symmetric way. The net charge transfer across the SAM||2P interface can be obtained by integrating over $\Delta\rho(z)$. The quantity $Q(z) = \int_0^z \Delta\rho(z')\mathrm{d}z'$ describes the total amount of charge per unit cell which is shifted from above to below a plane at position z (see middle panel of Figure 4.7a). The fact that $Q = 0$ right at the interface between the SAM and 2P for system **7** means that there is no net charge transfer between the two layers. Consistently, the electrostatic energy $E(z)$ obtained from solving the one-dimensional Poisson equation shows a small dip directly at the interface, but then virtually recovers its original value (Fig. 4.7a, bottom panel). The situation changes slightly for substituted SAMs: there, the interface becomes "asymmetric", that is, there is a nonvanishing charge transfer

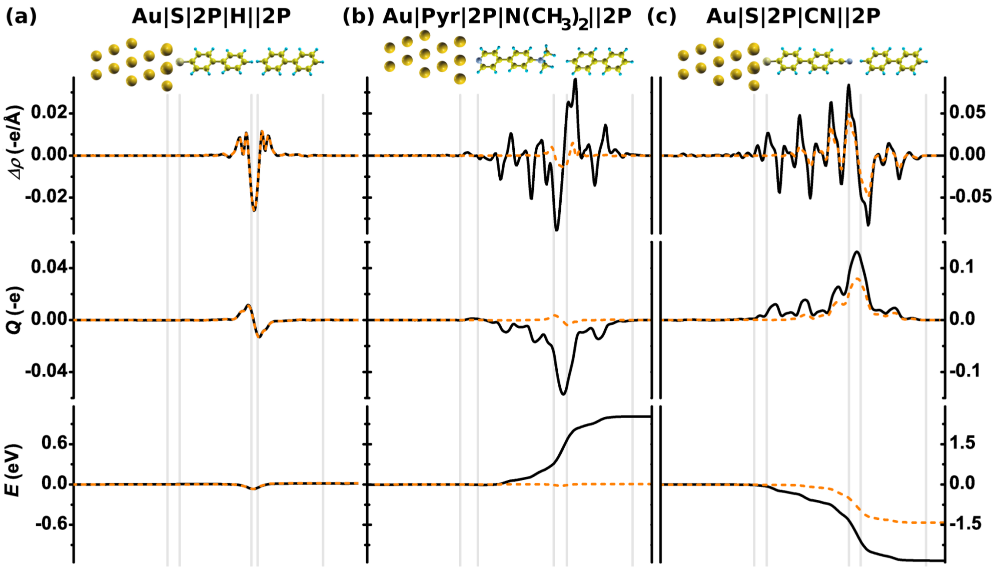

Figure 4.7: *Plane-integrated charge rearrangements, $\Delta\rho$, per unit cell (topmost panels), cumulative charge transfer along the z-axis per unit cell, Q (middle panels), and change in the potential energy of an electron, E, upon addition of 2P to the system (bottom panels) for systems **7** (a), **1** (b), and **11** (c); $\Delta\rho > 0$ indicates an increase of the electron density, and $\Delta\rho < 0$ a decrease. Black lines show the results for the addition of 2P to a metal|SAM systems, dashed orange lines for the pure SAM||2P interfaces. The y-scales in (c) differ by a factor of 2.5 from the respective scales in (a) and (b). Vertical lines and schematic pictures of the systems in the background serve as guides to the eye.*

between the head group and the neighboring part of the biphenyl layer. The consequence of this effect on the electron potential energy, E, however, remains <0.2 eV in the “vacuum-level alignment” regime.

In contrast, in the pinning cases, the significant values of $\Delta\Phi_{\mathrm{2P}}$ must be caused by some charge transfer. Intuitively, one might expect that this charge transfer should be between the OSC layer and the metal, as it prevents the occupied (unoccupied) states of the 2P layer from lying above (below) the metal Fermi level in thermodynamic equilibrium. Bearing in mind the large charge transfer distance, the absolute magnitude of the transferred charge could be comparably small to yield the necessary shift of the levels. The dominant role of the metal for the Fermi level pinning is also underlined by the observation that the pinning situation described above is observed only as long as the metal is present. Indeed, in a purely inorganic system, namely, for small Au islands separated from a Ag(001) surface by an insulating MgO layer, Simic-Milosevic *et al.*[79] found that electrons were transferred from the Ag/MgO interface region onto the Au islands.

Considering all that, it comes as a surprise that nothing like a metal to OSC charge transfer is observed in any of the investigated systems (*cf.* solid lines in Fig. 4.7b,c): The situation for the HOPS pinning case with the largest $\Delta\Phi_{\mathrm{2P}}$

(Au|S|2P|CN||2P; system **11**) is depicted in the uppermost panel of Fig. 4.5c. There is no long-range charge transfer between 2P and the Au substrate. Instead, two other effects give rise to $\Delta\Phi_{\mathrm{2P}}$: (i) Significant electron transfer occurs in the SAM||2P interface region from the 2P layer to the SAM as evidenced by pronounced peaks in $\Delta\rho$ and Q, which result in a sharp drop in the electrostatic energy E. (ii) Additionally, the SAM is polarized; that is, charge is redistributed within the SAM giving rise to a series of dipoles (see $\Delta\rho$ plot). The long-range transfer within the SAM remains relatively small as seen in the plot of Q. As a net effect, the potential energy drops by -2.84 eV, preventing the 2P HOPS from lying above E_{F} (compare Fig. 4.3c). The overall situation for LUPS pinning in Au|Pyr|2P|N(CH$_3$)$_2$||2P (system **1**) is depicted in Fig. 4.7b. The main qualitative difference to HOPS pinning is a reversal of the sign of the charge rearrangements, which is consistent with a reversal of the sign of $\Delta\Phi_{\mathrm{2P}}$. The notion that the observed charge rearrangements are characteristic of Fermi level pinning for OSCs on SAM-covered metals rather than a mere consequence of some type of surface reaction between the head groups of the SAM and the 2P layer is supported (i) by the fact that a qualitatively similar behavior is observed in all studied pinning cases and (ii) by the observation that $\Delta\rho$ extends over the whole SAM instead of just across the interfacial region.

As far as the metal-free systems are concerned (dashed lines in Fig. 4.7), there is no difference to the full system for **7**. As expected, also in **1** nothing but Pauli pushback in the immediate vicinity of the interface is observed (here in sharp contrast to the situation when the metal is present). For the situation where pinning occurs also at the organic/organic interface (shown here for **11**), the structure of the charge rearrangements in the region of the SAM||2P interface is similar to the situation observed when the metal is present (albeit with a smaller magnitude of $\Delta\rho$). The charge rearrangements on the phenyl ring next to the metal substrate, however, vanish in the purely organic/organic case; that is, the role of SAM polarization diminishes in the metal-free case.

In conclusion, inserting a SAM allows controlling the energy level alignment between an electrode and an organic semiconductor over a certain range in which vacuum-level alignment occurs between the SAM and the OSC. Beyond that range, which is determined by the energy gap of the OSC, Fermi level pinning close to the OSC states is observed and an additional work-function change $\Delta\Phi_{\mathrm{2P}}$ counteracts the SAM-induced work-function modification. The pinning situation changes completely in the absence of the metal. Nevertheless, in spite of the fact that the pinning and the magnitude of $\Delta\Phi_{\mathrm{2P}}$ are a clear consequence of the presence of the metal substrate, they are not related to any (long-range) charge transfer between the metal and the OSC. Instead, pinning is found to be a consequence of SAM backbone polarization in addition to local charge transfer at the organic-organic interface.

4.3 Methods

The density functional theory calculations were performed using the VASP code.[80] Valence electrons were described by a plane wave basis set (kinetic energy cutoff approx. 20 Ry) and valence-core electron interactions by the projector augmented wave (PAW) method.[81] A $5 \times 8 \times 1$ Monkhorst-Pack[82] k-point grid was chosen. A Methfessel-Paxton[83] occupation scheme with a broadening of 0.2 eV was used. In one case, CN|2P|H||2P, the smearing was reduced to 0.05 eV to prevent artifacts due to negative occupancies near E_F. Geometry relaxations were stopped as soon as all forces fell below 0.01 eV/Å. For electronic relaxations, two separate convergence criteria were applied: a stable dipole moment (tolerance: $\Delta\mu_z < \pm 0.002$ eÅ) over several self-consistent cycles, and a total energy $\Delta E < 1 \cdot 10^{-4}$ eV. The metal was resembled by five layers of Au(111) atoms. During geometry relaxations, the coordinates of the lower three layers were fixed (representing the bulk), while the upper two layers (representing the surface) were free to move. The pure organic/organic systems differ from the complete systems only by the removal of the metal atoms. No additional geometry optimizations were performed. Only in case of the thiolate docking group, a saturating hydrogen was added to the sulfur. The charge density differences $\Delta\rho$ were obtained by subtraction of the densities of the isolated parts of a system from the density of the corresponding system, that is, $\Delta\rho = \rho_{\mathrm{metal|SAM||2P}} - (\rho_{\mathrm{metal|SAM}} + \rho_{\mathrm{2P}})$ and $\Delta\rho = \rho_{\mathrm{SAM||2P}} - (\rho_{\mathrm{SAM}} + \rho_{\mathrm{2P}})$ for the full systems and the pure organic/organic interfaces, respectively. The one-dimensional plots were then generated by integration over the x, y plane of the unit cell, hence displaying the charge rearrangements per unit cell. Further details regarding the applied computational methodology and the used parameters are given in ref. 62. Three-dimensional representations of the systems were generated using XCrysDen.[84]

It should be noted that DFT calculations are known to notoriously underestimate the band gap of semiconductors (most relevant here for the 2P layer). An improved description could, for example, be achieved within the GW approximation.[85] Also, the band gap reduction in the vicinity of a metal as observed in three-terminal single-molecule devices[86] reminiscent of the Newns-Andersen model[87,88] could be accounted for in this way.[85] GW calculations for the present systems are, however, far beyond computational capacities. As our work is concerned with conceptual effects at metal/SAM/OSC interfaces, this poses no major problem. Moreover, focusing on the relative positions of energy levels, the following fundamental conclusions can be expected to hold largely independent of the chosen conjugated system. In fact, the "$1/n$ law" that the band gap of oligophenylenes decreases with increasing number n of phenyl rings renders DFT-calculated 2P *de facto* a suitable model for some longer chain oligomers.

When putting the 2P layer on top of the SAM, the strategy described in the Results and discussion section was pursued. In particular, the distance between the SAM and the 2P layer was chosen to avoid overlapping van der Waals spheres. The used geometries are supplied in Supporting Information.[i] We also carefully tested the dependence of the results on the variation of the distance between the SAM and 2P ($\Delta z = \pm 0.3$ Å) and on their relative in-plane alignment. The maximum changes in energy level alignments due to both kinds of variation were < 0.05 eV for all SAM head groups. Also, as far as the charge rearrangements and related quantities were concerned, the qualitative picture remained unchanged and also quantitative deviations were minor; this is discussed in detail in ref. 34.

Acknowledgment. Support by the European Commission through the STREP project ICONTROL (EC-STREP-033197) and by the FWF through project P20972-N20 is gratefully acknowledged. We thank the ZID of the TU Graz for providing computational resources. G.H. acknowledges financial support by the DFG through Sfb448 “Mesoscopically Organized Composites”.

Appendix 4.A

In this section, the above-described results shall be discussed in the context of the ICT (integer charge transfer)[67,75,76,89–92] and IDIS (induced density of interface states)[67,93–95] models. This is useful as (i) both models have been used to explain the properties of organic/organic interfaces also including the influence of a metal substrate,[65,66] and (ii) in particular the ICT approach has been used to successfully rationalize Fermi level pinning.[67,92]

Within the IDIS model, a notable perturbation of the molecular DOS is assumed when a molecule approaches a surface, even if the interaction between the two materials can be regarded as weak.[94] This modified DOS can be determined,[94] and by filling it with the charge of the isolated, neutral molecule, the charge neutrality level (CNL) is obtained. The position of the CNL is found to be quite insensitive to the interaction strength between the organic and the metal[93–95] and can hence be treated as an intrinsic property of the organic. If an organic heterojunction is in contact with a substrate, the unified IDIS model predicts the vacuum-level shift to be

$$\Delta\Phi_{\mathrm{2P}} = (1 - S_{\mathrm{OO}}) * (E_{\mathrm{CNL}} - \Phi_{\mathrm{mod}}) \qquad ,$$

where E_{CNL} is the charge neutrality level of the topmost organic layer (in our case 2P), Φ_{mod} is the Fermi energy of the SAM-covered substrate (*cf.* Fig. 4.6) and S_{OO} is a screening parameter depending only on the two organic materials.[65] The problem that arises when applying this model to the full set of systems that we investigated here is that, as E_{CNL} is regarded as an intrinsic property of the OSC, the screening parameter has to be one in the vacuum-level alignment regime (systems **4-7**) and then needs to change abruptly to zero when pinning occurs. Even if this were the case, pinning at the HOPS would be observed only if E_{CNL} were equivalent to the HOPS energy (**8-11**), while it needed to correspond to the LUPS for **1-3**. In that case, E_{CNL} can no longer be a materials parameter of the OSC in contradiction to the original assumption of the IDIS model. For a CNL within the gap, S_{OO} would effectively have to be a function of Φ_{mod} in order to predict the results depicted in Fig. 4.6, and hence would not only be determined by the two organic materials.

In contrast to the IDIS model, the ICT approach assumes that no significant hybridization occurs between the states at the interface.[66,67,89,92] This appears reasonable, as the model is typically applied to systems, where the OSC in question is separated from the conducting substrate by an insulating layer or another relatively thick OSC layer. A consequence of this lack of hybridization is that only an integer number of charges can be transferred between the conducting substrate and the organic layer. The slope parameter, S, becoming zero for certain substrate work functions as observed also in Fig. 4.4[66] is then associated with charge transfer to polaronic or bipolaronic levels of the OSC (the ICT states) together with a pinning of the Fermi level at these states. The ICT states are often found deep within the gap of the organic semiconductor, in particular, when dealing with amorphous materials or systems disordered at least at the interface. In such materials, charges are highly localized. The situation changes in highly crystalline and well-ordered substances with delocalized charges, where the pinning levels approach the original positions of the bands of the molecular crystals.[67,92] Intrinsically, only the latter case can be the outcome of a band structure calculation (unless inaccessibly large super cells were used). Considering these aspects, the results of the ICT model well match the outcomes of our study. Here, it needs to be mentioned that, in our calculations, the actual pinning position is influenced by the applied smearing of the electronic occupations which amounts 0.2 eV in the presented data.

Chapter 5

Electronic structure of pyridine-based SAMs on flat Au(111) surfaces: extended charge rearrangements and Fermi level pinning (ref. 96)

The previous chapter discussed pinning of a physisorbed layer on top of a SAM. One can instead also focus on the electronic states of the SAM itself. Actually, a case where the (unoccupied) states also in the SAM are pinned was found already in that chapter (see Fig. 4.3b) and another case of a LUMO-pinned pyridine-docked SAM was reported in ref. 70. To understand the relevant mechanism, the present chapter systematically varies the backbone length and tail group of such SAMs. This allows changing the energy and spatial distribution of the LUMO-derived band in order to understand to what extent the spatial shape of the pinned states controls the charge rearrangements upon binding.

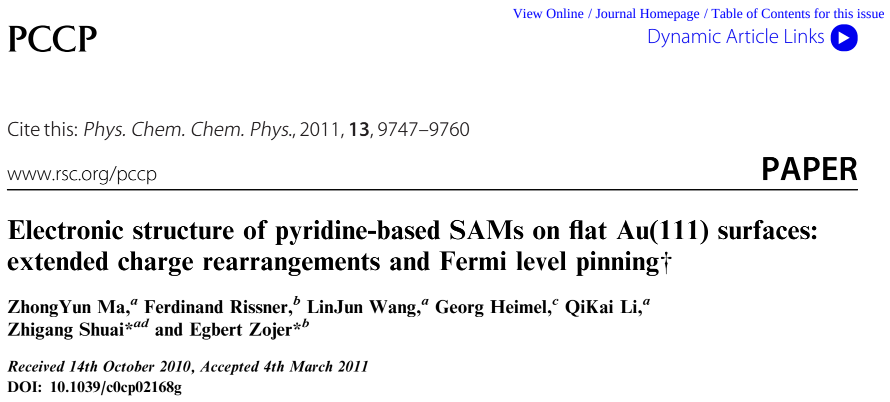
PCCP

View Online / Journal Homepage / Table of Contents for this issue
Dynamic Article Links

Cite this: *Phys. Chem. Chem. Phys.*, 2011, **13**, 9747–9760

www.rsc.org/pccp

PAPER

Electronic structure of pyridine-based SAMs on flat Au(111) surfaces: extended charge rearrangements and Fermi level pinning†

ZhongYun Ma,[a] Ferdinand Rissner,[b] LinJun Wang,[a] Georg Heimel,[c] QiKai Li,[a] Zhigang Shuai*[ad] and Egbert Zojer*[b]

Received 14th October 2010, Accepted 4th March 2011
DOI: 10.1039/c0cp02168g

Figure 5.1: *Header of the article ref. 96 showing its title and all contributing authors. Part of it including part of its ESI† are discussed in the following.*

This work was published[96] (Fig. 5.1) and only the part of it I have made significant contributions to (see Author contributions) is reproduced below.[i]

Author contributions. ZhongYun Ma came up with the idea of looking at pinned SAMs, has done nearly all of the calculations, and has written the initial drafts of the manuscript. Consequently, he is the first author of the article.[96] My most important contribution was interpreting and analyzing the results related to pinning together with ZhongYun. Specifically, this is the data presented in Fig. 5.4, the central plot of this work. The most surprising results are related to systems containing an amine tail group, where accumulation of charge *above* the SAM molecules was seen (see also refs. 34 & 50). To exclude that this resulted from methodological mistakes, I have done extensive tests. They are discussed in Sec. 5.4.4, which reproduces part of the Electronic supplementary Information[i] (ESI) of the original article. I will only mention the parts I have not contributed to significantly where they provide a necessary context. This is (i) a discussion of the binding process of the studied systems and (ii) the rather complicated electronic structure of the freestanding monolayers (before binding to the metal). Close lying σ- and π-states amongst the highest *occupied* orbitals made the analysis of these systems tricky and this is discussed in the original article in great detail. This was to a large extent done by Egbert Zojer, who has spent *a lot* of time understanding the changes in the electronic structure upon binding. He has further streamlined and improved the manuscript to be accessible to a broader audience.

Abstract. Density functional theory calculations are used to investigate the electronic structure of pyridine-based self-assembled monolayers (SAMs) on an Au(111) surface. We find that, when using pyridine docking groups, the bonding-induced charge rearrangements are frequently found to extend well onto the molecular backbone. This is in contrast to previous observations for the chemisorption of other SAMs, *e.g.*, organic thiolates on gold, and can be explained by a pinning of the lowest unoccupied states of the SAM at the metal Fermi-level. The details of the pinning process, especially the parts of the molecules most affected by the charge rearrangements, strongly depend on the length of the molecular backbone and the tail-group substituent. We also mention methodological shortcomings of conventional density functional theory that can impact the quantitative details regarding the circumstances under which pinning occurs and highlight a number of peculiarities associated with bond dipoles that arise from Fermi-level pinning.

5.1 Introduction

The main quantities of interest in the context of using SAMs in molecular/organic electronic devices are the SAM-induced work-function modification, $\Delta\Phi$, and the level alignment between the highest occupied and the lowest unoccupied

---

[i] Reproduced by permission of the PCCP Owner Societies. The original version is available online at `http://dx.doi.org/10.1039/c0cp02168g`.

π-states of the SAM (the HOPS and the LUPS) and the metal Fermi-level.[31,69] Processes crucially important for these quantities are the charge density rearrangements at the interface, $\Delta\rho_{\text{bond}}$, which are caused by the chemical bonding between the organic molecules and the metal surface. They induce a bond dipole (BD) at the interface that directly modifies $\Delta\Phi$ and ΔE_{LUPS} by an amount ΔE_{BD}.[69] In previous studies dealing with various molecules on Au(111) or Ag(111) surfaces, it has been found that the charge rearrangements in most instances are very much localized in the immediate vicinity of the docking group and the adjacent Au atoms.[61] This is in particular true for the commonly used thiolates, as has recently been confirmed by a comparative cluster-based study using density functional theory and Hartree–Fock based methods including also hybrid functionals.[97]

Also for pyridine docking groups, bonding-induced charge rearrangements confined to the interface have been found in certain systems.[98] However, especially for more extended conjugated backbones, they have also been observed to extend over a significant part of the molecules.[70] This has been attributed to Fermi-level pinning, which gives rise to particularly small charge injection barriers turning pyridine into a promising linker in molecular electronics for efficient electronic conductivity. In fact, pyridines have been used to secure molecular wires onto metal surfaces and between two metal electrodes,[99–105] and the pyridine–gold interaction was considered as both reasonably strong and highly flexible.[98]

In this contribution, we describe in detail the pinning process in pyridine linked SAMs, discussing the impact of both the length of the conjugated backbone and various tail-group substitutions (*cf.*, Fig. 5.2a), using DFT. For that, the systems studied here are an ideal test-bed, as, depending on the length of the backbone and the tail-group substituent, the frontier orbitals at which pinning occurs are localized on different parts of the molecules. Even if the latter were to some extent affected by shortcomings of current state of the art DFT (as will be discussed in the Methodology section), this does not affect the main conceptual conclusions of the paper linking orbital localization and Fermi-level pinning.

After a brief description of the studied model systems, we will describe and then critically evaluate the applied methodology. Then the hypothetical case of free-standing monolayers (*i.e.*, the situation in the absence of the gold substrate) is briefly described, followed by the central results of the work: the charge rearrangements resulting from the metal–SAM bonding with a particular focus on the details of pinning.

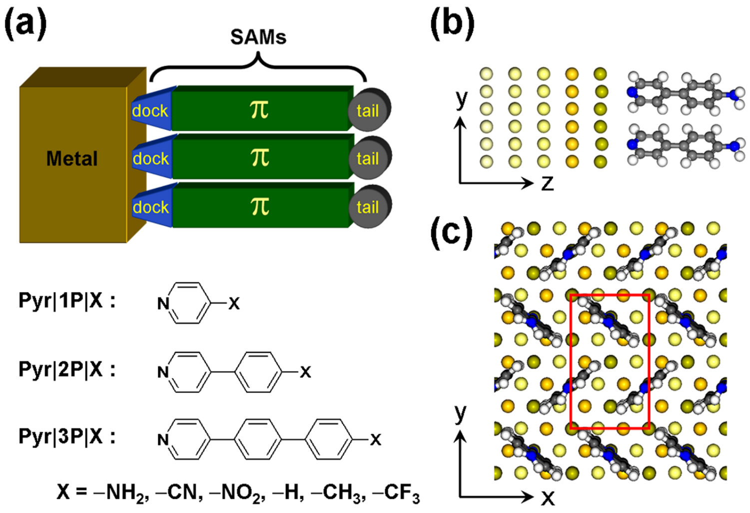

Figure 5.2: *(a) Top: Schematic representation of the metal/SAM systems investigated in this work. The SAM consists of the docking group (dock), the π-conjugated core (π), and the tail group (tail); bottom: nomenclature and chemical structures of the investigated molecules. 'X' denotes the tail-group substituent (see text). (b) Side and (c) top view of Pyr|2P|NH$_2$ as a representative SAM on a five-layer Au(111) slab. The red rectangle in (c) highlights the $p(3 \times \sqrt{3})$ surface unit cell. The various Au layers are displayed with different shading to ease the comparison between top- and side-view.*

5.2 Studied model systems

In Fig. 5.2a, we show the schematic structure of the SAM/metal interface. As a substrate, we choose a flat Au(111) surface as a reasonable first approximation, considering the fact that even for the much more widely investigated thiolates on Au, the details of the surface structure are still heavily debated (*cf.* corresponding discussion in refs. 3 & 31). Also for pyridines, different docking structures have been considered: Hou *et al.*[106] have shown by computational modeling that when pyridines adsorb on an Au ad-atom rather than a flat Au surface, this results in a shift of the molecular levels relative to the metal states in a way that Fermi-level pinning of the LUPS is favored. For the systems investigated here it can, thus, be concluded that the main impact of adsorption through an ad-atom would be the occurrence of Fermi-level pinning also in some of the few cases in which it does not happen on a flat surface. For systems that are pinned already on a flat surface docking through an ad-atom would merely increase the magnitude of the involved charge rearrangements.

It should also be mentioned that a variety of contact geometries has been considered in transport studies paying particular attention to the role of additional Au atoms in hollow sites on the Au(111) surface adjacent to the docking site. Both, for pyridine docked to a nominally flat surface[107] as well as for pyridines docked through ad-atoms[103] the calculations showed that the extra Au atoms shift the transmission spectra to higher energies. In fact, for transport measurements also the orientation of the molecular backbone relative to the electrodes has been shown to play a crucial role.[105] While such strongly tilted molecules are a realistic scenario in break-junction transport measurements, they should, however, not occur in the densely packed SAMs considered here.

The SAMs consist of three components, the docking groups, the backbones, and the tail-group substituents. In the present study, docking to the Au(111) surface occurs through the N atom of a pyridine ring, –Pyr; the length of the conjugated backbone varies from one to three rings (1P, 2P and 3P), and one electron donating (–NH_2) and two electron accepting (–CN and –NO_2) substituents have been considered for all conjugation lengths (see Fig. 5.2a). To get a comprehensive understanding of the tail-group substituent effect on the electronic structure of SAM-modified gold surfaces, we additionally include –H, –CH_3 and –CF_3 tail groups for the shortest backbone, 1P. In this context it should be mentioned that the dipole moments due to the tail-group substituents might have an adverse effect on the SAM-forming properties in experimental studies using the above-mentioned molecules. Monolayers of related molecules docked via thiolates have, however, been successfully investigated employing a variety of polar tail group substituents.[68,108–114]

In the following, we will use the nomenclatures Pyr$|n$P$|X$ and Au$|$Pyr$|n$P$|X$, with nP denoting a backbone with n rings (where the first ring is always the pyridine) and X specifying the tail-group substituent. The former syntax denotes the isolated monolayer, while the latter specifies the SAM bonded to the Au substrate.

To realize periodicity in two dimensions, we employed the repeated-slab approach. Five layers of gold atoms were used to represent the Au(111) surface (Fig. 5.2b), and two pyridine-based molecules were arranged in a p$(3 \times \sqrt{3})$ surface unit cell in a typical herringbone pattern (Fig. 5.2c). Following Bilić *et al.*,[98] we chose close to upright standing pyridines with the nitrogen atoms in the pyridine rings on-top of Au atoms as a starting geometry. A vacuum gap of > 20 Åwas introduced between the uppermost atom of the molecule and the subsequent periodic image of the slab to exclude spurious electronic interaction between neighboring slabs; to suppress the artificial electric field arising from imposing the periodic boundary conditions on the asymmetric slabs, a self-consistently determined dipole layer was introduced into the vacuum gap.[32,115] Isolated molecules were calculated in a 3D periodic box with the dimensions of $40 \times 40 \times 40$ Å.

5.3 Methodology

All calculations presented here are carried out using the Vienna *ab initio* Simulation Package (VASP)[80,116–118] at the DFT level. The PW91 exchange–correlation (*xc*) functional is chosen[119] using a plane-wave basis set with an energy cutoff of 20 Ryd. The projector augmented-wave method (PAW)[81,120] was applied to describe the valence-core interactions, which allows the use of the relatively low kinetic energy cutoff. For the self-consistent field calculations, we used an $8 \times 5 \times 1$ Monkhorst–Pack grid[82] of k-points together with a Methfessel–Paxton occupation scheme[83] and a broadening of 0.2 eV. Only spin-restricted (*i.e.*, unpolarized) calculations are reported here. When performing geometry optimizations, all atoms of the SAM and the top two gold layers were fully relaxed until the largest remaining force component was smaller than 0.01 $\mathrm{eV\,Å^{-1}}$, while the bottom three gold layers were kept fixed at their bulk positions with a lattice constant of $a_{\mathrm{fcc}} = 4.175$ Å.[62] A previous study based on optimizations with Cartesian coordinates in VASP has shown that the total energy is rather insensitive to the tilt angle of the long axes of the molecules with respect to the surface normal up to tilts of 15°.[98] In view of the tilt angle being a crucial parameter for the determination of the SAM-induced work-function modification and, thus, to obtain a better converged value for the molecular tilt, a recently developed geometry optimization scheme based on internal coordinates and the Direct Inversion in the Iterative Subspace (DIIS) algorithm has been used in combination with the external optimization tool GADGET.[121] In all systems studied here, the energy of the configuration obtained applying this strategy is lower than that achieved by the conventional strategy[62] employing the native damped molecular dynamics optimizer of VASP together with Cartesian coordinates. Although the differences are small (< 0.02 eV) for all pyridine based systems studied here, we found that the internal coordinate based optimizations give geometries that depend less on the initial starting geometries, making the results significantly more reproducible. All 3D isodensity representations shown throughout this paper and in the Electronic Supplementary Information[i] are produced using XCrySDen.[84]

As in this work we will be interested in pinning effects, a crucial parameter is the energetic alignment between the various SAM states and the metal Fermi-level. Therefore, especially the well known incorrect description of energy gaps by conventional DFT calculations needs to be addressed. The encountered problems include (i) the lack of derivative discontinuity of the functionals and the occurrence of the self-interaction error,[38] and (ii) the fact that screening at the metal–organic interface is not captured properly.[88,122] Factor (i) results in a too small gap and, therefore, "favors" Fermi level pinning;[ii] this complication is, however, at least partially offset by (ii), as the screening-induced narrowing of the gap of molecules above a metal is not captured by DFT; *i.e.*, one is dealing with a fortuitous partial cancellation of errors. Indeed, using the approach outlined above, good agreement between theory and experiment has been obtained for physical observables such as the adsorption-induced work-function change in a number of pinned systems. These include the strong

---

[ii] Note that the resulting incorrect description of the charge transfer can under certain circumstances also result in an incorrect value for the charging-induced shifts of the orbital energies. For isolated molecules, this effect can be very large,[123] although in the SAM its impact will be mediated by the very different far-field arising from collective effects, that has been discussed by Natan *et al.*[30]

acceptor F4TCNQ[124,125] and also PTCDA[126,iii] lying more or less flat on the (111) surfaces of all coinage metals and also the strong donors MV0[127] and TDAE[128] on Au(111). In fact, we are not aware of a case in which contradicting theoretical and experimental results have been documented. This is, however, certainly also a consequence of most investigated systems (especially all mentioned above) representing "strongly pinned" situations where very large charge transfer from/to the frontier orbitals occurs. In such cases, an incorrect description mostly affects the exact amount of transferred charge but not the level alignment. Regarding the nature of the frontier orbitals, one also must not forget that the self-interaction error more severely affects localized than delocalized orbitals,[42] which can result in some re-ordering of the states.

In isolated molecules, the use of hybrid functionals usually yields eigenvalues which compare well with experiment.[129–133] For extensive periodic calculations including metal substrates, hybrid functionals are, however, prohibitively expensive and would also not account for the above mentioned polarization effects (thus, potentially adversely affecting the above mentioned fortuitous cancellation of errors). Moreover, when studying the adsorption of CO on late 4d and 5d transition metal (111) surfaces using a number of non-local functionals, Stroppa and Kresse found that including non-local exchange "improves some but worsens other properties".[134] Nevertheless, we performed single-point calculations with the HSE functional on suitably small test systems, namely the free-standing Pyr|1P|H and Pyr|1P|NH_2 monolayers. There we did not observe inconsistencies compared to the PW91 calculations (for more details see ESI[i]).

Another shortcoming of (semi)local DFT, namely the neglect of van der Waals interactions is less of an issue here: First, it has been shown by Bilić *et al.*[98] that the PW91 functional provides a very reasonable description of the Au–pyridine bond. Secondly, the dimensions of the SAM unit cell are primarily determined by the periodicity of the Au(111) surface. Thus, van der Waals interactions, in a first approximation, will only affect the backbone tilt of the molecules. As we are dealing with densely packed SAMs, also this effect can be expected to be small. This can, for example, be inferred from a comparison of the measured reorientation of anthracene under hydrostatic pressure with calculations based on the local-density approximation as well as on gradient-corrected functionals.[135]

Finally, especially for the amine-substituted systems, also the choice of the basis set turns out to be an important issue, as is discussed in detail in the ESI[i] of the original article and also reproduced here in Sec. 5.4.4. We show that with an atomic-orbital type basis that does not include diffuse basis functions, qualitatively incorrect results are obtained. With the plane-wave basis used in the Vasp calculations one is, however, on the safe side and close to the situation

---

[iii] The only complication in the case of PTCDA is that there the neglect of van der Waals interactions results in a non-bonded situation and agreement with experiment is found only, when the adsorbate layer is put to the experimental adsorption distance.

that has been characterized as the complete-basis-set limit in ref. 98.

In conclusion, as far as quantitative predictions are concerned, the following results are certainly adversely affected by the above discussed, well known, shortcomings of DFT. Nevertheless, the main physical consequences, in particular the fundamental conclusions, through what mechanisms pinning occurs in SAMs and how it can, in general, influence bonding-induced charge rearrangements should not be affected.

5.4 Results and discussion

5.4.1 The isolated molecular monolayer

To understand the electronic structure of the interfaces formed between the metal and the SAM, it is useful to first discuss the hypothetical case of a free-standing monolayer (*i.e.*, in the absence of the gold substrate). In these calculations, the SAM atoms are frozen at the positions they adopt in the optimized geometry of the combined system. In Fig. 5.3a, the calculated electron electrostatic energy averaged over the x, y-plane of the unit cell is shown for Pyr|1P|CN as a representative example. As expected from fundamental electrostatics, the dipolar layer that the SAM approximately represents splits space into a region "left" of the docking-group ends of the monolayer with a vacuum level denoted by $E_{\mathrm{VL}}^{\mathrm{dock}}$ and a region "right" of the tail-group end of the monolayer with a vacuum level at $E_{\mathrm{VL}}^{\mathrm{tail}}$. The jump in vacuum energies, ΔE_{vac}, is related to the component of the molecular dipole moments perpendicular to the substrate, $\mu_{\perp}$, per unit-cell area, A, attenuated by an effective parameter describing depolarization by the neighboring dipoles, ϵ_{eff}:

$$\Delta E_{\mathrm{vac}} = -\frac{e\mu_{\perp}}{A\epsilon_0\epsilon_{\mathrm{eff}}} \tag{5.1}$$

Note that the latter must not be confused with the dielectric constant of the monolayer. Deviations arise especially for densely packed layers, where the internal field due to the tail-group substituents and, consequently, also the resulting charge rearrangements (related to ϵ_{eff}) qualitatively differ from the situation when applying a homogeneous field (associated with the dielectric constant) (for more details see ref. 136).

Due to the two different vacuum levels, the energy to remove (add) an electron from (to) the docking-group side differs from that for the tail-group side (see Fig. 5.3). Consequently, there are two ionization potentials (electron affinities), $\mathrm{IP}^{\mathrm{dock}}$ and $\mathrm{IP}^{\mathrm{tail}}$ ($\mathrm{EA}^{\mathrm{dock}}$ and $\mathrm{EA}^{\mathrm{tail}}$). Interestingly, as described first in ref. 61 for thiolates, changing the tail-group modifies the electrostatic energy only in the region of the substituent. The energy landscape in the region of the pyridine ring remains virtually unaffected by the different substituents (see Fig. 5.3b).

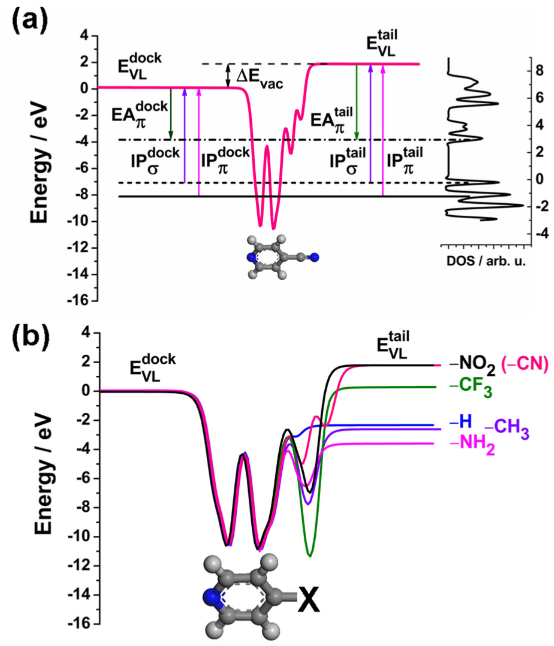

Figure 5.3: *Plane-averaged electron electrostatic energy of free-standing 2D molecular layers consisting of donor- and acceptor-substituted pyridines. (a) shows the representative case Pyr|1P|CN. For this layer also the two highest occupied and the lowest unoccupied bands are included and the meanings of the various ionization potentials and electron affinities are explained. These include the docking-group side and tail-group side vacuum level energy (E_{VL}^{dock} and E_{VL}^{tail}), the corresponding ionization potentials (IP_{σ}^{dock}, IP_{σ}^{tail}, IP_{π}^{dock} and IP_{π}^{tail}), as well as the electron affinities (EA_{π}^{dock} and EA_{π}^{tail}). The EA_{π}-values for all tail groups are given in Tab. 5.1. The role of the quantities defined with respect to the corresponding σ-states is not discussed here, but only in the original article. The plot to the right shows the density of states (DOS) of the layer. (b) shows equivalent electrostatic energy plots for all one-ring SAMs. They are aligned to E_{VL}^{dock}, which is justified by the resulting very similar average electrostatic energies in the region of the pyridine rings.*

A complication when determining $\mathrm{IP}^{\mathrm{dock}}$ and $\mathrm{IP}^{\mathrm{tail}}$ for pyridine-containing systems is that the choice of the most suitable frontier state for defining those quantities is ambiguous, especially in view of the fact that the free-standing monolayer is only an auxiliary system that shall later help to understand the bonded SAM. Thus, it is not useful to strictly associate the IP with the highest occupied state independent of its character and one needs to identify the nature of the state(s) associated with the peaks in the DOS. As the following deals exclusively with the pinning phenomena at *un*occupied states, the detailed discussion of the occupied states of the monolayers is skipped and the reader is referred to the original publication. As far as these lowest unoccupied states are concerned, the situation is much more straightforward, and they are always of π-character. The values for $\mathrm{EA}_{\pi}^{\mathrm{dock}}$ and $\mathrm{EA}_{\pi}^{\mathrm{tail}}$ are listed in Tab. 5.1. The situation is more complicated for Pyr|1P|NH_2 and Pyr|2P|NH_2, where we find some overlap of the first strong peak in the PDOS with a dispersing substituent-derived band. This will become relevant below when describing the charge-rearrangements and also in Sec. 5.4.4.

5.4.2 Interaction-induced charge rearrangements and the bond dipole

The next aspects that need to be understood before arriving at a conclusive picture of the electronic properties of the SAM-modified gold surfaces are the charge rearrangements upon bond-formation with the substrate, $\Delta\rho_{\mathrm{bond}}$, the associated amount of net charge transfer, Q_{bond}, and the resulting bond dipole, ΔE_{BD}. $\Delta\rho_{\mathrm{bond}}$ can be expressed as:

$$\Delta\rho_{\mathrm{bond}}(z) = \rho_{\mathrm{system}}(z) - \{\rho_{\mathrm{slab}}(z) + \rho_{\mathrm{monolayer}}(z)\} \qquad , \qquad (5.2)$$

where $\rho_{\mathrm{system}}(z)$, $\rho_{\mathrm{slab}}(z)$ and $\rho_{\mathrm{monolayer}}(z)$ are the x, y-plane integrated charge density of the combined SAM/metal system, the isolated metal slab, and the isolated monolayer, respectively. In the top part of Fig. 5.4, $\Delta\rho_{\mathrm{bond}}$ is shown for all chain lengths on Au(111) with –NH_2, –CN, and –NO_2 tail groups.

For the shortest chain, 1P, $\Delta\rho_{\mathrm{bond}}$ of Au|Pyr|1P|CN is mainly localized around the SAM/metal interface, *i.e.*, only very localized charge rearrangements between the metal and the docking group occur. This situation is strongly reminiscent of what has been observed for other docking groups including isocyanides and also thiolates,[70,137] at least when describing the bonding as a replacement of an S–H by an S–Au gold bond (see extensive discussion in ref. 138). The situation is very similar for Au|Pyr|1P|H, Au|Pyr|1P|CH_3, and Au|Pyr|1P|CF_3 as shown in ESI.[i] The bonding-induced charge rearrangements in Au|Pyr|1P|NH_2 and Au|Pyr|1P|NO_2, however, are qualitatively different. They extend along the whole backbone, and for the former, even significant charge rearrangements occur in the region of (respectively above) the substituent. Increasing the chain length (see Fig. 5.4b and c) results in charge rearrangements that extend along the whole backbone for all substituents.

Table 5.1: *Parameters characterizing the electronic structure of the hypothetical free-standing and adsorbed SAMs: EA_π denotes the electron affinities which correspond to adding an electron to the lowest unoccupied π-state. The superscripts "dock" and "tail" denote whether the electron is added from the vacuum on the docking-group or tail-group side of the SAM (cf., Fig. 5.3). ΔE_{vac} is the step in the electrostatic energy of an electron across the molecular monolayer. ΔE_{BD} is the energy shift due to the bond dipole. ΔE_{LUPS} give the energies of the LUPS relative to the metal-Fermi level, i.e., they are a measure for the hole- and electron-injection barriers. E_{corr}^{LUMO} denotes the shifts of the eigenenergies of the SAM resulting from changes in the molecular potential due to the bonding-induced charge rearrangements (for details, see main text), and $\Delta\Phi$ is the SAM-induced work-function modification. Pinned systems are written in italic letters.*

	free-standing SAM				adsorbed SAM		
Systems	$\mathrm{EA}_\pi^{\mathrm{dock}}$/eV	$\mathrm{EA}_\pi^{\mathrm{tail}}$/eV	ΔE_{vac}/eV	ΔE_{BD}/eV	ΔE_{LUPS}/eV	$E_{\mathrm{corr}}^{\mathrm{LUMO}}$/eV	$\Delta\Phi$/eV
$(\mathrm{Au}\vert)\mathrm{Pyr}\vert 1\mathrm{P}\vert \mathrm{H}$	3.46	1.13	-2.33	-0.94	0.79	0.00	-3.27
$(\mathrm{Au}\vert)\mathrm{Pyr}\vert 1\mathrm{P}\vert \mathrm{CH}_3$	3.54	0.93	-2.61	-0.95	0.77	0.05	-3.56
$(\mathrm{Au}\vert)\mathrm{Pyr}\vert 1\mathrm{P}\vert \mathrm{CF}_3$	3.65	3.95	0.30	-1.11	0.49	0.03	-0.81
$(Au\vert)Pyr\vert 1P\vert NH_2$	3.21	-0.41	-3.62	-0.16	1.29	-0.55	-3.77
$(Au\vert)Pyr\vert 2P\vert NH_2$	4.14	0.61	-3.53	-0.28	0.31	-0.47	-3.81
$(Au\vert)Pyr\vert 3P\vert NH_2$	4.62	1.00	-3.62	-0.33	0.26	0.00	-3.95
$(\mathrm{Au}\vert)\mathrm{Pyr}\vert 1\mathrm{P}\vert \mathrm{CN}$	3.97	5.75	1.78	-0.96	0.36	0.08	0.82
$(Au\vert)Pyr\vert 2P\vert CN$	4.54	6.31	1.77	-0.38	0.27	-0.04	1.39
$(Au\vert)Pyr\vert 3P\vert CN$	4.66	6.56	1.90	-0.28	0.24	-0.06	1.62
$(Au\vert)Pyr\vert 1P\vert NO_2$	4.85	6.65	1.80	-0.08	0.23	-0.08	1.72
$(Au\vert)Pyr\vert 2P\vert NO_2$	4.95	6.74	1.79	0.11	0.24	-0.16	1.90
$(Au\vert)Pyr\vert 3P\vert NO_2$	5.02	6.81	1.79	0.20	0.22	-0.20	1.99

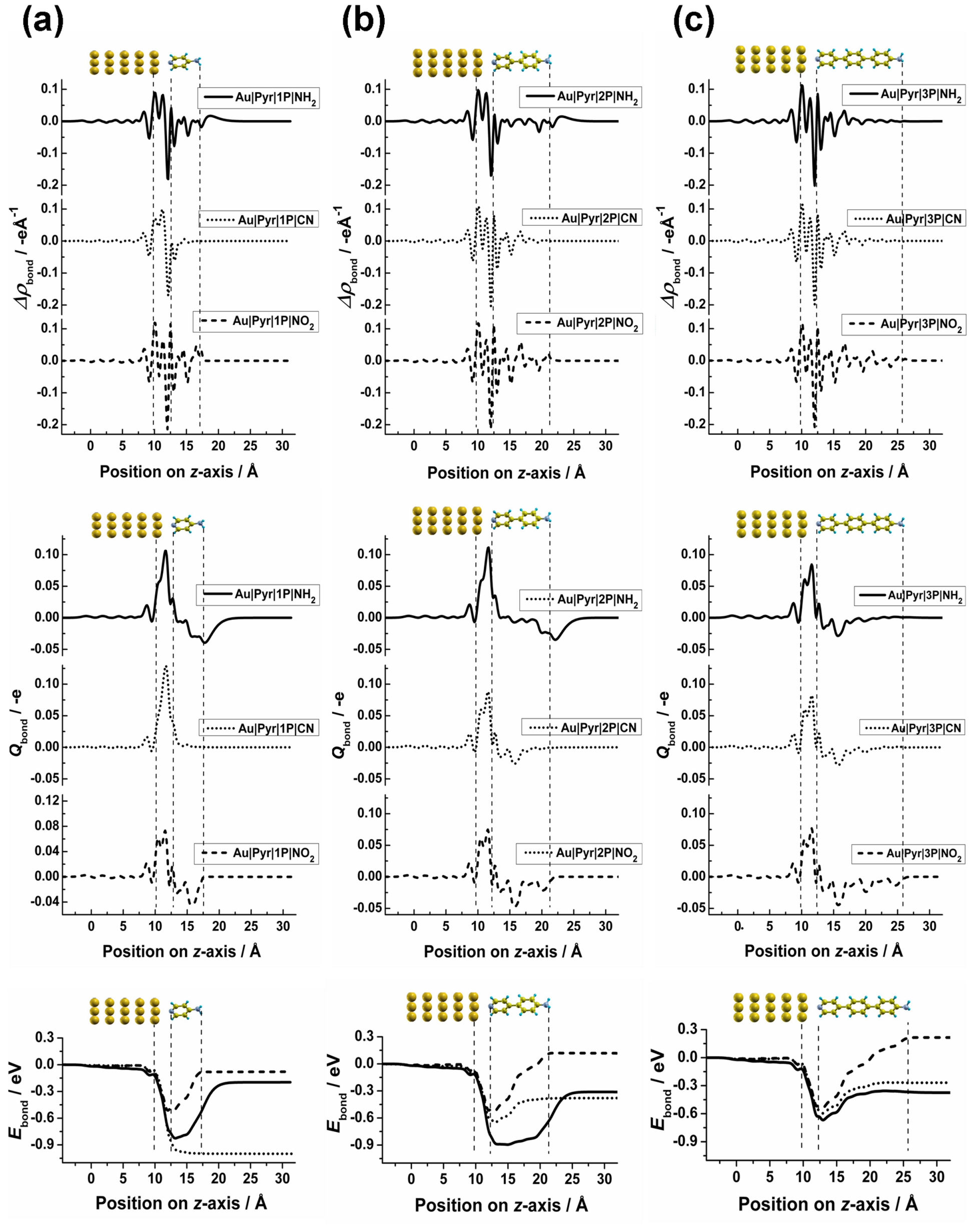

Figure 5.4: *Charge rearrangements upon bond formation, $\Delta\rho_{bond}$, net charge transfer, Q_{bond}, as well as the resulting change in electrostatic energy, E_{bond}, for the –NH_2 (solid line), –CN (dotted line) and –NO_2 (dashed line) substituted monolayers. (a), (b) and (c) show the situations for the one-, two- and three-ring systems, respectively. The vertical dashed lines mark the positions of the top Au layer, the N atom of the pyridine ring, and the topmost atom of the molecules.*

Further insight to what extent the charge rearrangements describe long-range charge transfer or local polarization can be obtained by integrating $\Delta\rho_{\text{bond}}$ over z.[28] The quantity $Q_{\text{bond}}(z)$, defined as:

$$Q_{\text{bond}}(z) = \int_{-\infty}^{z} \Delta\rho(z')\mathrm{d}z' \qquad , \tag{5.3}$$

yields the amount of electrons ($-e$) transferred from the region right of to the region left of a plane located at z. Plots of $Q_{\text{bond}}(z)$ are included in Fig. 5.4. They show that

(i) the most pronounced net transfer occurs in the immediate interface region;

(ii) there is no long-range charge transfer as indicated by $Q_{\text{bond}}(z)$ becoming zero at relatively small distances from the immediate interface region; instead the backbones are polarized and at no position z the net charge transfer significantly exceed *ca.* one tenth of an electron;[iv]

(iii) the degree of polarization decreases with the distance from the interface, which is best resolved for the longer $-NO_2$ substituted systems;

(iv) in Au|Pyr|1P|NH_2 and Au|Pyr|2P|NH_2 significant net rearrangements occur also in the substituent region.

The succession of regions with depletion and accumulation of electron density can in a simplified 1D-picture be viewed as a series of dipole layers. To quantify the modification of the electrostatic energy, E_{bond}, one needs to solve the 1D Poisson equation,

$$\frac{\mathrm{d}^2 E_{\text{bond}}(z)}{\mathrm{d}z^2} = \frac{e}{\epsilon_0 A}\Delta\rho_{\text{bond}}(z) \qquad , \tag{5.4}$$

where A is the area of the surface unit cell and ϵ_0 is the vacuum permittivity. The net shift in the potential landscape, the bond-dipole ΔE_{BD}, then corresponds to the difference in electrostatic energies far below and far above the monolayer where E_{bond} has become a constant. The values of ΔE_{BD} are listed in Tab. 5.1. Of the systems depicted in Fig. 5.4, only for Au|Pyr|1P|CN a situation reminiscent of "conventional" thiolates or also isocyanides[70] is found, *i.e.*, the change in E_{bond} is localized to the immediate vicinity of the interface region. In all other systems, the modification of E_{bond} extends onto the backbones consistent with what has been discussed above for the charge rearrangements.

In fact, one can distinguish between two contributions to $E_{\text{bond}}(z)$ (*cf.*, bottom plots in Fig. 5.4): a sharp decrease between the top Au layer and the nitrogen atoms and a more or less gradual increase along the backbone. For Au|Pyr|1P|NH_2 and Au|Pyr|2P|NH_2 one can even identify a third region corresponding to a relatively sharp increase around the substituent. The latter

---

[iv] In this context it should be noted that Bilić *et al.* described the pyridine-Au binding as "dispersive in nature, with significant contributions from the charge polarization effects but minimal contributions from charge transfer and covalent bonding".[98]

two contributions lead to a significant reduction of the large negative potential energy shift that arises from the charge rearrangements in the immediate Au–N region. As a consequence, while ΔE_{BD} is about -1.00 eV in all systems, where only the sharp drop in E_{bond} at the interface occurs (*i.e.*, in the one-ring systems with –H, $-CH_3$, $-CF_3$, and –CN substituents), it is reduced to a mere -0.16 and -0.08 eV in Au|Pyr|1P|NH_2 and Au|Pyr|1P|NO_2, respectively and becomes even positive for the more extended $-NO_2$ substituted SAMs. In the –CN substituted systems, the partial cancellation due to the opposing (positive) bond-dipole contributions manifests itself in a decrease of the absolute magnitude of ΔE_{BD} with chain length.

5.4.3 Reason for the delocalization of the charge rearrangements: Fermi-level pinning

To understand the origin of the unusual charge rearrangements in most of the systems discussed above, it is useful to first take a look at the corresponding densities of states projected onto the molecular parts at the interfaces. For the $-NH_2$, –CN and $-NO_2$ substituted systems with one and three rings they are shown in Fig. 5.5. For comparative reasons, Au|Pyr|1P|H is also included in that plot. In the latter system, E_{F} lies clearly inside the band gap of the SAM; for Au|Pyr|1P|NH_2, which displays the charge rearrangements "above" the substituent, we find the Fermi-level of the combined system at the location of a weak feature mentioned above and discussed in detail in Sec. 5.4.4. For Au|Pyr|1P|CN, E_{F} is right at the onset of the LUPS related peak, *i.e.*, the LUPS-derived states are not filled. In contrast, in the other systems E_{F} is somewhat shifted into the peak and the LUPS-derived band is partially occupied, albeit only to a very small degree.

The latter is a manifestation of the fact that the systems are in the regime of Fermi-level pinning and Au|Pyr|1P|CN might be considered to be right at the onset of pinning. This process shall be briefly explained for the three-ring systems in the following: When joining metal substrate and SAM, to a first approximation, the electrostatic energy of the combined system is given by a superposition of the individual systems, with the potential landscape of the SAM shifted by ΔE_{BD} relative to that of the metal.[31,70] For the relative alignment between the unoccupied states in the SAM and the metal Fermi-level, this means that it is approximately given by the work function of the metal, Φ, minus the docking-side electron affinity of the SAM, $\text{EA}_{\pi}^{\text{dock}}$, plus the bond-dipole ΔE_{BD}. As for an Au(111) surface Φ is calculated to be 5.22 eV, this would mean that the lowest unoccupied levels of all three-ring SAMs investigated (*cf.*, Table 5.1) here would come to lie below $\text{EA}_{\pi}^{\text{dock}}$, if ΔE_{BD} was -1.0 eV like in the cases where no pinning occurs. This is inconsistent with the establishment of thermodynamic equilibrium. As a consequence, charges need to be rearranged to induce extra dipole(s) that shift the molecular levels in a way that their occupation is consistent with thermodynamic equilibrium, which means that they will (partially) overlap with E_{F}.

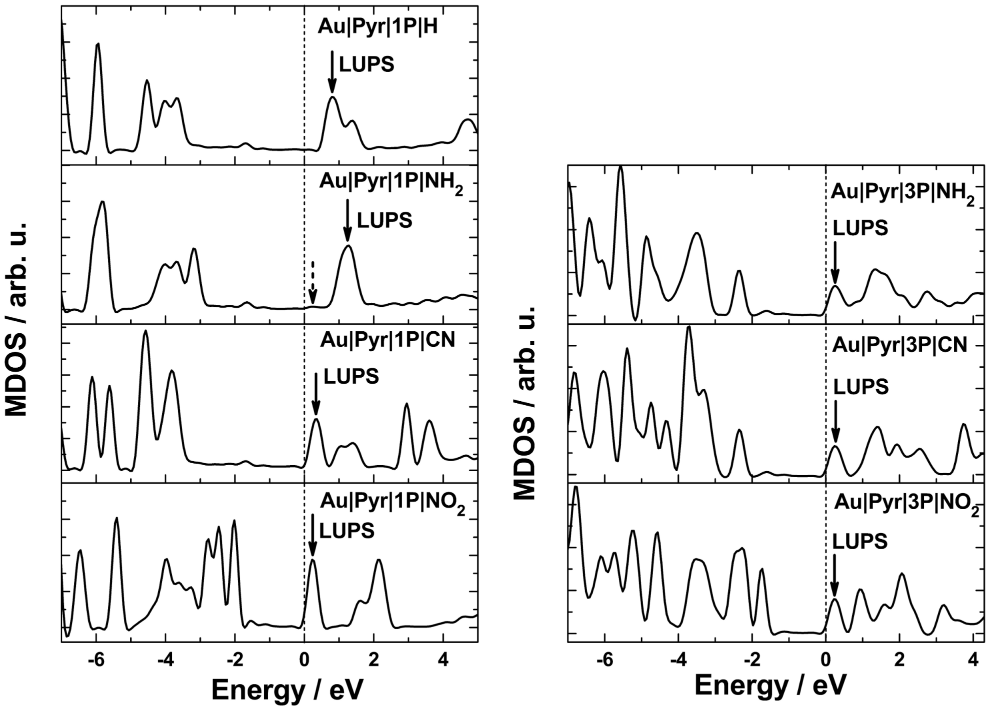

Figure 5.5: *Density of states projected onto the molecular region, MDOS, of the combined SAM-metal systems for the –NH_2, –CN and –NO_2 substituted monolayers with one (1P) and three (3P) conjugated rings. The PDOS of Au|Pyr|1P|H is also included to show a system far from Fermi level pinning. The Fermi levels are aligned to zero, and the positions of the LUPSs are indicated by arrows. The dashed arrow in the panel of Au|Pyr|1P|NH_2 highlights the dispersing band pinned at the Fermi level, which was mentioned above and will be discussed in detail in Sec. 5.4.4.*

For flat-lying adsorbates, this is usually achieved by a charge-transfer between metal and the adsorbate layer.[60,67] The amount of charge transfer and, consequently, the exact position of E_F relative to the molecular levels is, in a first approximation, determined by the magnitude of the bond-dipole that needs to be established to shift back the LUMO, although also more complex situations involving charge forward and backward donation have been observed.[124,125,139]

Interestingly, in SAMs the realignment does not proceed via long-range charge transfer, but is achieved by a polarization of the SAM (*cf.* $\Delta\rho_\mathrm{bond}(z)$ and $Q(z)$ plots in Fig. 5.4). The fact that the primary effect of pinning is not a (partial) filling of the LUPS is also clearly seen when comparing the associated local density of states with a 3D isodensity representation of the charge rearrangements. Such a comparison is shown in Fig. 5.6 for the particularly instructive case of a three-ring SAM bearing –NO_2 substituents. The LUPS (Fig. 5.6b) displays typical features of the molecular LUMO (Fig. 5.6a); the charge rearrangements (Fig. 5.6c and d), however, do not even resemble the LUPS and a polarization of several bonds is clearly resolved. Of note, a similar

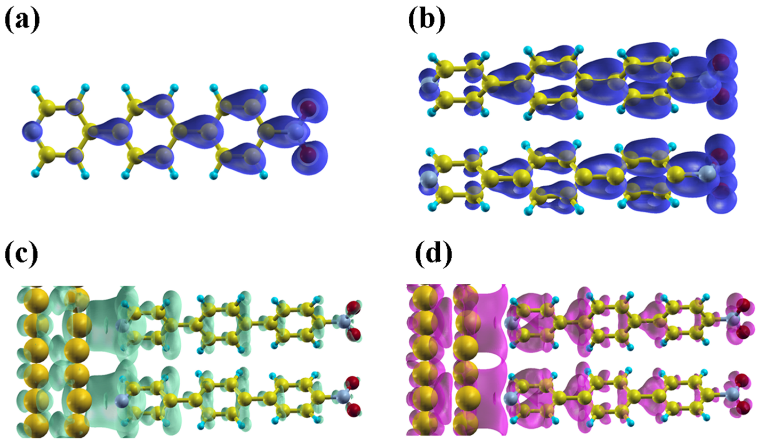

Figure 5.6: *The local density of states (LDOS) of the LUMO for the isolated Pyr|3P|NO_2 molecule (a), and of the LUPS of the Au|Pyr|3P|NO_2 combined system (b). (c), (d) A 3D isodensity representation of charge rearrangement for Au|Pyr|3P|NO_2 (only the top two layers of the Au-slab are shown). Electrons flow from regions shown in (c) to those depicted in (d).*

type of Fermi-level pinning that proceeds via the polarization of a molecular backbone rather than via long-range charge transfer has also been observed for a "pinned" molecular layer on top of a SAM.[50]

A finding that appears particularly surprising, at first glance, is that for the three-ring systems the same kind of pinning occurs for both donor and acceptor substitution. While a deep-lying LUMO prone to pinning does not come as a surprise for the acceptor substituted systems, donor substitution results in very small electron affinities in isolated molecules, rendering the unoccupied states high in energy. The latter, indeed, manifests itself in the tail-group side EAs reported for the –NH_2 substituted molecules in Tab. 5.1. But, as mentioned above, what determines the level alignment is EA_{π}^{dock}, which is only weakly affected by the substitution due to the peculiarities of "SAM electrostatics".[30,31] As a consequence, there is not necessarily a direct connection between simple molecular properties and the occurrence of pinning in a SAM.

What remains to be explained is the electron accumulation above the –NH_2 groups in Au|Pyr|1P|NH_2 and Au|Pyr|2P|NH_2, *i.e.*, the unusual pinning level encountered in these systems. It is associated with an unoccupied σ-state in the region of the –NH_2 group that spreads out far into space and, as a consequence, gives rise to a strongly dispersing band in the monolayer. Pinning now occurs at the bottom of that band (*cf.*, Au|Pyr|1P|NH_2 in Fig. 5.5).

To check to what extent the occurrence of this quite "unusual" state is an artifact of the used programs and methodologies, we performed an extensive series of tests employing a variety of band-structure and molecule-based codes using either plane-wave or different atomic-orbital type basis sets. These tests, which are reported in detail in the next section, showed that (i) such a state is found in all calculations and (ii) for sufficiently large basis sets it becomes the lowest-lying unoccupied state for the short-chained, –NH_2 substituted molecules. The relative position of that state might still be affected by the self-interaction error present in all DFT calculations based on (semi)local functionals (see discussion in the Methodology) section). Nevertheless, the observations reported here for Au|Pyr|1P|NH_2 and Au|Pyr|2P|NH_2 still provide valuable insight into what happens, when the electronic state responsible for Fermi-level pinning is not delocalized along the molecular backbone, but is rather found relatively far away from the immediate interface region. Such cases can also be encountered when studying pinned SAMs in which the conjugated backbone is separated from the metal by a non-conjugated spacer.

5.4.4 Understanding the bonding-induced charge rearrangements in Au|Pyr|1P|NH_2 and Au|Pyr|2P|NH_2

As described above, there is a large contribution from the tail group region to $\Delta\rho_{\text{bond}}$ (and thus Q_{bond} and E_{bond}) for Au|Pyr|1P|NH_2 and Au|Pyr|2P|NH_2, but not for any other system - including the closely related Au|Pyr|3P|NH_2. In order to study the origin of this peculiar shape of the $\Delta\rho_{\text{bond}}$ curves, we show the detailed 3D plots for the regions with negative $\Delta\rho_{\text{bond}}$ (electron depletion) and the regions with positive $\Delta\rho_{\text{bond}}$ (electron accumulation) separately in Fig. 5.7, using Au|Pyr|1P|NH_2 as an example. It can be seen that some electron density accumulates in a region above the -NH_2 groups. Still, although this accumulation is small (*cf.* small isodensity value used for producing that plot), it plays a significant role for the bond dipole in Au|Pyr|1P|NH_2 and Au|Pyr|2P|NH_2 (*cf.* Fig. 5.4a,b). In order to exclude that this surprising observation (*i.e.*, charge shifting to relatively far from the actual atoms of the SAM) is merely a consequence of an inadequate methodology, we performed extensive tests addressing the reliability of our VASP calculations in this respect.

As a first check, we tested the impact of changing several of the key parameters in the VASP calculations.[34] These include the cutoff energy for the plane wave basis (40 Ryd instead of 20 Ryd), the number of k-points, the smearing width and method, the type of pseudopotentials (hard instead of soft) and the xc-functional (PBE instead of PW91). It turned out that none of those measures qualitatively changed the charge rearrangements shown in Fig. 5.7.

In order to further test the influence of the basis functions, we repeated the calculations on the systems Au|Pyr|1P|NH_2 and Au|Pyr|2P|NH_2 applying the linear combination of atomic orbitals (LCAO) code SIESTA.[140] *I.e.*, in these calculations, instead of using a plane wave basis, atomic orbital type basis functions of double-zeta polarized (DZP) quality have been used. The same geometries as in the VASP calculations were used together with the PBE functional and the use of symmetric unit cells prevented spurious electrostatic interaction between neighboring slabs. Interestingly, the "unusual" charge rearrangements are completely absent in those calculations. This raises the important question which

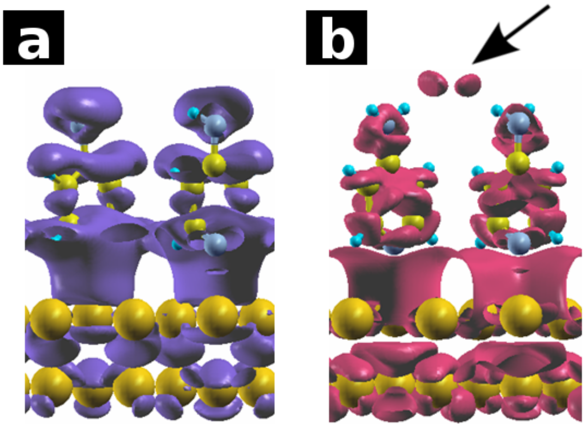

Figure 5.7: *3D isodensity representation of $\Delta\rho_{bond}$ for a SAM of Pyr|1P|NH_2 on a 5-layer Au(111) slab (only the top two layers are shown), isovalue=0.00072 e/Å^3. Electrons flow from the electron-depletion region (a) to the electron-accumulating region (b). The black arrow marks the accumulation of interest.*

code provides a more accurate description of the bond-dipole for the short chain –NH_2 substituted SAMs. Also the origin of the observed discrepancies needs to be clarified.

Therefore, we compared the eigenvalue spectra obtained with both codes for the isolated Pyr|2P|NH_2 molecule (in the geometry it adopts in the SAM). In this comparison we also used a third software package, TURBOMOLE 5.7.1,[141–143] because it allows to choose from a large variety of atomic-orbital based basis sets. In this way, we were able to obtain the eigenenergies using five different basis sets: a split-valence polarized basis (SVP)[144] and the augmented correlation-consistent basis sets aug-cc-PVDZ and aug-cc-PVTZ[145] in TURBOMOLE, a double-zeta polarized basis (DZP) in SIESTA and plane waves in VASP. In all cases, we used the PBE functional except in the VASP calculations where PW91 is used (*vide supra*).

The obtained energies of the Kohn-Sham orbitals are shown in Fig. 5.8. Except for the small basis set SVP, the eigenenergies between the different basis sets match very well for the occupied states; the small deviation of the plane-wave spectrum reflects the impact of the used functional. Clearly, the situation is more complex for the unoccupied orbitals. Here, one might argue that unoccupied Kohn-Sham orbitals are of limited meaning anyway, but one has to keep in mind that upon Fermi level pinning the lowest unoccupied band actually becomes partially occupied without changing its nature (see discussion above). Therefore, looking at the unoccupied states in the non-bonded molecules and layers is of some significance in the present case.

Although the overall correspondence between the VASP (plane-wave) and the SIESTA (DZP) calculation is not too bad, there are also certain differences. Most importantly, the state marked as “L+3”, *i.e.* LUMO+3, in the plane-wave

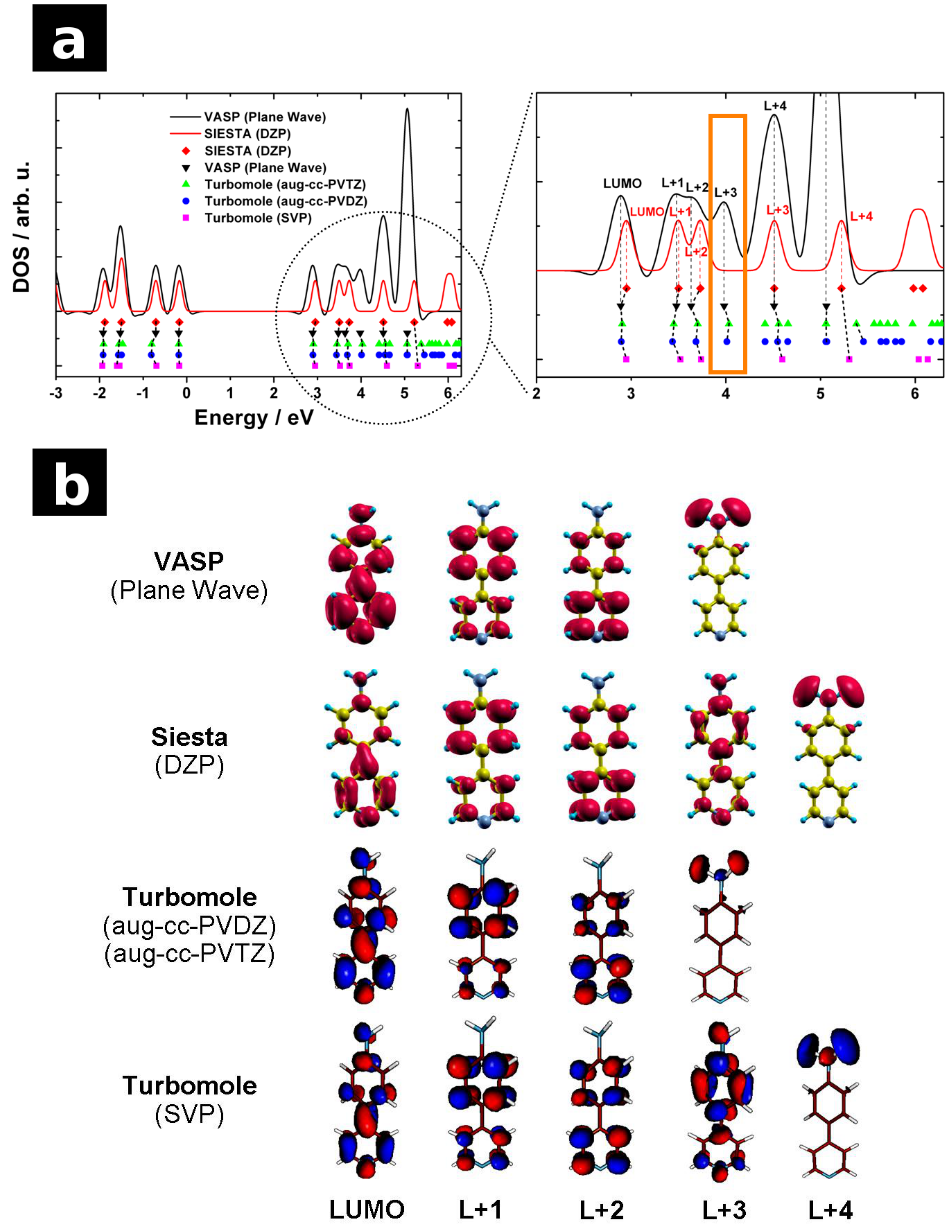

Figure 5.8: *(a) top: DOS of the isolated Pyr|2P|NH_2 molecule obtained from DFT calculations employing* Vasp *and* Siesta *codes with different basis sets; bottom: corresponding eigenvalues from the* Vasp*,* Siesta*, and* Turbomole *calculations (indicated by different symbols). For the sake of clarity, a zoom in is shown for the unoccupied states. The equivalent eigenvalues (in the energy interval from -2 to 5.5 eV) are connected by the dashed lines as a guide to the eye. The zero points in the horizontal axis represent the onset of the HOMO peak. (b) 3D representation of the unoccupied states as obtained in the various calculations.*

spectrum seems to be missing when using DZP. A closer look at the real-space representation of those orbitals (given in Fig. 5.8 for each basis set) reveals that this is not the case: this orbital is found to be the "L+4" with DZP and at about 1.5 eV above its plane-wave equivalent. Such a result can be interpreted in the context of MacDonald's theorem,[146,147] according to which the eigenvalues obtained using a certain incomplete basis set are upper limits and approach the correct values as the basis set approaches completeness. Although the chosen basis sets do not approach completeness in any systematic way, it can be easily observed that the eigenvalues are shifted down with increasing basis set quality. This already strongly indicates the superiority of the plane-wave calculations over DZP and such an interpretation is further backed up by the presented TURBOMOLE calculations. While the TURBOMOLE SVP eigenvalues are reminiscent of the SIESTA DZP results, both aug-cc basis sets nicely reproduce the VASP plane-wave spectrum.

This "problematic" unoccupied orbital (*i.e.*, the LUMO+3 in the VASP calculations of the isolated molecule) turns out to be the key to understand the peculiar charge rearrangements in Au|Pyr|1P|NH_2 and Au|Pyr|2P|NH_2. Starting from the molecular eigenspectrum it is possible to understand the electronic structure of SAMs formed from those molecules and consequently the charge rearrangements upon adsorption.

To avoid unneeded complexity, we continue the discussion for the one-ring system. Fig. 5.9a and b compare the DOS of molecule and monolayer of the Pyr|1P|NH_2 molecules along with the corresponding real-space representations. Besides the obvious similarities, there is an important difference: The molecular LUMO does not constitute the lowest unoccupied band in the monolayer. Instead, a very broad band originating from the molecular LUMO+1 is found as the valence band, where the pronounced dispersion is the reason for the low amplitude of the peak. This is a consequence of the electrostatic landscape in such a SAM, *cf.* Fig. 5.3b above. An orbital localized at the very "right" end of the Pyr|xP|NH_2 SAM is shifted down in energy way more than an orbital delocalized over a large part of the molecule such as the LUMO. This way, the molecular L+1 is shifted to below the LUMO in the monolayer. As contact to the metal is established and Fermi-level pinning occurs, it thus becomes involved in the pinning process (see Fig. 5.9c). This is also nicely illustrated by a comparison of the 3D isodensity representation (Fig. 5.9c) and the corresponding onset of the valence band (Fig. 5.9b).[v]

Having discussed those peculiarities, it is now also possible to explain their absence in the very similar system Au|Pyr|3P|NH_2. Because the length of the conjugated backbone is increased from 1P to 3P, the energy gap decreases, causing the π-conjugated LUMO to shift downwards. Correspondingly, the

---

[v] In the adsorbed SAM, this peak appears even weaker than in panel b. This is because the very delocalized states extend to far above the substituent groups. As a consequence, they are not fully captured in the scheme that calculates projected densities of states in the VASP program. While panels a and b in Fig. 5.9 show the total DOS, in panel c only the projected DOS (MDOS) is depicted.

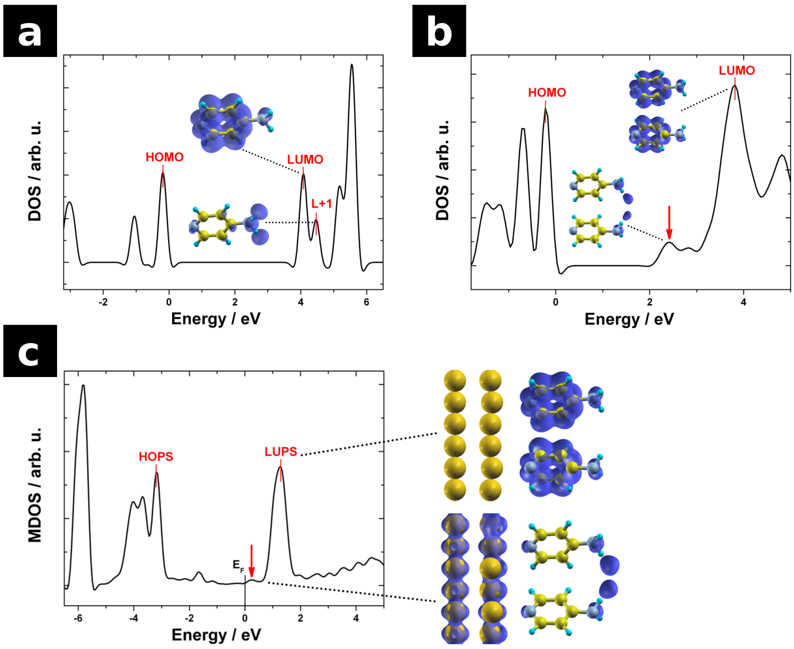

Figure 5.9: *The density of states (DOS) of the Pyr|1P|NH_2 molecule, (a), the isolated monolayer, (b, not including Au substrate), and the combined system Au|Pyr|1P|NH_2, (c). The zero points in the horizontal axis represent the onset of the HOMO peak in the isolated systems (a, b) and the Fermi level in the combined system (c), respectively. The insets shows the LDOS plots for the LUMO/LUPS and the localized tail-group states ("L+1" state in (a) and the states that the arrows point to in (b) and (c), which we attribute to the low energy part of a dispersing band originating from what is originally the LUMO+1).*

energetic distance between LUMO and the localized state responsible for the discussed charge rearrangements increases in the isolated molecule. Although the latter state shifts down in energy in the molecule-to-monolayer transition in each system, it does not cross the LUMO anymore for the 3P backbone. This is illustrated in Fig. 5.10, which shows the energetic distance between both involved states in the molecular and SAM configuration for all three backbone lengths.

5.4.5 Work-function modification & pinning-controlled electron injection barriers

The above considerations provide us with all the information necessary for understanding the change in the work function of the substrate due to the adsorption of the SAM, $\Delta\Phi$. The values of $\Delta\Phi$ for all studied SAMs are listed in Tab. 5.1. $\Delta\Phi$ arises from a simple superposition of the bond dipole and the change in the electrostatic potential induced by the hypothetical free-standing SAM;[54,61,64,148] *i.e.*, it is given by:

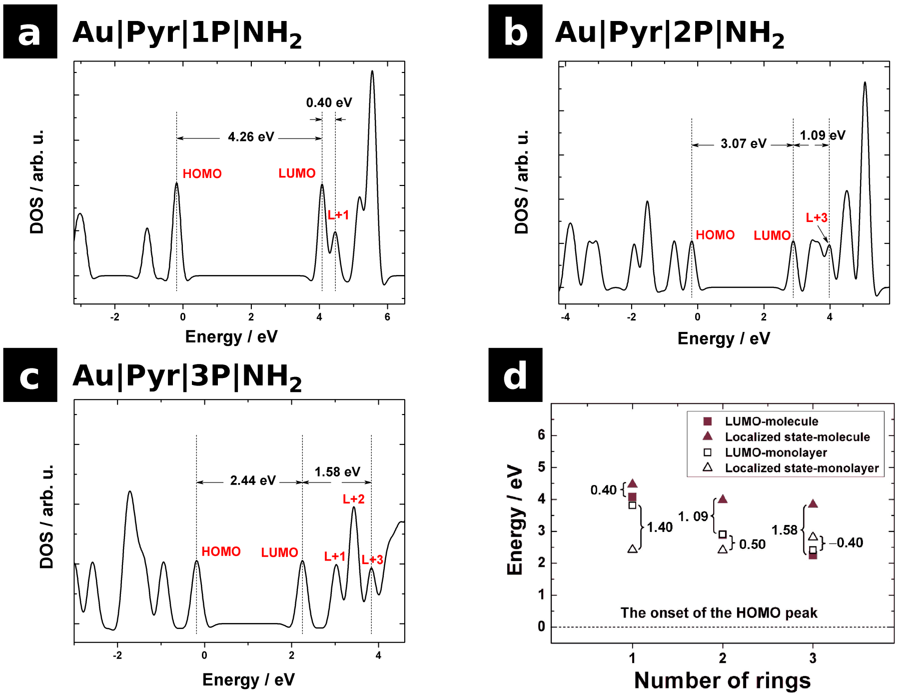

Figure 5.10: *DOS and energy gaps between the LUMO and the HOMO, state localized at the –NH$_2$ group for 1-,(a), 2-,(b), and 3-ring (c) –NH$_2$ substituted molecules. The zero points in the horizontal axis represent the onset of the HOMO peaks. Panel (d) compares the chain-length dependence of the energetic positions of the LUMO (square) and the localized states (triangles) for the Pyr|nP|NH$_2$ (n = 1, 2, 3) isolated molecules (filled symbols) and monolayers (open symbols). The energies are given relative to the onset of the HOMO.*

$$\Delta\Phi = \Delta E_{\mathrm{vac}} + \Delta E_{\mathrm{BD}} \qquad . \tag{5.5}$$

Considering the present systems, the adsorption of the SAM to form Au|Pyr|1P|H results in a pronounced work-function reduction by −3.27 eV. It arises, on the one hand, from the intrinsic dipole moment of pyridine ($\Delta E_{\mathrm{vac}} = -2.33$ eV) and, on the other hand, from a bond-dipole amounting to $\Delta E_{\mathrm{BD}} = -0.94$ eV, characteristic of the pyridine group in the absence of Fermi-level pinning.

Substitution with a donor gives rise to a larger work-function decrease, as here ΔE_{BD} and ΔE_{vac} are of the same sign. In the case of the –NH$_2$ substituted SAMs, the net effect is, however, smaller than what one might have expected, as a consequence of the significantly reduced (negative) ΔE_{BD} because of Fermi-level pinning.

For the case of acceptor substitution in the absence of Fermi-level pinning, the large negative "intrinsic" ΔE_{BD} of the pyridine docking group limits the achievable work-function change. In fact, for Au|Pyr|1P|CF$_3$, $\Delta\Phi$ remains negative and for Au|Pyr|1P|CN it adopts "only" a value of +0.82 eV. Only when ΔE_{BD} becomes less negative for the pinned two- and three-ring –CN substituted SAMs and Au|Pyr|1P|NO$_2$, a significant increase of the work function can be expected. This is further enhanced for Au|Pyr|2P|NO$_2$ and Au|Pyr|3P|NO$_2$,

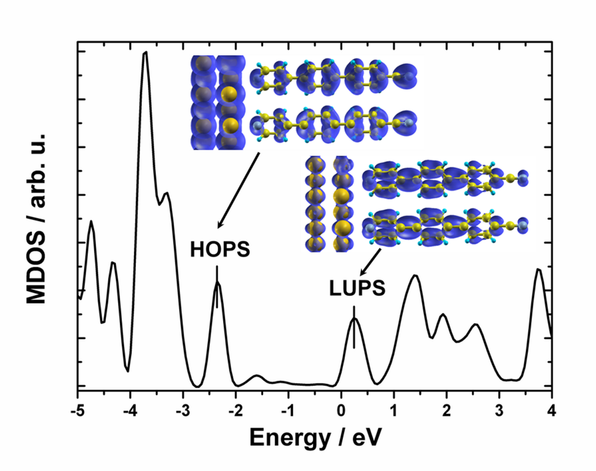

Figure 5.11: *Density of states projected onto the molecular region, MDOS, of the Au|Pyr|3P|CN combined SAM–metal system. The insets show the local density of states (LDOS) of the corresponding HOPS and LUPS, only the top two Au layers are shown. The Fermi energy is set to zero.*

where ΔE_{BD} becomes positive (*vide supra*). The relative order of $\Delta\Phi$ in the latter SAMs is then not determined by the order of ΔE_{vac} (a property of the monolayer) but rather by how "positive" ΔE_{BD} gets due to pinning (a consequence of the interaction between the SAM and the metal).

In the pinning cases, an expression alternative to eqn. (5.5) can be used to describe the work-function of the SAM-covered metal, Φ_{mod}. In a way, it reflects the involved physics more directly as it relates Φ_{mod} to the energy of the pinning level: Because the position of the LUPS is fixed at a difference ΔE_{LUPS} from the metal Fermi-level, the effective work function Φ_{mod} differs from the tail-group side electron affinity $\mathrm{EA}^{\mathrm{tail}}$ only by this value (plus a typically small correction term $E_{\mathrm{corr}}^{\mathrm{LUMO}}$ explained in the following section), yielding:

$$\Phi_{\mathrm{mod}} = \Phi + \Delta\Phi = \mathrm{EA}^{\mathrm{tail}} + \Delta E_{\mathrm{LUPS}} - E_{\mathrm{corr}}^{\mathrm{LUMO}} \qquad . \tag{5.6}$$

When analyzing the LDOS of all LUPS peaks one finds that they display π-character and are delocalized along the whole backbone, as shown in Fig. 5.11 for the example of Au|Pyr|3P|CN (the data for the other SAMs can be found in the ESI[i]). In this way, they constitute an efficient channel for charge transport, which - as a consequence of pinning - is found in close vicinity to the Fermi energy ($\Delta E_{\mathrm{LUPS}} = 0.24$ eV). Naturally, very similar values of ΔE_{LUPS} are found[vi] for all systems in which pinning at the LUPS occurs and also in Au|Pyr|1P|CN, where one is already close to pinning. As a consequence, if such a SAM was used in a molecular junction, efficient transport would set in already at very low bias voltages. In fact, a further reduction of the transport gap could only be achieved using radical SAMs, a topic to be discussed in the next chapter.

[vi] The actual value of ΔE_{LUPS} in a pinned system is, of course, also influenced by the chosen broading of the DOS.

5.5 Summary and conclusions

To summarize, we have systematically investigated the interfacial properties of pyridine-docked SAMs on Au(111) at the DFT level. Significant deviations from more conventional SAMs are observed for the bonded layers, where in most studied systems the Fermi level gets pinned at the lowest unoccupied molecular states. This gives rise to charge-rearrangements that extend along the whole molecular backbone, which are not associated with long-range charge transfer but rather with a local polarization of the SAM. As a net-effect, the magnitude of the bond-dipole, which amounts to -1 eV in the non-pinned systems, is reduced and the bond-dipole becomes even positive for –NO_2 substituted systems containing two or three rings along the backbone. What appears somewhat surprising at first glance is that (beyond a certain chain length) an equivalent pinning situation is observed for strongly donating and strongly accepting substituents, in spite of the fact that the associated molecular electron affinities differ significantly. This can again be explained by the peculiarities of SAM electrostatics.

The main impact of the pinning at the LUPS on the SAM-induced work-function modifications is that it reduces the work-function reduction by donor substituted SAMs and boosts the work-function increase due to acceptor substituted SAMs. As far as the level alignment between the Fermi level and the SAM states is concerned, a very small barrier to electron injection is found for all pinned systems. As without pinning the unoccupied molecular states would come to lie even below E_{F}, pinning at the unoccupied states essentially reduces the injection barriers for holes into the occupied states.

The results of this work highlight how much Fermi-level pinning can alter the electronic properties of SAMs, showing that it can be beneficial for certain quantities and types of SAMs, while it is detrimental for others.

Acknowledgments. The authors thank Leeor Kronik and Amir Natan for stimulating discussions regarding the shortcomings of density functional theory and Tomáš Bučko for providing and acquainting us with the GADGET code. Financial supports by the Ministry of Science and Technology of China through the 973 program (Grants 2011CB932304, and 2011CB8084050), National Science Foundation of China (Grants 20833004 and 20920102031) and by the Austrian Science Fund FWF through project P20972-N20, are gratefully acknowledged.

Chapter 6

Radical self-assembled monolayers on Au(111) formed by the adsorption of closed-shell molecules (ref. 149)

Having discussed physisorbed and chemisorbed SAMs, the present chapter deals with a conceptually different class of interfaces. Recently, SAMs of radical molecules have attracted attention because of their interesting electronic, magnetic and optical properties (see below for references). It is specifically interesting that redox reactions can induce (optical, magnetic, electronic) switching behavior. This chapter discusses an aspect (to the best of my knowledge) not yet considered, namely that species which are closed-shell in gas phase can *become radicals upon adsorption* onto the metal surface. The focus here is on the

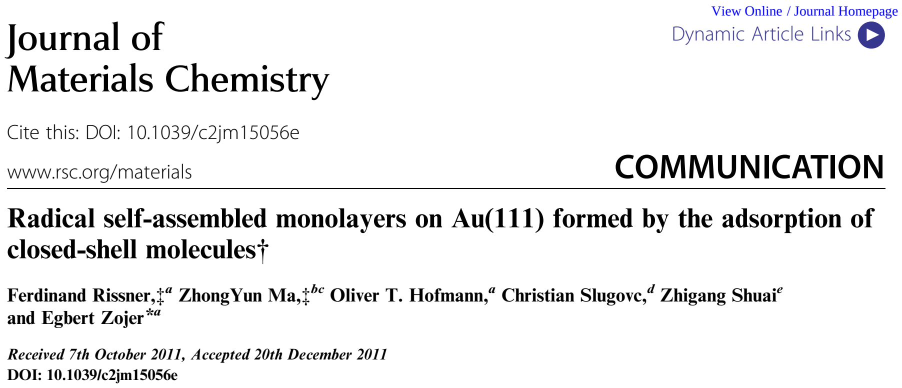

Journal of
Materials Chemistry

View Online / Journal Homepage
Dynamic Article Links

Cite this: DOI: 10.1039/c2jm15056e

www.rsc.org/materials

COMMUNICATION

Radical self-assembled monolayers on Au(111) formed by the adsorption of closed-shell molecules†

Ferdinand Rissner,‡[a] ZhongYun Ma,‡[bc] Oliver T. Hofmann,[a] Christian Slugovc,[d] Zhigang Shuai[e] and Egbert Zojer*[a]

Received 7th October 2011, Accepted 20th December 2011
DOI: 10.1039/c2jm15056e

Figure 6.1: *Header of the article ref. 149 showing its title and all contributing authors. This chapter is essentially identical to the article including its Electronic supplementary Information.*

consequences of "radicalization" on the interfacial electronic structure and how it changes by reduction of the molecules. This work was published[149] (Fig. 6.1) and is

Reproduced by permission of The Royal Society of Chemistry. A slightly modified version of the article including its Electronic Supplementary Information is reproduced and the original version is available online at http://dx.doi.org/10.1039/C2JM15056E.

Author contributions. The initial idea of studying such molecules is due to Egbert Zojer and Lorenz Romaner. Quite similar to Chapter 5, ZhongYun Ma has done most calculations (and many more which are not included here) before I have joined the project. I did so in early summer 2011, which gave me the great chance for a research visit in Prof. Shuai's group in Beijing. I looked through all the data and worked on the interpretation of the systems. For the latter, some additional calculations were necessary. I have further written the manuscript after returning to Graz. Especially Oliver Hofmann and Egbert Zojer contributed with many discussions about the interpretation and Christian Slugovc helped making the story more "chemical" and came up with the idea of reduction of the molecules. Final changes that made the manuscript accessible to a broader audience were done collectively.

Abstract. Using density-functional theory band-structure calculations, we show how the exothermic adsorption of conjugated closed-shell organic semiconductor molecules on an Au(111) surface can turn them into radicals. For this to happen, we suggest using a thiocarbonyl docking group instead of the commonly applied thiols. The radicalization of the absorbed molecules resulting from the formation of the Au–S bond leads to reduced electron- and hole-injection barriers. The calculations predict two energetically close solutions for the adsorbed monolayer, one being non-magnetic and metallic and one being magnetic with reduced density of states at the Fermi energy. Appendix 6.B briefly discusses to what extent the quinoidal molecules are similar to the pyridines - see previous chapter - and explains why the electronic properties of the Au(111)/quinoidal interfaces differ so much from the results shown there.

6.1 Introduction

In the field of molecular electronics,[150] the alignment of the molecular electronic states with respect to the Fermi level of the metal, E_F, is the key quantity for understanding and tuning the characteristics of molecular junctions.[151] Unfortunately, it cannot be easily predicted, as it is sensitively determined by several factors besides the electronic levels of the molecule. Most generally, these are substrate-adsorbate interactions and intermolecular interactions within the adsorbate layer.[31] Both depend on the exact geometry of the interface, as collective phenomena[30] and depolarization effects[152] determine the properties of well-ordered densely packed self-assembled monolayers (SAMs), but do not occur in isolated molecules. Consequently, individual molecules and such surrounded by like molecules in the form of a SAM can differ greatly in their electronic properties.[26] Understanding and controlling the relevant factors is thus of considerable interest in order to tune, *e.g.*, charge-injections barriers. A relatively easy prediction of the barriers is possible if the highest occupied [lowest unoccupied] states in the organic material were above [below] the metal Fermi energy in the hypothetical case of no metal/molecule interaction, *i.e.*, vacuum level alignment. Then, so-called Fermi level pinning takes place and fixes occupied [unoccupied] states close to E_F.[96]

Only relatively recently, also the properties of metal/organic interfaces involving radical molecules/SAMs have become a topic of heightened interest (see ref. 153 and references therein). The conductance of radicals at small bias voltages was found to be by orders of magnitude larger than that of closed-shell molecules.[17,154] This can be easily understood in a spin-restricted picture, *i.e.*, when assuming α- and β-spin states to be identical. Then, because the highest occupied orbital of the radical is only singly occupied, in the corresponding SAM one is dealing with a half-filled valence band that in thermodynamic equilibrium must align with E_F. In that case, the metallic character extends onto the SAM.[154,i] The overall situation can be somewhat modified when relaxing the above-mentioned condition of forcing α- and β-spins states to be equal, as discussed below, but it has been argued (see Supporting Information of ref. 154) that also in a situation with uncompensated spins small injection barriers are realized for electrons and holes simultaneously. Another peculiar feature of such radical monolayers is that they can be easily chemically oxidized or reduced. This lead to the development of redox-sensitive, surface-confined molecular optical and magnetic switches.[155]

In the present contribution we describe how a radical character can be realized in a SAM consisting of closed-shell molecules. This is achieved by using a docking group whose bonding situation is fundamentally altered by the reaction with the metal. For that purpose, we propose the thiocarbonyl group, where binding to Au(111) results in the formation of a new bond rather than the replacement of an existing one. The latter is the case, for example, when replacing the S–H bond by an S–Au bond in thiols, the most commonly used docking groups in molecular electronics. To investigate thiocarbonyl-bonded SAMs, we studied densely-packed layers of the three closed-shell molecules **1-3** shown in Fig. 6.2. They are all characterized by a quinoidal backbone and bear either electron accepting (**1** and **2**) or electron donating (**3**) tail groups. Although the molecules under investigation to the best of our knowledge have not yet been studied in experiments (while **1** has been considered in a theoretical study[156]), their synthesis or the synthesis of closely related species should be

---

[i] We note in passing that this (qualitative) picture neglects the charging energy and the lack of derivative-discontinuity of the exchange-correlation functional, which results in a finite difference between the ionization energy and electron affinity of the SAM (where the overall effect - at least of the charging energy - can be expected to be strongly reduced due to screening by the metal substrate).

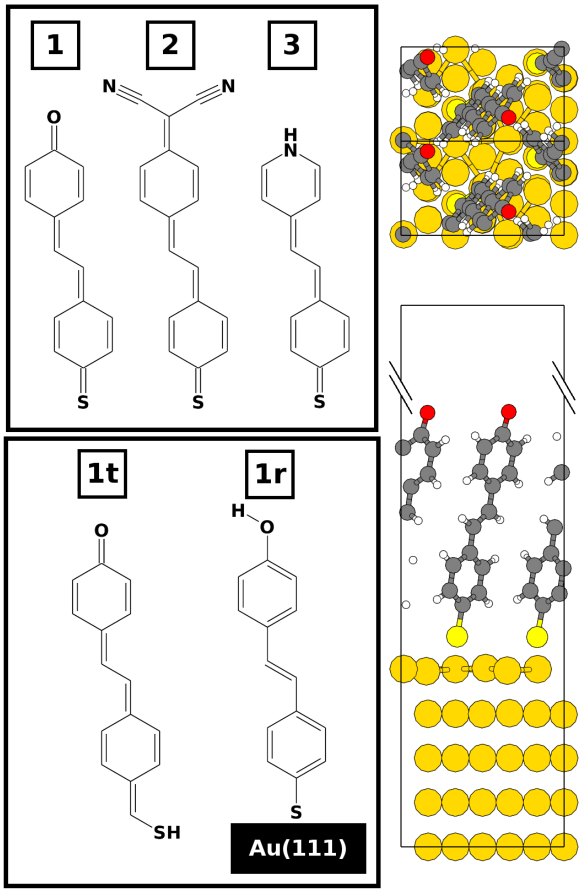

Figure 6.2: *Left: Chemical structures of the closed-shell molecules **1**-**3**; **1t** is analogous to **1**, but bearing a mercaptomethylene docking group; **1r** is the reduced version of **1** after it has been bonded to the Au(111) surface. Right: Top and side view of the unit cell used in the periodic calculations.*

feasible.[157]

6.2 Results & discussion

Our computational work relies on density-functional theory (DFT) based band-structure calculations using the PW91 functional and electronic states were broadened by 0.2 eV (for further details, see Methods section. We studied molecules **1-3** arranged in a herringbone-packed, upright-standing monolayer on Au(111) infinitely extended in two dimensions, where the metal substrate is represented by five Au layers. Since we lack corresponding experimental information, we chose a $(3 \times \sqrt{3})$ surface unit-cell containing two molecules (see Fig. 6.2), as this is often found for aromatic thiol-docked SAMs;[68] this implies that no large-scale reconstructions are considered here. We chose relatively extended molecules, as for them a higher degree of order can be expected.[158] The adsorption energy per molecule is defined as

$$E_{\mathrm{ads}} = \frac{1}{2}\left\{E_{\mathrm{Au(111)+SAM}} - (2E_{\mathrm{mol}} + E_{\mathrm{Au(111)}})\right\} \qquad , \tag{6.1}$$

i.e., the difference in energy between the bonded and isolated subsystems. Despite neglecting van der Waals contributions for methodological reasons (see Methods section), we find sizable exothermic values of −0.58 eV (−56.0 kJ/mol), −0.56 eV (−54.0 kJ/mol) and −0.33 eV (−31.8 kJ/mol) per molecule for **1**, **2** and **3**, respectively. This indicates that such monolayers can indeed be formed and will be reasonably stable. Here, it should be mentioned that for thiols, replacing the S–H with an S–Au bond is calculated to be even slightly endothermic using the same methodology (while breaking the finally formed thiolate–Au bond again costs a considerable amount of energy in excess of 1 eV (96.5 kJ/mol)).[62]

For the adsorbed SAMs consisting of molecules **1-3**, the densities of states projected onto the molecular layers (PDOS) at energies close to E_F are shown in the left panel of Fig. 6.3. The spin-restricted calculations (shown as black areas) are characterized by peaks around E_F that are only half-filled, a result expected for radicals under these conditions (*vide supra*); only in **1**, a somewhat more complex situation occurs, as there are overlapping peaks in the DOS close to E_F. The real-space representations (local density of states, LDOS) of the states contributing to this half-filled peak are shown in the right panel, integrated between E_F and $E_\mathrm{F} \pm 0.1$ eV, respectively. In all three systems they are reminiscent of the closed-shell molecular LUMO (see corresponding LDOS plots).

As radicalization implies the existence of unpaired electrons, relaxing also the spin degree of freedom can lead to a spin-polarized solution at lower energy. Indeed, using a proper initial guess for the magnetization (see Methods section) we find such solutions with different α- and β-spin densities of states, shown in light and dark gray color in Fig. 6.3. The calculated stabilization of the α- and destabilization of the β-states are quite small, which is why both peaks remain close to E_F and very similar injection barriers are found for electrons and holes. Note, however, that the extent of the predicted splitting depends on the chosen density functional and we find it to increase when using a hybrid functional (*cf.*, discussion in Appendix 6.A). In this context it is, however, worth remembering that Crivillers *et al.*[17] did observe a huge increase in the low-bias conductivity in related radical molecules compared to their closed-shell counterparts, which supports the notion that radical formation significantly reduces the transport gap. The fundamental difference between the study in ref. 17 and the present one is that Crivillers *et al.* adsorbed radicals directly onto a properly primed Au surface, while we here suggest a strategy to start with closed-shell systems and then form the radical through the binding to the substrate.

The different number of electrons in the α- and the β-spin manifold in the spin-unrestricted calculations also implies that the closed-shell molecules **1-3** change their magnetic properties upon adsorption. Each of the unit cells is

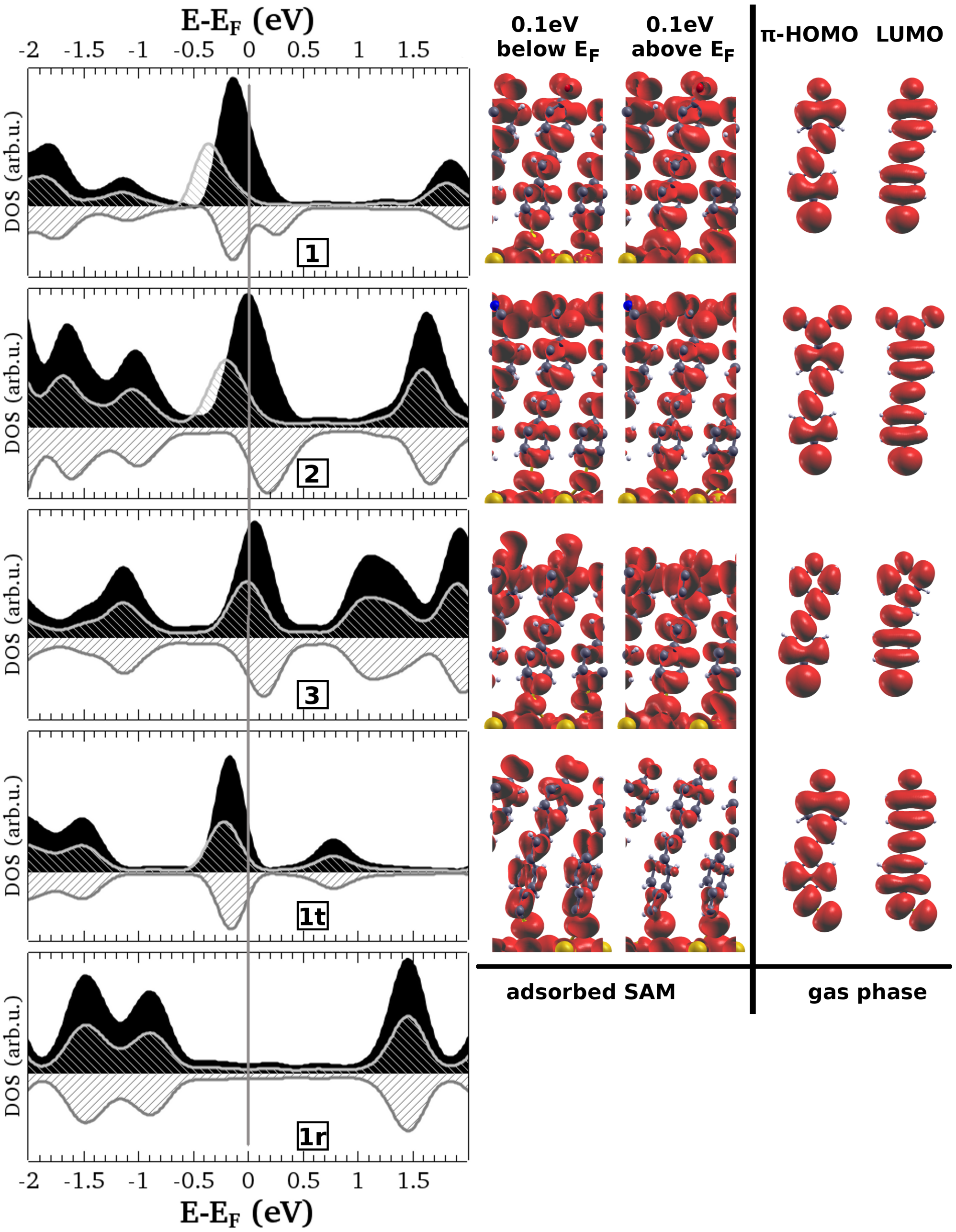

Figure 6.3: *Left: Spin-restricted (black) and spin-unrestricted (up/down: light/dark gray) PDOS of all investigated adsorbed monolayers, aligned at the Fermi energy E_F (vertical gray line). Right: LDOS plots in energy windows of 0.1 eV below and above E_F for the adsorbed monolayers of molecules* ***1****,* ***2****,* ***3*** *and* ***1t****. In addition, the LDOSs of the respective gas phase π-HOMO*[*] *and LUMO orbitals is shown.*

[*] *Note that in the PW91 calculations of the isolated molecules, a localized σ-orbital is found as HOMO and the delocalized π-orbital is only the HOMO-1. This is not the case in calculations using a hybrid functional, which can be rationalized as an orbital-dependent self-interaction error in the PW91 calculation.*[42,159]

characterized by an uncompensated spin, which in the case of the PW91 based calculations amounts to 1.70 (**1**), 1.55 (**2**), and 0.65 μB (**3**), respectively. The exact values for these magnetic moments should be considered with some caution, as a larger splitting between the α- and β-manifolds as expected, *e.g.*, for hybrid functionals (*vide supra*) would most likely modify these values. They are also to some extent influenced by the chosen broadening of the electronic states (see Methods section). Independent of these technical details, each molecule bears a non-vanishing magnetic moment, *i.e.*, the monolayer is calculated to be ferromagnetic. Ferromagnetic organic materials are indeed known,[160,161] but it has to be kept in mind that the periodic boundary-conditions in the band-structure calculation enforce parallel alignment of the spins in all unit cells. Thus, on the basis of our calculations it also cannot be excluded that the actual monolayer displays paramagnetic properties (*cf.* ref. 155). As a side note, we also mention that magnetic phenomena at the Au–S interface have been discussed in various contexts in the literature (see for instance refs. 162–164).

An interesting observation is also that for the investigated systems, the spin-unrestricted solutions are lower in energy by only 0.04 eV (**1**), 0.02 eV (**2**) and < 0.01 eV (**3**) than the spin-restricted ones. These values are in the order of $k_\mathrm{B}T$, suggesting that for the present molecules both a spin-unrestricted solution (ferro/paramagnetic with a non-vanishing transport gap) as well as spin-unpolarized solution (diamagnetic with the highest bands half-filled by electrons of opposite spins rendering the system metallic – *vide supra*) might well coexist at room temperature. Their relative stability (and thus the fundamental magnetic and electronic properties of the SAMs) could then very well be controlled by chemical substitution or external stimuli like applying a magnetic field. These observations certainly warrant further investigations.

To illustrate that the formation of a radical SAM (be it ferro/paramagnetic or not) upon adsorption of molecules **1-3** is solely due to the thiocarbonyl docking group and not a consequence, for example, of the quinoidal backbone of the studied molecules, we also calculated the PDOS for molecule **1t** (Fig. 6.2) on Au(111). Apart from the thiocarbonyl group being replaced by a mercaptomethylene group, this (closed-shell) system is identical to **1** and we assumed the same unit cell in the calculation.[ii] The corresponding PDOS around E_F and the related LDOS are also shown in Fig. 6.3. We observe pinning of the fully occupied HOMO-derived peak at E_F (*cf.* also ref. 96) and find the empty LUMO-derived states well above E_F.[iii] Moreover, no spin-unrestricted solution is found (see gray curves for **1t** in Fig. 6.3).

The mechanism responsible for the generation of the radical upon bonding

---

[ii] We note that upon adsorption, the hydrogen might actually reduce the molecule rather than being desorbed as H_2, rendering also **1t** a radical. We don't consider this possibility here as our intention is to demonstrate the role of only the docking group on the interfacial electronic structure.

[iii] Note that this band gap can be viewed only as a lower limit, as semi-local functionals such as PW91 are known to underestimate the band gap of semiconductors.

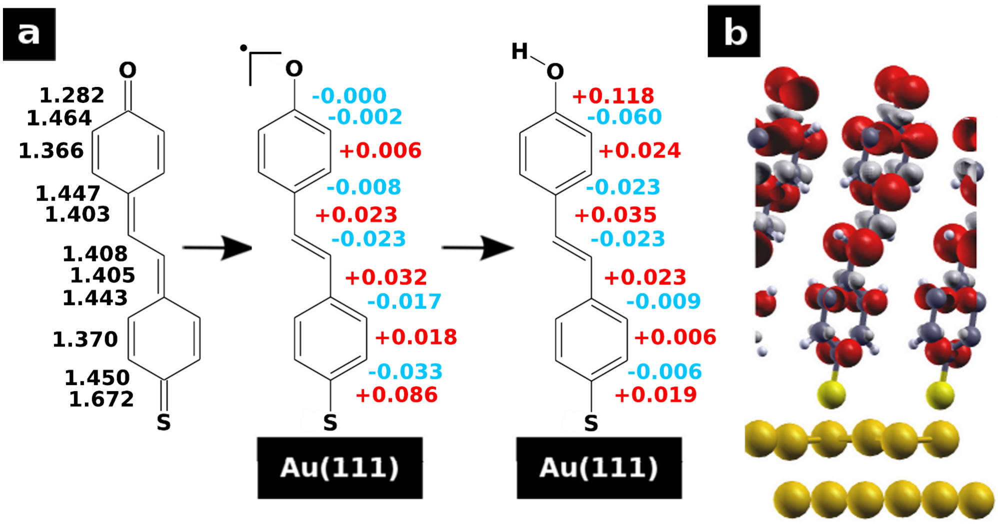

Figure 6.4: *(a) Mechanism of radicalization upon adsorption and subsequent reduction; gas phase bond lengths and respective bond length changes are indicated. (b) Spin density of the adsorbed molecules (red: excess α-spin; light gray: excess β-spin.*

is sketched in left and center part of Fig. 6.4a for molecule **1**: The formation of the new Au–S bond causes a decrease of electron density in the S=C bond and, thus, leads to a significant elongation of this bond. The new situation can be essentially described as an Au–S–C unit, in which one electron of the S=C bond is used for the formation of the Au–S bond. Consequently, an unpaired electron is generated and accommodated all over the molecule, which now bears an increased aromatic character (see indicated bond length changes). This delocalization of the uncompensated spin can be seen in the calculated spin-density (*i.e.*, the difference between α- and β-charge densities) of the adsorbed molecules shown in panel b of Fig. 6.4. This shows that the quinoidal/aromatic nature of the backbone is important for the radical's delocalization, while its formation is a consequence of using a thiocarbonyl docking group (see comparison between **1** and **1t**).

As mentioned, redox-switching of the optical and magnetic properties of closely related molecules has been found experimentally.[155] To show the effect of chemical reduction on the interfacial electronic structure, we studied also a variant of the Au(111)/**1** interface in which the carbonyl groups were reduced (*i.e.*, where the carbonyl groups were replaced by hydroxyl groups). This yielded the SAMs denoted as **1r** in Fig. 6.2. The resulting bond-length changes indicate a further increase of the aromatic character of the backbone (see center and right part of Fig. 6.4a) and the molecules adopt a closed-shell structure now also on the surface. As a result, the gap between the (now fully occupied) HOMO- and the LUMO-derived states drastically increases (bottom panel of Fig. 6.3). The absence of Fermi-level pinning (that is still observed for **1t**, *vide supra*) implies an equally drastic increase of the charge-injection barriers, consistent with above mentioned experimental observations.[17,155]

6.3 Summary

To summarize, we propose the thiocarbonyl group as a potentially interesting docking group for use in self-assembled monolayers on noble metals. A radicalization of closed-shell molecules is induced upon bonding to the substrate, for which we find clearly exothermic adsorption energies of 0.33 - 0.58 eV (32 - 56 kJ/mol) per molecule. The electronic and magnetic properties of the resulting SAMs are fundamentally different from thiolate-bonded but otherwise analogous molecules. Charge-injection barriers are modified and energetically extremely close solutions for non-magnetic metallic and magnetic monolayers with reduced density of states at E_{F} are found. We speculate that one of these solutions could be stabilized with respect to the other by a molecular design approach, and further show how level-alignment and magnetic properties in such SAMs can be switched by redox-reactions.

6.4 Methods

The density-functional theory calculations were performed using the VASP code.[80] Valence electrons were described by a plane-wave basis set (kinetic energy cutoff of approx. 20 Rydberg) and valence-core electron interactions by the projector augmented-wave (PAW) method.[81,120] A $8 \times 5 \times 1$ Monkhorst-Pack[82] k-point grid was chosen and a Methfessel-Paxton occupation scheme with a broadening of 0.2 eV was used. The metal was modeled by five layers of Au(111) atoms and the resulting unit cell was periodically repeated in all three directions. To exclude spurious interactions between subsequent slabs, a vacuum gap of > 20 Åwas introduced together with a dipole layer within that vacuum gap to compensate for the asymmetry of the slab. Geometry optimizations were performed using a damped molecular dynamics based scheme until forces fell below 0.01 eV/Å. The convergence criterion for electronic relaxations was set to a maximum total energy change of $\Delta E < 1 * 10^{-7}$ eV, which guarantees also a sufficient convergence of the unit cell's dipole moment. During geometry relaxations, the coordinates of the lower three gold layers were fixed (representing the bulk), while the upper two layers (representing the surface) were free to move. Further details regarding the applied computational methodology and the employed parameters are given in ref. 62. Representations of the systems were generated using XCrysDen.[84] An isovalue of 0.0015 e/Å^3 was chosen for the LDOS plots and 0.01 a.u. for the orbital plots in Fig. 6.5.

Van der Waals forces, which are not included in conventional semi-local DFT but available via correction schemes,[165,166] were not accounted for. This was not considered necessary, as the fundamental electronic changes described here would be hardly affected by the moderate changes in the tilt- or herringbone-angle such a correction would most likely predict. It would, however, change the absolute values of the adsorption energies. Considering the overall similarity of the chosen molecules, these changes are expected to be rather similar for each system.

To arrive at a spin-polarized electronic structure, we assumed initial magnetic moments of 1 μB for all carbon atoms in the unit cell and 0 μB for the remaining atoms. An antiferromagnetic solution could not be found (using the initial guess of 1 μB for the carbon atoms of one molecule and -1 μB for the carbons of the other molecule). These test calculations converged to the spin-unpolarized solution without magnetization. We note that reducing the Methfessel-Paxton smearing from 0.2 eV to 0.00862 eV (100 K) gave the same magnetic moments for the systems with molecules **1** and **3**, while for **2** a value of 0.78 μB instead of the reported 1.55 μB was found.

The bond lengths used to produce Fig. 6.4a were calculated considering the average values of equivalent bonds (ignoring the minor deviations due to the fact that, strictly speaking, no symmetry-equivalent bonds exist in these molecules). In the adsorbed layers, averaging was done over both molecules in the unit cell.

Acknowledgment. The authors thank LJ Wang for help with the calculations and L. Kronik, G. Heimel, G. Gescheidt, M. Aichhorn, L. Beverina and G. Pagani for fruitful discussions. We are grateful to the Scientific Computing section of the ZID of the Graz University of Technology for providing computational resources. Also financial support by the Austrian Science Fund (FWF): P20972-N20 is gratefully acknowledged. ZS is supported by the "Foundation for Innovative Research Groups of the National Natural Science Foundation of China (21121004)".

Appendix 6.A Dependence of the spin-splitting in the isolated molecule 1 on the chosen *xc*-functional

It is well known that semi-local DFT calculations underestimate the gap of semiconductors, and hybrid functionals usually increase the gap compared to the semi-local result.[38] As discussed above, after adsorption of molecules **1**-**3**, the relevant gap is the difference between α- and β-channel of the SOMO (singly occupied molecular orbital)-derived band. While hybrid calculations can be easily done for open boundary conditions, they are computationally demanding in periodic systems. Calculating the complete metal/SAM interface using a hybrid functional is a quite formidable task that we have recently mastered for closed-shell SAMs,[159] but we have not yet succeeded for spin-polarized calculations and are also not aware that anyone else has. Because of this, we only tested the dependence of the α-HOMO/β-LUMO gap for the gas phase radical derived from **1**. It was obtained by reducing the thiocarbonyl group with atomic hydrogen (see Fig. 6.5). The resulting α-HOMO and β-LUMO are shown in Fig. 6.5 and the LDA, GGA and B3LYP gap are given. While

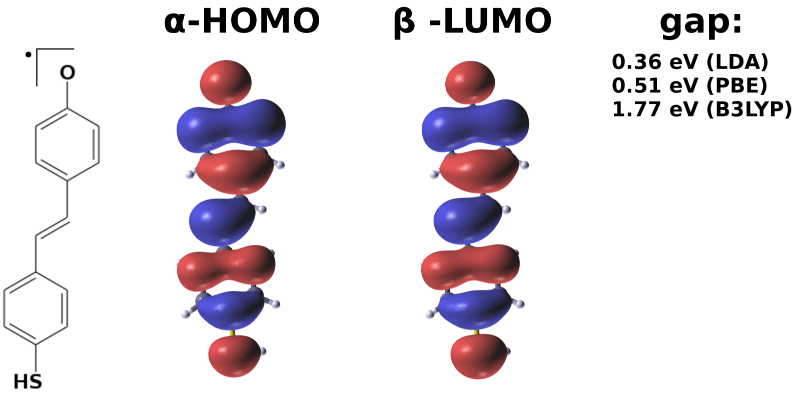

Figure 6.5: *Gas phase radical derived from molecule **1** (see Fig. 6.2) by addition of a hydrogen atom, its α-HOMO and β-LUMO and the related gap for different functionals.*

for all functionals both orbitals are reminiscent of the closed-shell LUMO (see Fig. 6.3), the gap strongly depends on the chosen functional, changing by almost 1.5 eV between LDA and B3LYP.

It is, however, far from trivial to transfer this functional-dependence of the gap to the calculations of the adsorbed monolayer presented in the main text, as in the latter situation the molecular electronic structure is severely modified. The two main reasons for this are the dielectric screening in the monolayer due to the neighboring molecules and the screening by the nearby metal.[85,167,168] Both effects reduce the band gap, and both effects are missed by semi-local as well as hybrid functionals. Because of this, the error of the results presented in the main text (using the semi-local PW91 functional) is most likely smaller than the data in Fig. 6.5 suggests.

Appendix 6.B Why doesn't all this happen also when pyridines are adsorbed on gold?

Fig. 6.6 compares the molecules of Chapter 5 with those discussed here. Also there, closed-shell molecules were adsorbed on the gold surface and also there a new bond was formed at the interface (rather than an existing one replaced, as is the case for thiols). Although pinning was observed for pyridines, the LUPS were found pinned with their onset at E_F (see Fig. 5.5) as opposed to the half-filled states shown in Fig. 6.3 (for non-spinpolarized calculations). Accordingly, no spin-polarized PDOS could be found for pyridines in test calculations (not shown).

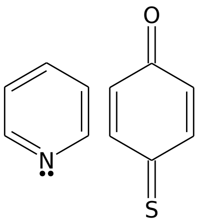

Figure 6.6: *Chemical structure of pyridine and thioquinone molecules.*

A possible explanation[iv] for this difference is, that pyridine is an aromatic ring just like benzene, where the nitrogen atom contributes to the ring with three of its valence electrons. The remaining two valence electrons are called the nitrogen “lone pair”. It is those electrons which bind to the surface when pyridine is adsorbed. The electrons belonging to the aromatic ring are hardly affected as this would decrease aromaticity and, thus, increase the energy.

The situation is different for (thio)quinones. They can gain energy by increasing aromaticity, and this can be achieved by redistribution of conjugated electrons into the SAM-metal bond, as described in the main text of this chapter (see Fig. 6.4).

[iv] Thanks to Oliver Hofmann!

Part II

Self-Induced Electric Fields.

Chapter 7

Preface

The previous part has focused on interfaces, *i.e.*, the relative alignment of the electronic states in neighboring (bonded) materials. This is part of the following chapters as well, but the focus now changes to the electronic structure of the SAM itself and how it is modified by *intermolecular electrostatic interactions*. As the molecular dipoles get closer during monolayer formation, the corresponding electric fields lead to surprising electronic properties of the SAMs.

Plenty of literature exists on the effect of electric fields on molecules and monolayers.[169–178] Most importantly, electric fields change the HOMO-LUMO (band) gap and the localization of the orbitals. The above-cited studies focus on the effect of externally applied fields.

The effect of dipoles incorporated in SAMs has been subject to plenty studies as well (for a review, see ref. 31). The parallel arrangement of dipoles introduces a step in the electrostatic potential energy in analogy to a plate capacitor and this leads to anisotropy in the electronic properties of the layer: depending on which side of the monolayer electrons are extracted (added), the ionization potential (electron affinity) differs. This effect has been confirmed experimentally (see, for instance, refs. 179 & 180). The relevant electric field is generated collectively. This is, it is exclusively due to the permanent electric dipoles of the SAM-forming molecules. These dipoles are usually attached to the molecules as end-group substituents, and, therefore, the major part of each molecule is *not* exposed to the corresponding field (see Chapter 8 and refs. 61, 28 & 30).

The following chapters focus on what could be called *field engineering*: controlling the electric field in the SAM by placing intramolecular dipoles accordingly. When such molecules assemble, the collective action of the dipoles generates the wanted electric field within the SAM. Its effect on the electronic structure is then studied as a function of the relevant quantities, such the SAM packing density, molecular length, or (in case of mixed SAMs) the mixing ratio.

Chapter 8 discusses monolayers in which neighboring molecules carry dipoles of alternating direction, and this results in the density of states of the monolayer being totally different from the one of the pristine components; in this sense, mixing creates a new material. In this work we could distinguish, by means of non-selfconsistent calculations, between effects that are of electrostatic interaction and such that are not - *i.e.*, (de)polarization effects which rearrange charges.

Chapters 9 & 10 deal with a qualitatively different arrangement of dipoles. Here, instead of end-group substituents the backbone of the molecules carries an electric dipole and, as a consequence, the total dipole is a function of the molecular length. In such a situation, the self-induced electric field in the SAM penetrates throughout the monolayer and truly modifies its "internal" electronic structure. It will turn out that the situation can be analyzed as if an external electric field was acting on the layer, although no external source is present.

The oligopyrimidine molecules used in these studies are difficult to describe with DFT, as localized and delocalized orbitals are found amongst the highest occupied states. In Chapter 9 it is shown that this leads to an orbital self-interaction error (SIE), see Sec. 2.1 & ref. 42. We show that using the hybrid functional HSE is a relatively "cheap" way of correcting the SIE for these molecules. Having found a suitable methodology, the chapter studies the transition from a single molecule to a closely packed monolayer, which corresponds to successively increasing the electric field across the layer (as it is determined by the density of dipoles). In analogy to the quantum-confined Stark effect known from inorganic semiconductor quantum-wells, a significant reduction of the band gap and localization of the electronic states is found.

Chapter 10 discusses the question of what is the effect when such molecules are elongated by attaching further polar repeat units. This is done in gas phase as well as in the periodic SAM configuration, and in both cases the evolution of dipole and band gap are compared with the limit of the truly periodic cases (the "wire" in gas phase and the "bulk" for the SAM). They do not coincide. For instance, the band gap vanishes in the long-SAM limit but the bulk is (of course) semiconducting. This is rationalized mainly on electrostatic grounds - as the cause for all this is the self-induced electric field.

Chapter 8

The electronic structure of mixed self-assembled monolayers (ref. 181)

Also the present chapter studies monolayers of molecules to which polar groups are attached. As opposed to the previous part, different groups are attached to molecules of the same monolayer, which then form a *binary* or *mixed* SAM.

Such layers are interesting from the perspective of collective phenomena, as mixing introduces inhomogeneity to the distribution of the electric field. This is reflected in the electronic properties of the SAM. It also made the analysis more tricky as a one-dimensional picture is not enough anymore. Consequently, line-averaged instead of plane-averaged plots will often be used.

The Electronic Structure of Mixed Self-Assembled Monolayers

Ferdinand Rissner,† David A. Egger,† Lorenz Romaner,‡,† Georg Heimel,§ and Egbert Zojer†,*

†Institute of Solid State Physics, Graz University of Technology, Petersgasse 16, 8010 Graz, Austria, ‡Chair of Atomistic Modelling and Design of Materials, University of Leoben, Franz-Josef-Strasse 18, 8700 Leoben, Austria, and §Institut für Physik, Humboldt-Universität zu Berlin, Brook-Taylor-Strasse 6, 12489 Berlin, Germany

ARTICLE

Figure 8.1: *Header of the article ref. 181 showing its title and all contributing authors. This chapter is essentially identical to the article and part of its Supporting Information.*[i]

The work was published[181] (Fig. 8.1) in essentially the form presented below.[i]

---

[i] Reproduced with permission from ACS Nano. Copyright 2010 American Chemical Society. Essentially the original article is reproduced together with part of its Supporting Information. The original version is available online at `http://dx.doi.org/10.1021/nn102360d`.

Author contributions. In this work I could build on initial studies of Lorenz Romaner who has provided a useful unit cell and some information about his preliminary results. From that point I have done all the calculations, analysis, an extensive search in literature, have written the first draft of the manuscript and came up with the idea of doing the non-selfconsistent calculations. All other authors have contributed with frequent, lively and exciting discussions about the interpretation of the results. Beyond this, particularly Georg Heimel and Egbert Zojer helped improving the conceptual and linguistic clarity of the manuscript.

Abstract. The electronic structure of mixed self-assembled monolayers (SAMs) on Au(111) surfaces is modeled using slab-type density-functional theory calculations. The studied molecules have a dipolar character induced by polar and electron donating or accepting tail-group substituents. The resulting electronic structure of mixed layers is found to differ qualitatively from a simple superposition of those of the respective pure layers. Specifically, the positions of the frontier electronic states are shifted relative to the metal Fermi level, with the sign and magnitude of that shift depending on the dipole moment of the molecules and the mixing ratio in the film. This appears counterintuitive considering previous investigations, in which it has been shown that, for densely packed layers, tail-group substituents have no impact on the interfacial energy-level alignment. The seeming contradiction can be lifted by considering the local electrostatic interactions within the films in both mixed and homogeneous monolayers. Beyond that, we show that mixed SAMs provide an efficient tool for continuously tuning substrate work functions over a range that far exceeds that accessible by merely changing the coverage of homogeneous layers, with the net effect depending linearly on the mixing ratio in agreement with recent experimental findings.

8.1 Introduction

Covalently bonded self-assembled monolayers (SAMs)[1,2,182] on noble metals are of ever increasing importance[183,184] for a variety of applications.[56,185–187] Their electronic properties are exploited in organic (opto)electronic devices to tune electrode properties, which can lead to a significant improvement of device performance.[54,56–58,64] In particular, the alignment of the frontier energy levels in the organic semiconductor with the Fermi level of the electrode needs to be optimized.[59,60,188] In this context, the effective work function, Φ, of the electrode is the single most important parameter, which needs to be adjusted through the employment of suitable SAMs. A key quantity of interest is, therefore, the SAM-induced work-function modification, $\Delta\Phi$.

Besides using SAMs for "mere" surface modification, in the quest for ultimate miniaturization, the molecular monolayer itself[7,21,189,190] or even individual molecules[102,150,191–196] can be used as the functional entity of a device. For such applications, the alignment between the SAM and the metal states is of key importance, as the positions of the highest occupied and lowest unoccupied π-states in the SAM relative to the Fermi level of the electrodes determine the tunneling barriers for hole and electron transport.

Great effort has been made to understand and control the electronic properties of SAM-modified surfaces, both experimentally[148,197] and through computational modeling.[31,69,137,198,199] In-depth knowledge on the impact of the docking chemistry,[70,200] the molecular polarizability,[201] depolarization effects,[28,63,136,202,203] and (dipolar) donor- and acceptor substituents[61,198] has been seen to be of uttermost importance for designing molecular structures that lead to SAMs with the desired characteristics.

An alternative approach for tuning SAM properties is to fabricate mixed layers of different functional molecules.[114,204–209] Following this strategy, Wu *et al.*[210] have shown that, by combining SAMs of alkanethiols and fluorinated alkanethiols, the substrate work function can be adjusted in an almost linear fashion as a function of the mixing ratio. The fabrication of well-ordered mixed layers is an experimental challenge and phase segregation is frequently observed.[206,211–216] While for some applications this can be exploited,[217] mixing at the molecular level is usually desired. One approach to prevent segregation is to intentionally generate defects in a well-ordered homogeneous SAM by electron irradiation or UV light exposure. In this way, a place-exchange reaction can be promoted in which part of the molecules are replaced by another component to obtain a mixed film.[208,218,219] Another strategy to realize mixed SAMs is to attach both functional groups of interest to the same molecule.[213,220–223] Silien *et al.*[209] succeeded in using a network of flat-lying molecules as mask[224] for patterning a binary SAM on the nanoscale and Pace *et al.*[225] have shown that under certain circumstances it is possible to produce crystalline mixed domains. In layers ordered that well, one can exploit the fact that the local electrostatic environment of adsorbed molecules crucially impacts their properties. Such considerations have, for example, been used for explaining the mixing-ratio dependent ultraviolet photoelectron spectroscopy (UPS) results observed for mixed pentacene and perfluoro-pentacene layers.[226] Furthermore, in single-molecule transport experiments the conductivity is distinctly different for isolated molecules and for molecules assembled in a monolayer;[26] such a situation is in some sense reminiscent of a previous computational study[28] in which SAMs at reduced coverage but essentially in their monolayer geometries have been investigated. We are, however, not aware of a computational study that provides a systematic investigation explaining the peculiar properties of a mixed SAM that consists of two different functional molecules. Here, we provide such a study. Specifically, we address the question of how the electronic properties of a molecular layer change when it is patterned on a subnanometer scale. As we will show in the following, the electronic properties of a mixed SAM differ qualitatively from what one might naively derive from the properties of the two neat layers, with each of them consisting of only one of the constituent molecules of the mixed SAM. Resolving that puzzle will require us to disentangle several effects and will reveal electrostatic intermolecular interactions in SAMs as the key issue. To comprehend our observations on mixed monolayers, it is both instructive and revealing to contrast these findings against the properties of homogeneous monolayers.

8.1.1 The system

For the present study, we chose to investigate biphenylthiolate-based SAMs adsorbed on the Au(111) surface (Fig. 8.2) because such SAMs have been subject to extensive experimental[68,227–233] and computational[28,61–63,70,136,198,202] studies. For methyl-substituted biphenylthiolates on the Au(111) surface a $5\times8\times1$ unit cell has been suggested,[68,232] which serves as an important input for our calculations. These rely on density-functional theory (DFT) based, slab-type band-structure calculations in which the interface is modeled by five metal layers on top of which the molecules are adsorbed. As shown in Fig. 8.2b, the surface unit cell contains two inequivalent molecules arranged in a herringbone pattern, which is typical for oligophenylenes.[234] For mixing ratios other than 1:1, a multiple of the cell was chosen. The tilt of the molecular backbone with respect to the surface normal changed only moderately between the systems and was in the range of $14-21^\circ$. Further details on the applied methodology can be found in the Methods section. The molecules are assumed to bond to the flat metal surface via a thiolate group, which will be referred to as the docking group in the following. In this context, it should be mentioned that the actual structure of the Au/thiolate interface is still subject to controversy,[3] but its details do not impact the main conclusions of the present paper.

By substituting the terminal hydrogen atoms of the biphenylthiolates with strong (polar) donor or acceptor groups (the tail groups), the direction and magnitude of the molecular dipole moment can be controlled. Here, we chose amino ($-NH_2$) and cyano (–CN) tail groups as they carry intrinsic dipole moments that point in opposite directions and are very strong donors and acceptors, respectively. Fig. 8.2a,b shows the case of a 1:1 mixing ratio of those tail groups. We note that the role of docking and tail group substituents in such SAMs is well understood[70] and that the results of the present article can be expected to be transferable to other chemical groups of similar functionality, that is, polar donor and acceptor substituents. The electronic properties of homogeneous layers of both amino- or cyano-substituted biphenylthiolate SAMs have been described in the literature and are briefly reviewed here, as they are key to understanding the properties of mixed layers:[28,136] At dense packing, the $-NH_2$ substitution has been predicted to decrease the work function of the Au (111) surface, while –CN tail groups are expected to increase it.[61,70] Additionally, the *a priori* unexpected observation has been made that the substituent (and, thus, the molecular ionization potential) has no impact on the relative alignment of the metal Fermi level and the highest occupied π-states,[61] at least as long as the SAM packing density was sufficiently high.[28] In other words, the energetic distance between the Fermi level and the highest occupied π-states (HOPS), ΔE_{HOPS}, is identical for both SAMs. The same behavior was observed also

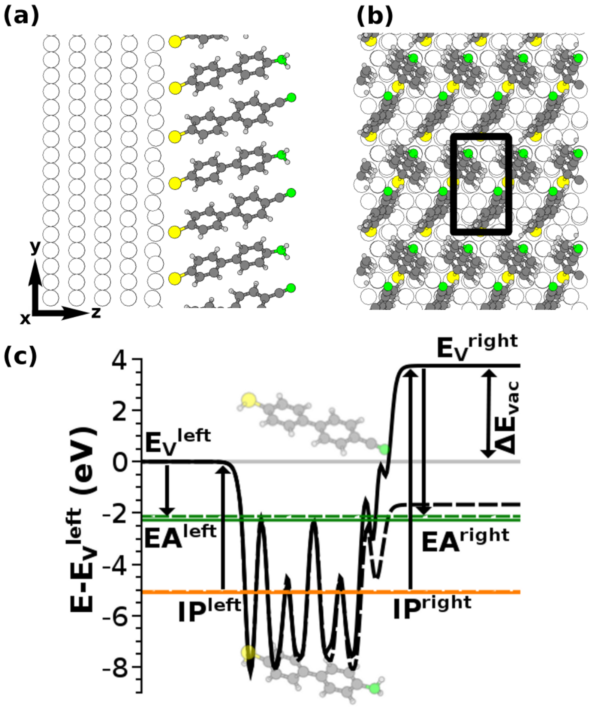

Figure 8.2: *Side (a) and top (b) view of the biphenylthiolate SAM on a five-layer Au(111) slab. In the depicted case, cyano and amino substituents are mixed in a ratio of 1:1. The Cartesian directions are indicated. The black rectangle marks the* $p(3 \times \sqrt{3})$ *surface unit cell and the molecules are packed in a herringbone pattern. (c)* x, y*-averaged electrostatic energy of an electron across a hypothetical free-standing densely packed homogeneous SAM (solid [dashed] line: cyano- [amino-] tail group). Left- and right side vacuum energy* (E_v)*,* $\Delta E_{vac} := E_v^{right} - E_v^{left}$*, ionization potential (IP), and electron affinity (EA) are indicated.*

for more polarizable (*e.g.*, polyene) and less polarizable (*e.g.*, aliphatic) backbones.[201]

This phenomenon can be explained on electrostatic grounds,[31,69] considering that a 2D extended dipole layer divides space into two regions with vacuum levels differing by an energy proportional to the dipole density as dictated by the Helmholtz equation. This is schematically shown in Fig. 8.2c, where the plane-averaged electron electrostatic energy for a (hypothetical) free-standing SAM is shown. The two vacuum-level energies, $E_\mathrm{v}^\mathrm{left}$ and $E_\mathrm{v}^\mathrm{right}$, differ by an amount ΔE_vac. Consequently, also a left- and a right-sided ionization potential, $\mathrm{IP}^\mathrm{left}$ and $\mathrm{IP}^\mathrm{right}$, and electron affinity, $\mathrm{EA}^\mathrm{left}$ and $\mathrm{EA}^\mathrm{right}$, need to be defined. They can be approximated by the energetic difference between the highest occupied (lowest unoccupied) states of the SAM and the respective vacuum levels. The tail-group substituents change the potential energy only on “their side” of the monolayer. Moreover, their impact on the potential energy landscape within the SAM is restricted to their immediate vicinity, consistent with the electrostatic properties of a densely packed dipole layer[30] and depolarization effects within the SAM.[28,63,136,152,202,203,235] Therefore, also the eigenstates within the SAM are hardly affected by tail-group substitution.

What eventually determines the alignment between the potential wells of the metal substrate and the SAM are only the left-sided vacuum level of the SAM, the position of the vacuum level above the metal surface, and the bond dipole that results from bonding-induced charge rearrangements.[69,137,200] The latter are largely localized in the docking-group region and on the top Au layers, resulting in the bond dipole being tail group-independent at full coverage.[61] As a consequence, tail-group substitution with a donor- or acceptor group hardly affects ΔE_{HOPS}, the offset between Fermi energy and HOPS.

8.2 Results and discussion

8.2.1 SAMs adsorbed on Au(111)

Bearing these properties of the homogeneous monolayers in mind, one might expect that also in the mixed system there should be only a single pronounced maximum in the density of states that is derived from the highest occupied states of all constituent molecules. This is, however, not the case as can be seen in Fig. 8.3. There, the calculated density of states projected onto the SAM (PDOS) is shown for the system depicted in Fig. 8.2, namely –NH_2 and –CN substituted biphenylthiolates on Au(111) at a mixing ratio of 1:1.

It displays a pronounced double peak structure between *ca.* -0.5 and -1.5 eV. To understand its origin, we calculated the densities of states projected onto the two subsystems, that is, only on the –NH_2 substituted (blue line in Fig. 8.3) and –CN substituted (red line in Fig. 8.3) biphenylthiolates within the mixed SAM. Their comparison clearly shows that the highest peaks belonging to the respective subsystems do not coincide in the mixed monolayer; rather, the highest PDOS peak is localized only on the –NH_2 substituted molecules. This can also be inferred from the corresponding local density of states (LDOS) shown as the right inset of Fig. 8.3 which, furthermore, confirms the π-character of the corresponding molecular orbital. The highest peak that also comprises states on –CN substituted molecules is found at 0.4 eV lower energies. From the LDOS plot, those states are confirmed as the HOPS of the –CN substituted sub-system that energetically overlap with the tails of the HOPS peak and a lower-lying state on the –NH_2 substituted subsystem. Considering that charge-carrier injection depends exponentially on the barrier height that results from the level alignment, a shift by 0.4 eV is a sizable effect. Moreover, this surprising finding shows that the electronic structure of the mixed SAM qualitatively differs from that of both the –CN and the –NH_2 substituted SAMs. There, as discussed in the previous section, the respective HOPS peaks in the homogeneous layers at full coverage are calculated to be within 0.03 eV (at -0.96 for the –NH_2 substituted and -0.99 eV for the –CN substituted SAM).[61]

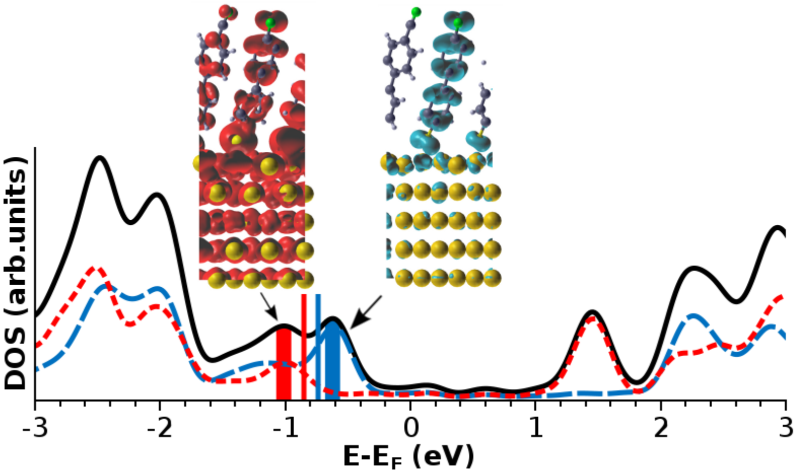

Figure 8.3: *Projected density of states of the mixed SAM on Au(111) with a 1:1 mixing ratio (black line). The dashed blue and dotted red lines show the projections onto only the –*NH_2 *(blue) and –CN (red) substituted subsystems. The insets depict the local densities of states integrated in the energy windows shaded in blue and red, respectively (thick vertical bars). It corresponds to the charge densities in these energy ranges. The thin red and blue vertical lines indicate the positions of the HOPS peak maxima of both components in absence of the respective other fragment (i.e., at half coverage). All curves are aligned to the Fermi energy,* E_F.

The next issue to be clarified is whether the PDOS of the mixed SAM is merely a superposition of the PDOSs of the two subsystems, that is, a –CN and an –NH_2 substituted SAM at half coverage. This is necessary because it has been shown in ref. 28 that, upon reducing the SAM coverage, the energetic difference between the HOPS peaks of –CN and –NH_2 substituted SAMs increases. This effect is not unexpected considering that in the limiting case of an “infinitely” dilute monolayer one ought to arrive at the “isolated molecule” situation and the energy levels of isolated donor- and acceptor-substituted molecules clearly differ from each other. We find, however, that such effects become relevant only at coverages well below 0.5 (the coverage of the individual subsystems of the mixed SAM). This is indicated by the thin vertical lines in Fig. 8.3 that show the respective HOPS peaks for the half-coverage SAMs at −0.74 eV (–NH_2) and −0.85 eV (–CN), respectively;[ii] that is, coverage-dependent shifts contribute only about 25% to the overall peak splitting observed in the mixed monolayer. The homogeneous half- and full-coverage systems will serve as reference systems for the remainder of this article. This is useful since the comparison allows strictly distinguishing between effects that can be observed already in the homogeneous subsystems (like coverage-dependent depolarization[28]) and such that arise from specific interaction of the two SAM components and, thus, go beyond a mere superposition of the properties of the subsystems.

[ii] The smaller (negative) values in both half-coverage systems compared to full coverage are a consequence of the coverage dependent bond dipole.[28] The slight differences in the peak positions compared to ref. 28 (there values of −0.78 and −0.86 eV were found) are due to the improved geometry optimization scheme used in the present study.

8.2.2 SAMs in the absence of the metallic substrate

At this point the question arises, which kind of interaction between the monolayer constituents is responsible for the unexpected electronic structure of the mixed SAM. To disentangle contributions from molecule/molecule and metal/molecule interactions, we discuss the hypothetical situation of a free-standing SAM next. This system is realized by removing the metal slab and saturating the thiolates with hydrogen atoms.[61]

As the left-sided vacuum level is most relevant for the alignment of the SAM states with the metal Fermi energy (*cf.*, Fig. 8.2c and corresponding discussion), the DOS of the different free-standing SAMs is best aligned at $E_\mathrm{v}^\mathrm{left}$, that is, the vacuum level at the side of the SAM that approaches the metal upon adsorption. The results for the mixed monolayer and the –NH_2 and –CN substituted biphenylthiolates at full coverage are shown as thick solid lines in the respective panels of Fig. 8.4. As the two molecules in the surface unit cell are not symmetry equivalent even in the homogeneous SAMs, it is useful to partition the total DOS of the layer into the contributions of the two symmetry-inequivalent subsystems. The results are indicated as dark gray and crossed light gray areas. We find that (i) in the homogeneous layers, the inequivalence of the two molecules in the surface unit cell is essentially irrelevant for their level alignment; (ii) both, for the homogeneous –NH_2 and –CN substituted SAMs, the HOPS peak is found at approximately -5.1 eV; that is, also in the free-standing layers the tail-group substituent has almost no impact on the position of the HOPS relative to $E_\mathrm{v}^\mathrm{left}$;[61] (iii) in the mixed SAM (top panel), the splitting of the eigenstates is even more pronounced in the absence of the metallic substrate (*ca.* 0.7 eV instead of 0.4 eV). This is because the HOPS peaks associated with the –NH_2 and –CN substituted molecules are shifted up by 0.43 eV and down by 0.23 eV compared to the homogeneous layers, as indicated by the dashed black arrows. The assignment of the various peaks to the different molecules is nicely confirmed by the insets, which show the local densities of states (corresponding to the charge density) within an energy window of 0.1 eV around the respective DOS peaks. Like for the adsorbed SAM, we have also calculated the DOS of the individual components of the mixed monolayer, that is, the free-standing –CN and –NH_2 SAMs at half-coverage, in the absence of the respective other fragment. This allows discriminating the effects arising from interaction between the individual components from a mere superposition of their respective DOS. Like in Fig. 8.3, the resulting HOPS-peak positions are plotted as vertical lines in the topmost panel. They essentially coincide. This comparison clearly shows that the contribution of packing-density effects to the level splitting vanishes in the absence of the metallic substrate.

8.2.3 Explaining the electronic structure of mixed monolayers

Electrostatics.

The above results allow the conclusion that the qualitative differences between homogeneous and mixed monolayers are due to molecule/molecule interactions.

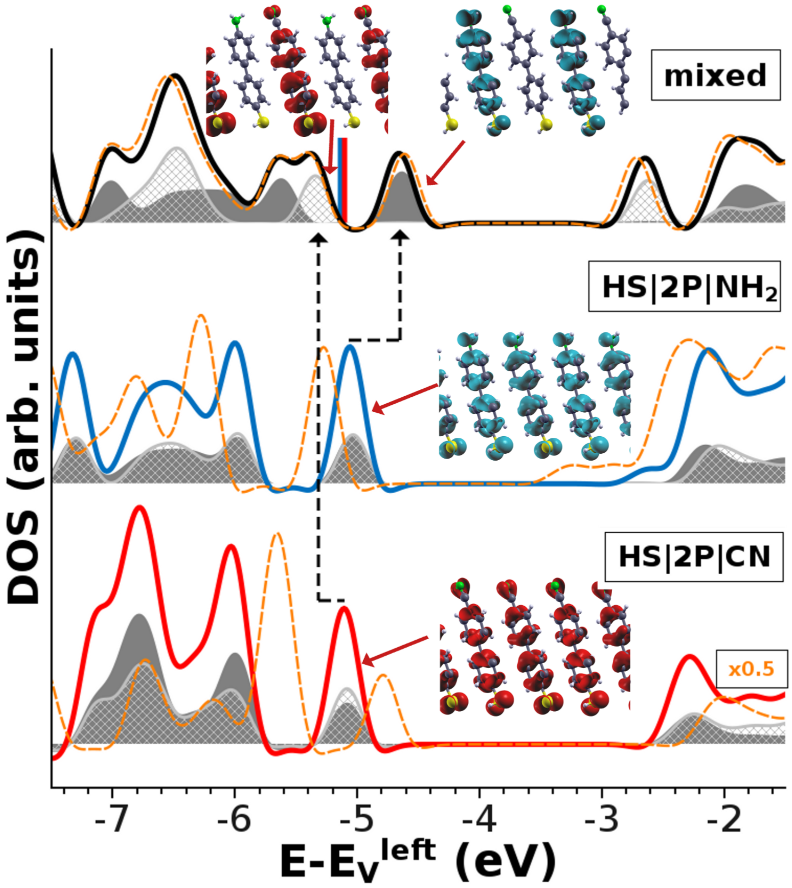

Figure 8.4: *DOS of the free-standing mixed and the respective pristine SAMs (top to bottom). The dark gray filled and light gray crossed areas show the DOS projected onto the two inequivalent components of the respective monolayers separately. The insets show the charge density in real space (LDOS) in energy windows of 0.1 eV around the respective peak maxima. The dashed black arrows indicate the splitting of the HOPS levels in the mixed layer compared to the pure layers. Dashed orange lines show the DOS resulting from non-selfconsistent (nscf) calculations in which no (de)polarization is allowed upon merging the two components. For details see text. In the bottom panel, the nscf-DOS is divided by 2 to save space. The two touching vertical lines in the topmost panel show the HOPS positions for both components in the absence of the respective other fragment in analogy to Fig.* 8.3*. All curves are aligned at the vacuum energy on the thiol side of the SAM,* E_v^{left} *(cf. Fig.* 8.2*c).*

The interaction with the metal plays a mitigating role, as upon adsorption the splitting between the HOPS states of the –NH_2 and –CN substituted subsystems is reduced to about half (*cf.*, Figs. 8.3 and 8.4). A significant contribution to the intermolecular interaction between polar molecules is electrostatic. To elucidate the role of such electrostatic interactions, we have calculated the potential energies for an electron in the two subsystems (–NH_2 and –CN substituted monolayers at half coverage), $E_{\mathrm{NH_2}-1/2'}$ and $E_{\mathrm{CN}-1/2''}$. Prime and double prime denote the two inequivalent sites for the molecules in the unit cell. The results are shown in Fig. 8.5a for a few neighboring cells averaged along the x-axis of the unit cell (*cf.* Fig. 8.2). Isodensity lines spaced by 0.1 eV clearly show that, compared to the common zero defined as the energy of the "left" vacuum level, the electrostatic energy in the region between the molecules decreases continuously for the –NH_2 substituted biphenylthiols, while it increases for the –CN substituted molecules. This region between the molecules at half coverage is where the additional molecules will be located in a densely packed SAM. Therefore, when going from half to full coverage, the additional molecules are embedded in the electrostatic energy landscape of the same type of molecules in a homogeneous monolayer, while they feel the electrostatic energy landscape of the other type of molecules in a mixed monolayer. In the latter case, this shifts the eigenstates of the –NH_2 substituted molecules up in energy and those of the –CN substituted molecules down, resulting in the peculiar level alignment discussed above.[iii] This mechanism is schematically summarized in Fig. 8.5b, where the electrostatic potential energy landscape is sketched for the half-coverage SAMs with the tail-group dipole moments pointing toward the right (1a) and toward the left (1b), respectively. Their HOPS levels are drawn as gray (green) bars. Panel 2 shows the changes in potential energy that affect the molecules in subsystems 1a and 1b upon merging. *I.e.*, it schematically combines the electrostatic potential energy arising from the –CN substituted sub-system at the position where the –NH_2 substituted molecules are found in the mixed SAM and *vice versa*. The energy levels of the molecules are modified accordingly: The HOPS of molecules belonging to subsystem 1a are shifted up and states in subsystem 1b are shifted down in energy. This results in the situation shown in panel 3. We note that, because of the nature of this effect, a prerequisite for an experimental confirmation of the predicted level-splitting by ultraviolet photoelectron spectroscopy (UPS) measurements is a mixing of the differently substituted molecules at the molecular scale.

[iii] At this point, it should be mentioned that the ionic relaxations we performed indicate that the mixed components interact also in terms of their geometry. For the donor headgroup –NH_2, two distinctly different conformations are possible. The plane of the pyramidal –NH_2 substituent can be oriented such that it reduces or increases the total molecular tilt angle with respect to the surface normal. For pure layers, both conformations are essentially equivalent in energy although they imply significantly different work-function modifications.[201] This changes in the mixed SAMs. Here, the geometry relaxes to the conformation in which a larger dipole moment perpendicular to the surface is associated with the –NH_2-substituted molecules so that they better compensate for the strong dipoles due to the –CN groups. This is consistent with the tendency of mixed SAMs to approach a situation with a net-dipole moment of zero as found experimentally.[214]

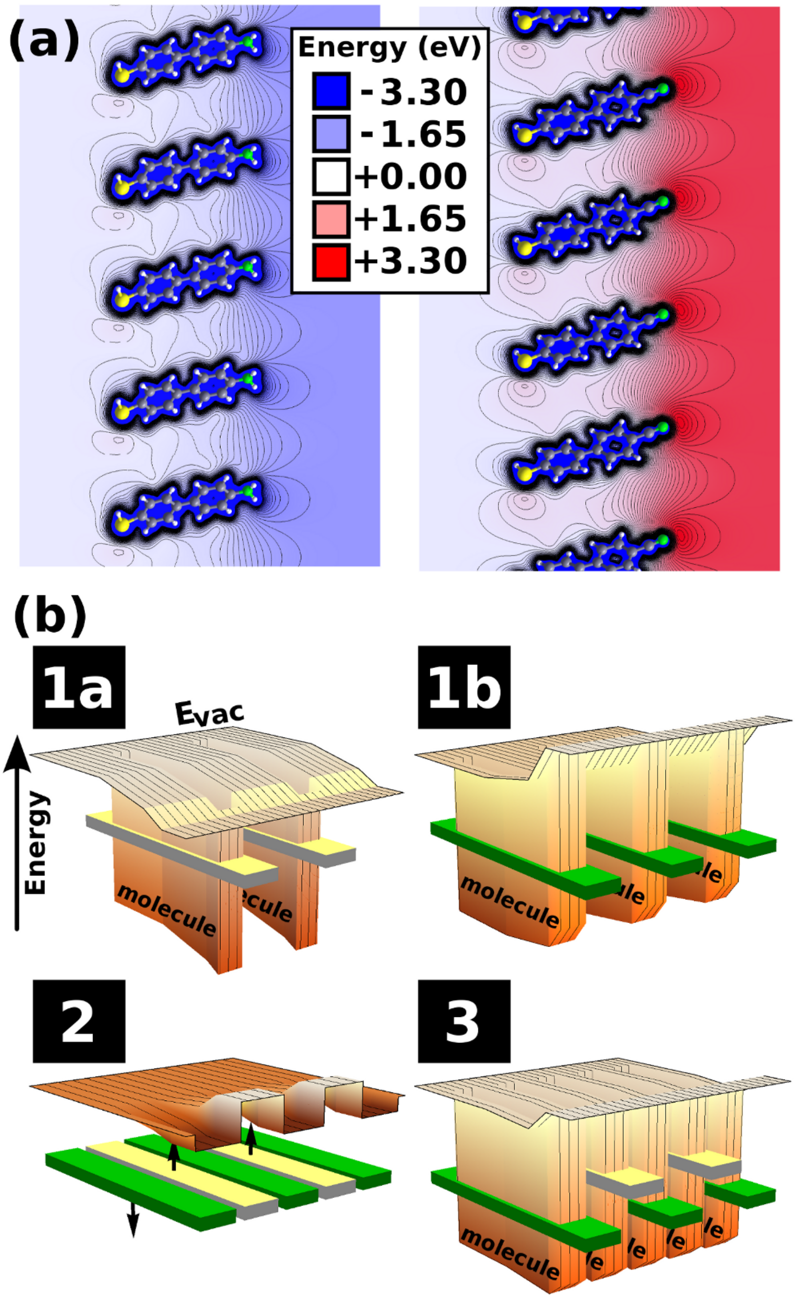

Figure 8.5: *(a) Electrostatic energies $E_{NH_2-1/2'}$ (left) and $E_{CN-1/2''}$ (right) across the components of the mixed monolayer. The plots are averaged along the x-axis of the unit cell (cf. Fig. 8.2) and aligned at E_v^{left}; the unit of energy is eV and isolines are drawn every 0.1 eV. (b) Schematic illustration of the electrostatic situation in mixed SAMs. Panels 1a and 1b show the potential energy landscape in the two subsystems before mixing. HOPS levels are drawn as gray (green) bars. Panel 2 shows the changes in potential energy that affect the molecules in the subsystems upon mixing and how those changes shift their eigenstates. The situation after mixing is shown in panel 3.*

Polarization and depolarization.

Following the same line of argument for the respective homogeneous layers, this explanation implies a corresponding downward (upward) shift of the eigenvalues for the homogeneous –NH_2 (–CN) substituted layers upon increasing the packing density from half to full coverage. Hence, it seemingly contradicts the findings discussed above, which show that such shifts do virtually not occur between half and full coverage in the free-standing monolayer (*cf.* Fig. 8.4). The reason for this is that the arguments in the Electrostatics subsection do not yet account for a second effect: When two half-coverage monolayers are merged to a full-coverage layer, the field originating from molecules in one half influences the molecules in the respective other half of the layer by depolarization or polarization.

Depolarization is a well-known effect in SAMs[28,63,136,152,202,203,235] and is a consequence of the fact that the electron cloud of every molecule within the SAM is polarized by the electric field that is the superposition of the fields generated by all other molecules in the SAM. In homogeneous layers, this field induces a dipole that points in the direction opposite to the intrinsic dipole of the molecule, thus reducing its dipole moment. Depolarization can be very large, especially for SAMs with highly polarizable backbones.[201] In a mixed monolayer, the opposite effect is to be expected. The antiparallel orientation of neighboring dipoles within the SAM leads to a mutual polarization giving rise to increased dipole moments.

To quantify the polarization and depolarization effects, we have plotted the DFT-calculated changes in the electrostatic energy that result from the interaction between two half-coverage subsystems in Fig. 8.6a. The leftmost plot shows the difference in the electrostatic energy between the mixed monolayer, E_{mixed}, and the respective sublattices, $\Delta E_{\mathrm{mixed}} = E_{\mathrm{mixed}} - (E_{\mathrm{NH_2}-1/2'} + E_{\mathrm{CN}-1/2''})$. The central and rightmost plots show the equivalent quantities for the homogeneous –NH_2 and –CN substituted SAMs when going from half to full coverage; these are defined as $\Delta E_{\mathrm{NH_2}} = E_{\mathrm{NH_2}} - (E_{\mathrm{NH_2}-1/2'} + E_{\mathrm{NH_2}-1/2''})$ and $\Delta E_{\mathrm{CN}} = E_{\mathrm{CN}} - (E_{\mathrm{CN}-1/2'} + E_{\mathrm{CN}-1/2''})$, respectively. The main observations in Fig. 8.6a are that

(i) the sign of $\Delta E_{\mathrm{mixed}}$ alternates between neighboring molecules as well as within each molecule;

(ii) the most pronounced changes in energy are confined to the vicinity of the tail-group substituents. The energy decreases by up to 0.5 eV near the –NH_2 substituents while the increase near the –CN groups is only up to 0.2 eV, consistent with the fact that the field at the locations of the –NH_2 groups (due to the –CN dipoles) is much larger than the field in the spatial region of the –CN groups (caused by –NH_2 dipoles; *cf.* also Fig. 8.5a).

(iii) Overall, those effects largely cancel: the change in electrostatic energy decreases only by 0.1 eV across the mixed SAM.

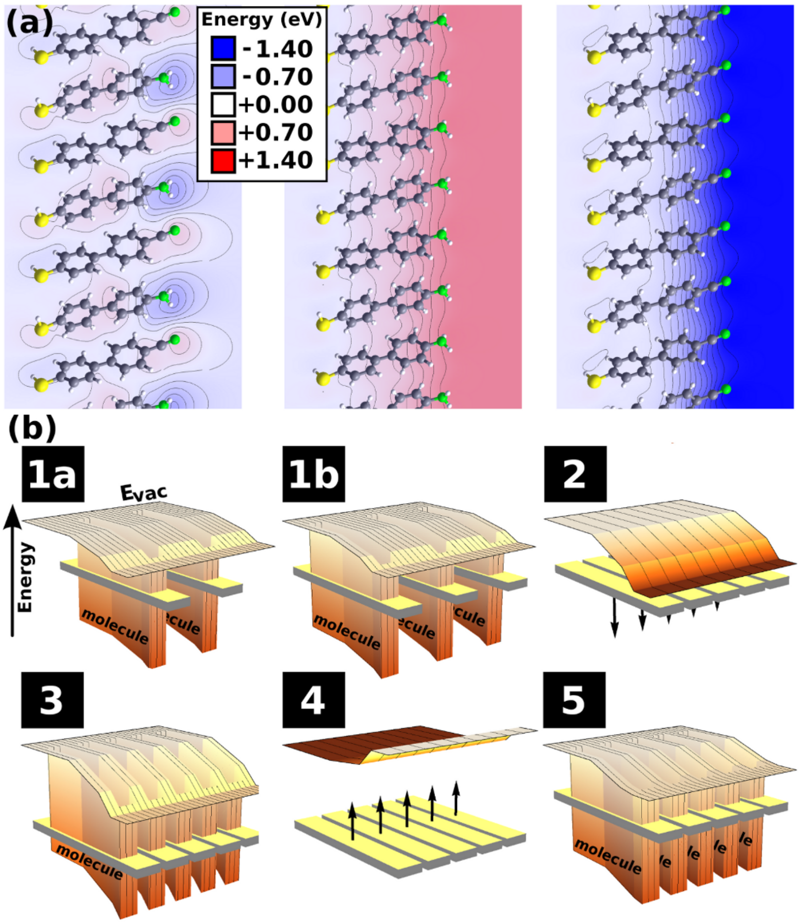

Figure 8.6: *(a) Effect of (de)polarization on the electron electrostatic energy* ΔE_{mixed} *(left),* ΔE_{NH_2} *(center), and* ΔE_{CN} *(right) when combing the components of the mixed SAM (left) and when doubling the packing density of the respective pure layers from half to full coverage (center and right). See text for the definition of these quantities. The energies are averaged along the x-axis of the unit cell (cf. Fig. 8.2) and isolines are drawn every 0.1 eV. (b) Sketch of the electrostatic energy landscape for increasing the packing density of a homogeneous* $-NH_2$ *SAM from half to full coverage. Similar to Fig. 8.5b, panels 1a and 1b show the potential energy landscape in the two subsystems before mixing; HOPS levels of* $-NH_2$ *substituted molecules are drawn as gray bars. Panel 2 shows the changes in potential energy that affect the molecules in the two subsystems upon mixing and how those changes shift their respective HOPS. The situation after mixing but prior to depolarization is shown in panel 3. Panel 4 shows the changes in potential energy which affect the molecules in the subsystems due to depolarization effects. The final situation (panel 5) differs from the mere electrostatic sum of the two half-coverage SAMs shown in panel 3.*

(iv) No such cancellation is found in the homogeneous case. The signs of ΔE_{NH_2} and ΔE_{CN} are opposite but remain unchanged throughout the whole monolayer, resulting in sizable overall changes of +0.7 eV (for $-\mathrm{NH}_2$) and −1.3 eV (for –CN) due to depolarization effects. In sharp contrast to the mixed case, isolines are to a good approximation parallel and significant changes in the electrostatic energy are found in the spatial region encompassing the second phenyl ring and the tail-group.

On the basis of these data it is perfectly plausible to assume that this change in electrostatic energy again shifts the HOPS energy in the respective homogeneous layers. The direction of that shift is such that it compensates for the shift discussed in the Electrostatics subsection, that is, up (down) for the $-\mathrm{NH}_2$ (–CN) substituted subsystem. In other words, when going from half to full coverage in a homogeneous SAM, the shift of the orbital energies induced by the fields that arise from the electrostatic interaction between the two subsystems (the effect discussed in the Electrostatics subsection) is fully compensated by the consequence of depolarization. In analogy to the scheme for the mixed SAM (Fig. 8.5b), a sketch of the mechanisms proposed for homogeneous layers is shown in Fig. 8.6b. Panels 1-3 correspond to the purely electrostatic picture described already in Fig. 8.5b for the mixed case. The non-negligible impact of depolarization on the HOPS energy is illustrated in panel 4, and panel 5 sketches the final energetic situation.

In the mixed case, because the sign of $\Delta E_{\mathrm{mixed}}$ within each molecule changes and because the most pronounced changes in energy are restricted to the vicinity of the tail-group substituents, the net contribution of polarization to the shift of the HOPS energies can be expected to be only of minor importance (*i.e.*, an effect analogous to that sketched in panel 4 of Fig. 8.6b does not occur). The inequivalence of the changes in electrostatic energy in homogeneous and mixed SAMs are caused by the equivalent, respectively, different signs of the (de)polarization induced charge rearrangements (see appendix or Supporting Information[i]) that eventually determine the changes in electrostatic energy via the 3D Poisson equation.

To test the above explanations and to quantify potential oversimplifications in the purely electrostatics-based explanation provided in the previous section, the role of those (de)polarization effects on the resulting DOS have to be considered. This can be done by calculating the DOS of the mixed and homogeneous full-coverage SAMs in a non-selfconsistent (nscf) way. To that end, we fix the charge density of the full-coverage SAM artificially to the sum of the (self-consistent) charge densities calculated for the two subsystems. This prevents any changes of the charge density due to (de)polarization and thus allows an estimation of the relative importance of (de)polarization processes for the correct, self-consistently calculated DOS. For details on the nscf-calculations, see the Methods section. The resulting nscf-DOSs are drawn as dashed orange lines in the corresponding panels of Fig. 8.4. For the mixed SAM, the nscf-DOS practically matches the self-consistently calculated one (solid black line).

This is plausible in the light of observations (i) and (ii) made above when discussing Fig. 8.6a and shows that the assumption of minor impact of polarization on the DOS is surprisingly well justified. For the homogeneous –NH_2 (–CN) substituted SAM, the nscf-DOS is shifted to lower (higher) energies, that is, the depolarization effects included only in the fully self-consistent calculations significantly impact the DOS (solid blue and red lines). In other words, our straightforward electrostatic model established in the Electrostatics subsection is indeed well-suited to rationalize the observations for the mixed SAM, while it fails for homogeneous layers, where depolarization effects have to be included.

The above considerations do not allow definitely excluding minor contributions from the exchange-correlation interaction between the two half-coverage subsystems of a full-coverage SAM, but they suggest the following semiquantitative picture for intramolecular interactions within SAMs and the resulting level alignment: Upon proceeding from half to full coverage, the electrostatic energy landscape created by the donor- (acceptor-)substituted subsystem (shown in Fig. 8.5) decreases (increases) the eigenenergies of the molecules that occupy the second adsorption site in the surface unit cell. If the latter bear a different substituent, that is, if one is dealing with a mixed monolayer, the impact of (de)polarization is negligible and the positions of the HOPS in the two subsystems are largely determined by this potential energy landscape (*cf.* Fig. 8.5b). As a consequence, a significant energetic splitting between the respective HOPS peaks is observed (*cf.* Fig. 8.4, top panel). In a homogeneous SAM, the abovementioned downward (upward) shift of the molecular states is largely compensated by the respective upward (downward) shifts due to depolarization (shown in Fig. 8.6b). As a net effect, there is only a very small difference between the positions of the HOPS peaks upon going from half to full coverage[28] or when replacing donor by acceptor substituents in a homogeneous SAM[61] (*cf.*, Fig. 8.4).

8.2.4 Impact of the mixing ratio

As a next step, we will discuss the impact of the mixing ratio. To that aim, we have studied a densely packed –NH_2 substituted SAM in which an increasing fraction of the –NH_2 substituents is replaced by –CN groups in steps of 25%. In this way, mixing ratios of 1:0, 3:1, 1:1, 1:3, and 0:1 are realized (for details on the considered surface unit cells, see Methods section). We first present the results for the free-standing mixed SAMs. Fig. 8.7a shows data for the HOPS positions associated with the –NH_2 (–CN) substituted subsystems as blue triangles (red circles). The IP^{left} values for homogeneous SAMs at the corresponding submonolayer coverages are also included as light gray, open symbols.[28] This again allows discriminating between packing-density related effects relevant for each subsystem separately and the interaction between the subsystems. We note that in ref. 28, the molecular tilt angle was kept constant at its value at full coverage for all lower packing densities. This procedure is useful for modeling and facilitates a comparison with the mixed systems of the present study. In a real-world experiment, however, geometry-induced effects of a changing

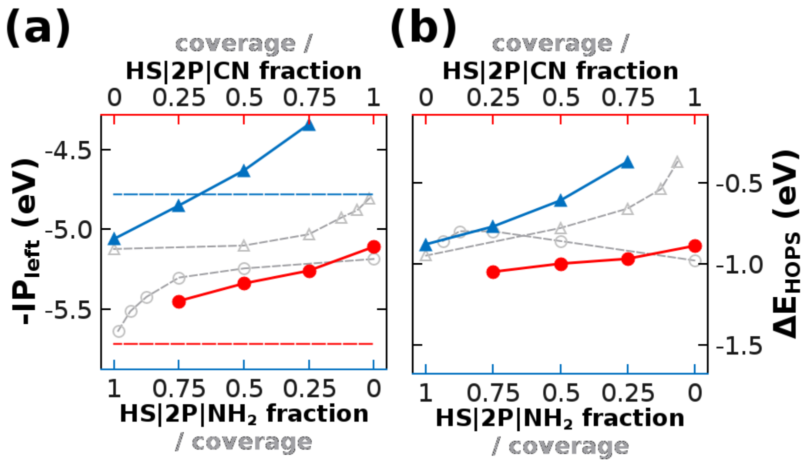

Figure 8.7: *Energies of the HOMO-derived states with respect to the left vacuum energy* E_v^{left} *(a) and the metal Fermi energy (b) in the free-standing (a) and adsorbed (b) mixed monolayers, respectively. Blue triangles (red circles) show data for the amino- (cyano-)substituted component. Open gray triangles and circles depict the same quantities as a function of the packing density (rather than fraction), reproduced from ref. 28. The dash-dotted horizontal blue (red) line in panel a shows the HOMO energy for the isolated amino- (cyano-)substituted biphenylthiol molecule (taken from Fig. 3 in ref. 28). The widths of the energy windows in panels a and b are the same.*

molecular (and dipole moment) orientation are to be expected. Naturally, the two data sets should coincide at –CN fractions of 0 and 1. The reason for the minor deviations we find in Fig. 8.7 between our new data (colored) and the data taken from ref. 28 (gray) is that we have used a more sophisticated geometry-optimization scheme here (details in the Methods section); this, however, has no impact on the following discussion. Furthermore, the ionization potentials of the isolated molecules (also taken from ref. 28) are indicated by horizontal dash-dotted lines.

Fig. 8.7a shows that, for the mixed monolayer, the positions of the HOPS peaks associated with the two subsystems depend approximately linearly on the mixing ratio. The slope for the –NH$_2$ related HOPS peak is higher. Hence, both the absolute positions of the levels and their splitting depend on the mixing ratio. In other words, reading the plot from left to right corresponds to increasing the fraction of –CN substituted molecules mixed into the –NH$_2$ substituted SAM, which causes a pronounced upward shift of the HOPS of the latter. Mixing amino-terminated molecules into the –CN substituted SAM (*i.e.*, reading the plot from right to left) has the opposite effect on its HOPS levels, but with smaller magnitude than for the -NH$_2$ substituted molecules. This can be rationalized by the smaller change in the electrostatic energy landscape induced by the –NH$_2$ substituted SAM in the region of the –CN substituted molecules (*cf.* Fig. 8.5). Note that (de)polarization effects are negligible only at a 1:1 mixing ratio, while for the 1:3 and 3:1 cases one has to expect a situation intermediate between 1:1 mixing and homogeneous films.

For the HOPS energies at submonolayer coverage (light gray symbols), qualitatively different evolutions are observed. This is not surprising as depolarization-related shifts have greater influence in those systems (*cf.* also the Polarization and depolarization subsection). For the limit of zero coverage, $\mathrm{IP}^{\mathrm{left}}$ converges toward the IP of the isolated molecule (horizontal dash-dotted lines), as they form the "natural" limit in homogeneous SAMs.[28] Interestingly, this does not apply to the position of the HOPS of the minority component in mixed SAMs upon approaching the homogeneous film limit (*cf.*, filled red and blue symbols). This is because these molecules are embedded into a polar medium (*i.e.*, a close-packed SAM) rather than in vacuum.

As deduced already from a comparison of Figs. 8.3 and 8.4, the metal mitigates the above-described effects to a certain extent. Fig. 8.7b shows the energetic offset ΔE_{HOPS} between the metal Fermi level and the highest occupied π-states after adsorption. Light gray data points for reduced coverages are again reproduced from ref. 28. While for the coverage-dependent calculations on homogeneous SAMs there are significant differences between the trends depicted in Fig. 8.7a and Fig. 8.7b, for the mixed monolayers only the magnitude of the splitting changes and the slope of the evolution of ΔE_{HOPS} with the mixing ratio is smaller than that of $\mathrm{IP}^{\mathrm{left}}$ for both SAM components. For homogeneous SAMs, the substantial changes in the evolutions induced by the bonding to the metal can be unambiguously associated with a depolarization of the bonding-induced charge transfer at the metal/thiolate bond, that is, a reduced bond dipole at higher coverages.[28] In contrast, such effects do not occur in the mixed monolayers as changing the mixing ratio has no impact on the density of the thiolate groups on the surface. Moreover, it has been shown that in densely packed SAMs tail-group substitution hardly affects the bonding-induced charge rearrangements at the gold/molecule interface.[61] As a consequence, the bond dipole, which, besides $\mathrm{IP}^{\mathrm{left}}$, is the main quantity determining ΔE_{HOPS},[70] hardly changes with the mixing ratio.

8.2.5 SAM-induced work-function changes in mixed monolayers

Understanding the bond dipole in mixed monolayers is an important prerequisite for analyzing the second key electronic parameter of SAMs on metal surfaces, namely the SAM-induced work-function modification, $\Delta\Phi$. The latter can be conveniently understood as the sum of the vacuum-level shift between the "left" and "right" sides of the free-standing monolayer (*cf.* Fig. 8.2c) denoted as ΔE_{vac} and a second step in the electrostatic potential energy due to the bond dipole, ΔE_{BD}.[61,69] The DFT-calculated ΔE_{vac} and $\Delta\Phi$ are shown as black, solid squares and black, open diamonds in Fig. 8.8. With respect to ΔE_{vac}, $\Delta\Phi$ is more or less rigidly shifted to more negative energies by $\Delta E_{\mathrm{BD}} = -1.17 \pm 0.03$ eV. On the one hand, this confirms that the bond dipole is independent of the SAM composition. On the other hand, it underlines that the key to understanding the evolution of $\Delta\Phi$ with the SAM mixing ratio is understanding the

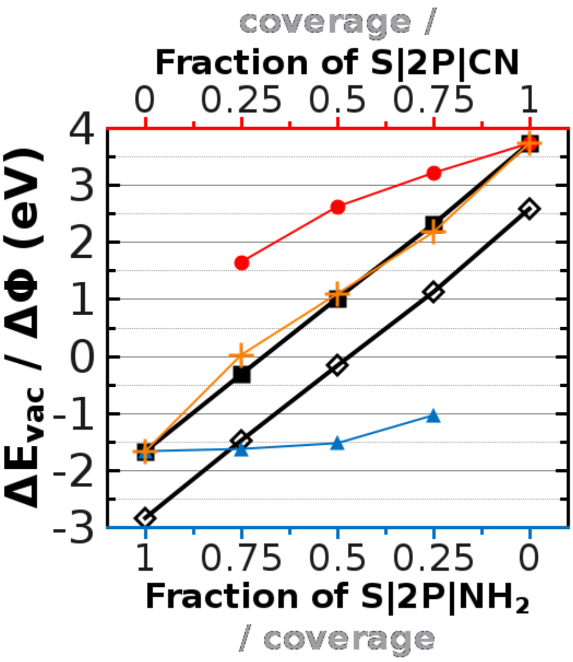

Figure 8.8: *Change of the electron electrostatic energy, ΔE_{vac}, across the free-standing mixed SAM as a function of the mixing ratio (black squares), ΔE_{vac} across the mixed components in absence of the respective other fragment (blue triangles, –NH_2; red circles, –CN substituted component), their sum (orange crosses), and the SAM-induced work-function modification, $\Delta\Phi$, (open black diamonds). Note that per definition the impact of the bond-dipole, ΔE_{BD}, is given by $\Delta E_{BD} = \Delta\Phi - \Delta E_{vac}$.*

evolution of ΔE_{vac}, that is, the property of the free-standing monolayer.

Both ΔE_{vac} and $\Delta\Phi$ display a close to linear evolution with the –NH_2 to –CN ratio. For the related system of alkanethiols mixed with fluorinated alkanethiols on a silver surface this linear dependence was also experimentally observed for $\Delta\Phi$.[210] At a first glance, this might appear somewhat surprising, considering that $\Delta\Phi$ and ΔE_{vac} have been shown to increase in a strongly sublinear fashion with coverage in homogeneous SAMs due to depolarization effects.[28,235] Such a behavior is observed also here, when calculating only the homogeneous subsystems corresponding to 25%, 50%, 75%, and 100% coverage shown as red circles and blue triangles in Fig. 8.8. The sublinearity in the coverage is particularly pronounced for the –NH_2 substituted SAM, where ΔE_{vac} increases only from -1.04 to -1.67 eV between 25% and full coverage.

Nevertheless, the trend for the mixed system should then, to a first approximation, be recovered by a simple addition of the contributions of the individual subsystems, as ΔE_{vac} is essentially an “electrostatic” quantity. The results of such an addition are shown as orange crosses in Fig. 8.8. Especially at half coverage, this procedure yields a value virtually identical to the fully self-consistently calculated one (black squares). This is not unexpected, considering the only very weak polarization effects resulting in an almost vanishing $\Delta E_{\mathrm{mixed}}$ when combining the two half-coverage systems to a 1:1 mixed monolayer (see discussion of Fig. 8.6). For the 3:1 and 1:3 mixing ratios the self-consistent values are slightly shifted in the direction of the minority component, indicating that the latter is impacted by polarization effects to a somewhat larger extent.

From a practical point of view, the main conclusion that can be drawn from Fig. 8.8 is that, if one is able to fabricate a molecular-level mixed SAM, this opens up a way for tuning substrate work-functions over a much wider range than would be possible by changing the coverage using only a single component, where one is limited by depolarization effects. Finally, the linearity of all important SAM properties with the mixing ratio (*cf.*, Fig. 8.7 and Fig. 8.8) significantly facilitates the prediction of the interfacial properties.

8.3 Conclusions

We investigated molecular-level mixed SAMs of donor- and acceptor-substituted biphenylthiolates on the Au(111) surface by means of slab-type DFT calculations. We find a splitting of the electronic states associated with the SAM components in contrast to the respective pristine layers, where the end-group substitution has no impact on the alignment of the highest occupied π-state relative to the metal Fermi level. This shows that the electronic structure of molecularly mixed SAMs differs significantly from the mere superposition of its components. The differences can be rationalized by the electrostatic interaction between the sublattices of the mixed-SAM components. Polarization and depolarization effects are shown to play virtually no role for the level alignment in a mixed SAM at 1:1 mixing ratio. We furthermore show that the mixing-ratio dependences of the quantities of interest for applications, namely band alignment and work-function modification, show qualitatively entirely different evolutions than they do as a function of coverage in homogeneous SAMs. In particular, the strongly sublinear dependence on the coverage due to pronounced depolarization is absent in mixed SAMs. This results in an almost perfectly linear relationship between the work-function change as well as the level alignment and the mixing ratio in heterogeneous SAMs.

8.4 Methods

The density-functional theory calculations were performed using the VASP code.[80] Valence electrons were described by a plane-wave basis set (kinetic energy cutoff of approximately 20 Ry) and valence-core electron interactions by the projector augmented-wave (PAW) method.[81,120] $5 \times 8 \times 1$ and $4 \times 8 \times 1$ Monkhorst-Pack[82] k-point grids were chosen for the 1:0, 1:1, 0:1, and for the 3:1 and 1:3 mixing ratios, respectively. A Methfessel-Paxton occupation scheme with a broadening of 0.2 eV was used. Geometry optimizations were performed using nonredundant internal coordinates based on the DIIS (direct inversion in the iterative subspace) method as implemented in the GADGET tool.[121] This approach is clearly superior to optimization in Cartesian coordinates for systems like those studied here. Ionic relaxations were stopped as soon as every force component fell below 0.01 eV/Å. For electronic relaxations, two separate convergence criteria were applied: a total energy change $\Delta E < 1 \cdot 10^{-4}$ eV and a step in the electrostatic energy (which is proportional to the dipole moment per area) of 0.01 eV. The metal was modeled by five layers of Au(111) atoms and the resulting unit cell was periodically repeated in all three directions. To exclude spurious interactions between subsequent slabs, a vacuum gap of > 20 Åwas introduced in the z-direction together with a dipole layer within that vacuum gap to compensate for the asymmetry of the slab. During geometry relaxations, the coordinates of the lower three gold layers were fixed (representing the bulk), while the upper two layers (representing the surface) were free to move. Mixing ratios of 3:1 and 1:3 were realized by doubling the length of the shorter lattice vector pointing along the x-axis, thus obtaining surface unit cells comprising four molecules (the respective surface unit cells are included in the Supporting Information[i]). Finer steps would require prohibitively large unit cells; already for a ratio of 1:3 (3:1), unit cells comprising 4 molecules and 60 gold atoms are needed. After setting the mixing ratio, the ionic positions were reoptimized. The free-standing SAMs were investigated in the geometry obtained by relaxation in the adsorbed state and the thiolates were saturated by hydrogen atoms. When summing up the charge densities of two subsystems to obtain the input density for a non-selfconsistent (nscf) calculation, the PAW occupancies were left unchanged at their values in the subsystems. We note that, strictly speaking, the nscf-DOS cannot be interpreted as the DOS in absence of polarization since, precisely because of the lack of self-consistency, the corresponding orbital energies are not eigenvalues of the Kohn-Sham Hamiltonian of the system. Rather, the applied procedure should be seen as a method of estimating the importance of (de)polarization on the energy levels. Projected densities of states were calculated using the projection scheme implemented in the VASP code for the PAW method, which is an approximation as an unambiguous partitioning is impossible. A consequence of this scheme is that, usually, the sum of the projections onto all sub-systems does not completely recover the full density of states (*cf.* Fig. 8.4). Nevertheless, the qualitative picture is well preserved. Further details regarding the applied computational methodology and the used parameters are given in ref. 62. Representations of the systems and the potential energy landscapes were generated using XCrysDen.[84]

Acknowledgment. We thank the ZID of the TU Graz for providing computational resources. Support by the FWF through project P20972-N20 is gratefully acknowledged. We thank Dr. T. Bučko for providing and acquainting us with the GADGET code and Dr. M. Marsman for his kind help concerning the non-selfconsistent calculations.

Appendix 8.A

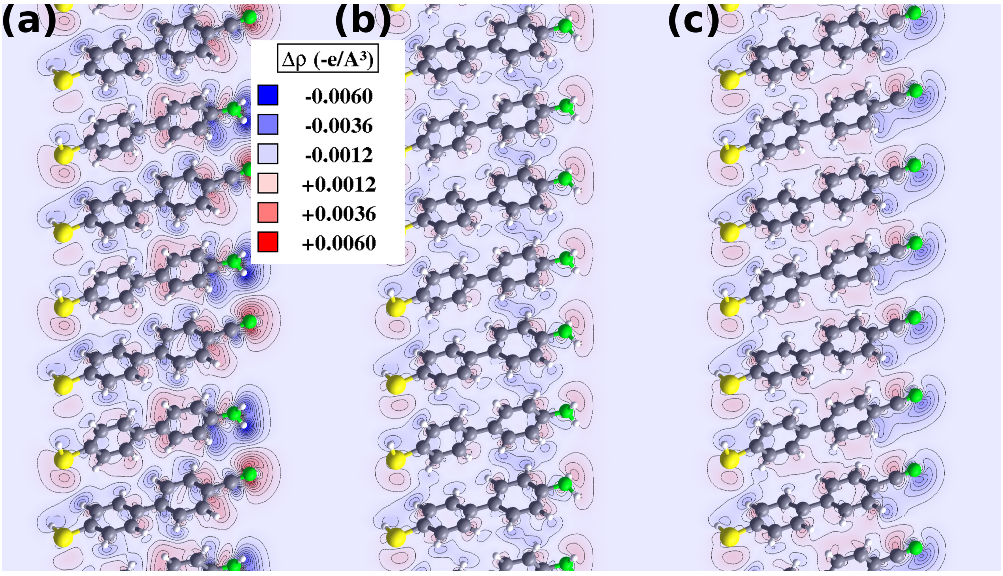

Figure 8.9: *(De)polarization charge rearrangements corresponding to the modifications of the electrostatic energy depicted in Fig. 8.6a. (a) depicts the mixed case, (b) the amino- and (c) the cyano-substituted case. They are averaged over the x-axis of the unit cell and share the scale depicted as inset. Isolines are drawn every 0.0005 e/A*^{3}.

Chapter 9

Collectively induced Quantum-Confined Stark Effect in monolayers of molecules consisting of polar repeating units (ref. 159)

Having discussed laterally alternating dipoles, another approach of field engineering is to consecutively align dipoles along the backbone of each SAM-forming molecule. This is done by chosing a repeat unit with a permanent electric dipole moment. As a result, the electric field penetrates the layer and severely modifies the electronic properties compared to gas phase.

This work was published[159] (see Fig. 9.1). The only noteworthy difference between this chapter and the original publication is that Section 9.2.2 here con-

JACS JOURNAL OF THE AMERICAN CHEMICAL SOCIETY

ARTICLE

pubs.acs.org/JACS

Collectively Induced Quantum-Confined Stark Effect in Monolayers of Molecules Consisting of Polar Repeating Units

Ferdinand Rissner,[†,‖] David A. Egger,[†,‖] Amir Natan,[‡,¶] Thomas Körzdörfer,[§] Stephan Kümmel,[§]
Leeor Kronik,[‡] and Egbert Zojer[*,†]

[†]Institute of Solid State Physics, Graz University of Technology, 8010 Graz, Austria
[‡]Department of Materials and Interfaces, Weizmann Institute of Science, 76100 Rehovoth, Israel
[§]Theoretical Physics IV, University of Bayreuth, 95440 Bayreuth, Germany

Figure 9.1: *Header of the article ref. 159 showing its title and all contributing authors. This chapter is essentially identical to the article and part of the Supporting Information.*[i]

tains a part of what became the Supporting Information of the original article.[i]

Author contributions. Collectivity is not only the topic of the article,[159] also the work has been done "collectively": many authors contributed and two of them did so equally (David Egger and I). I have done most of the calculations, an extensive literature search, did the analysis and have written the initial drafts of the manuscript. The project can be viewed as continuation of David's master thesis[236] and he has been involved in the "pyrimidines"-project from the very beginning. He has further managed to overcome several problems with our cluster and succeeded in finishing the excessively demanding HSE-calculations of the full metal/SAM systems. His main contributions, however, were of conceptual nature when we have spent dozens of hours discussing the studied systems. He has further made essential contributions in improving the readability of the manuscript, together with my supervisor Egbert Zojer. Egbert also came up with the idea of analyzing these systems in analogy to the QCSE (quantum-confined Stark Effect) in the first place, and he has done several test calculations on the polarizability, dipole moment and gap (shown in the Supporting Information of the original article) while I was in Beijing.

An important part of the work was the evaluation of the used methodology. This was done following the strategy presented in ref. 42. We started this part of the project during my stay at Leeor Kronik's group at the Weizmann Institute of Science in Rehovoth, Israel, where Leeor and Amir Natan have introduced me to the topic of self-interaction and exact exchange, and to the Parsec code co-developed in the group. Amir and I were then, however, not able to reproduce the calculations in ref. 42, which is why Thomas Körzdörfer and Stephan Kümmel - two of the authors of that work - assisted us. Thomas has further done the self-interaction correction calculations and has patiently explained to me the details of the SIE in refs. 42 & 43.

Abstract. The electronic structure of terpyrimidinethiols is investigated by means of density-functional theory calculations for isolated molecules and monolayers. In the transition from molecule to self-assembled monolayer (SAM), we observe that the band gap is substantially reduced, frontier states increasingly localize on opposite sides of the SAM, and this polarization in several instances is in the direction opposite to the polarization of the overall charge density. This behavior can be analyzed by analogy to inorganic semiconductor quantum-wells, which, as the SAMs studied here, can be regarded as semiperiodic systems. There, similar observations are made under the influence of a, typically external, electric field and are known as the quantum-confined Stark effect. Without any external perturbation, in oligopyrimidine SAMs one encounters an energy gradient that is generated by the dipole moments of the

---

[i] Reproduced with permission from Journal of the American Chemical Society. Copyright 2011 American Chemical Society. It is modified so that it includes also part of the Supporting Information (in Section 9.2.2). The original version is available online at `http://dx.doi.org/10.1021/ja203579c`.

pyrimidine repeat units. It is particularly strong, reaching values of about 1.6 eV/nm, which corresponds to a substantial electric field of 1.6×10^7 V/cm. Close-lying σ- and π-states turn out to be a particular complication for a reliable description of the present systems, as their order is influenced not only by the docking groups and bonding to the metal, but also by the chosen computational approach. In the latter context we demonstrate that deliberately picking a hybrid functional allows avoiding pitfalls due to the infamous self-interaction error. Our results show that when aiming to build a monolayer with a specific electronic structure one can not only resort to the traditional technique of modifying the molecular structure of the constituents, but also try to exploit collective electronic effects.

9.1 Introduction

Self-assembled monolayers (SAMs) of organic molecules on noble metals have raised enormous interest over the past decades[1,2,164,182–184] and have become important for a number of applications.[56,185–187] SAMs, and even individual molecules, are subject to research also as the active elements in molecular electronic devices.[7,21,102,150,186,189–196,237,238] There, especially, the alignment of the states in the SAM relative to the metal Fermi-level as well the degree of "delocalization" of the transport channels between the electrodes are of uttermost importance.[59,60,105,188,239]

When functional molecules are assembled into SAMs as the active region of electronic devices, control of the electronic structure can be achieved by tuning the properties of the isolated molecule via targeted chemical substitution. Relating molecular and SAM properties, is, however, far from trivial, and the peculiarities of SAM electrostatics have been pointed out repeatedly.[27,31,61,63,164,199,202,240–245] They are essentially related to the fact that well-ordered SAMs of polar molecules correspond to quasi-infinite dipolar layers splitting space into two regions with different vacuum energies with the magnitude of this difference depending on the molecular dipole moments.[31] The latter can be modified by attaching polar donor or acceptor substituents (so-called tail groups) to otherwise apolar molecules, which in the individual molecules significantly modifies the positions of the eigenstates such as the highest occupied molecular orbital (HOMO) relative to the common vacuum level. Surprisingly, however, the level alignment between the SAM states and the Fermi-level of the substrate is typically tail-group independent.[61,201] This finding has been rationalized by an electrostatic decoupling of the attached polar groups from the molecular backbones in combination with depolarization effects within the SAM, thus underlining the impact of collective interaction of molecules on the properties of monolayers.[30,181]

Another approach to adjust molecular dipole moments is to use polar building blocks such as pyrimidines to form molecular backbones, which then can be bonded to metal surfaces by suitable docking groups, *e.g.*, thiolates.[246] By attaching this docking group to one or the other "end" of the oligopyrimidine molecule, two variants with opposite dipole orientation can be realized (*cf.*, "3N$^{\text{up}}$" and "3N$^{\text{down}}$" in Fig. 9.2a).[246] Monolayers formed from these molecules display a number of intriguing and *a priori* unexpected features, whose discussion and explanation provide interesting new insights into effects that can be exploited to alter the electronic structure of SAMs, especially when they are made of oligomers with polar repeat units. These are briefly outlined in the following:

I. As mentioned above, tail-group substitutions in many cases[61,201] change the molecular eigenenergies but do not impact the level alignment at a metal/organic interface. We find that the exact opposite is true for 3N$^{\text{up}}$ and 3N$^{\text{down}}$ gold/monolayer systems: The frontier molecular orbital energies for 3N$^{\text{up}}$ and 3N$^{\text{down}}$molecules are essentially identical, whereas for 3N$^{\text{up}}$ and 3N$^{\text{down}}$monolayers the alignment of the electronic states with the gold Fermi-level is totally different.[246]

II. External fields have been shown to modify orbital (band) energies, the frontier orbital (band) gap, and the energetic ordering of the electronic states in molecules and monolayers;[169–178] related mechanisms have recently been suggested also for inorganic cluster assemblies.[247] The field distorts and localizes eigenstates,[177,178] and recent studies imply that such processes are relevant also when the field originates from dipoles embedded within the layer,[240,241] resulting in a shift in the optical absorption spectrum.[169,170] Internally generated electric fields can be expected to be at work also in pyrimidine-based SAMs, as every pyrimidine unit carries an electric dipole moment. In contrast to tail-group substituted SAMs, where the resulting potential gradient is confined essentially to the substituent region,[30,61,136] the distributed dipoles in an oligopyromidine SAM give rise to a potential gradient throughout the entire monolayer. The associated effective internal fields are comparably large (in the range of 10^7 V/cm), which makes oligopyrimidines an ideal test-bed for studying their impact on the electronic structure of a SAM. This aspect, to the best of our knowledge, has not yet been studied systematically.

III. Upon increasing the SAM packing density and thereby the electric field, the molecular dipoles depolarize each other. Such (de)polarization effects in SAMs arising from internal[28,136,202] as well as external[136,248,249] electric fields have been the topic of several studies. Here we explain why, in spite of the depolarization of the overall charge density, the collectively generated field polarizes rather than depolarizes the electron densities associated with the frontier orbitals.

In addressing the above aspects, we establish a microscopic understanding of the relevant physicochemical processes in SAMs of molecules consisting of repeated dipolar building blocks. In particular, we describe collective effects that strongly modify SAM properties and, thus, need to be considered in "molecular design" approaches and their optimization. Prior to discussing the electronic structure of the oligopyrimidine layers, it is, however, necessary to provide some details on the chosen model system and also to clarify an important methodological issue that arises from the use of density-functional theory (DFT). The latter is essential, as DFT is the only approach allowing for a realistic, fully quantum-mechanical treatment of two-dimensional periodic arrangements of the size explored here.

9.2 Results and discussion

9.2.1 The system

The focus of the present contribution is on processes within the molecular monolayer. Therefore, as a first step we avoid effects involving the interaction with a metallic substrate by excluding the metal from most of our calculations. This is insofar justified as numerous studies have found that the bonding-induced charge rearrangements are confined to the very vicinity of the docking groups,[70,200] unless so-called Fermi-level pinning occurs.[96] Such charge rearrangements should, thus, have only a minor effect on the field distribution within the SAM, which is crucial for the effects discussed in this paper. Moreover, in densely packed monolayers the collectively induced electric field acting within the monolayer virtually does not extend onto the metal for electrostatic reasons, as its decay length amounts to only roughly one-sixth of the interdipole distance.[30] The docking chemistry and the interaction with the metal, however, directly affect the order of σ- and π-states. This is addressed later in the paper.

In ref. 246, where certain properties of the bonded monolayer are discussed, a herringbone arrangement of the oligopyrimidinethiols in the $(\sqrt{3}\times 3)$ Au(111) surface unit-cell has been assumed. This is a plausible choice, as it has been reported that the related biphenylthiols arrange in this way on Au(111).[68] In fact, oligophenylenes generally tend to crystallize in the herringbone pattern,[234] and this might hold true also for longer oligopyrimidinethiols. At least for monopyrimidinethiols, however, this appears not to be the case: For them, a mixed structure of flat lying and upright standing molecules in larger unit cells has been reported.[250,251] The situation is further complicated by the observation that for substituted monopyrimidinethiols the molecules were found to arrange in parallel rows at an even less dense packing.[252] As we are not aware of a work in which assemblies of unsubstituted oligopyrimidinethiols of the type shown in Fig. 9.2 have been studied, it is a plausible compromise to consider such parallel orientations, but in a denser packing of one molecule per $(\sqrt{3} \times 3)$ cell (shown in Fig. 9.2b). Also from a practical point of view the chosen surface unit-cell is convenient as it allows an easy comparison of the various systems and between the electronic structure of isolated and assembled molecules. For consistency with previous work,[28,246] where each $(\sqrt{3} \times 3)$ cell contained two molecules in $\Theta = 1/2$. Finally, we note that in test calculations on the herringbone-packed SAM at the coverage used in ref. 246 we qualitatively recover the results reported below.

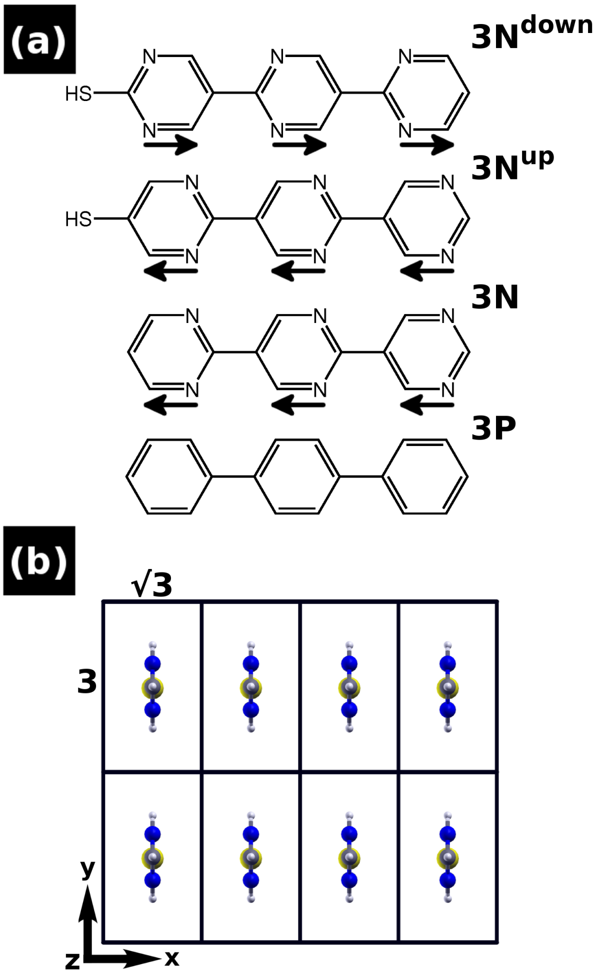

Figure 9.2: *(a) Molecular structures of the terpyrimidinethiols ([2,5′:2′,5″-terpyrimidine]-2″-thiol, $3N^{down}$, and [2,5′:2′,5″-terpyrimidine]-5-thiol, $3N^{up}$), unsubstituted terpyrimidine (3N), and terphenyl (3P). The permanent dipole moments of the pyrimidines are indicated by black arrows (direction defined as pointing from negative to positive charge). (b) Top view of the investigated monolayers in the ($\sqrt{3} \times 3$) surface unit-cell. The Cartesian axes are indicated.*

9.2.2 Determining a suitable computational approach

Several of the occupied low binding-energy orbitals of pyrimidines were shown to display σ-character, which is not very common for conjugated molecules. In fact, it is known from experiments that the HOMO of pyrimidine is of σ-symmetry,[253] and that this can change due to substituents.[254,255] Because the π-orbitals are typically more delocalized, the spatial shape of the low binding-energy states of oligopyrimidines varies considerably. For such a situation, drastic failures of a (semi-)local DFT-based description have been reported.[42,129,256] The reason for this is the infamous self-interaction error (SIE) of common density functionals, *i.e.*, the unphysical interaction of each orbital with itself.[38,45] Intuitively, the SIE is related to the localization of an orbital as one might expect that a strongly localized orbital is subject to more spurious self-repulsion than a more delocalized one.[45] This trend has indeed been observed,[42] although the complete picture obtained from a detailed analysis of the various contributions to the error is more subtle (see ref. 43 and our discussion below). When energetically neighboring orbitals carry markedly different amounts of self-interaction energy, this can severely distort the electronic structure, *i.e.*, change the ordering of these states. Typical routes to correct for self-interaction are to perform self-interaction correction (SIC)[38,42,46,256] or GW calculations.[129,132,257,258] Often, also hybrid functionals give satisfactory results,[38,129–133,259,260] although this is not purely due to self-interaction correction.[46] A further complication in the present study is that a method of sufficient accuracy is needed which is readily applicable to both molecules and periodic systems at reasonable computational cost.

Because we are not aware of any experimental data for thiolated oligopyrimidines to compare our calculations with, it is indispensable to carefully evaluate the theoretical modeling methods. To this end, we follow the strategy presented in ref. 42 (& 256), where a simple-to-evaluate predictor for the presence of a strongly orbital-dependent SIE has been proposed. To date, it is applicable only to finite systems. To evaluate the importance of self-interaction in the present systems, we performed this test for the $3\mathrm{N}^{\mathrm{up}}$ molecule. The predictor calculates the SIE for each Kohn-Sham orbital, *i.e.*, the amount of Coulomb self-repulsion that is not cancelled by exchange-correlation (xc) self-attraction. It is, per definition, given by:

$$e_i = \left\langle \varphi_i \left| v_{\mathrm{H}}[|\varphi_i|^2] \right| \varphi_i \right\rangle + \left\langle \varphi_i \left| v_{xc}[|\varphi_i|^2, 0] \right| \varphi_i \right\rangle \tag{9.1}$$

where $v_{\mathrm{H}}[|\varphi_i|^2]$ and $v_{xc}[|\varphi_i|^2, 0]$ denote the Hartree and the used exchange-correlation potential for each orbital charge density $|\varphi_i|^2$; as in ref. 42 (& 256), we use the spin-polarized LDA (local density approximation) for v_{xc}. Here, we will focus on the HOMO-10 to HOMO, which in our case are the molecular valence orbitals number 36 to 46. The differences in the orbital SIE, e_i, relative to the value calculated for the HOMO level, $\Delta e_i := (e_i - e_{46})$, are shown in orange color in Fig. 9.3a.[ii]

[ii] When comparing gas-phase calculations with experimental spectra a constant, orbital-

Indeed, strongly varying values are found for the high-lying orbitals, which are most important for applications. This indicates that the SIE is an issue in computationally describing oligopyrimidinethiols. Real-space representations of the orbital charge densities $|\varphi_i|^2$ for the HOMO-10 to HOMO ($i = 36...46$) are shown in panel b of Fig. 9.3. From visual inspection, one can distinguish between orbitals mainly localized on one of the pyrimidine rings (no. 46, 45, 43, 42, 39, 36) and orbitals more delocalized over the molecular backbone (44, 41, 40, 38, 37), where both groups contain σ- and π-states. The e_i essentially quantify this visual impression of localization: the largest Δe_i are found for orbitals 39 and 36; orbitals 46, 43 and 42 have a very similar Δe_i and decreasing values of Δe_i are found for the other orbitals with increasing delocalization. This is independent of the character of the orbitals (*i.e.*, σ or π). We note that calculating e_i using the GGA (general gradient approximation) functional PBE instead of LDA did not give a different picture (not shown). This is in accordance with the general observation that the GGA, although often quantitatively superior to LDA, does not succeed in correcting for qualitative failures of the local density approximation.[38]

Clearly, these results emphasize the importance of using a description that is free from spurious self-interaction. To achieve this goal, we employ the generalized optimized effective potential (GOEP) method introduced in ref. 41. In contrast to traditional SIC methods, the GOEP methodology allows us to completely correct for the one-electron self-interaction errors in (semi)local density functionals without leaving the comforting mathematical framework of Kohn-Sham theory. In the present manuscript, we further make use of the Krieger-Li-Iafrate approximation (GKLI), which has been shown to accurately reproduce the results of numerically far more demanding full GOEP calculations.[41] As expected from the evaluation of eqn. (9.1), the correction of self-interaction using the GKLI methodology provides for major changes in the occupied eigenvalue spectrum of the $3\mathrm{N}^{\mathrm{up}}$ molecule.

The relative orbital energy shifts $\Delta\epsilon_i^{\mathrm{GKLI}} := (\epsilon_i^{\mathrm{GKLI}} - \epsilon_i^{\mathrm{LDA}}) - (\epsilon_{\mathrm{HOMO}}^{\mathrm{GKLI}} - \epsilon_{\mathrm{HOMO}}^{\mathrm{LDA}})$ obtained from a GKLI calculation are depicted in Fig. 9.3a in green color. Besides the sign, we find systematic differences between Δe_i and $\Delta\epsilon_i^{\mathrm{GKLI}}$. This is insofar expected, as there is only an approximate correlation between the SIE and its correction.[43] Different to Δe_i, the values $\Delta\epsilon_i^{\mathrm{GKLI}}$ are primarily sensitive to the character of an orbital, *i.e.*, there is a common correction for all σ- (no. 46, 45, 43, 42, 40, 37) and all π-states (no. 44, 41, 39, 38, 36), respectively, irrespective of the intuitive impression of localization, quantified nicely by Δe_i. Most importantly, the SIC shifts the HOMO-2 up in energy by 0.59 eV to above the LDA-HOMO, demonstrating that the SIE severely distorts the electronic structure of terpyrimidinethiols.

---

independent SIE is only of minor importance as it can be accounted for by a rigid shift of the spectrum. For the alignment of the electronic states in a SAM with the metallic Fermi level of the substrate this is not sufficient, as will be discussed below.

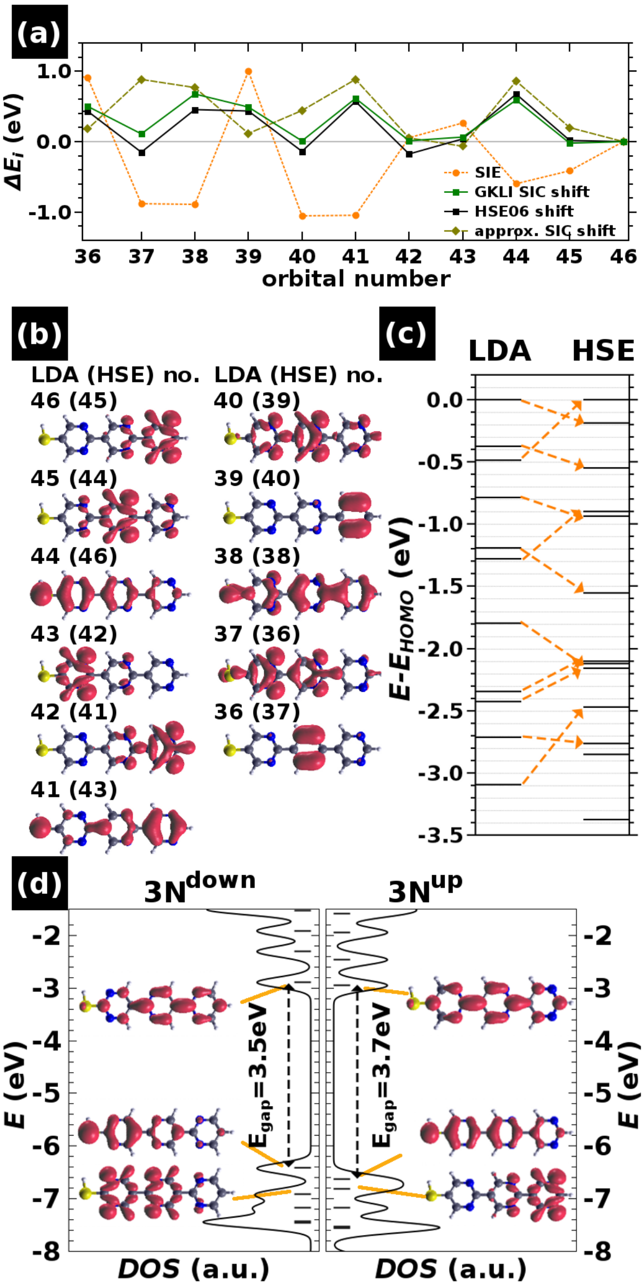

Figure 9.3: *Self-interaction error and electronic structure of the isolated $3N^{up}$ molecule. In (a), the self-interaction error of the LDA orbital energies according to eqn. (9.1) is shown (orange) together with the GKLI SIC (green), the HSE corrections (black) and the approximate SIC (eqn. (9.2), olive). All quantities are given relative to the value for the HOMO (orbital 46). (b) Orbital charge densities $|\varphi_i|^2$ for the 11 highest occupied LDA orbitals; HSE orbital indices are given in parenthesis. (c) LDA (left) and HSE (right) orbital energies, aligned to the respective HOMO energy. The arrows link the LDA and HSE orbital energies. (d) Absolute HSE-computed eigenenergies of $3N^{down}$ (left panel) and $3N^{up}$ molecule (right panel), broadened by a Gaussian with $\sigma = 0.1$ eV. The insets show orbital charge densities of the frontier states; the HOMO-LUMO gap is indicated.*

Perdew and Zunger[45] have proposed a simple-to-evaluate scheme for approximate SIC which proved surprisingly successful for organic semiconductor molecules in an adapted form.[42,43,256] At this point, it is interesting to evaluate the accuracy of this scheme for the present systems. Without actually going through the demanding procedure of self-consistent self-interaction correction, it can be evaluated solely on the basis of LDA quantities:

$$\epsilon_i^{\text{corr}} = -0.94 \int (|\varphi_i|^2)^{4/3} \mathrm{d}^3 r - \left\langle \varphi_i \left| v_c^{\text{LDA}}[|\varphi_i|^2, 0] \right| \varphi_i \right\rangle \qquad , \tag{9.2}$$

where the estimated SIC-corrected eigenvalues are given as $\epsilon_i^{\text{LDA}} + \epsilon_i^{\text{corr}}$ in Rydberg units.[256] The values $\Delta\epsilon_i^{\text{corr}} := (\epsilon_i^{\text{corr}} - \epsilon_{46}^{\text{corr}})$ are shown in Fig. 9.3a in brown color. It can be seen that the most important feature of the SIC, namely the shift of the HOMO-2 to above the LDA-HOMO, is reproduced in this approximation. This good agreement is, however, lost at higher binding energies.

An alternative approach to obtain improved orbital energies is the use of hybrid functionals. Hybrid functionals including only a fraction of exact exchange, however, only partially correct self-interaction. The reason for the often found good comparability with experiment and SIC or GW calculations for the low binding energy states is rather involved: In addition to the partial correction of self-interaction, the non-local potential operator part of hybrid functionals also partially circumvents another well-known deficiency of semi-local density functionals, namely the lack of derivative discontinuities in the exchange-correlation potential.[46] Moreover, it also partly mimics the non-local character of the self-energy operator in GW calculations.[261] The combination of these aspects then often results in the above-mentioned good comparability. A functional which is readily applicable to both molecular and periodic systems is the Heyd-Scuseria-Ernzerhof screened-exchange hybrid functional, HSE06,[262–264] where the long-range part of the Fock exchange is absent by construction. As discussed in ref. 130, the absence of the long-range Fock exchange is not detrimental to the molecular electronic structure, as it hardly influences the highly localized orbitals which exhibit a large SIE. The black data points in Fig. 9.3a depict the correction to the LDA orbital energies as calculated with HSE, again relative to the shift of the LDA-HOMO, $\Delta\epsilon_i^{\text{HSE}} := (\epsilon_i^{\text{HSE}} - \epsilon_i^{\text{LDA}}) - (\epsilon_{\text{HOMO}}^{\text{HSE}} - \epsilon_{\text{HOMO}}^{\text{LDA}})$.[ii] Clearly, HSE and GKLI corrections compare very well. This way the two approaches mutually support each other and we conclude that HSE is well suited for describing the systems at hand.

Fig. 9.3c compares the orbital energies according to LDA and HSE calculations to provide a different view on the effect of the corrections on the eigenenergies. The respective HOMO energies are set to zero and the orbital shifts are indicated by dashed arrows. The most important effect, the change of symmetry from σ to π of the frontier orbital is nicely visible.

Finally, it should be mentioned that also the hybrid HSE suffers from a few shortcomings related to molecule-molecule and molecule metal interaction:

It does not account for the narrowing of the fundamental gap by dielectric screening in the SAM as this effect requires non-local correlation.[85] In case of molecules adsorbed on a metallic substrate,[85] it also misses the further narrowing of the gap due to polarization of the metal as this will generally require both long-range exchange[265] and long-range correlation[266] neither of which is present with HSE.[168,iii] In the following sections we are, however, concerned with processes that go beyond dielectric band gap narrowing and that happen within the SAM, *i.e.*, processes that can be studied also in absence of the metal substrate. Still they are of collective nature and, therefore, it is an absolute must to treat them by periodic calculations. As a consequence, HSE appears as a viable compromise between feasibility and accuracy of the obtained results. When in Section 9.2.7 the adsorbed layer is discussed, the relevant shortcomings should be kept in mind.

9.2.3 Molecule-to-monolayer transition

With the appropriate tools in hand, we can now turn to first calculating the molecular and then the monolayer properties. Fig. 9.3d shows the density of states (DOS) of $3\mathrm{N}^{\mathrm{up}}$ and $3\mathrm{N}^{\mathrm{down}}$ molecules as calculated with HSE. This plot illustrates that the position of the thiol docking group has only minor impact on the molecular electronic structure. The ordering of the frontier orbitals is the same with all frontier orbitals having π-character (see insets), and also the eigenvalues are comparable; the gap differs by only 0.2 eV.

Assembling the polar molecules into a monolayer creates a two-dimensional array of dipoles, μ, which give rise to a change in the electron electrostatic energy between the docking- and the tail-group sides of the SAM. The net effect is described via the Helmholtz solution to the Poisson equation ($\Delta E_{\mathrm{vac}} = -e\mu/\epsilon_0 A$) and is proportional to the areal dipole density.[69,267] In densely packed SAMs, in which ΔE_{vac} originates from polar tail-group substituents (the commonly studied situation), the corresponding shift in the potential landscape is strongly confined to the region of the tail-group.[61] This can be explained by purely electrostatic arguments, as it can be shown that for a square two-dimensional array of point dipoles the decay-length of the field is equivalent to the interdipole distance divided by 2π.[30] In SAMs consisting of polarizable molecules, this confinement is further enhanced by depolarization effects.[28,63,136,152,181,201–203,235,249]

The situation is markedly different for oligopyrimidines as shown for a $3\mathrm{N}^{\mathrm{up}}$ SAM at the highest investigated packing density, $\Theta = 1/2$, in Fig. 9.4a. As the total molecular dipole originates from each of the dipolar pyrimidine rings, ΔE_{vac} is established across the SAM in a more or less continuous way.[246] Even though the plane-averaged electrostatic energy displayed in Fig. 9.4a oscillates due to the nuclei, one can clearly see that it is superimposed with an approxi-

---

[iii] The situation is complicated by the fact that the actual screening will depend on the distance between the orbital and the metal substrate; *i.e.*, differently localized orbitals can be expected to be differently affected by the screening.

mately linear potential gradient, which is due to the combination of the fields generated by the pyrimidine dipoles. This is best seen when averaged over the length scale of interatomic distances (red curve).[iv],[268] The collectively generated potential-energy gradient exists only within the SAM and can be associated with an effective internal field. The magnitude of that "collectively-induced" field can be estimated to be 1.6 eV/nm from the overall potential energy increase and the thickness of the monolayer. Such simple model considerations have been found to be of great explanatory power in previous studies of inorganic systems,[269–271] and in the following sections we describe how they are applicable also to oligomeric SAMs made of molecules that consist of polar repeat units. In passing, we mention that one should be able to observe this potential gradient, for example, by high-resolution X-ray photoelectron spectroscopy experiments,[272,273] as it results in the core electrons of carbon and nitrogen atoms in the backbone being located at different relative electrostatic energies.

Also in oligopyrimidine SAMs, the overall magnitude of ΔE_{vac} is reduced by the above-mentioned depolarization effects, as can be inferred from its sublinear increase with packing density shown by the green diamonds in Fig. 9.4b. A comparison between the trend for 3N (green diamonds) and $3\mathrm{N}^{\mathrm{up}}$ (black squares) shows that the thiol docking group does not qualitatively influence the overall electrostatic situation. In $3\mathrm{N}^{\mathrm{down}}$, the pyrimidines are oriented differently (see Fig. 9.2a), which reverses the sign of ΔE_{vac}, keeping its magnitude, however, largely unchanged (orange disks; note the reversed scale).

The overall situation of the free-standing SAM in Fig. 9.4a can be viewed in analogy to the well-understood case of an (inorganic) semiconductor quantum-well under the influence of an electric field. In semiconductor quantum-wells the field is typically externally applied, although the role of internal fields is well acknowledged (for instance, see ref. 274). Here we are dealing exclusively with the latter: a packing-density dependent collectively induced field that originates from the distributed molecular dipoles within the system. In both, semiconductor quantum-wells and oligopyrimidine SAMs, one has to deal with infinitely extended periodic systems in the x- and y-direction, while there are a finite number of repeat units in z-direction. As a consequence, the wave functions of the quantum-well retain their Bloch-type character in x- and y-direction (*i.e.*, they can be described as lattice-periodically modulated plane waves), while in z-direction the so-called envelope-function approximation comes into play.[275] There, the plane-wave parts of the Bloch-type states, which require infinite periodicity, are replaced by the eigenfunctions of the quantum-well (reflecting the well properties); the lattice-periodic parts of the wave functions still determine which band the states are associated with. Describing the orbitals of oligomers (like terpyrimidine) in such a quasiband structure picture is a well established concept[276] which is consistent with Hückel theory[139] and has been confirmed experimentally by inelastic electron scattering[277–279] and photoelectron spec-

---

[iv] We average E over the length scale of interatomic distances, $a = 1.5$ Å, using the equation $\hat{E}(z) = \frac{1}{2a}\int_{z-a}^{z+a} E(z')\mathrm{d}z'$ to reduce the oscillations due to the ionic potential wells.

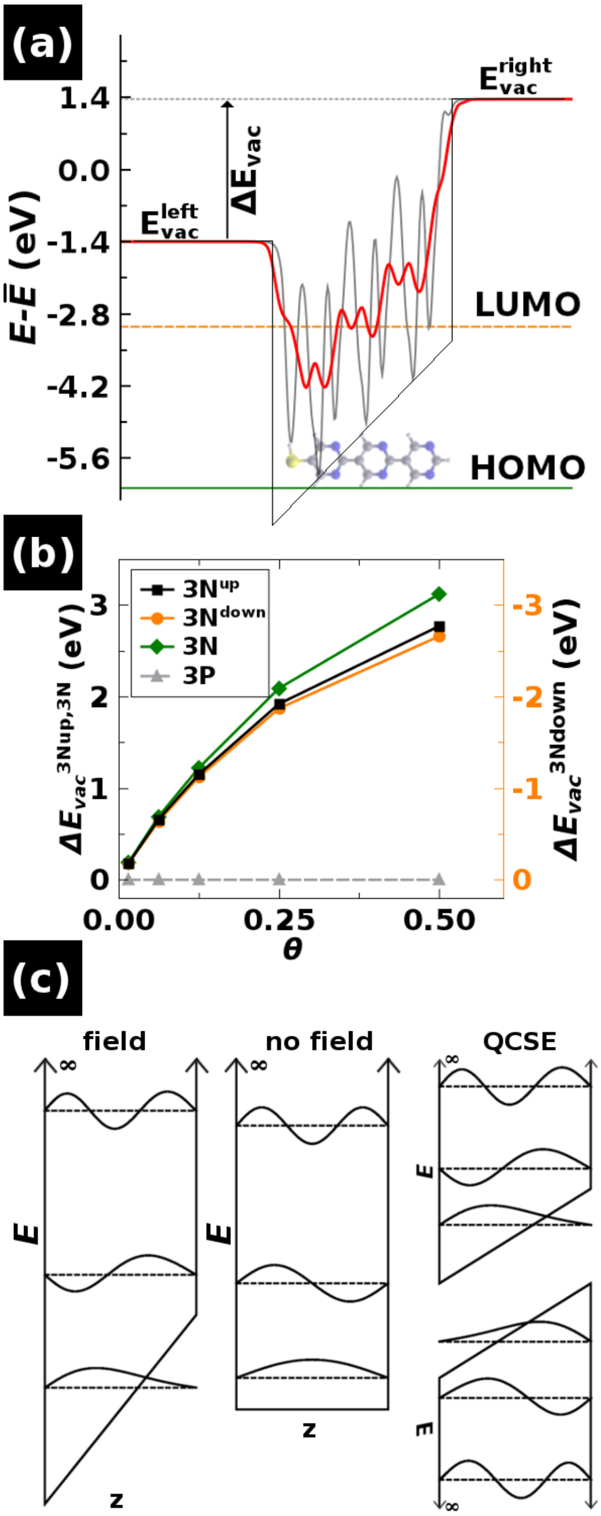

Figure 9.4: *(a)* (x, y)*-averaged electrostatic energy* E *of an electron across a hypothetical free-standing* $3N^{up}$*-SAM at* $\Theta = 1/2$ *(gray curve; for details on the further averaged red curve, see text). The molecule in the background and the "box-potential" serve as guide to the eye. The zero of the energy axis is set to the average of the left and the right vacuum energy,* $\bar{E} = (E_{vac}^{left} + E_{vac}^{right})/2$*. (b) Step in the electrostatic energy across the SAM,* $\Delta E_{vac} = E_{vac}^{right} - E_{vac}^{left}$*, as a function of the SAM packing density* Θ *for* $3N^{up}$ *(black squares),* $3N^{down}$ *(orange disks), 3N (green diamonds). The flat evolution for the apolar 3P SAM (gray triangles) is shown for comparison (see Fig. 9.2b for the molecular structures). Note that the energy scale is reversed for* $3N^{down}$*. (c) Sketches of the potential and the lowest eigenstates of 1D potential wells with infinitely high barriers for a particle in a box exposed to an electric field (left panel) and without electric field (middle panel). The rightmost panel sketches the situation encountered for the envelope functions in the valence and conduction bands that are responsible for the quantum-confined Stark effect (QCSE) in a semiconductor quantum-well structure.*

troscopy.[280–283]

The envelope functions play a defining role for the properties of the orbitals and are key to understanding the electronic structure of the SAMs discussed here. When, for the sake of simplicity, infinitely high barriers are assumed, the well-known eigenfunctions of such a quantum-well in the presence of a constant potential gradient (*i.e.*, a homogeneous electric field) are linear combinations of Airy functions.[284] The few lowest are depicted in the left panel of Fig. 9.4c. In contrast to the field-free situation (middle panel of Fig. 9.4c), they are polarized by the electric field. The lowest state shows pronounced localization on the low-energy (left) side of the well and for moderate fields the probability density for higher states increases in the high-energy (right) side of the potential well.[284–286] This phenomenon of qualitatively different localization for different states has been denoted as anomalous polarization in the literature,[285,286] and is relevant for the discussion below.

For describing both the valence and the conduction band, one has to keep in mind that holes carry a positive charge, which reverses the corresponding potential well leading to the situation depicted in the right panel of Fig. 9.4c. The latter is characteristic of the quantum-confined Stark effect (QCSE). It is exploited, for example, in absorptive modulators, where the confinement imposed by the well-structure is necessary to prevent dissociation of the excitons.[275,287] The simple picture in Fig. 9.4c implies that (i) the gap between the occupied and unoccupied states should decrease upon increasing the field strength (in the oligopyrimidines this means increasing the packing density); (ii) electrons and holes are localized at opposite edges of the quantum structure; (iii) the degree of this localization should increase with the field.

9.2.4 Collectively induced QCSE: Band gap and localization

We start our discussion with terpyrimidine, where no thiol group is attached (3N in Fig. 9.2a). Comparing the DOS of this molecule with that of the corresponding SAM ($\Theta = 1/2$) in the upper panel of Fig. 9.5, it is found that the HOMO-LUMO gap is reduced by no less than 0.8 eV. In contrast, the gap of the nonpolar terphenyl (3P in Fig. 9.2a) remains essentially unchanged upon monolayer formation (Fig. 9.5, lower panel). Consequently, it is the continuous electric field induced within the ensemble of 3N molecules which is responsible for the observed reduction of the band gap in the spirit of the above-described QCSE. This is consistent with the results of others for molecules[169–174,176] and SAMs[169,170,177] in electric fields. It also implies that the calculated gap-reduction is not a consequence of dielectric screening by neighboring molecules, an effect that is not captured by hybrid calculations (*cf.*, Determining a Suitable Computational Approach section).

The real-space representations in Fig. 9.5 can also be associated with the collectively induced QCSE: In the case of terphenyl (lower panel), both HOMO and LUMO are delocalized over the molecule, and this does not change upon

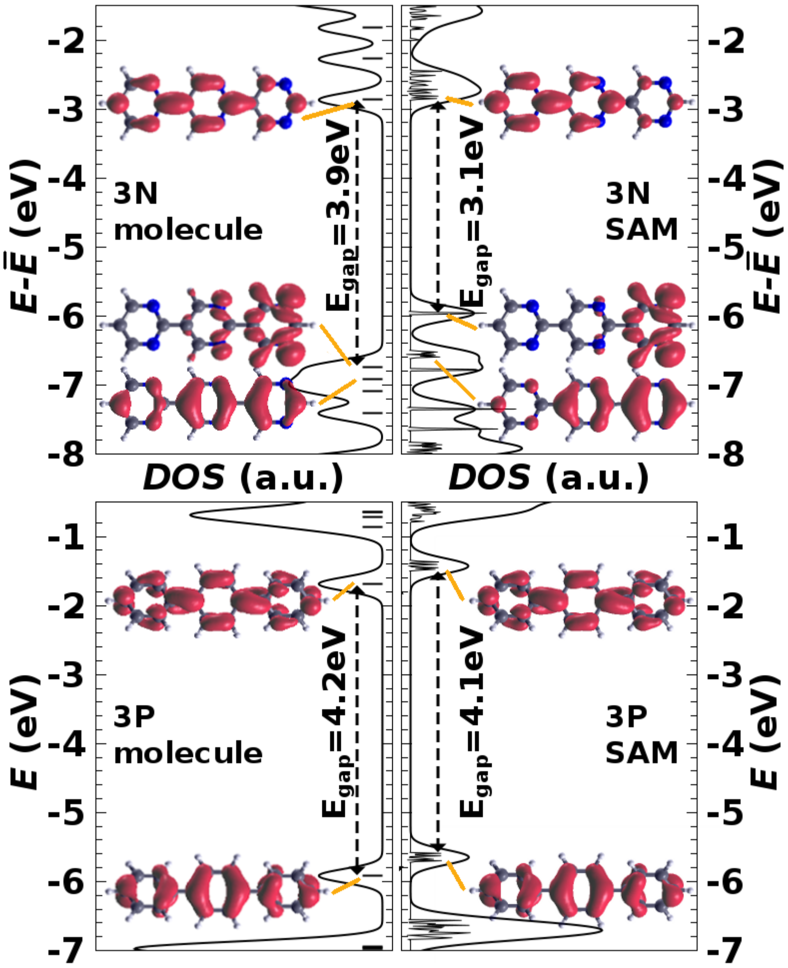

Figure 9.5: *Density of states (DOS) for the 3N (upper panels) and 3P (lower panels) molecules (left panels) and high-coverage SAMs ($\Theta = 1/2$, right panels), aligned at the average electrostatic energy across the SAM, at $\bar{E} = (E_{vac}^{left} + E_{vac}^{right})/2$ (cf. Fig. 9.4a). The thick black curves are Gaussian-broadened ($\sigma = 0.1$ eV) convolutions of the results of the calculation. The insets show orbital/band charge densities of the frontier states, and the band gap is indicated. It is determined from the onsets of the respective nonbroadened DOS peaks.*

monolayer formation. In contrast, for terpyrimidine the HOMO and LUMO are to some degree localized on opposite ends of the molecule already in the isolated system (molecular effect). This localization is further enhanced in the monolayer (collective effect). Because the electrostatic energy increases across the SAM (*cf.*, Fig. 9.4a), this corresponds to a localization of the HOMO level at the high-energy side of the SAM as in the QCSE model in Fig. 9.4c (right panel). In other words, the corresponding electron density is shifted along the electric field. Note that this is counterintuitive from the perspective of depolarization effects (Fig. 9.4a), as the total electron density is (naturally) shifted opposite to the electric field direction as a consequence of the negative charge of electrons.

To better quantify this effect, we calculated orbital charge-densities of the frontier states integrated over the (x, y)-plane using the definition given in the Methods section. They are shown for the isolated 3N molecule as orange areas in the upper panels of Fig. 9.6. The black curves show the corresponding charge densities for the bands derived from these orbitals in the SAM ($\Theta = 1/2$). As inferred already from the contour plots in Fig. 9.5, HOMO contributions on the central ring are shifted to the rightmost pyrimidine and “virtual” charge density corresponding to the molecule’s LUMO accumulates on the leftmost ring at the expense of the rightmost ring. This trend is even more clearly resolved when plotting the respective charge-density differences, $\Delta\rho_i(z) = \rho_i^{\mathrm{SAM}}(z) - \rho_i^{\mathrm{mol}}(z)$, in the central panel of Fig. 9.6, where red (blue) areas show accumulation (depletion) of electron density. In this context it is also useful to plot the cumulative charge rearrangement, $Q_i(z)$, defined as $Q_i(z) = \int_0^z \Delta\rho_i(z')\mathrm{d}z'$ (see bottom panel of Fig. 9.6). $Q_i(z) > 0$ gives the number of electrons that have been transferred from the region right of z to its left. For $Q_i(z) < 0$, the direction of the charge transfer is reversed. The latter quantity shows that the effect of self-localization is sizable: for the HOMO, 0.3 electrons are accumulated on the rightmost ring. The reorganization of the LUMO is of the same magnitude, but opposite in sign.

9.2.5 Collectively induced QCSE: Eigenenergies

The above findings lead to the question of how the collectively induced electric field influences the electronic structure of the SAM beyond orbital localization. The simplified potential wells in Fig. 9.7a sketch the electrostatics across the SAM at low (gray) and high (black) packing density. The orange markings illustrate how the energy is changed differently at different positions in the well. As the orbitals are differently localized along the long molecular axis already in the isolated molecule and even more so in the SAM (*supra)*, it can be expected that their energies are differently affected by increasing the packing density (and, thus, increasing the internal field). To illustrate that such shifts are actually observed, Fig. 9.7b shows the evolution of the HOMO, HOMO-1, and LUMO derived states of 3N as a function of the packing density relative to $\bar{E} = (E_{\mathrm{vac}}^{\mathrm{left}} + E_{\mathrm{vac}}^{\mathrm{right}})/2$ (*cf.*, Fig. 9.4a). The HOMO shifts up by up to 0.9 eV, while the LUMO is destabilized by only 0.1 eV, consistent with the

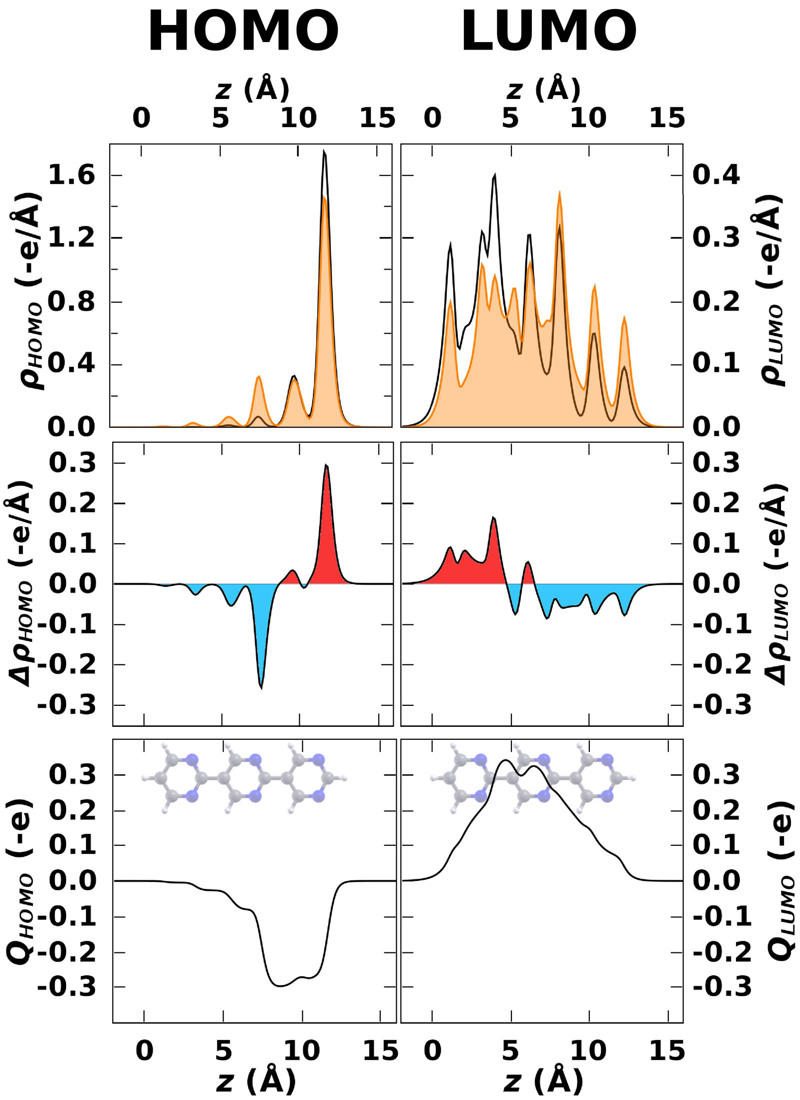

Figure 9.6: *Upper panels: (x, y)-plane-integrated orbital charge-densities for the HOMO and LUMO of 3N, to quantify orbital localization in the direction of the long molecular axis (orange areas). The black curves show the corresponding data for the band derived from those orbitals in the SAM at $\Theta = 1/2$. Middle panels: Charge rearrangements $\Delta\rho_i(z) = \rho_i^{SAM}(z) - \rho_i^{mol}(z)$ for the HOMO (left) and LUMO (right) upon monolayer formation. Red (blue) areas show accumulation (depletion) of electron density. Lowest panels: Cumulative charge rearrangements $Q_i(z)$ for these states upon monolayer formation. The molecules in the background serve as guide to the eye.*

above-discussed gap-reduction by 0.8 eV. The observation that the LUMO is destabilized instead of stabilized (as one might expect from its localization) is most likely due to the somewhat arbitrary choice of the average vacuum level as energy reference, but could also be an indication that, while the model in Fig. 9.7a provides a consistent qualitative picture of the situation, it does not reproduce all quantitative details.

Furthermore, the energetic distance between HOMO and HOMO-1 is increased by nearly 0.4 eV (*cf.*, Fig. 9.5) because of the very different localization of those states. As a consequence, the π-π^* gap (*i.e.*, the gap between the HOMO-1 and the LUMO) is reduced by only 0.4 eV. An interesting observation concerns the significant shifts already at very low packing densities. The energy difference between HOMO and HOMO-1, for example, is increased by 0.2 eV already between $\Theta = 1/64$ (considered as the isolated molecule) and $\Theta = 1/8$, and the gap is reduced even more. This clearly shows that the observed orbital-energy shifts are primarily of electrostatic origin, fully consistent with the occurrence of a collectively induced QCSE.

9.2.6 QCSE and depolarization

Finally, it needs to be understood how the fact that the HOMO is shifted toward the "right" side of the SAM upon increasing the packing density (which corresponds to increasing the molecular dipole) can be reconciled with the generally observed depolarization effects in polar SAMs. That the latter occur also in oligopyrimidine SAMs can be inferred, for example, from the sublinear increase of ΔE_{vac} with coverage in Fig. 9.4b. This can only be explained by the total charge density reacting in a qualitatively different manner to the electric field than the charge density associated with the HOMO-derived band.

To explain that, it is useful to identify "related" molecular orbitals. This can be done by applying the quasiband picture outlined earlier, in which each orbital of an oligomer is interpreted as the product of a quantum-well eigenfunction (the envelope function) and a function derived from an orbital of a single repeat unit (*e.g.*, the HOMO or LUMO of pyrimidine).[139,275–283] The latter then determines which quasiband a given orbital of the oligomer belongs to, with the number of states in a quasiband equaling the number of repeat units. Fig. 9.8a shows the orbitals related in this way to the HOMOs and LUMOs of 3N and 3P. As terphenyl is an apolar molecule, sine functions are suitable envelope functions (*cf.*, middle panel of Fig. 9.4c).[281] In contrast, significant asymmetries are found in the orbitals of terpyrimidine, which is due to the envelope functions in this polar molecule being better described by linear combinations of Airy functions (*cf.*, left panel of Fig. 9.4c). Note that, although this very simple model does not quantitatively reproduce the localization of each orbital, its value is evident as it perfectly reproduces the changes of sign of the wave functions along the backbone.

Bearing in mind that the QCSE "picture" in the rightmost panel of Fig. 9.4c

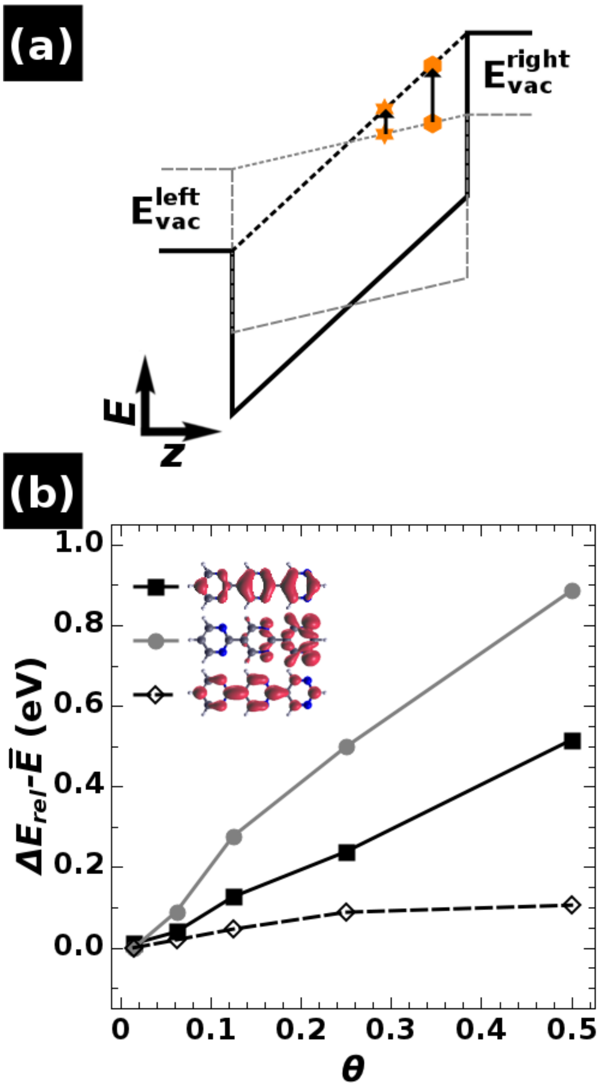

Figure 9.7: *Simplified sketch of the electron electrostatic energy across a SAM of 3N molecules at low (dashed gray) and high (solid black) packing density. The orange symbols illustrate for two positions how the energy is changed differently at different positions in the well upon increasing the SAM packing density. (b) Energetic shifts of the HOMO (black squares), HOMO-1 (gray circles), and LUMO (black diamonds) derived bands in a SAM of 3N molecules upon increasing the SAM packing density Θ, aligned at the average electrostatic energy $\bar{E} = (E_{vac}^{left} + E_{vac}^{right})/2$ (cf. Fig. 9.4a). The energies are determined from the onsets of the respective peaks in the DOS.*

is derived from the envelope-function approximation, it is useful to consider all orbitals belonging to a quasiband "simultaneously". The corresponding $\Delta\rho_i(z)$- and $Q_i(z)$-plots for the HOMO-related states (the HOMO-2 and the HOMO-3) in 3N are, therefore, included in Fig. 9.8b. For the lowest-lying orbital (HOMO-3) the opposite trend than for the HOMO is observed (*cf.*, Fig. 9.6); *i.e.*, electron density is shifted to the left part of the molecule. The HOMO-2, on the other hand, experiences a shift of charge density from the perimeters to the center of the molecule, almost perfectly canceling the combined effect of HOMO and HOMO-3. Indeed, the sum of all three $Q_i(z)$ (Fig. 9.8b, lower right panel, black curve) shows that the net polarization due to the HOMO-related quasiband essentially vanishes. This simultaneous occurrence of polarization and anomalous polarization within a quasiband is fully consistent with previous findings for the eigenfunctions of quantum-wells (*cf.*, Fig. 9.4c).[284–286] Whether a small polarization or depolarization remains within a given quasiband then depends on the details of the involved orbitals. The overall response obtained from summing over all orbitals must, of course, reflect a depolarization (*cf.*, Fig. 9.8b, lower right panel, gray curve). Interestingly, the maximum of this net cumulative transfer amounts to < 0.1 electrons, which is only about 1/4 of what is observed for the HOMO alone.

9.2.7 Bonding the SAM to the metal substrate: Experimentally accessible quantities

Attaching the monolayer to the metal substrate can conceptually be viewed as a two-step process: First a docking group needs to be attached to the terpyrimidine SAM, which then binds the layer to the metal. The attachment of the docking group has two consequences: (i) It determines in which orientation the terpyrimidines are bonded to the metal and whether they induce a work-function decrease (3N$^{\mathrm{down}}$) or a work-function increase (3N$^{\mathrm{up}}$) (*cf.*, ΔE_{vac} in Fig. 9.4b and ref. 246). (ii) Typically, docking group orbitals will hybridize with the states of the terpyrimidines. For thiols, the latter is evident already in Fig. 9.3d, where for the isolated molecules we find the HOMO to display π-character, as the corresponding 3N orbital (the HOMO-1) has been destabilized due to the contribution of the sulfur to the molecular π-system. As a consequence of the orbital localization in terpyrimidine (*cf.*, Fig. 9.5), the effect is more pronounced in 3N$^{\mathrm{down}}$. Consistently, there the degree of localization of the highest occupied π-state is increased by the thiol, whereas it is decreased for 3N$^{\mathrm{up}}$.

In 3N$^{\mathrm{down}}$, when forming a monolayer from the isolated molecules, the collectively induced field is oriented such that it enhances the localization of the HOMO (and HOMO-1) and strongly destabilizes it relative to the average vacuum level. This results in the particularly small band gap of 2.8 eV (see left plot of Fig. 9.9a). In the 3N$^{\mathrm{up}}$ case the highest occupied σ-type orbital experiences a similar shift as in 3N$^{\mathrm{down}}$, while the energetic position of the highest occupied π-state relative to $\bar{E}$ is hardly affected by the collectively induced field. This results in the gap of the 3N$^{\mathrm{up}}$ SAM being of σ-π^* character as in

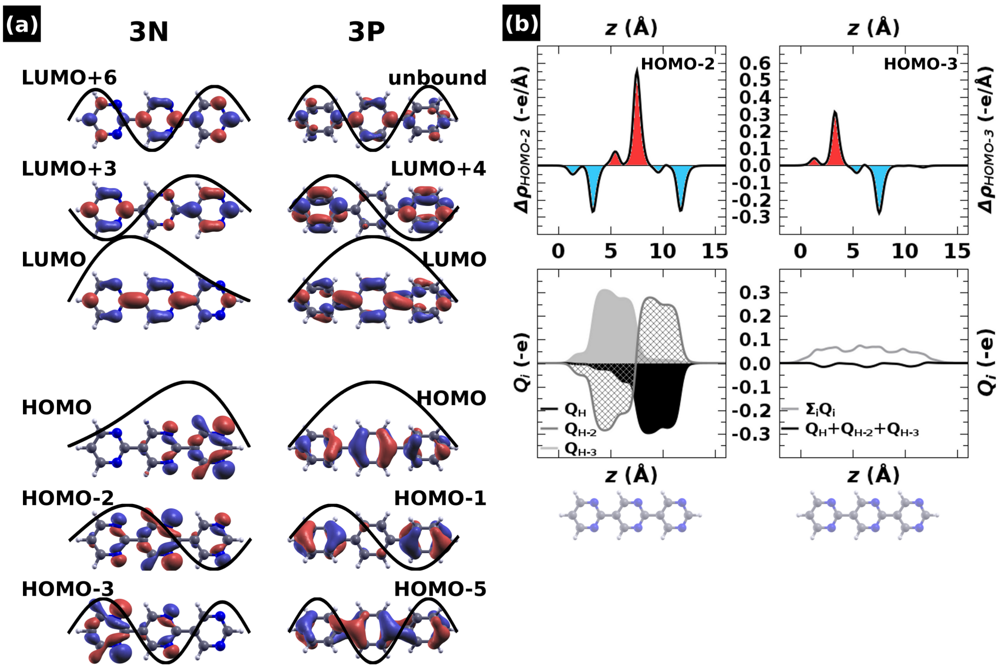

Figure 9.8: *(a) Isodensity plots for related occupied (lower plots) and unoccupied (upper plots) molecular orbitals of 3N (left) and 3P (right).** *Also shown are schematic standing-wave envelope functions. (b) Upper panels: Charge rearrangements* $\Delta\rho_i(z) = \rho_i^{SAM}(z) - \rho_i^{mol}(z)$ *for the HOMO-2 (left) and HOMO-3 (right) upon monolayer formation. Red (blue) areas show accumulation (depletion) of electron density. For the equivalent plot for the HOMO, see Fig. 9.6. Lower panels: Cumulative charge rearrangements upon SAM formation. Left panel:* $Q_i(z)$ *for the three related states HOMO (black), HOMO-2 (crossed gray), and HOMO-3 (light gray) of 3N. Right panel: Sum over the three* Q_i*-curves shown in the left panel (black color) and sum over the* Q_i *of all occupied states (gray color).*

* *Orbital plots (instead of charge density plots) are chosen to illustrate the correspondence between the sign of a wave function and the associated envelope function.*

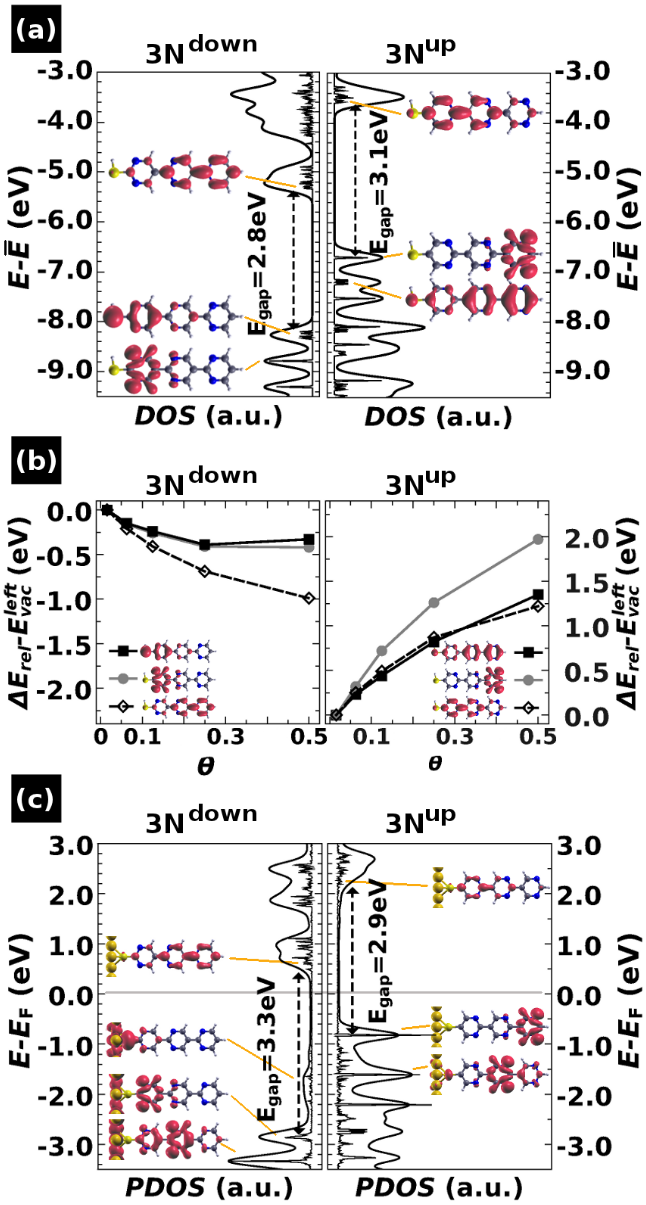

Figure 9.9: *(a) DOS of 3N^{down} and 3N^{up} SAMs at $\Theta = 1/2$, aligned at the average electrostatic energy across the SAM, $\bar{E}$ (see Fig. 9.4a). The thick black curves are Gaussian-convolutions ($\sigma = 0.1$ eV) of the results of the calculation. The insets show band charge-densities of the frontier states, and the band gap is indicated. It is determined from the onsets of the respective nonbroadened DOS peaks. (b) Energetic shifts of the HOMO, HOMO-1, and LUMO derived bands in a SAM of 3N^{down} (left) and 3N^{up} (right) molecules relative to the molecular eigenvalues upon increasing the SAM packing density Θ. The energies are determined from the onsets of the respective peaks in the DOS. They are aligned at the left vacuum energy E_{vac}^{left}; the absolute molecular eigenvalues (approximated by $\Theta = 1/64$) are -6.52 eV (-6.57 eV), -7.02 eV (-6.74 eV), and -3.02 eV (-2.90 eV) for the π-HOMO, σ-HOMO, and LUMO of 3N^{down} (3N^{up}). (c) DOS of the full metal/SAM system projected onto the molecular region (PDOS) for the 3N^{down} and 3N^{up} SAMs, with broadening and insets as in part a. Used energy windows for the LDOS insets: 0.2 eV around the peak maxima for the occupied states, 0.3 eV above the onsets of the lowest unoccupied states, and 0.8 eV for the broad intragap states. Only a small fraction of metal atoms is shown. The Fermi energy is indicated as gray horizontal line.*

the terpyrimidine SAM (*cf.*, Fig. 9.9a). A similar situation is encountered also when considering isocyanide as docking group. Also there the π-electrons of the –NC group hybridize with the π-system of 3N, modifying orbital localization and the packing-density dependent shifts of the eigenenergies. A more detailed discussion is contained in the Supporting Information.[i]

To understand qualitatively how the collectively induced QCSE affects the alignment between the molecular states and the Fermi-level, *i.e.*, addressing question **I** raised in the Introduction, it is useful to analyze the position of the electronic states relative to the vacuum level at the docking-group end of the SAM ($E_{\mathrm{vac}}^{\mathrm{left}}$ in Fig. 9.4a) as detailed in refs. 70, 69 & 31.[v]

The alignment of the states relative to $E_{\mathrm{vac}}^{\mathrm{left}}$ for $3\mathrm{N}^{\mathrm{down}}$ and $3\mathrm{N}^{\mathrm{up}}$ shown in Fig. 9.9b can be understood in a straightforward manner from the schematic sketch in Fig. 9.7a and the localization of the orbitals in the isolated molecules (Fig. 9.3c) and the monolayers (Fig. 9.9a). In $3\mathrm{N}^{\mathrm{down}}$, the potential energy gradient is opposite to that sketched in Fig. 9.7a. This is, compared to $E_{\mathrm{vac}}^{\mathrm{left}}$ all states are shifted down in energy upon increasing the field (*i.e.*, increasing the packing density). The effect is relatively weak for the HOMO and the HOMO-1 as a result of their localization close to the docking-group end of the SAM and amounts to only *ca.* 0.5 eV. For the $3\mathrm{N}^{\mathrm{up}}$ SAM, the energy gradient is opposite to that in $3\mathrm{N}^{\mathrm{down}}$, resulting in an upward shift of all states for increasing coverage. The net shift between the isolated molecule and the $\Theta = 1/2$ SAM amounts to *ca.* 1.3 eV for the (SAM) HOMO-1 and the LUMO and becomes as large as 2.0 eV for the (SAM) HOMO, which is localized on the ring furthest away from the docking group end of the SAM. This already strongly suggests that the level alignment of the $3\mathrm{N}^{\mathrm{up}}$ and $3\mathrm{N}^{\mathrm{down}}$ SAMs bonded to the metal will differ by several electron volts as a result of the collectively induced QCSE. This is a spectacular effect, considering that the molecular ionization potentials of $3\mathrm{N}^{\mathrm{up}}$ and $3\mathrm{N}^{\mathrm{down}}$ are essentially the same.

To obtain a more complete picture, one needs to explicitly consider the bonding to the metal. This is a computationally formidable task when using hybrid functionals. We also note that it is still not fully quantitative (*cf.*, Determining a Suitable Computational Approach section).

Fig. 9.9c shows the density of states projected onto the SAM region (PDOS) and the local density of states plotted for certain energy ranges[vi] for the $3\mathrm{N}^{\mathrm{down}}$ and $3\mathrm{N}^{\mathrm{up}}$ metal-adsorbed SAMs. Also, in the presence of the metal the frontier states are localized on opposite "ends" of the monolayer in the $3\mathrm{N}^{\mathrm{up}}$ and

---

[v] This is useful as it has been shown that this quantity together with the metal work-function and the potential energy shift due to the bonding-induced charge redistributions determines the level-alignment. The bonding-induced energy shift, however, is only weakly affected by the nature of the molecular backbone as long as one does not encounter Fermi-level pinning.

[vi] Used energy windows for the local DOS insets: 0.2 eV around the peak maxima for the occupied states, 0.3 eV above the onsets of the lowest unoccupied states, and 0.8 eV for the broad intragap states.

$3N^{\mathrm{down}}$ SAMs, and indeed a completely different level alignment is found in the two systems. While for $3N^{\mathrm{down}}$ the unoccupied states are closest to the Fermi-level (see Fig. 9.9c), it is the occupied states for $3N^{\mathrm{up}}$.[246,vii] However, the thiolate/Au bond also modifies the SAM electronic structure. First, strongly dispersing metal-induced intragap states appear around 1.7 eV below the Fermi-level (overlapping with sharper peaks for $3N^{\mathrm{up}}$). They are strongly localized on the S atom (see inset for $3N^{\mathrm{down}}$). This changes its hybridization with the π-electrons of the backbone upon adsorption, and the π-states no longer have any weight on the S-atom unlike in the freestanding SAMs shown in Fig. 9.9a. The highest occupied π-states are strongly stabilized and for both SAMs shift down to partly overlap with the next σ-states. This has next to no influence on the band gap of $3N^{\mathrm{up}}$ (see Fig. 9.9c). However, adsorption changes the symmetry of the $3N^{\mathrm{down}}$ HOMO, and the gap is again opened by 0.5 eV. Interestingly, this way a value close to the HSE-computed gas phase gap is reached (although with different character of the HOMO).

Having analyzed the electronic structure of the SAM bonded to the metal substrate one can now wonder how the effects described in the paper would impact experimentally accessible physical observables. Beyond the potential of directly imaging the collectively induced electric field in pyrimidine SAMs by high resolution XPS mentioned earlier, especially the QCSE-induced shifts of the eigenenergies should have drastic effects. The different positions of the molecular states relative to the Fermi-level will strongly impact charge-carrier injection into oligopyrmidine SAMs, for example, in scanning tunneling microscopy and spectroscopy experiments. For a given tunnel bias, it will also result in drastically different tunneling microscopy images. In fact, the results in Fig. 9.9c imply that for imaging $3N^{\mathrm{down}}$ SAMs a negative tip bias inducing the tunneling of electrons might be preferable, while the opposite (*i.e.*, a preferred tunneling of holes) applies to $3N^{\mathrm{up}}$ SAMs. The different level alignment for the two terpyrimidine orientations should also be observable in UV photoelectron spectroscopy and will modify the effective injection barrier when using SAMs to modify the work function of metal electrodes in organic devices. Charge transport through oligopyrimidine layers will be affected also by orbital localization effects, as they tend to deteriorate the transmittance of the transport channels. Moreover, excitation energies in oligopyrimidine layers will be reduced and two-photon photoemission provides a technique to study the relevant excited states.[288] Whether or not certain experimental observations are indeed due to the collectively induced QCSE can then be checked in an (at least conceptually) straightforward manner, as they should all display a distinct dependence on the molecular packing density that might, for example, be varied by forming mixed monolayers with “inert” molecules.

[vii] In the GGA calculations of ref. 246, pinning of the HOMO-derived band at E_{F} was found. These states are shifted to well below E_{F} due to the significantly increased band gap when using HSE.

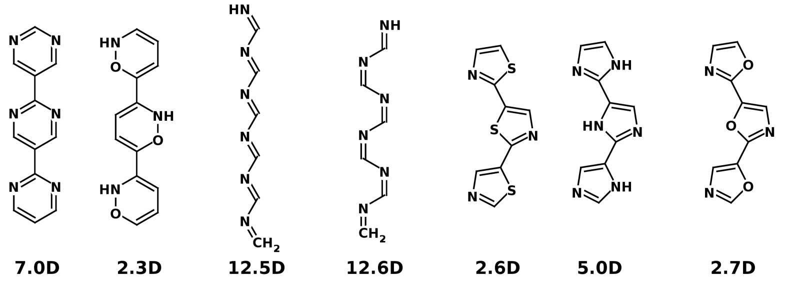

Figure 9.10: *Alternative molecules (names given in the Supporting Information*[i]*) consisting of polar building blocks with equivalent numbers of heteroatoms along the backbone. The HSE06/6-311++G(d,p) calculated total molecular dipole moments are also listed, and terpyrimidine is included for the sake of comparison.*

9.2.8 Relevance of the QCSE beyond oligopyrimidines

As stressed repeatedly, all above effects are essentially caused by the collectively generated electric fields. Therefore, they should by no means be limited to oligopyrimidines, but occur in any SAMs made of molecules with a distributed dipole character, *i.e.*, molecules consisting of a series of polar building blocks. A few examples for alternative (mostly heterocyclic) molecules are shown in Fig. 9.10. A quick theoretical screening shows that most of them have appreciable dipole moments, which for the methineimines is even larger than in the oligopyrimidines; *i.e.*, while the above-described effects are expected to be weaker for the displayed oxazines, thiazoles, imidazoles, and oxazoles, they should be significantly stronger in the methineimines. While the latter have been treated theoretically,[289] their synthesis will pose a considerable challenge.

9.3 Summary and conclusions

In summary, using a carefully selected theoretical approach that accounts for the infamous self-interaction error of density-functional theory, we have shown that the electronic structure of oligopyrimidine SAMs is strongly influenced by the electric field that results from a collective action of the intrinsic molecular dipole moments: Upon gradual transition from the isolated molecule to the densely packed monolayers, we observe (i) an increasing localization (and anomalous polarization) of the molecular orbitals (respectively the real space representations of the associated bands), (ii) a significant decrease of the computed band gap by up to 0.8 eV, and (iii) concomitantly, a strong impact of the collectively induced electric field on the level alignment with the metal Fermi-level. These trends can be rationalized combining the quasiband/envelope-function picture with the Quantum-Confined Stark effect typically observed in semiconductor quantum-wells under the influence of strong external fields. The peculiarity of the present systems is that here the potential energy gradient within the layer is collectively induced by the interacting polar molecular building blocks. For the sake of clarity, these effects are primarily discussed for the hypothetical freestanding monolayers, but essentially prevail also when the SAMs are bonded to a metal substrate.

The above considerations underline that periodically assembled molecules can display properties that hugely differ from those they possess in gas phase. Therefore, when designing molecular building blocks for novel self-assembled materials and hybrid systems, collective effects have to be carefully considered. This is particularly relevant when working with molecules containing polar building blocks, where electrostatic effects can have a huge impact on the electronic properties. Apart from complicating the bottom-up design of new systems, the presented results, however, also provide tools that can be exploited as additional handles for tuning the properties of also more complex systems than the ones discussed here. As a long-term vision, one could imagine exploiting collective electrostatic effects that occur as a result of monolayer formation to shift the electronic levels "by design" in various parts of extended molecules giving molecular electronics a "collectively-controlled" twist.

9.4 Methods

All molecular geometries were obtained by optimizations with the PBE functional using the Gaussian 03[290] package and the aug-cc-pVTZ basis set. Subsequent LDA and GKLI calculations were done with the Parsec real-space code[41,291,292] and norm-conserving pseudopotentials[293] and HSE06 calculations with the Vasp code[80] with a plane-wave basis set (kinetic energy cutoff of approximately 20 Ry) and the projector augmented-wave (PAW) method.[81,120] For LDA and PBE, the comparability of the eigenvalues resulting from the different codes was carefully tested. For details on the GKLI methodology the reader is referred to the original publication.[41]

In the periodic calculations, a Methfessel-Paxton occupation scheme with the temperature set to 100 K (0.00862 eV) was used, and Monkhorst-Pack[82] k-point grids of $8 \times 5 \times 1$, $4 \times 5 \times 1$, $2 \times 5 \times 1$, $2 \times 2 \times 1$ and $1 \times 1 \times 1$ were chosen for the SAM packing densities of 1/2, 1/4, 1/8, 1/16, and 1/64, respectively. The corresponding unit cells were obtained by doubling the short lattice vector (see Fig. 9.2b) once ($\Theta = 1/4$) and twice ($\Theta = 1/8$); $\Theta = 1/16$ was obtained by doubling the shorter lattice vector of the cell at $\Theta = 1/8$, and $\Theta = 1/64$ by again doubling both lattice vectors. The latter was used as approximation for the isolated molecule. Even at such low packing density, ΔE_{vac} does not vanish exactly. We have found values $\Delta E_{\text{vac}} < 0.2$ eV, and account for this in Figs. 9.5, 9.7b, and 9.9b by using the reference energy $\bar{E}$ (and $E_{\text{vac}}^{\text{left}}$ in Fig. 9.9b) also in the case of the isolated molecule. The molecular geometries were not reoptimized in the periodic calculations, and the molecules were oriented parallel to the z-axis of the unit cell (see Fig. 9.2); this procedure facilitates an easy comparison of molecular orbitals and orbital-derived bands. To exclude spurious interaction between subsequent slabs in the z-direction, a vacuum gap of > 20 Åwas introduced together with a dipole layer within the vacuum to compensate for the net dipole moment of the slab.

Orbital charge-densities $\rho_i(z)$ were defined as

$$\rho_i(z) = \int_0^a \int_0^b \sum_{\mathbf{k}} \varphi^*_{i,\mathbf{k}}(x,y,z)\varphi_{i,\mathbf{k}}(x,y,z)\mathrm{d}x\mathrm{d}y \tag{9.3}$$

in units of $-e/\text{Å}$, with a and b being the lattice constants of the surface unit-cell and e the (positive) elementary charge. The sum is taken over all reciprocal-space vectors $\mathbf{k}$ included in the calculation. Note that the unit cell size (*i.e.*, a and b) and the included vectors $\mathbf{k}$ differ for "isolated" and periodic systems as detailed above. $\rho_i(z)$ comprises the charge of a non-spin-polarized band; *i.e.*, the area below a curve amounts to 2 electrons.

Five layers of the nonrelaxed Au(111) surface in the above-used p($\sqrt{3} \times 3$) unit cell were used for the calculations on the full metal/SAM systems. No geometry relaxation of the upright-standing molecules was performed, and the position of the bonded sulfur atom was determined from previous work.[246]

Representations of the systems were generated with XCrysDen.[84] 3D orbital/band charge density plots were generated at the isovalue of 0.02 $-e/\text{Å}^3$. HSE06 calculations for the orbital representations in Fig. 9.8a and dipole moments in Fig. 9.10 were done with Gaussian 09[294] using the 6-311++G(d,p) basis set. An isovalue of 0.04 a.u. was used.

Acknowledgment. The authors thank A.M. Kelterer, O.T. Hofmann, C. Slugovc, Z.Y. Ma, and L.J. Wang for fruitful discussions, and Z.Y. Ma from the Institute of Chemistry of the Chinese Academy of Sciences also for support with the Gaussian HSE06 calculations. We thank the ZID of the TU Graz for providing computational resources. The research was largely funded by the Austrian Science Fund (FWF): P20972-N20. D.A.E. is recipient of a DOC-fellowship of the Austrian Academy of Sciences. T.K. acknowledges financial support by the Alexander-von-Humboldt-Foundation. S.K. acknowledges financial support by GRK 1640 and the German-Israeli-Foundation. L.K. acknowledges financial support by the Israel Science Foundation, the German-Israeli-Foundation, and the Lise Meitner Minerva Center for Computational Chemistry.

Chapter 10

Dimensionality effects in the electronic structure of molecules consisting of polar repeating units

Fig. 9.4 in the previous chapter has shown that the potential energy across a SAM of terpyrimidine(thiol) molecules increases continuously. In other words, each pyrimidine ring contributes to about a third to the total value of ΔE_{vac}.[246] In a discussion with Amir Natan during my visit at the Weizmann Institute, he came up with the idea of further elongating the molecules. According to our understanding of these systems the gap should completely vanish for molecules of sufficient length, and he had actually seen this in calculations on related molecules. When I started the calculations it seemed natural to compare the "long SAM"-limit generated this way to the limit of infinite-length SAMs, *i.e.*, the bulk. Amir suggested comparing the data also to the corresponding series of gas phase molecules - and in addition to that I wanted to know the truly periodic solution of an infinite wire: this way the idea of studying dimensionality effects in such systems was completed.

This chapter is a draft that is supposed to evolve to a proper article eventually. I am thankful for many interesting discussions with Egbert Zojer, Oliver Hofmann and David Egger. I want to acknowledge also Amir's and Leeor Kronik's feedback on the very first report I have written about these calculations. As the following is work in progress, I am solely responsible for its content.

Abstract. Using density-functional theory we studied the electronic properties of oligopyrimidinethiol monolayers as a function of the number of pyrimidine units. The dipole moment increases linearly with increasing length but remains constant above a critical length. At the same time, the band gap decreases linearly until it vanishes at the critical length. This is at seeming variance with the non-linear evolution known for conjugated organic molecules. We explain these findings by collective electrostatics and comparison to gas phase calcula-

tions, where the non-linear decrease of the gap is restored. The gas phase dipole moment, however, increases linearly without limit. In 1D as well as in 2D, the limit of infinite length (periodicity) is discussed and does *not* coincide with the long-molecule limit (including the molecular ends). We further relate our results to the field of (inorganic) polar oxide surfaces, where such phenomena have been observed by others.

10.1 Introduction

It is well established that understanding the properties of self-assembled monolayers (SAMs) crucially depends on understanding the collective effects that occur in such systems (see, for instance, refs. 27 & 31). This is true because of the geometry of the problem. An infinitely extended two-dimensional system can often be modeled properly by 1D electrostatics (whereas in gas phase one can not go below 3D). In other words, the mere presence of neighboring molecules completely modifies the electrostatic situation.[30,31]

A specifically interesting system is oligopyrimidinethiol (Fig. 10.1). It consists of the polar repeating unit pyrimidine, which allows for systematically changing the molecular dipole moment via the number of connected monomers. The thiol group's purpose is to facilitate binding to a metallic substrate. For (substituted) monopyrimidinethiols it has been shown that well-ordered SAMs form on Au(111)[250–252] and attaching more than one pyrimidine is possible as well;[295,296] the latter studies have found rectification (diode) behaviour in related systems experimentally. We have systematically investigated oligopyrimidinethiol molecules and SAMs in the past[159,246] and have shown that the collective effects which emerge in the molecule-to-monolayer transition profoundly impact the SAM electronic structure. Besides pronounced localization effects of the electronic states, the band gap is significantly narrowed as a function of the SAM packing density. These observations can be analyzed in analogy to the quantum-confined Stark effect known from inorganic semiconductor quantum wells, with the electric field across the monolayer being self-induced by the molecular dipoles.[159] We have also shown that the work function of a Au(111) surface changes linearly with the number of pyrimidine units upon adsorption of oligopyrimidinethiol SAMs. This is due to each ring adding an additional constant dipole moment to the molecules embedded in the SAM. A natural limit to this way of work-function modification is given by thermodynamic equilibrium: beyond a certain number of pyrimidine rings, counterdipoles form to guarantee that the metal Fermi energy is always found within the band gap of the SAM.[246]

This dependence of the SAM electronic structure on the length of the molecular backbone is a not yet discussed effect and constitutes the main topic of the present contribution. We will find and explain that the band gap decreases linearly with the number of monomers in the SAM, at least in principle without limit. Surprising by itself, this result also warrants explanation because it is well documented that the length-dependence of the (optical) gap of conjugated

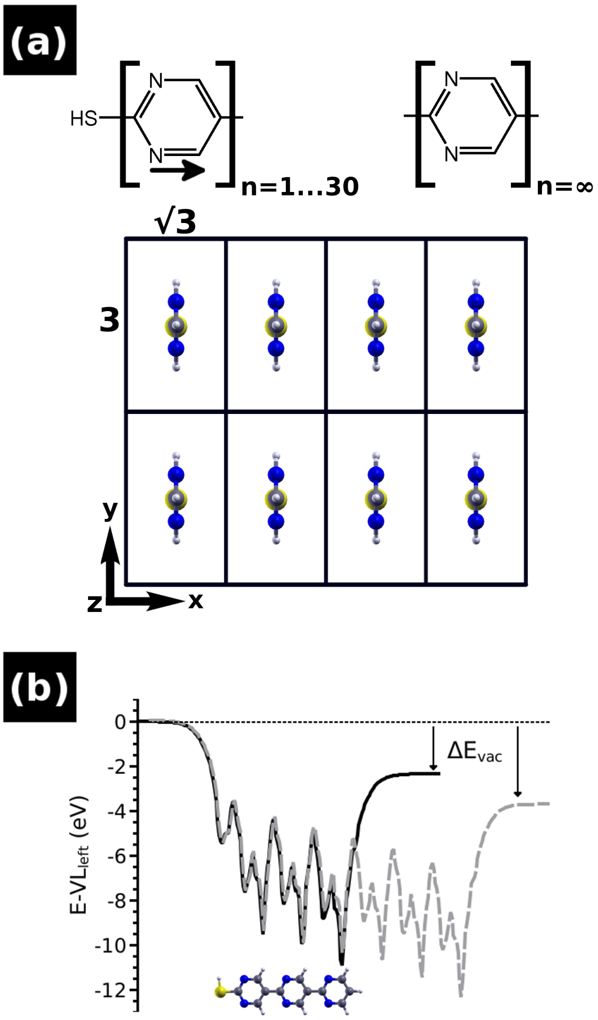

Figure 10.1: *Studied oligopyrimidinethiol molecules. a) Top: Molecules with up to 30 pyrimidines (left plot) and the polymer limit (right plot). The black arrow indicates the electric dipole moment of the monomers. Bottom: upright standing molecules in the two-dimensional unit cell used in the calculations and often found for organic thiols on Au(111) [see ref. 159 for a detailed discussion]. b)* (x, y)*-averaged electrostatic energy of an electron across such monolayers for three (solid black) and six (dashed gray) pyrimidine rings, aligned at the 'left' vacuum energy. The step in energy across the layer,* ΔE_{vac}*, is indicated.*

organic molecules is *not* linear.[297] We thus compare our observations to equivalent calculations on isolated oligopyrimidinethiols and find that the linear gap reduction is present only in the SAM, *i.e.*, it is of collective nature.

10.2 Methods

All used geometries are based on the fully geometry-optimized terpyrimidinethiol (using the PBE functional and the aug-cc-pVTZ basis set in Gaussian 03[290]) by adding additional (or removing) rings. Subsequent 2D-periodic PBE calculations were done with the PARSEC real-space code[33,291,292] and norm-conserving pseudopotentials.[293] The temperature was set to 100 K and an 8×5 Monkhorst-Pack[82] k-point grid was used. The molecules were arranged in parallel in the unit cell shown in Fig. 10.1 (see next section). Tests of the applied methodology were done using Gaussian 03 and are not shown here (applied exchange-correlation functional and polarizability). In the bulk-limit, a unit-cell height of 4.42 Å and a $8 \times 5 \times 20$ Monkhorst-Pack k-point grid was used; 20 k-points were also used in the 1D-periodic calculation (with the same unit-cell height). In periodic calculations, the band gap was determined as the gap between the onsets of the respective peaks in the density of states (DOS). Projected DOS plots were generated using Gaussian convolutions of width 0.05 eV and ionic radii of 1.5 bohr.

10.3 Results and discussion

10.3.1 The system

The chosen unit cell is sketched in Fig. 10.1a and its use has been motivated earlier.[159] Fig. 10.1b illustrates the electrostatic situation in such a monolayer by plotting the (x, y)-plane averaged electrostatic energy of an electron across the SAM (*i.e.*, along the z-direction) for two backbone lengths. In addition to the oscillation of the ionic potential wells, an overall decrease in energy is seen. This potential gradient is due to the embedded (pyrimidine) dipoles and is approximately constant.[246] In other words, a self-induced constant electric field acts on the layer.[159] The net change in electrostatic energy ΔE_{vac} is described via the Helmholtz solution to the Poisson equation[30,31,267] as:

$$\Delta E_{\mathrm{vac}} = \frac{-e\mu_{\perp}}{\epsilon_0 A} \tag{10.1}$$

Here, e is the positive elementary charge, ϵ_0 the vacuum permittivity, A the area per molecule and $\mu_{\perp}$ the dipole moment along the z-direction. For 1 to 30 rings, the net dipole per molecule (orange stars) and the related ΔE_{vac} (black diamonds) are shown in Fig. 10.2a. Both change in a linear fashion up to a critical number of rings.[i] At a length of approx. 9[i] pyrimidines, a sudden

---

[i] As discussed below and in more detail in the Supporting Information (to be written), this

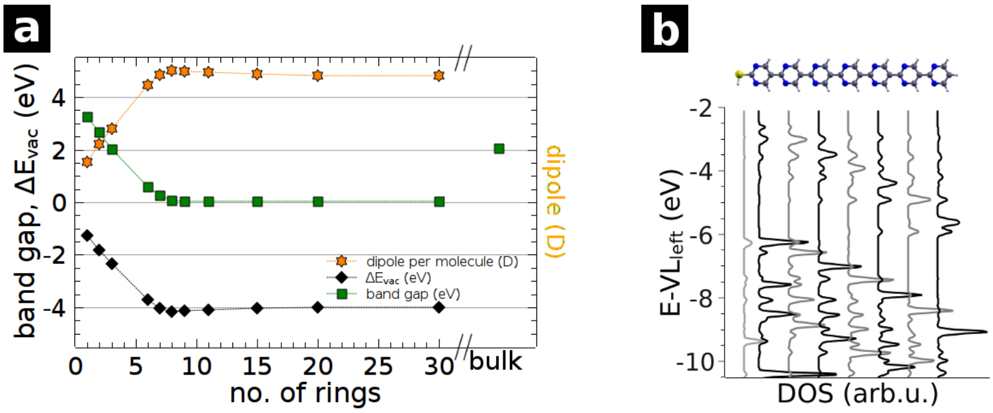

Figure 10.2: *Length-dependent electronic structure of oligopyrimidinethiol SAMs. a) Dipole moment per molecule (orange stars), related step electrostatic energy* ΔE_{vac} *(black diamonds) and band gap (green squares) for all studies backbone lengths. b) Density of states projected onto the thiol group and the individual pyrimidine rings of the monolayer with 7 monomers; the molecule serves as guide to the eye and the left vacuum energy is set to zero.*

kink is found and for longer chains the dipole and ΔE_{vac} remain constant. This observation cannot be understood on its own. It is related to the evolution of the second quantity of interest: the band gap of the monolayer, shown as green squares in Fig. 10.2a. Interestingly enough, it changes linearly as well and this trend stops only when the gap vanishes. Beyond this length - also approx. 9 rings - the gap remains zero and formally this organic semiconductor becomes semi-metallic. This comes as a surprise and asks for clarification. Naturally, the question of the bulk electronic structure of this material arises as it is the limit of the presented data series. It is calculated by removing the thiol and applying periodic boundary conditions also in z-direction (sketched in Fig. 10.1a) and shown as the rightmost data point in the plot. In seeming contradiction with the counterintuitive zero-gap situation for arbitrarily long molecules, the bulk material is, more compatible with intuition, a proper semi-conductor with a GGA-gap of approx. 2.1 eV.

Insight is provided by the density of states projected onto each of the pyrimidine layers separately, shown in panel b. The dipole-induced electric field shifts the local electronic structure at each pyrimidine ring down in energy with respect to its 'left' neighbor. The magnitude of this shift is proportional to the dipole moment per pyrimidine ring in the SAM and as a result, highest occupied and lowest unoccupied bands are localized on opposite 'ends' of the slab.[159] Each ring reduces the band gap by the same amount leading to the linear relationship shown in Fig. 10.2a. Above a critical number of rings (approx. 9 with GGA), this mechanism would shift unoccupied states to below occupied ones, a situation not consistent with thermodynamic equilibrium. In a

---

critical length depends on the details of the chosen methodology. The existence of a critical length, however, does not. The presented result is most likely a lower limit to the actual critical length.

self-consistent electronic structure calculation, this is prevented by charge rearrangements which induce counterdipoles of sufficient magnitude and a zero-gap situation results for every molecular length greater than the critical length. Consequently, the layer is semiconducting everywhere (locally) but the (global) band gap is closed between the opposing surfaces of the slab.

Such a situation is reminiscent of polar (oxide) surfaces.[298,299] There, surfaces with non-zero perpendicular dipole moment are well known and denoted Tasker Type III surfaces.[300] In thermodynamic equilibrium, the macroscopic dipole has to be compensated in one way or another. The possibility of electronic relaxation as found by a self-consistent calculation has been acknowledged in literature.[299] However, more common relaxation mechanisms are atomic rearrangements at the surface or adsorption/desorption processes, which can also compensate for the macroscopic electric field across the material. The presented calculations cannot predict anything but electronic relaxation and it would certainly be interesting to check this by studying the system experimentally. This specific question, however, is not the focus of the present work. Our results clearly show that for short and intermediate length oligopyrimidines the gap can be controlled linearly over a great range. The smaller the gap, the farther valence and conduction band are separated spatially, an effect which will impact electronic excitations. In inorganic systems, polar surfaces have traditionally been studied for semi-infinite crystals. Only relatively recently finite-size effects have been discussed and for thin-enough slabs the absence of electric-field compensation was predicted.[301] Although difficult, layer-by-layer growth of polar surfaces can be realized experimentally[302] and indeed strong indication of surface metallization was found.[303]

Also in the field of organic surface science, related results have been reported.[49] It was shown that, under dark conditions, voltages of up to 28 V are established across thin films of polar molecules,[47,48] which decay upon light illumination.

The seeming contradiction between long-molecule limit of the band gap (0 eV) and the corresponding bulk solution (2.1 eV) can be attributed to surface contributions not present in a bulk calculation. In the 2D-periodic configuration, the calculation gives a constant energy difference ΔE_{vac} for all lengths above the critical number of rings. Consequently, the energy gradient across the slab decreases with increasing backbone length and vanishes in the limit of infinite length. Yet a constant ΔE_{vac} remains between opposing surfaces which closes the (global) band gap. If the surfaces are explicitly excluded from the calculation by applying periodic boundary conditions, ΔE_{vac} is no more defined and the electronic structure in the bulk of the material results (the macroscopically present ΔE_{vac} is excluded). Which approach better describes reality depends on the experimental situation, *i.e.*, the actual number of rings and the active compensation mechanism.[304]

The above described evolution of the band gap is clearly due to collective electrostatic interaction as it is directly related to the evolution of ΔE_{vac}

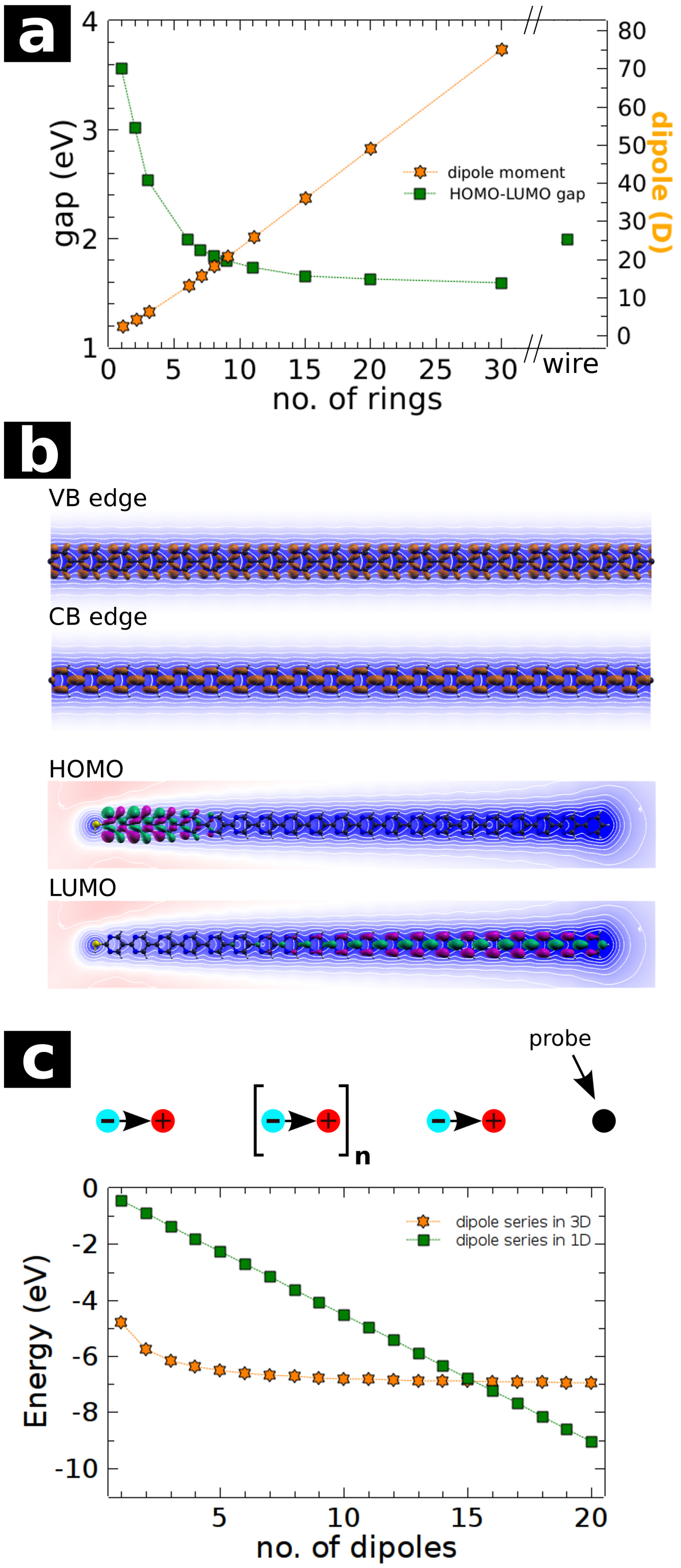

Figure 10.3: *Length-dependent electronic structure of oligopyrimidinethiol molecules. a) Dipole moment (orange stars, right scale) and HOMO-LUMO gap (green squares, left scale) as a function of the backbone length; the wire limit of the (direct) band gap is also shown. b) Real-space representations of the valence and conduction band edges (charge densities, isovalue 0.0001 eÅ^3) and gas phase HOMO-LUMO orbitals (isovalue 0.002 Å^{-6}), above electron potential energy contour plots at approx. 3.6Åbelow the molecular backbone; isolines are drawn every 0.1 eV above (red) and below (blue) the vacuum energy (white). c) model of a chain of dipoles (top panel) and electron energy near its end ('probe') in 3D (orange stars) and 1D electrostatics (green squares) as a function of the chain length. Chosen parameters: dipoles of electron charges and a length of 0.5 Å were used; the distance between equivalent charges is 1.5 Å and the distance between probing electron and rightmost positive elementary charge is 1 Å.*

described by eqn. (10.1). It is fundamentally different from the non-linear evolution of the optical gap of conjugated organic molecules, where a zero-gap situation is not approached for long backbones.[297] Thus it is interesting to calculate the evolution of the gap also for gas phase oligopyrimidinethiol, and the result is shown in Fig. 10.3a (green squares). The non-linearly saturating evolution of the gap is fundamentally different from the gap of the SAM (*cf.* green squares in Fig. 10.2a). No critical backbone length is found and the dipole moment (shown as orange stars) increases linearly without any saturation behavior. The latter is reasonable in the light of the former, as in the SAM the only reason for a limited maximum dipole moment is the very existence of a critical length. The slope, of course, exceeds the one in Fig. 10.2a as there the molecular dipoles are depolarized by the neighboring dipoles, an effect not present in gas phase.

There is also a common feature of the 1D and 2D configurations: also in gas phase, the "long-molecule" limit of gap between highest occupied and lowest unoccupied molecular orbital (HOMO and LUMO) does not coincide with the 1D-periodic polymer limit, and the frontier states are localized on opposite ends of the molecule (shown for 20 rings in Fig. 10.3b). Comparable to the 2D configuration, this is due to the applied periodic boundary condition of a periodic potential. It does not allow for the overall potential energy decrease along the molecule generated by the pyrimidine dipoles, which shifts the molecular HOMO (LUMO) up (down) in energy, *cf.* potential energy contour plots below orbital plots; they become cell-periodic (Γ-)states in the wire limit and the electron density of the corresponding band edges are also shown in Fig. 10.3b.

The magnitude of the HOMO-LUMO gap converges despite the fact that the dipole moment, which controls the gap in the 2D-periodic configuration, does not. This is possible because the electrostatic situation can be approximated by the one-dimensional Poisson equation in the SAM, while its 3D pendant is needed to sketch gas phase electrostatics. In 1D, the Coulomb potential of a charge (*i.e.*, a charged plate) is proportional to the distance r from the plate, and the change in potential energy across a neutral charge density $\rho(z)$ is proportional to its dipole moment (*cf.*, eqn. (10.1)). Consequently, the electrostatic impact of each pyrimidine dipole does not decay even at infinite distance. The simplest possible model to sketch this is shown in the upper panel of Fig. 10.3c, a chain of fixed and non-polarizable alternating charges. The lower panel shows as green squares the evolution of the electron electrostatic energy near a point at the end of the array (indicated by the black dot in the model). In 1D electrostatics, its energy decreases linearly as the number of dipoles to its left is increased (approximating the SAM situation). In 3D electrostatics (isolated molecule), however, the Coulomb potential of each charge decays with $1/r$. Consequently, the electron energy at the molecular ends (where the frontier states are localized) converges to a constant value with increasing chain length (shown as orange stars). This is, the effect of the dipole potential on the molecular ends saturates with increasing length and consequently its influence on the well-known length-dependence of the gap[297] is only minor.

10.4 Summary

We have shown that the polar building blocks of oligopyrimidinethiols render them interesting candidates for SAMs with tunable electronic properties, as their band gap decreases linearly with the molecular length. Even a zero-gap configuration might exist and the discrepancy between long-molecule limit and bulk has been discussed. By comparison to single-molecule data we have shown that the linear change of the band gap is of collective nature, and we have related our results to studies in the field of polar surfaces where similar observations have been made in inorganic systems.

Chapter 11

Summary

Part I has discussed pinning phenomena at metal/organic(/organic) interfaces. Several general conclusions can be drawn from it and several questions arise.

In Chapter 4, pinning of occupied and unoccupied states of an organic material (biphenyl) was studied, where the layer was separated from the metal by a SAM spacer layer which was used to adjust the effective work function of the metal over a huge range. It was found that, although E_{F} is determined only by the metal and although pinning is clearly triggered by the metal, there is no charge transfer from or to the metal. Instead, the allegedly inactive interlayer is polarized, and charge is transferred between the organic layers. This means the interlayer acts as a dielectric which completely screens the potential difference between the pinned materials.

Chemisorbed instead of physisorbed molecules were discussed in Chapter 5, which dealt with molecules bonded directly to the metal (*i.e.*, no spacer layer was present). Pinning at unoccupied states was studied and it was found that also here pinning does not induce charge transfer between the subsystems. Rather, thermodynamic equilibrium is established by a polarization of the SAM, visible best in Fig. 5.6. Interestingly, which parts of the molecules are polarized does depend on the localization of the pinned orbital, and this is shown most lucidly for the amine-headed molecules, where the pinned orbital - at least in the calculations - is located essentially *above* the molecules.

Pinning of the pyridines fixes the unoccupied states near the Fermi energy. Adsorption can also change the SAM electronic structure in a more “radical” way. This was discussed in Chapter 6, where a strategy was presented to generate radicals *via* adsorption. Furthermore, the effect of reduction of the radicals on the electronic structure was shown. In these molecules, occupied as well as unoccupied molecular states are present very close to the metal Fermi energy. This gives rise to several questions that warrant further investigations:

- (Most likely) the discussed effects are actually *not* collective in nature. The radical-formation happens for chemical reasons upon Au–S bond formation, a process in which each molecule is involved individually and irrespective of its surroundings. One can thus speculate that the interfacial electronic properties are very stable with respect to defects, disorder or coverage - criteria absolutely essential for collective effects. So far we have not followed this line of thought.

- It is also not clear whether the small injection barriers are actually related to Fermi level pinning. Leaving the non-spinpolarized picture, there does not seem to be an *a priori* reason for the highest occupied (lowest unoccupied) spin-orbitals to be in resonance with E_{F}. One can easily imagine a situation in which (due to an improved *xc*-functional) the respective states are (de)stabilized and shift farther away from E_{F}. This implies that such systems should be revisited as soon this becomes possible by using suitable functionals.
- Related to this is the interpretation of the spin-dependent results. We found different magnetic moments in the unit cell for each system and it would be interesting to understand which factors control this property. Suitable substituents could be used to (de)stabilize the spinpolarized solution with respect to the nonpolarized one, and one should also consider calculating the spin-dependent current-voltage characteristics of such SAMs when sandwiched between two electrodes.

Different arrangements of dipoles and their effect on the electronic properties of the dipole-carrying molecules were discussed in Part II.

Chapter 8 focused on mixed monolayers and has found that the electronic structure of a mixed layer differs qualitatively from the simple superposition of its components. As pointed out very lucidly by Georg Heimel,[i] mixing can be understood as a partial cancellation of the collective effects that act in each of the individual layers before mixing. This, of course, is itself a collective effect as it relies on the strictly periodic arrangement of the two sub-layers.

Chapters 9 & 10, most generally, dealt with dimensionality effects in molecules composed of repeated dipoles. The addressed oligopyrimidines turned out to be subject to an orbital-dependent self-interaction error, shown by a simple predictor for self-interaction. Using the relatively "cheap" hybrid functional HSE was found to be a sufficient cure for these molecules, as the results compared well with (much more expensive) self-interaction correction. This was shown in Chapter 9, which studied the transition from 0D (single molecule) to 2D (closely packed monolayer) and found a reduction of the band gap and localization of the electronic states. This can be analyzed in analogy to the quantum-confined Stark effect and is triggered by increasing the SAM packing density (0D→2D transition). The effect depends on the strength of the electric field, which again is a function of the inter-dipole distance (the packing density).

---

[i] He did so in his talk at the ESPMI-VI conference in Karlsruhe, Germany in September 2011.

Chapter 10 has discussed the transition from 0D to 1D, this is, the effect of elongating a gas phase molecule that consists of repeated dipoles. The long-molecule limit was compared to the wire limit (1D periodic boundary conditions) and they do not coincide. Furthermore, the transition from 2D to 3D is studied by elongating the very same molecules when arranged in a SAM. The corresponding long-SAM limit was compared to the truly periodic bulk system (3D periodic boundary conditions) and once more they do not coincide. Most importantly, the bulk system is semiconducting, whereas there is no gap in the long-SAM limit. As all this is caused by the internally generated electric fields, these results were rationalized essentially by electrostatic considerations. The relation to phenomena well known in the field of polar (oxide) surfaces was pointed out.

Altogether, this work has pointed out the importance of taking into account collective electrostatic effects when analyzing the electronic properties of thin layers of polar molecules and their interfaces with metallic substrates or organic materials. It was shown that "simply" by arranging dipoles properly, the electronic properties (like band gap and localization of frontier states) of such systems can be tuned. Following this approach, one could study systems where more elaborate dipole distributions are used. For instance, it might be possible to reduce the gap of a SAM of polar repeat units also *locally* (*i.e.*, suppressing the shown localization effects) if, repeatedly, several pyrimidine units pointing one direction were followed by such pointing in the opposite direction. The size of the gap could then be controlled by adjusting the number of aligned monomers.

Appendix A

Comparing two geometry optimization strategies

One of the problems in modeling the systems discussed throughout this work is finding a reasonable geometry (see Methodological prologue). Finding an energy minimum is a difficult task even after having chosen a certain unit cell - which greatly reduces the degrees of freedom of the system already. Obviously, this is so not because of the substrate (being a simple fcc crystal) but because of the molecules with many, often very soft degrees of freedom. This chapter compares (from a large pool of possible choices) two strategies for solving this problem.

The calculations were performed when Tomáš Bučko has provided us with the GADGET code,[121] a tool that allows for using sophisticated geometry optimization strategies. He has greatly helped us not only by explaining all its features patiently, but also by discussing and overcoming several convergence issues. He has further implemented the substrate detection algorithm discussed below and kept us updated with new versions of the code. I have done most of the calculations, with the following exceptions: Anna M. Track has produced the data and plot shown in Sec. A.3.3 and LinJun Wang has provided the converged geometries of systems **2T** and **B*X*** which were used as starting points for the discussed post-optimizations. The chapter, however, was written by me and I am solely responsible for its content.

Results on the low-coverage system (Sec. A.3.1) are in part reproduced from my diploma thesis.[34]

Abstract. The geometry of various metal/SAM systems is optimized using two different optimization schemes: a damped molecular dynamics procedure (dMD) and a strategy based on internal coordinates and direct inversion in the iterative subspace (IC-DIIS). The converged geometries in general depend on the chosen scheme, where the latter relaxes to more reliable results, often of significantly lower energy.

A.1 Introduction

The experimental realization of well-ordered monolayers is a non-trivial task. Various phases may coexist[68] or the layers can be defective.[305] Also in calculations (DFT or molecular dynamics), multiple energetic minima related to different molecular geometries are often found (for example in ref. 306). Even when the layer is well-ordered, its structure influences its functionality quantitatively as well as qualitatively.[28,29] For instance, the work function can be increased at full but decreased at low coverage.[29] Although the important role of geometric aspects is well recognized, usually no emphasis is put on the optimization technique used in the computational investigation of SAMs.

This is the topic of this appendix. A simple damped molecular dynamics (dMD) relaxation in Cartesian coordinates is compared to a more sophisticated strategy based on internal coordinates and direct inversion in the iterative subspace (IC-DIIS). For the geometry optimization of molecular systems, the general superiority of internal coordinates over Cartesians is well known, regarding speed as well as the quality of the results.[307–313] Increased efficiency is reported also for periodic systems,[121] where internal coordinates have not been used that extensively.[121,314–316] Needless to say, also with IC-DIIS there is no guarantee for finding the global minimum.

When relaxing metal/SAM interfaces, an internal-coordinates (IC) based optimizer is useful as it describes the relevant degrees of freedom in the molecular part of the unit cell more directly. These are, for instance, the tilt of the molecules with respect to the surface and the metal/molecule distance (relevant in case of flat-lying molecules). An additional advantage - not discussed here - is that internal coordinates give great freedom in defining constrained degrees of freedom. Amongst others, angles and bond lengths can be fixed (in linear combinations, if needed).

No IC-based optimizer is available with Vasp, the code used here for the DFT calculations. The free external optimizer Gadget[121] is used for this purpose and the results are compared with geometries obtained using a damped molecular dynamics (dMD) strategy and Cartesian coordinates as implemented in Vasp. The latter was traditionally used in our group as it usually converges smoothly also for bad initial guesses. The primary effect of the new optimization strategy is that conformations of moderately or even significantly lower total energy are found in every single case studied; for very shallow potential energy surfaces, where the energy is only insignificantly lower, the final geometry at least depends less on the initial guess. In some cases, the predicted work-function modification, $\Delta\Phi$, is changed notably and in Sec. A.3.3 an example is shown where simulated and experimental STM image compare well with IC-DIIS, but not with dMD. However, convergence is not always obtained easily and some pathological cases were found. To improve the performance in those optimizations, Tomáš has implemented a substrate detection algorithm. It enables separating the molecular from the metallic part when generating internal coordinates, which helps in many cases as shown for two examples in Sec. A.3.4.

A.2 Methodology

General. All calculations are DFT-based slab-type band structure calculations using VASP[80] together with the PW91 exchange-correlation functional. Valence electrons are described by a plane wave basis set (kinetic energy cut-off of approx. 20 Rydberg) and the projector augmented wave (PAW) method[81,120] is used for valence-core electron interactions. A $>$ 20 Å vacuum gap and dipole compensation are employed to separate subsequent slabs, preventing chemical and electrostatic interaction between neighboring surfaces. In low-coverage calculations ($\Theta = 1/8$) on the biphenylthiol SAM, a $(2\sqrt{3} \times 6)$rect cell and a $4 \times 2 \times 1$ Monkhorst-Pack k-point grid[82] are used. For the densely-packed SAMs a $(\sqrt{3} \times 3)$rect surface unit cell[68] and a $8 \times 5 \times 1$ Monkhorst-Pack k-point grid are chosen. Only for the anthraceneselenol system, a $(\sqrt{3} \times 4)$rect surface unit cell is used as obtained experimentally[317] with a $8 \times 4 \times 1$ Monkhorst-Pack k-point grid. The 1^{st} order Methfessel-Paxton[83] occupation scheme with a broadening of 0.2 eV is used in all calculations.

The metal is modeled by five layers of Au(111) atoms. During geometry relaxations, the coordinates of the lower three layers are fixed (representing the bulk) while the upper two layers (representing the surface) are free to move. No molecular constraints are imposed.

The optimizations are stopped as soon as all remaining forces are < 0.01 eV/Å (0.02 eV/Å for $\Theta = 1/8$ and 0.026 eV/Å for the anthraceneselenol system[318,319]). Note that the applied convergence criteria differ slightly between VASP and GADGET. While in VASP the norm of the force vector acting on each nucleus is checked for convergence, GADGET demands convergence of each component of the force vector; this criterion is less strict. For electronic relaxations, two separate convergence criteria are applied: a stable dipole moment (tolerance: $\Delta\mu_z < \pm 0.002$ eÅ ($\Delta\mu_z < \pm 0.008$ eÅ for $\Theta = 1/8$)) over several self consistent cycles, and a total energy $\Delta E < 1.10^{-4}$ eV.

STM images were simulated using the Tersoff-Hamann approach.[320,321] For calculating isosurfaces of constant current, the local density of states (LDOS) was integrated between the Fermi energy of the system and below the first occupied double feature in the molecular density of states.[318,319] To obtain more realistic images and to account for the finite experimental resolution, the calculated LDOS was averaged over 59 points on the model of a spherical tip with a diameter of 2Å.[62] The open source code XCrysDen[84] is used to generate visualizations of the systems. Further details on the methodology are discussed elsewhere.[62]

Optimization Engines. Several geometry optimization schemes are implemented in the VASP code. Traditionally our group used the damped molecular dynamics (dMD) optimization recommended in the VASP manual for bad initial guesses. In dMD, damped equations of motion, $\ddot{\vec{x}} = -2\alpha\vec{F} - \mu\dot{\vec{x}}$, are solved at

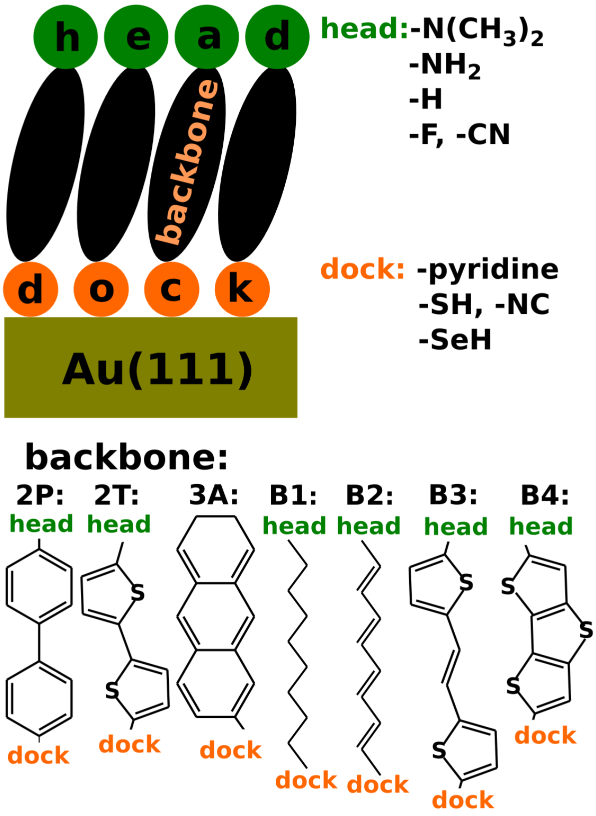

Figure A.1: *Schematic representation of the investigated systems. The various molecular backbones are connected to the metal surface via one of the docking groups; the properties of the SAM can be further modified by head-group substitutions.*

each time step, where the user chooses the constants α and μ.

Also GADGET offers various optimization engines, and the strategy based on internal coordinates and the geometric direct inversion in the iterative subspace method (IC-DIIS) is used here.[121,322,323] In IC-DIIS, the Hesse matrix is inverted on the basis of a harmonic expansion of the total energy in order to extrapolate to an approximately-zero-force configuration. Several previous geometries are taken into account by minimization of an error vector. Since the calculation of the Hessian is computationally expensive, a guess for an initial Hesse matrix is crucial. An update scheme is used to correct the approximate Hessian on the basis of the current forces; throughout this work, Fischer's model Hessian[324] is used together with the BFGS (Broyden-Fletcher-Goldfarb-Shanno) update algorithm.[121]

A.3 Results

In the following, the investigated slabs are denoted by the naming convention metal|dock|backbone|head, where the only metal surface considered is the Au(111) surface. Thiolate (S|), pyridine (Pyr|), isocyanide (CN|) and selenolate (Se|) groups serve as docking groups and various acceptors (fluorine (|F) and cyano (|CN)), donors (amine (|NH_2) and dimethylamine (|$N(CH_3)_2$) and hydrogen (|H) as head groups. As described elsewhere,[70] those groups can be understood as a toolbox for adjusting the level alignment (dock) and the work function (dock and head). Docking and head group are connected by a rod-like (π-conjugated) molecular backbone. **2P** (**2T**) denotes a backbone consisting of 2 phenyl (thiophene) rings, **3A** stands for anthracene and **B1** (**B2**) denotes an alkane (conjugated alkene) chain as backbone. Finally, **B3** and **B4** stand for two additional thiophene-based backbones. Fig. A.1 gives a quick overview over the structure of the systems; their in-depth investigation was part of previous work.[50,70,201,318,319]

A.3.1 Low coverage

Geometry.

It is useful to discuss first a SAM at a coverage low enough to exclude influences of mutual steric hindrance between the molecules. At a coverage of $\Theta = 1/8$ (see Fig. A.2), the molecules have plenty space to relax freely during the optimization and the potential energy surface is extremely shallow with respect to the molecular tilt. The reference SAM S|2P|H is discussed, where electrostatic interaction does not play an important role either because of its small dipole moment. Fig. A.2a depicts the geometry chosen as starting point of the optimizations. It corresponds to almost upright standing molecules. The angle ψ denotes the tilt of the molecular backbone with respect to the surface normal. It is defined as the angle between the z-axis and the vector connecting the lowermost carbon (nitrogen in case of pyridine) and the uppermost carbon atom belonging to the backbone of the SAM molecules. φ stands for the intramolecular inter-ring twist angle.

The converged geometries as found by dMD (red) and IC-DIIS (green) are shown in panel b; the huge difference in the two results is visible immediately. The dMD optimization leaves the molecular geometry essentially unchanged throughout the optimization (see also Tab. A.1). The molecules shift towards the gold surface and the inter-ring twist is enhanced from 7° to 15°. The tilt angle remains the same. In sharp contrast to that, the geometry obtained using IC-DIIS differs significantly from the initial geometry. Tilt and twist of $\psi = 11°$ and $\varphi = 7°$ are changed tremendously to $\psi = 55°$ and $\varphi = 37°$. In terms of the total energy the results are totally equivalent within the precision of the calculations[i] (Tab. A.1). This shows that (i) the potential energy surface with respect to the tilt angle is extremely shallow and that (ii) the IC-DIIS optimizer is much more likely to suggest geometry changes which are big in Cartesian coordinates.

---

[i] The 1st-order Methfessel-Paxton smearing with 0.2 eV broadening leads to an entropy term (inaccuracy) of roughly 0.02 eV in these calculations. One could reduce it by increasing the order or reducing the smearing; neither is done here to stay consistent with the methodology used in the high-coverage calculations.

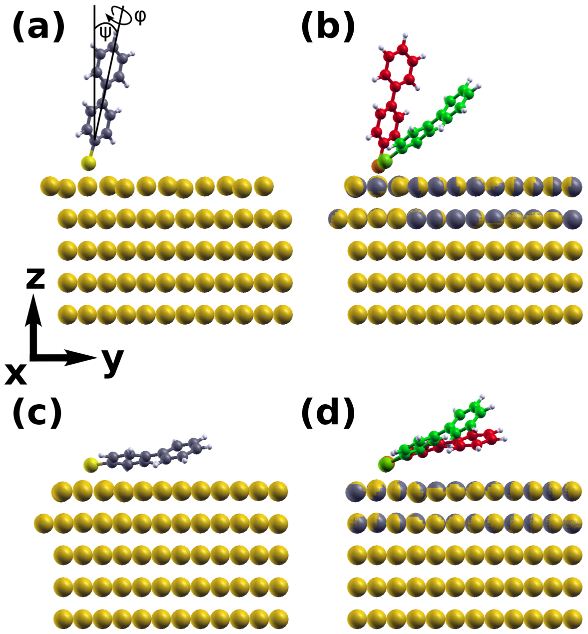

Figure A.2: *Side view of Au|S|2P|H at low coverage ($\Theta = 1/8$) before (a) and after (b) the geometry optimization. Tilt and twist angle ψ and φ are indicated in panel (a). The red and green geometries in panel (b) depict the converged geometry as found by dMD and IC-DIIS, respectively. (c) Initial geometry of Test 2, with the IC-DIIS result depicted in panel (b) tilted by 30° about the x-axis (the used coordinate system is indicated) using the sulfur atom as center of rotation. (d): dMD (red / dark gray) and IC-DIIS result (green) of Test 2. Where gold atoms appear dark gray, the difference between IC-DIIS and dMD positions is big enough to be visible.*

Table A.1: *Comparison of dMD and IC-DIIS results for Au|S|2P|H at low coverage ($\Theta = 1/8$): total energy E per unit cell (containing one molecule) in eV, work-function modification $\Delta\Phi$, backbone tilt angle ψ and inter-ring twist angle φ in °. ‚Test 1' (‚Test 2') denotes an optimization where the initial geometry is obtained by tilting the IC-DIIS result about the x-axis by 15° (30°) towards the surface with the sulfur atom as center of rotation. For the parenthesized dMD tilt angle in Test 2, see text.*

	geometry	E/cell [eV]	$\Delta\Phi$ [eV]	tilt ψ [°]	twist φ [°]
original	initial	–	–	11	7
	dMD	:=0	−0.62	11	15
	IC-DIIS	−0.01	−0.33	55	37
Test 1	initial	+0.17	–	68	37
	dMD	+0.04	−0.31	69	36
	IC-DIIS	−0.00	−0.32	60	38
Test 2	initial	+2.47	–	82	37
	dMD	+0.14	−0.30	73 (87)	23
	IC-DIIS	−0.00	−0.31	64	37

To test the reproducibility of those structures, the dependence of the final geometry on the initial guess is tested. The IC-DIIS result is modified to obtain starting points of two further optimizations, 'Test 1' and 'Test 2'. The molecules are tilted about the x-axis of the cell by additional 15° (Test 1) and 30° (Test 2). The sulfur atom is used as center of rotation and tilt angles of 68° (Test 1) and 82° (Test 2) are obtained this way. Note that the latter conformation (shown in Fig. A.2c) corresponds to practically flat-lying molecules.

dMD did not recover the original geometry in both additional optimizations. For the moderate starting tilt (Test 1, not shown in Fig. A.2) the final total energy is only slightly higher than in the original calculation, despite the large difference in both angles. The unrealistically large initial tilt of $\psi = 82°$, in contrast, leads to a conformation of significantly higher energy (Fig. A.2c). Instead of decreasing the tilt of the molecules to enhance the metal-molecule distance to a reasonable value, dMD introduces a kink between the phenyl rings by only reducing the tilt of the lower ring (to 73°) while that of the upper ring is increased to 87° (red geometry in panel d).[ii]

In the IC-DIIS optimizations, the tilt is changed to 60° and 64° (panel d, green molecule) in the respective tests, both equivalent in energy. It doesn't recover the original geometry exactly, but the respective tilt angles are within approx. 10° (Tab. A.1).

Note that the molecular tilt would probably vary less softly if the calculations properly included van der Waals forces. The intention here was to illustrate that the different optimizers tend to search along different paths in phase space. IC-DIIS varies degrees of freedom easily which, in dMD, correspond to a highly coupled motion of many nuclei (for instance, tilting the molecule). This observation suggests that different geometries might result also in other systems, where closer packing implies significant differences in energy.

It also begs the question what causes the differences. Trying to solve this puzzle, several parameters of the optimization with GADGET have been varied. Specifically,

(i) DIIS has been replaced with the optimization engine RFO,

(ii) Fischer's initial Hessian was replaced with a simple diagonal matrix in internal coordinates,

(iii) Fischer's initial Hessian was replaced with a simple diagonal matrix in Cartesian coordinates.

Furthermore, the original calculation (Fischer's Hessian and DIIS) was repeated using Cartesian coordinates for the optimization steps and Hessian updates, and this was done also for tests (ii) and (iii). It is important to note that internal coordinates are needed also in these tests. They are used for Fischer's Hessian

---

[ii] When the relaxation is continued until the largest gradient is < 0.01 eV/Å, a twist of 32° is found and tilts of 69° and 78° for the two phenyl rings. The total energy then amounts to $E = +0.05$ eV compared to the original dMD result in Tab. A.1

which is intrinsically "internal" and, of course, also for the diagonal matrix in test (ii).

Table A.2: *Results of tests (ii) and (iii), calculated using internal and Cartesian coordinates.*

		Test (ii)	Test (iii)
internal c.	tilt ψ [°]	48	12
	twist φ [°]	37	25
Cartesian c.	tilt ψ [°]	12	19
	twist φ [°]	37	32

Replacing DIIS with RFO does not change much: $\psi = 54°$ and $\varphi = 37°$ are found. More interestingly, replacing internal with Cartesian coordinates (while sticking to DIIS and Fischer's model Hessian) did not change much either: $\psi = 56°$ and $\varphi = 37°$.

The remaining tests are summarized Tab. A.2. The twist angle increases significantly in each test. The tilt angle remains small in all tests except for the combinations IC+(ii). From this one can conclude that - although it is not the only factor - the choice of the initial Hessian is important for the final geometry.

Work-function modification.

The work-function modification $\Delta\Phi$ depends on the dipole density projected onto the direction perpendicular to the surface, μ_z/A (see, for instance, Chapter 5). It is, thus, to a certain extent controlled by the molecular tilt angle. Also the metal-molecule interaction is angle-dependent and this again is reflected in the bond dipole (Chapter 5). Biphenylthiol has a small dipole moment and accordingly the tilt-angle dependence of μ_z is negligible (not shown). This effect will be more important for larger dipole moments (next section). More relevant here is the angle-dependent bond dipole. Fig. A.3 shows the charge rearrangements upon bonding between metal and SAM, $\Delta\rho(z)$, the cumulative charge rearrangements $Q(z)$, and the effect on the potential energy E, leading to the so-called bond-dipole.[iii] For the upright standing conformation, the charge rearrangements reach farther along the z-axis (see $\Delta\rho(z)$, $Q(z)$) compared to the tilted geometry. This increases the bond dipole and as a result, $\Delta\Phi$ differs by 0.29 eV (*cf.* Tab. A.1). In this case this is about 100%.

Note that also the changed inter-ring twist has a certain effect. It changes the conjugation which influences the band gap. For the free-standing, hydrogen-saturated monolayer the gap of 3.11 eV in the dMD result ($\varphi = 15°$) is increased moderately by about 0.2 eV to 3.30 eV using IC-DIIS ($\varphi = 37°$). In the adsorbed monolayer, however, this difference is again reduced to approx. 0.1 eV.

[iii] See Chapter 5 for definitions of and details on these quantities.

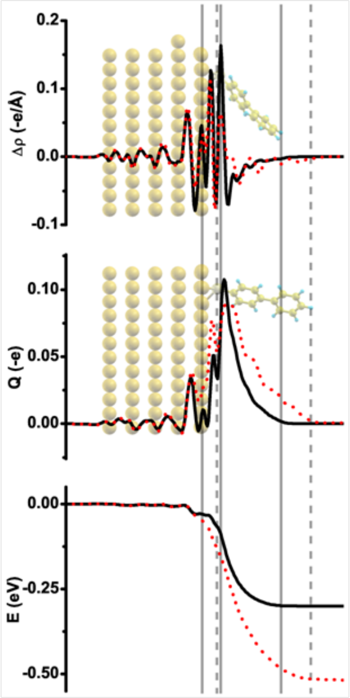

Figure A.3: *Charge rearrangements $\Delta\rho(z)$ upon adsorption of the HS|2P|H SAM at $\Theta = 1/8$, integrated over the plane parallel to the gold surface (top panel); cumulative charge rearrangement $Q(z)$ (middle panel) and their effect on the electron electrostatic energy (bottom panel). Curves corresponding to the IC-DIIS (dMD) geometry are depicted as solid black (dotted red) lines. Vertical lines and pictures in the background serve as guide to the eye.*

A.3.2 High coverage systems

The previous subsection has focused on the influence of the optimizer on the final geometry and work function in a system characterized by an extremely shallow potential landscape with respect to the tilt angle. Accordingly the results are equivalent in energy. The capability of the IC-DIIS to positively abandon the initial geometry was found.

For a series of interfaces, most of them available from previous work, IC-DIIS based optimizations were performed starting from the dMD-converged geometries. The SAMs vary in i) the docking group, ii) the backbone and iii) the terminal group (*cf.* Fig. A.1). Tab. A.3 compares some of the key quantities before and after post-optimization; significant changes are shown in bold ($\Delta E \geq 0.05$ eV/cell, $\Delta\Phi \geq 0.3$ eV and $\Delta\psi \geq 5°$).

In the upper part of the table, biphenyl derivatives with various docking- and head group substituents are listed. For the isocyanide docking group, only minor changes are found. For the sulfur-docked systems, moderate changes of the total energy are found related to tilt angles increased by roughly 5°. The opposite effect is seen for the pyridine-docked SAMs, were (with one exception) the molecules prefer a completely upright-standing configuration. Different to the thiol-docked systems, the energy remains almost the same.

Molecular backbones **B*X*** and **2T** are more accessible to geometric variations at this coverage. For each of those systems the energy is *significantly*[iv]

[iv] Some of the calculations have been presented already in ref. 201, where much smaller

Table A.3: *Comparison of dMD results and IC-DIIS post-optimizations for various systems at full coverage: total energy E per unit cell (containing two molecules) in eV, work-function modification ΔΦ in eV and backbone tilt angle ψ in °. Significant changes are shown in bold ($\Delta E \geq 0.05$ eV/cell, $\Delta\Phi \geq 0.3$ eV and $\Delta\psi \geq 5°$). The dMD variants of the 2P-based systems marked with ** are as used in ref. 50. Data on systems marked with * is reproduced from ref. 201 and for further details on Au|Se|Ant (marked with ***), see ref. 318, 319.*

system	geometry	E/cell [eV]	ΔΦ [eV]	tilt ψ [°]
Au|CN|2P|CN**	dMD	:=0	2.07	13 / 12
	IC-DIIS	−0.016	2.04	13 / 13
Au|CN|2P|F*	dMD	:=0	−0.37	12 / 12
	IC-DIIS	−0.018	−0.37	11 / 11
Au|CN|2P|NH$_2^{**}$	dMD	:=0	−3.23	12 / 12
	IC-DIIS	−0.017	−3.24	10 / 10
Au|CN|2P|H**	dMD	:=0	−2.12	12 / 12
	IC-DIIS	−0.019	−2.14	8 / **7**
Au|S|2P|CN^{*,a}	dMD	:=0	2.57	12 / 13
	IC-DIIS	**−0.088**	2.58	**18 / 20**
Au|S|2P|F**	dMD	:=0	0.23	11 / 12
	IC-DIIS	**−0.076**	0.29	**16 / 18**
Au|S|2P|NH$_2^{*,b}$	dMD	:=0	−2.45	16 / 19
	IC-DIIS	−0.010	−2.48	16 / 18
Au|S|2P|H**	dMD	:=0	−1.54	11 / 11
	IC-DIIS	**−0.069**	−1.43	15 / **17**
Au|Pyr|2P|CN**	dMD	:=0	1.29	11 / 10
	IC-DIIS	−0.010	1.31	9 / 8
Au|Pyr|2P|F	dMD	:=0	−1.33	11 / 10
	IC-DIIS	−0.018	−1.29	**3 / 3**
Au|Pyr|2P|NH$_2^{**}$	dMD	:=0	−3.86	10 / 10
	IC-DIIS	−0.023	−3.83	**1 / 1**
Au|Pyr|2P|H**	dMD	:=0	−3.05	10 / 10
	IC-DIIS	−0.035	−3.03	**0 / 0**
Au|S|B1|NH$_2^{*}$	dMD	:=0	−1.99	3 / 6
	IC-DIIS	**−0.120**	−1.86	**12** / 10
Au|S|B1|CN^{*,a}	dMD	:=0	0.95	6 / 9
	IC-DIIS	**−0.259**	**0.43**	**19 / 20**
Au|S|B2|NH$_2^{*,b}$	dMD	:=0	−3.09	6 / 6
	IC-DIIS	**−0.318**	**−2.68**	**27 / 27**
Au|S|B2|CN^{*,a}	dMD	:=0	2.00	8 / 10
	IC-DIIS	**−0.347**	**1.49**	**26 / 26**
Au|S|2T|NH$_2^{*}$	dMD	:=0	−2.90	4 / 6
	IC-DIIS	**−0.147**	**−2.58**	**17 / 24**
Au|S|2T|CN*	dMD	:=0	2.30	6 / 6
	IC-DIIS	**−0.152**	**1.95**	**18 / 22**
Au|S|B3|NH$_2^{*}$	dMD	:=0	−2.97	6 / 8
	IC-DIIS	**−0.201**	**−2.63**	**25 / 20**
Au|S|B3|CN*	dMD	:=0	2.22	8 / 8
	IC-DIIS	**−0.209**	**1.89**	**20 / 24**
Au|S|B4|NH$_2^{*}$	dMD	:=0	−2.78	12 / 12
	IC-DIIS	**−0.331**	−2.86	**6** / 8
Au|S|B4|CN*	dMD	:=0	2.05	12 / 12
	IC-DIIS	**−0.237**	**2.42**	**3** / 9
Au|Se|3A***	dMD	:=0	−1.46	6 / 2
	IC-DIIS	**−0.212**	−1.37	**19 / 10**

[a] The numbers deviate from those published in ref. 201, as there the maximal bond length for the automatic generation of internal coordinates was not chosen big enough. Because of this some degrees of freedom (and the corresponding forces) were not taken into account.

[b] The numbers deviate from those published in ref. 201, as there the geometry was modified manually during the optimization in order to find the optimal orientation of the –NH$_2$ group.

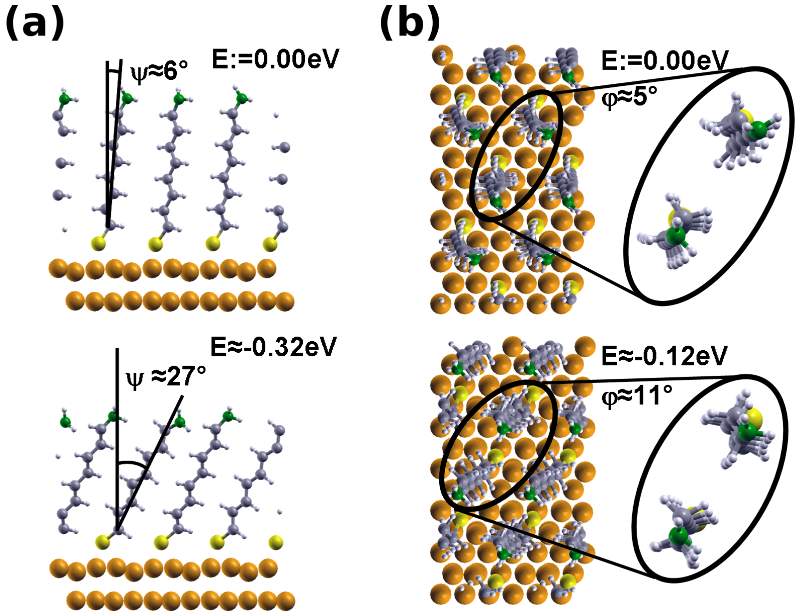

Figure A.4: *dMD (top) and IC-DIIS based (bottom) geometries for* $Au|S|B2|NH_2$ *(a) and* $Au|S|B1|NH_2$ *(b). (a) shows both results in side view, where the bottom three gold layers are hidden; (b) shows the system from the top, with insets zoomed from appropriate angles. Differences in the backbone tilt angle (averaged over both molecules) and total energy per unit cell are indicated.*

reduced during the post-optimization, accompanied by notable changes in all listed quantities. Fig. A.4 illustrates the geometry changes where they are specifically pronounced, for $Au|S|B2|NH_2$ and $Au|S|B1|NH_2$. The tilt angle ψ is enhanced by 21° during the post-optimization of $Au|S|B2|NH_2$, panel (a). Panel (b) depicts the top view of the two $Au|S|B1|NH_2$ results, showing that also the direction of the tilt changes. As the insets show, a notable twist throughout the backbone is found in the dMD conformation (best seen from the hydrogen atoms). It is almost perfectly removed during the post-optimization.

Note that the backbones $\mathbf{B}\boldsymbol{X}$ are extremely flexible and because of this it is ***difficult to reproduce a certain geometry in the calculations*** with IC-DIIS. Already small changes in the initial geometry can lead to different results and convergence is not easily obtained. In fact, quite some patience was needed to get converged results at all.

The backbones discussed so far are characterized by different degrees of flexibility. Anthracene (**3A**) is an example for an inflexible backbone. Still, a significantly lower energy was found with IC-DIIS and this turned out to be important for the analysis of the experimental STM picture of this system (see ref. 318, 319 for the original publication).

---

reductions in energy ahve been reported. This is because there the maximally allowed bond length for the generation of internal coordinates was not chosen big enough, and because of this not all degrees of freedom were detected (and the corresponding forces neglected).

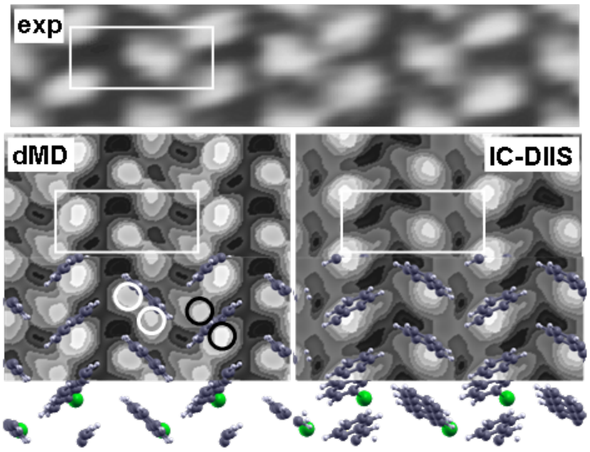

Figure A.5: *Top: Experimental STM image of Au|Se|3A showing two spots per unit cell referred to two molecules per unit cell, reproduced from ref. 318, 319 (and also ref. 317). Bottom: (left: dMD, right: IC-DIIS optimized results) plain calculated STM images (topmost part), calculated STM images cutting through the uppermost benzyl-ring of the anthracene backbone (middle region) and the Se|3A molecules alone (lowermost fraction). The surface unit cell is indicated as a white rectangle in each picture, white and black circles emphasize the relative position of the STM spot relative to the backbone. Modified with permission from ref. 318, 319 (and also ref. 317). Copyright 2010 American Chemical Society.*

A.3.3 Anthraceneselenoles on Au(111)

Anthracene-2-selenolat on Au(111) shows particularly nice long range order[317] and was characterized in detail in a joint experimental and computational study.[318,319] When it comes to reproducing the experimental STM image, choosing a proper optimizer turns out to be important. Figure A.5 shows experimental and calculated STM image of the optimized structures. The dMD optimization leads to more upright standing molecules (6° and 2° for the two molecules) compared to IC-DIIS with larger tilt angles of 19° and 10°.[318,319,v] This leads to quite different simulated STM images: two bright spots per molecule in case of dMD and only one with IC-DIIS. Furthermore, the position of the STM spots with respect to the molecular backbone is different. The dMD structure allows, for one molecule, the interpretation of one STM spot on each side of the backbone (black circles in Fig. A.5) while for the other molecule two spots are visible on the same side of the backbone (white circles). This is qualitatively different to the IC-DIIS structure and only the latter can be viewed as a reasonably correct reproduction of the experimental image, which shows one spot per molecule (two per unit cell).

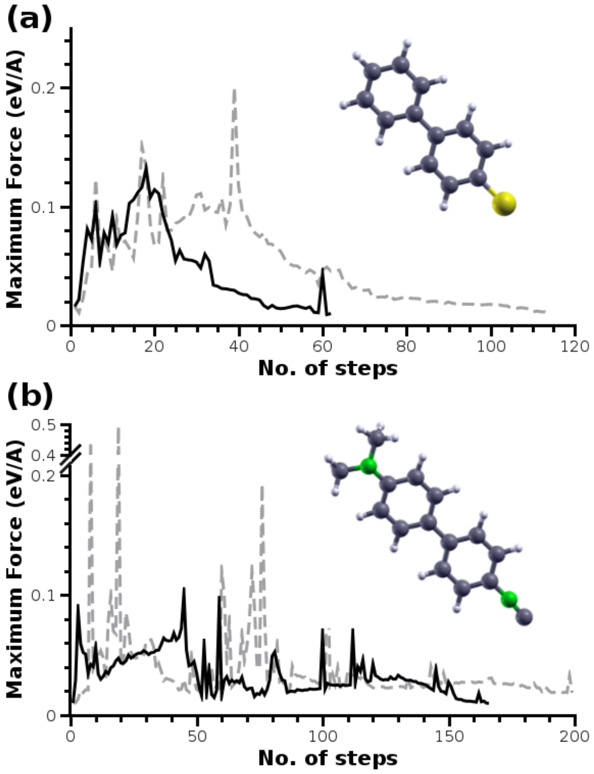

Figure A.6: *Convergence of the maximum force component acting on a nucleus using IC-DIIS for Au|S|2P|H (a) and Au|CN|2P|$N(CH_3)_2$ (b) at full coverage. Solid black and dashed gray lines depict the progress of optimization as found with enabled and disabled substrate detection, respectively; the SAM-forming molecules are schematically depicted.*

A.3.4 Substrate detection

dMD optimizations usually converge very smoothly. During IC-DIIS optimizations the forces often do not decrease monotonically. Depending on the system at hand, convergence is reached more or less easily and some calculations suffer from serious convergence problems. One reason for these problems is peculiar to the metal/SAM unit cell. It usually consists of a metallic substrate and two molecules. Those three fractions are connected by only few atoms and because of this, only few internal coordinates are generated to describe their relative geometry. To better describe the situation in internal coordinates, Tomáš Bučko implemented a substrate detection algorithm. It distinguishes molecules from metal on the basis of the coordination number of each atom. The available degrees of freedom are then described in the following way;: the unit cell is devided into several fractions (1 for the metal and 1 for each molecule), and these fractions are connected by scaled reciprocal distance ($5/R$) coordinates.[311] The entries in the initial Hessian that correspond to these new coordinates have to be set manually as they are not known by Fischer's model; suitable val-

---

[v] The tilt angle in this case is defined as the angle between the molecular plane and the z-axis for comparability with experiment, see refs. 317 & 318, 319.

ues have to be found empirically and in both tests a value of 1/100 was used. Fig. A.6 shows a comparison of the maximum remaining force of optimizations performed with and without substrate detection for two systems. In panel (a), Au|S|2P|H, the number of steps until convergence (0.01 eV/Å) was reduced to about half. Panel b shows a more problematic case (Au|CN|2P|N(CH_3)$_2$) where convergence could be reached only with enabled substrate detection within the preset limit of 200 steps.[vi] The substrate detection did not influence the final geometries much.

A.4 Summary

For a series of quite different metal/SAM systems, two geometry optimization schemes (denoted as IC-DIIS and dMD) were compared with respect to final geometry, energy and predicted work-function modification and in one case also the predicted STM image. These quantities differ significantly in part of the systems and IC-DIIS leads to lower-energy conformations in every case. Convergence, however, is not always easily obtained and part of the problem is specific to the metal/SAM unit cells. A substrate detection algorithm helps improving the performance by identifying molecules and substrate as different fragments and introducing proper coordinates to connect them.

[vi] Without substrate detection another 92 steps were needed for convergence after restarting the optimization.

Bibliography

(1) Ulman, A. *Chem. Rev.* **1996**, *96*, 1533–1554, DOI: 10.1021/cr9502357 (cit. on pp. 1, 72, 95).

(2) Schreiber, F. *J. Phys. Condens. Matter* **2004**, *16*, R881–R900, DOI: 10.1088/0953-8984/16/28/R01 (cit. on pp. 1, 72, 95).

(3) Vericat, C.; Vela, M.; Benitez, G.; Carro, P.; Salvarezza, R. *Chem. Soc. Rev.* **2010**, *39*, 1805–1834, DOI: 10.1039/b907301a (cit. on pp. 1, 34, 74).

(4) Wang, D.; Wan, L.-J.; Bai, C.-L. *Mater. Sci. Eng., R* **2010**, *70*, 169–187, DOI: 10.1016/j.mser.2010.06.016 (cit. on p. 1).

(5) Ciesielski, A.; Samorì, P. *Nanoscale* **2011**, *3*, 1397–1410, DOI: 10.1039/c0nr00914h (cit. on p. 1).

(6) Flood, A. H.; Ramirez, R. J. A.; Deng, W.-Q.; Muller, R. P.; Goddard, W. A. I.; Stoddart, J. F. *Aust. J. Chem.* **2004**, *57*, 301 –322, DOI: 10.1071/CH03307 (cit. on p. 1).

(7) Pace, G.; Ferri, V.; Grave, C.; Elbing, M.; von Hänisch, C.; Zharnikov, M.; Mayor, M.; Rampi, M. A.; Samorì, P. *Proc. Natl. Acad. Sci. U.S.A.* **2007**, *104*, 9937–9942, DOI: 10.1073/pnas.0703748104 (cit. on pp. 1, 72, 95).

(8) Gutzler, R.; Sirtl, T.; Dienstmaier, J. F.; Mahata, K.; Heckl, W. M.; Schmittel, M.; Lackinger, M. *J. Am. Chem. Soc.* **2010**, *132*, 5084–5090, DOI: 10.1021/ja908919r (cit. on p. 1).

(9) Bissell, R. A.; Córdova, E.; Kaifer, A. E.; Stoddart, J. F. *Nature* **1994**, *369*, 133–137, DOI: 10.1038/369133a0 (cit. on p. 1).

(10) Tseng, H.-R.; Wu, D.; Fang, N. X.; Zhang, X.; Stoddart, J. F. *ChemPhysChem* **2004**, *5*, 111–116, DOI: 10.1002/cphc.200300992 (cit. on p. 1).

(11) Green, J. E.; Choi, J. W.; Boukai, A.; Bunimovich, Y.; Johnston-Halperin, E.; DeIonno, E.; Luo, Y.; Sheriff, B. A.; Xu, K.; Shin, Y. S.; Tseng, H.-R.; Stoddart, J. F.; Heath, J. R. *Nature* **2007**, *445*, 414–417, DOI: 10.1038/nature05462 (cit. on p. 1).

(12) Banerjee, I.; Pangule, R. C.; Kane, R. S. *Adv. Mater.* **2011**, *23*, 690–718, DOI: 10.1002/adma.201001215 (cit. on p. 1).

(13) Mandler, D.; Kraus-Ophir, S. *J. Solid State Electrochem.* **2011**, *15*, 1535–1558, DOI: 10.1007/s10008-011-1493-6 (cit. on p. 2).

(14) Samanta, D.; Sarkar, A. *Chem. Soc. Rev.* **2011**, *40*, 2567–2592, DOI: `10.1039/c0cs00056f` (cit. on p. 2).

(15) Domingo, N.; Bellido, E.; Ruiz-Molina, D. *Chem. Soc. Rev.* **2012**, *41*, 258–302, DOI: `10.1039/c1cs15096k` (cit. on p. 2).

(16) Ratera, I.; Veciana, J. *Chem. Soc. Rev.* **2012**, *41*, 303–349, DOI: `10.1039/c1cs15165g` (cit. on p. 2).

(17) Crivillers, N.; Munuera, C.; Mas-Torrent, M.; Simão, C.; Bromley, S. T.; Ocal, C.; Rovira, C.; Veciana, J. *Adv. Mater.* **2009**, *21*, 1177–1181, DOI: `10.1002/adma.200801707` (cit. on pp. 2, 57, 59, 62).

(18) Ma, H.; Yip, H.-L.; Huang, F.; Jen, A. K.-Y. *Adv. Funct. Mater.* **2010**, *20*, 1371–1388, DOI: `10.1002/adfm.200902236` (cit. on p. 2).

(19) Vilan, A.; Yaffe, O.; Biller, A.; Salomon, A.; Kahn, A.; Cahen, D. *Adv. Mater.* **2010**, *22*, 140–159, DOI: `10.1002/adma.200901834` (cit. on p. 2).

(20) DiBenedetto, S. A.; Facchetti, A.; Ratner, M. A.; Marks, T. J. *Adv. Mater.* **2009**, *21*, 1407–1433, DOI: `10.1002/adma.200803267` (cit. on p. 2).

(21) Akkerman, H. B.; Blom, P. W.; de Leeuw, D. M.; de Boer, B. *Nature* **2006**, *441*, 69–72, DOI: `10.1038/nature04699` (cit. on pp. 2, 72, 95).

(22) Song, H.; Reed, M. A.; Lee, T. *Adv. Mater.* **2011**, *23*, 1583–1608, DOI: `10.1002/adma.201004291` (cit. on p. 2).

(23) McCreery, R. L.; Bergren, A. J. *Adv. Mater.* **2009**, *21*, 4303–4322, DOI: `10.1002/adma.200802850` (cit. on p. 2).

(24) van der Molen, S. J.; Liljeroth, P. *J. Phys. Condens. Matter* **2010**, *22*, 133001, DOI: `10.1088/0953-8984/22/13/133001` (cit. on p. 2).

(25) Karthäuser, S. *J. Phys. Condens. Matter* **2011**, *23*, 013001, DOI: `10.1088/0953-8984/23/1/013001` (cit. on p. 2).

(26) Selzer, Y.; Cai, L.; Cabassi, M. A.; Yao, Y.; Tour, J. M.; Mayer, T. S.; Allara, D. L. *Nano Lett.* **2005**, *5*, 61–65, DOI: `10.1021/nl048372j` (cit. on pp. 2, 57, 73).

(27) Deutsch, D.; Natan, A.; Shapira, Y.; Kronik, L. *J. Am. Chem. Soc.* **2007**, *129*, 2989–97, DOI: `10.1021/ja068417d` (cit. on pp. 2, 95, 122).

(28) Romaner, L.; Heimel, G.; Zojer, E. *Phys. Rev. B* **2008**, *77*, 045113, DOI: `10.1103/PhysRevB.77.045113` (cit. on pp. 2, 43, 69, 73, 74, 76, 77, 82, 85–88, 96, 97, 103, 136).

(29) Li, Y.; Lu, D.; Swanson, S. A.; Scott, J. C.; Galli, G. *J. Phys. Chem. C* **2008**, *112*, 6413–6421, DOI: `10.1021/jp7111044` (cit. on pp. 2, 136).

(30) Natan, A.; Kronik, L.; Haick, H.; Tung, R. T. *Adv. Mater.* **2007**, *19*, 4103–4117, DOI: `10.1002/adma.200701681` (cit. on pp. 3, 36, 46, 56, 69, 76, 95–97, 103, 122, 124).

(31) Heimel, G.; Rissner, F.; Zojer, E. *Adv. Mater.* **2010**, *22*, 2494–2513, DOI: 10.1002/adma.200903855 (cit. on pp. 3, 33, 34, 44, 46, 56, 69, 73, 75, 95, 115, 122, 124).

(32) Neugebauer, J.; Scheffler, M. *Phys. Rev. B* **1992**, *46*, 16067–16080, DOI: 10.1103/PhysRevB.46.16067 (cit. on pp. 5, 35).

(33) Natan, A.; Benjamini, A.; Naveh, D.; Kronik, L.; Tiago, M.; Beckman, S.; Chelikowsky, J. *Phys. Rev. B* **2008**, *78*, 075109, DOI: 10.1103/PhysRevB.78.075109 (cit. on pp. 5, 124).

(34) Rissner, F. SAM-Induced Work Function Modification and Energy-Level Alignment at the Interface between Organic Semiconductors., diploma thesis, Graz: University of Technology, Feb. 2009 (cit. on pp. 6, 13, 18, 29, 32, 47, 135).

(35) Hohenberg, P.; Kohn, W. *Phys. Rev.* **1964**, *136*, B864–B871, DOI: 10.1103/PhysRev.136.B864 (cit. on pp. 6, 7).

(36) Kohn, W. *Rev. Mod. Phys.* **1999**, *71*, 1253–1266, DOI: 10.1103/RevModPhys.71.1253 (cit. on p. 7).

(37) Almbladh, C.-O.; von Barth, U. *Phys. Rev. B* **1985**, *31*, 3231–3244, DOI: 10.1103/PhysRevB.31.3231 (cit. on p. 7).

(38) Kümmel, S.; Kronik, L. *Rev. Mod. Phys.* **2008**, *80*, 3–60, DOI: 10.1103/RevModPhys.80.3 (cit. on pp. 7, 9, 36, 64, 99, 100).

(39) Görling, A. *Phys. Rev. A* **1996**, *54*, 3912–3915, DOI: 10.1103/PhysRevA.54.3912 (cit. on p. 7).

(40) Chong, D. P.; Gritsenko, O. V.; Baerends, E. J. *J. Chem. Phys.* **2002**, *116*, 1760–1772, DOI: 10.1063/1.1430255 (cit. on p. 7).

(41) Körzdörfer, T.; Kümmel, S.; Mundt, M. *J. Chem. Phys.* **2008**, *129*, 014110, DOI: 10.1063/1.2944272 (cit. on pp. 8, 100, 118).

(42) Körzdörfer, T.; Kümmel, S.; Marom, N.; Kronik, L. *Phys. Rev. B* **2009**, *79*, 201205, DOI: 10.1103/PhysRevB.79.201205 (cit. on pp. 8, 37, 60, 70, 94, 99, 102).

(43) Körzdörfer, T. *J. Chem. Phys.* **2011**, *134*, 094111, DOI: 10.1063/1.3556979 (cit. on pp. 8, 94, 99, 100, 102).

(44) Nolting, W., *Grundkurs Theoretische Physik 3: Elektrodynamik*, 9th ed.; Springer-Lehrbuch; Springer: Berlin Heidelberg, 2011 (cit. on p. 8).

(45) Perdew, J.; Zunger, A. *Phys. Rev. B* **1981**, *23*, 5048–5079, DOI: 10.1103/PhysRevB.23.5048 (cit. on pp. 9, 99, 102).

(46) Körzdörfer, T.; Kümmel, S. *Phys. Rev. B* **2010**, *82*, 155206, DOI: 10.1103/PhysRevB.82.155206 (cit. on pp. 9, 99, 102).

(47) Ito, E.; Washizu, Y.; Hayashi, N.; Ishii, H.; Matsuie, N.; Tsuboi, K.; Ouchi, Y.; Harima, Y.; Yamashita, K.; Seki, K. *J. Appl. Phys.* **2002**, *92*, 7306, DOI: 10.1063/1.1518759 (cit. on pp. 14, 126).

(48) Tsutsumi, J.; Yoshida, H.; Murdey, R.; Sato, N. *Appl. Phys. Lett.* **2009**, *95*, 182901, DOI: 10.1063/1.3254217 (cit. on pp. 14, 126).

(49) Koch, N.; Zojer, E.; Rajagopal, A.; Ghjisen, J.; Johnson, R.; Leising, G.; Pireaux, J.-J. *Adv. Funct. Mater.* **2001**, *11*, 51–58, DOI: 10.1002/1616-3028(200102)11:1<51::AID-ADFM51>3.0.CO;2-Q (cit. on pp. 14, 126).

(50) Rissner, F.; Rangger, G. M.; Hofmann, O. T.; Track, A. M.; Heimel, G.; Zojer, E. *ACS Nano* **2009**, *3*, 3513–3520, DOI: 10.1021/nn9010494 (cit. on pp. 17, 18, 32, 46, 139, 144).

(51) Baldo, M.; Forrest, S. *Phys. Rev. B* **2001**, *64*, 085201, DOI: 10.1103/PhysRevB.64.085201 (cit. on p. 18).

(52) Parker, I. *J. Appl. Phys.* **1994**, *75*, 1656–1666, DOI: 10.1063/1.356350 (cit. on p. 18).

(53) van Woudenbergh, T.; Blom, P.; Huiberts, J. *Appl. Phys. Lett.* **2003**, *82*, 985, DOI: 10.1063/1.1543255 (cit. on p. 18).

(54) Campbell, I.; Kress, J.; Martin, R.; Smith, D.; Barashkov, N.; Ferraris, J. *Appl. Phys. Lett.* **1997**, *71*, 3528–3530, DOI: 10.1063/1.120381 (cit. on pp. 19, 51, 72).

(55) Bruner, E. L.; Koch, N.; Span, A. R.; Bernasek, S. L.; Kahn, A.; Schwartz, J. *J. Am. Chem. Soc.* **2002**, *124*, 3192–3193, DOI: 10.1021/ja012316s (cit. on p. 19).

(56) Bock, C.; Pham, D.; Kunze, U.; Käfer, D.; Witte, G.; Wöll, C. *J. Appl. Phys.* **2006**, *100*, 114517, DOI: 10.1063/1.2400507 (cit. on pp. 19, 72, 95).

(57) Yan, H.; Huang, Q.; Cui, J.; Veinot, J.; Kern, M.; Marks, T. *Adv. Mater.* **2003**, *15*, 835–838, DOI: 10.1002/adma.200304585 (cit. on pp. 19, 72).

(58) Asadi, K.; Gholamrezaie, F.; Smits, E. C.; Blom, P. W.; de Boer, B. *J. Mater. Chem.* **2007**, *17*, 1947–1953, DOI: 10.1039/b617995a (cit. on pp. 19, 72).

(59) Ishii, H.; Sugiyama, K.; Ito, E.; Seki, K. *Adv. Mater.* **1999**, *11*, 605–625, DOI: 10.1002/(SICI)1521-4095(199906)11:8<605::AID-ADMA605>3.0.CO;2-Q (cit. on pp. 19, 72, 95).

(60) Koch, N. *ChemPhysChem* **2007**, *8*, 1438–1455, DOI: 10.1002/cphc.200700177 (cit. on pp. 19, 23, 45, 72, 95).

(61) Heimel, G.; Romaner, L.; Brédas, J.-L.; Zojer, E. *Phys. Rev. Lett.* **2006**, *96*, 196806, DOI: 10.1103/PhysRevLett.96.196806 (cit. on pp. 19–21, 24, 25, 33, 38, 51, 69, 73, 74, 76, 78, 85, 87, 95, 96, 103).

(62) Heimel, G.; Romaner, L.; Brédas, J.-L.; Zojer, E. *Surf. Sci.* **2006**, *600*, 4548–4562, DOI: 10.1016/j.susc.2006.07.023 (cit. on pp. 19, 28, 36, 59, 63, 74, 90, 137).

(63) Sushko, M. L.; Shluger, A. L. *Adv. Funct. Mater.* **2008**, *18*, 2228–2236, DOI: 10.1002/adfm.200701305 (cit. on pp. 19, 73, 74, 76, 82, 95, 103).

(64) de Boer, B.; Hadipour, A.; Mandoc, M.; van Woudenbergh, T.; Blom, P. *Adv. Mater.* **2005**, *17*, 621–625, DOI: 10.1002/adma.200401216 (cit. on pp. 19, 51, 72).

(65) Betti, M.; Kanjilal, A.; Mariani, C.; Vázquez, H.; Dappe, Y.; Ortega, J.; Flores, F. *Phys. Rev. Lett.* **2008**, *100*, 027601, DOI: `10.1103/PhysRevLett.100.027601` (cit. on pp. 19, 29).

(66) Braun, S.; de Jong, M. P.; Osikowicz, W.; Salaneck, W. R. *Appl. Phys. Lett.* **2007**, *91*, 202108, DOI: `10.1063/1.2806938` (cit. on pp. 19, 22, 29, 30).

(67) Braun, S.; Salaneck, W. R.; Fahlman, M. *Adv. Mater.* **2009**, *21*, 1450–1472, DOI: `10.1002/adma.200802893` (cit. on pp. 19, 29, 30, 45).

(68) Azzam, W.; Fuxen, C.; Birkner, A.; Rong, H.-T.; Buck, M.; Wöll, C. *Langmuir* **2003**, *19*, 4958–4968, DOI: `10.1021/la020868y` (cit. on pp. 19, 35, 58, 74, 97, 136, 137).

(69) Heimel, G.; Romaner, L.; Zojer, E.; Brédas, J.-L. *Acc. Chem. Res.* **2008**, *41*, 721–729, DOI: `10.1021/ar700284q` (cit. on pp. 19, 24, 33, 73, 75, 76, 87, 103, 115).

(70) Heimel, G.; Romaner, L.; Zojer, E.; Brédas, J.-L. *Nano Lett.* **2007**, *7*, 932–940, DOI: `10.1021/nl0629106` (cit. on pp. 19–21, 24, 25, 31, 33, 40, 43, 44, 73, 74, 87, 97, 115, 139).

(71) Charbonneau, G.-P.; Delugeard, Y. *Acta Crystallogr., Sect. B: Struct. Sci* **1977**, *33*, 1586–1588, DOI: `10.1107/S0567740877006566` (cit. on p. 21).

(72) Koller, G.; Berkebile, S.; Krenn, J. R.; Netzer, F. P.; Oehzelt, M.; Haber, T.; Resel, R.; Ramsey, M. G. *Nano Lett.* **2006**, *6*, 1207–1212, DOI: `10.1021/nl0606291` (cit. on p. 21).

(73) Käfer, D.; Ruppel, L.; Witte, G. *Phys. Rev. B* **2007**, *75*, 085309, DOI: `10.1103/PhysRevB.75.085309` (cit. on p. 21).

(74) Oehzelt, M.; Koller, G.; Ivanco, J.; Berkebile, S.; Haber, T.; Resel, R.; Netzer, F. P.; Ramsey, M. G. *Adv. Mater.* **2006**, *18*, 2466–2470, DOI: `10.1002/adma.200600476` (cit. on p. 21).

(75) Crispin, A.; Crispin, X.; Fahlmann, M.; Berggren, M.; Salaneck, W. R. *Appl. Phys. Lett.* **2006**, *89*, 213503, DOI: `10.1063/1.2396899` (cit. on pp. 22, 23, 29).

(76) Osikowicz, W.; de Jong, M. P.; Salaneck, W. R. *Adv. Mater.* **2007**, *19*, 4213–4217, DOI: `10.1002/adma.200700622` (cit. on pp. 22, 29).

(77) Seki, K.; Ito, E.; Ishii, H. *Synth. Met.* **1997**, *91*, 137–142, DOI: `10.1016/S0379-6779(98)80075-1` (cit. on p. 23).

(78) Kahn, A.; Koch, N.; Gao, W. *J. Polym. Sci., Part B: Polym. Phys.* **2003**, *41*, 2529–2548, DOI: `10.1002/polb.10642` (cit. on p. 23).

(79) Simic-Milosevic, V.; Heyde, M.; Lin, X.; König, T.; Rust, H.-P.; Sterrer, M.; Risse, T.; Nilius, N.; Freund, H.-J.; Giordano, L.; Pacchioni, G. *Phys. Rev. B* **2008**, *78*, 235429, DOI: `10.1103/PhysRevB.78.235429` (cit. on p. 26).

(80) Kresse, G.; Furthmüller, J. *Phys. Rev. B* **1996**, *54*, 11169–11186, DOI: 10.1103/PhysRevB.54.11169 (cit. on pp. 28, 35, 63, 89, 118, 137).

(81) Kresse, G.; Joubert, D. *Phys. Rev. B* **1999**, *59*, 1758–1775, DOI: 10.1103/PhysRevB.59.1758 (cit. on pp. 28, 36, 63, 89, 118, 137).

(82) Monkhorst, H. J.; Pack, J. D. *Phys. Rev. B* **1976**, *13*, 5188–5192, DOI: 10.1103/PhysRevB.13.5188 (cit. on pp. 28, 36, 63, 89, 118, 124, 137).

(83) Methfessel, M.; Paxton, A. *Phys. Rev. B* **1989**, *40*, 3616–3621, DOI: 10.1103/PhysRevB.40.3616 (cit. on pp. 28, 36, 137).

(84) Kokalj, A. *Comp. Mater. Sci.* **2003**, *28*, 155–168, DOI: 10.1016/S0927-0256(03)00104-6 (cit. on pp. 28, 36, 63, 90, 119, 137).

(85) Neaton, J.; Hybertsen, M. S.; Louie, S. G. *Phys. Rev. Lett.* **2006**, *97*, 216405, DOI: 10.1103/PhysRevLett.97.216405 (cit. on pp. 28, 65, 103).

(86) Kubatkin, S.; Danilov, A.; Hjort, M.; Cornil, J.; Brédas, J.-L.; Stuhr-Hansen, N.; Hedegård, P.; Bjørnholm, T. *Nature* **2003**, *425*, 698–701, DOI: 10.1038/nature02010 (cit. on p. 28).

(87) Norsko, J. *Rep. Prog. Phys.* **1990**, *53*, 1253–1295, DOI: 10.1088/0034-4885/53/10/001 (cit. on p. 28).

(88) Newns, D. *Phys. Rev.* **1969**, *178*, 1123–1135, DOI: 10.1103/PhysRev.178.1123 (cit. on pp. 28, 36).

(89) Braun, S.; Osikowicz, W.; Wang, Y.; Salaneck, W. R. *Org. Electron.* **2007**, *8*, 14–20, DOI: 10.1016/j.orgel.2006.10.006 (cit. on pp. 29, 30).

(90) Braun, S.; Salaneck, W. R. *Chem. Phys. Lett.* **2007**, *438*, 259–262, DOI: 10.1016/j.cplett.2007.03.005 (cit. on p. 29).

(91) Tengstedt, C.; Osikowicz, W.; Salaneck, W. R.; Parker, I. D.; Hsu, C.-H.; Fahlman, M. *Appl. Phys. Lett.* **2006**, *88*, 053502, DOI: 10.1063/1.2168515 (cit. on p. 29).

(92) Fahlman, M.; Crispin, A.; Crispin, X.; Henze, S.; de Jong, M.; Osikowicz, W.; Tengstedt, C.; Salaneck, W. *J. Phys. Condens. Matter* **2007**, *19*, 183202, DOI: 10.1088/0953-8984/19/18/183202 (cit. on pp. 29, 30).

(93) Vázquez, H.; Flores, F.; Kahn, A. *Org. Electron.* **2007**, *8*, 241–248, DOI: 10.1016/j.orgel.2006.07.006 (cit. on p. 29).

(94) Vázquez, H.; Oszwaldowski, R.; Pou, P.; Ortega, J.; Pérez, R.; Flores, F.; Kahn, A. *Europhys. Lett.* **2004**, *65*, 802–808, DOI: 10.1209/epl/i2003-10131-2 (cit. on p. 29).

(95) Vázquez, H.; Gao, W.; Flores, F.; Kahn, A. *Phys. Rev. B* **2005**, *71*, 041306(R), DOI: 10.1103/PhysRevB.71.041306 (cit. on p. 29).

(96) Ma, Z.; Rissner, F.; Wang, L.; Heimel, G.; Li, Q.; Shuai, Z.; Zojer, E. *PCCP* **2011**, *13*, 9747–9760, DOI: 10.1039/c0cp02168g (cit. on pp. 31, 32, 57, 61, 97).

(97) Della Sala, F.; Fabiano, E.; Laricchia, S.; D'Agostino, S.; Piacenza, M. *Int. J. Quantum Chem.* **2010**, *110*, 2162–2171, DOI: 10.1002/qua.22548 (cit. on p. 33).

(98) Bilić, A.; Reimers, J. R. *J. Phys. Chem. B* **2002**, *106*, 6740–6747, DOI: 10.1021/jp020590i (cit. on pp. 33, 35–38, 43).

(99) Hébert, P.; Le Rille, A.; Zheng, W.; Tadjeddine, A. *J. Electroanal. Chem.* **1998**, *447*, 5–9, DOI: 10.1016/S0022-0728(98)00035-7 (cit. on p. 33).

(100) Lipkowski, J.; Stolberg, L. In *Adsorption of molecules at metal electrodes*, Lipkowski, J., Ross, P., Eds.; VCH: New York, 1992; Chapter Molecular adsorption at gold and silver electrodes, pp 171–238 (cit. on p. 33).

(101) Crossley, M. J.; Burn, P. L.; Langford, S. J.; Prashar, J. K. *J. Chem. Soc., Chem. Commun* **1995**, 1921–1923, DOI: 10.1039/C39950001921 (cit. on p. 33).

(102) Xu, B.; Tao, N. J. *Science* **2003**, *301*, 1221–1223, DOI: 10.1126/science.1087481 (cit. on pp. 33, 72, 95).

(103) Stadler, R.; Thygesen, K.; Jacobsen, K. *Phys. Rev. B* **2005**, *72*, 241401, DOI: 10.1103/PhysRevB.72.241401 (cit. on pp. 33, 34).

(104) Li, X.; Hihath, J.; Chen, F.; Masuda, T.; Zang, L.; Tao, N. *J. Am. Chem. Soc.* **2007**, *129*, 11535–11542, DOI: 10.1021/ja072990v (cit. on p. 33).

(105) Kamenetska, M.; Quek, S. Y.; Whalley, A.; Steigerwald, M.; Choi, H.; Louie, S. G.; Nuckolls, C.; Hybertsen, M.; Neaton, J.; Venkataraman, L. *J. Am. Chem. Soc.* **2010**, *132*, 6817–6821, DOI: 10.1021/ja1015348 (cit. on pp. 33, 35, 95).

(106) Hou, S.; Ning, J.; Shen, Z.; Zhao, X.; Xue, Z. *Chem. Phys.* **2006**, *327*, 1–9, DOI: 10.1016/j.chemphys.2006.02.013 (cit. on p. 34).

(107) Wang, C.; Batsanov, A. S.; Bryce, M. R.; Martín, S.; Nichols, R. J.; Higgins, S. J.; García-Suárez, V. M.; Lambert, C. J. *J. Am. Chem. Soc.* **2009**, *131*, 15647–15654, DOI: 10.1021/ja9061129 (cit. on p. 34).

(108) Kang, J. F.; Liao, S.; Jordan, R.; Ulman, A. *J. Am. Chem. Soc.* **1998**, *120*, 9662, DOI: 10.1021/ja9811871 (cit. on p. 35).

(109) Liao, S.; Shnidman, Y.; Ulman, A. *J. Am. Chem. Soc.* **2000**, *122*, 3688–3694, DOI: 10.1021/ja9905804 (cit. on p. 35).

(110) Kang, J. F.; Ulman, A.; Liao, S.; Jordan, R.; Yang, G.; Liu, G.-y. *Langmuir* **2001**, *17*, 95–106, DOI: 10.1021/la001217+ (cit. on p. 35).

(111) Ballav, N.; Schüpbach, B.; Dethloff, O.; Feulner, P.; Terfort, A.; Zharnikov, M. *J. Am. Chem. Soc.* **2007**, *129*, 15416–15417, DOI: 10.1021/ja0751882 (cit. on p. 35).

(112) Malicki, M.; Guan, Z.; Ha, S. D.; Heimel, G.; Barlow, S.; Rumi, M.; Kahn, A.; Marder, S. R. *Langmuir* **2009**, *25*, 7967–7975, DOI: 10.1021/la9004104 (cit. on p. 35).

(113) Manolova, M.; Boyen, H.-G.; Kucera, J.; Groß, A.; Romanyuk, A.; Oelhafen, P.; Ivanova, V.; Kolb, D. M. *Adv. Mater.* **2009**, *21*, 320–324, DOI: 10.1002/adma.200801634 (cit. on p. 35).

(114) Kankate, L.; Turchanin, A.; Gölzhäuser, A. *Langmuir* **2009**, *25*, 10435–10438, DOI: 10.1021/la902168u (cit. on pp. 35, 73).

(115) Natan, A.; Kronik, L.; Shapira, Y. *Appl. Surf. Sci.* **2006**, *252*, 7608–7613, DOI: 10.1016/j.apsusc.2006.03.052 (cit. on p. 35).

(116) Kresse, G.; Furthmüller, J. *Comp. Mater. Sci.* **1996**, *6*, 15–50, DOI: 10.1016/0927-0256(96)00008-0 (cit. on p. 35).

(117) Kresse, G.; Hafner, J. *Phys. Rev. B* **1993**, *47*, 558–561, DOI: 10.1103/PhysRevB.47.558 (cit. on p. 35).

(118) Kresse, G.; Hafner, J. *Phys. Rev. B* **1994**, *49*, 14251–14269, DOI: 10.1103/PhysRevB.49.14251 (cit. on p. 35).

(119) Tsuzuki, S.; Lüthi, H. P. *J. Chem. Phys.* **2001**, *114*, 3949–3957, DOI: 10.1063/1.1344891 (cit. on p. 35).

(120) Blöchl, P. *Phys. Rev. B* **1994**, *50*, 17953–17979, DOI: 10.1103/PhysRevB.50.17953 (cit. on pp. 36, 63, 89, 118, 137).

(121) Bučko, T.; Hafner, J.; Ángyán, J. G. *J. Chem. Phys.* **2005**, *122*, 124508, DOI: 10.1063/1.1864932 (cit. on pp. 36, 90, 135, 136, 138).

(122) Yan, L.; Lu, D.; Galli, G. *J. Chem. Theory Comput.* **2009**, *5*, 881–886, DOI: 10.1021/ct800465f (cit. on p. 36).

(123) Bilić, A.; Reimers, J. R.; Hush, N. S. *J Chem Phys* **2005**, *122*, 094708, DOI: 10.1063/1.1850455 (cit. on p. 36).

(124) Romaner, L.; Heimel, G.; Brédas, J.-L.; Gerlach, A.; Schreiber, F.; Johnson, R. L.; Zegenhagen, J.; Duhm, S.; Koch, N.; Zojer, E. *Phys. Rev. Lett.* **2007**, *99*, 256801, DOI: 10.1103/PhysRevLett.99.256801 (cit. on pp. 37, 45).

(125) Rangger, G. M.; Hofmann, O. T.; Romaner, L.; Heimel, G.; Bröker, B.; Blum, R.-P.; Johnson, R. L.; Koch, N.; Zojer, E. *Phys. Rev. B* **2009**, *79*, 165306, DOI: 10.1103/PhysRevB.79.165306 (cit. on pp. 37, 45).

(126) Romaner, L.; Nabok, D.; Puschnig, P.; Zojer, E.; Ambrosch-Draxl, C. *New J. Phys.* **2009**, *11*, 053010, DOI: 10.1088/1367-2630/11/5/053010 (cit. on p. 37).

(127) Bröker, B.; Blum, R.-P.; Frisch, J.; Vollmer, A.; Hofmann, O.; Rieger, R.; Müllen, K.; Rabe, J.; Zojer, E.; Koch, N. *Appl. Phys. Lett.* **2008**, *93*, 243303, DOI: 10.1063/1.3049616 (cit. on p. 37).

(128) Böhlin, J.; Unge, M.; Stafström, S. *J. Phys. Condens. Matter* **2008**, *20*, 315008, DOI: 10.1088/0953-8984/20/31/315008 (cit. on p. 37).

(129) Dori, N.; Menon, M.; Kilian, L.; Sokolowski, M.; Kronik, L.; Umbach, E. *Phys. Rev. B* **2006**, *73*, 195208, DOI: 10.1103/PhysRevB.73.195208 (cit. on pp. 37, 99).

(130) Marom, N.; Hod, O.; Scuseria, G. E.; Kronik, L. *J. Chem. Phys.* **2008**, *128*, 164107, DOI: `10.1063/1.2898540` (cit. on pp. 37, 99, 102).

(131) Marom, N.; Kronik, L. *Appl. Phys. A* **2009**, *95*, 159–163, DOI: `10.1007/s00339-008-5007-z` (cit. on pp. 37, 99).

(132) Palummo, M.; Hogan, C.; Sottile, F.; Bagalá, P.; Rubio, A. *J. Chem. Phys.* **2009**, *131*, 084102, DOI: `10.1063/1.3204938` (cit. on pp. 37, 99).

(133) Sauther, J.; Wüsten, J.; Lach, S.; Ziegler, C. *J. Chem. Phys.* **2009**, *131*, 034711, DOI: `10.1063/1.3180818` (cit. on pp. 37, 99).

(134) Stroppa, A.; Kresse, G. *New J. Phys.* **2008**, *10*, 063020, DOI: `10.1088/1367-2630/10/6/063020` (cit. on p. 37).

(135) Hummer, K.; Puschnig, P.; Ambrosch-Draxl, C. *Phys. Rev. B* **2003**, *67*, 184105, DOI: `10.1103/PhysRevB.67.184105` (cit. on p. 37).

(136) Romaner, L.; Heimel, G.; Ambrosch-Draxl, C.; Zojer, E. *Adv. Funct. Mater.* **2008**, *18*, 3999–4006, DOI: `10.1002/adfm.200800876` (cit. on pp. 38, 73, 74, 76, 82, 96, 103).

(137) Rusu, P.; Giovannetti, G.; Brocks, G. *J. Phys. Chem. C* **2007**, *111*, 14448–14456, DOI: `10.1021/jp073420k` (cit. on pp. 40, 73, 76).

(138) Wang, L.; Rangger, G. M.; Ma, Z.; Li, Q.; Shuai, Z.; Zojer, E.; Heimel, G. *PCCP* **2010**, *12*, 4287–4290, DOI: `10.1039/b924306m` (cit. on p. 40).

(139) Hoffmann, R. *Rev. Mod. Phys.* **1988**, *60*, 601–628, DOI: `10.1103/RevModPhys.60.601` (cit. on pp. 45, 104, 110).

(140) Soler, J. M.; Artacho, E.; Gale, J. D.; García, A.; Junquera, J.; Ordejón, P.; Sánchez-Portal, D. *J. Phys. Condens. Matter* **2002**, *14*, 2745–2779, DOI: `10.1088/0953-8984/14/11/302` (cit. on p. 47).

(141) Ahlrichs, R.; Bär, M.; Häser, M.; Horn, H.; Kölmel, C. *Chem. Phys. Lett.* **1989**, *162*, 165–169, DOI: `10.1016/0009-2614(89)85118-8` (cit. on p. 48).

(142) Treutler, O.; Ahlrichs, R. *J. Chem. Phys.* **1995**, *102*, 346–354, DOI: `10.1063/1.469408` (cit. on p. 48).

(143) Furche, F.; Ahlrichs, R. *J. Chem. Phys.* **2002**, *117*, 7433–7447, DOI: `10.1063/1.1508368` (cit. on p. 48).

(144) Schäfer, A.; Horn, H.; Ahlrichs, R. *J. Chem. Phys.* **1992**, *97*, 2571–2577, DOI: `10.1063/1.463096` (cit. on p. 48).

(145) Woon, D. E.; Dunning, T. H. *J. Chem. Phys.* **1993**, *98*, 1358–1371, DOI: `10.1063/1.464303` (cit. on p. 48).

(146) MacDonald, J. *Phys. Rev.* **1933**, *43*, 830–833, DOI: `10.1103/PhysRev.43.830` (cit. on p. 50).

(147) Karwowski, J. *Mol. Phys.* **2004**, *102*, 1213–1219, DOI: `10.1080/00268970410001728708` (cit. on p. 50).

(148) Zehner, R. W.; Parsons, B. F.; Hsung, R. P.; Sita, L. R. *Langmuir* **1999**, *15*, 1121–1127, DOI: `10.1021/la981114f` (cit. on pp. 51, 73).

(149) Rissner, F.; Ma, Z.; Hofmann, O. T.; Slugovc, C.; Shuai, Z.; Zojer, E. *J. Mater. Chem.* **2012**, in press, DOI: `10.1039/c2jm15056e` (cit. on pp. 55, 56).

(150) Reed, M.; Zhou, C.; Muller, C.; Burgin, T.; Tour, J. *Science* **1997**, *278*, 252–254, DOI: `10.1126/science.278.5336.252` (cit. on pp. 56, 72, 95).

(151) Xue, Y.; Datta, S.; Ratner, M. A. *J. Chem. Phys.* **2001**, *115*, 4292–4299, DOI: `10.1063/1.1391253` (cit. on p. 56).

(152) Gershevitz, O.; Sukenik, C. N.; Ghabboun, J.; Cahen, D. *J. Am. Chem. Soc.* **2003**, *125*, 4730–4731, DOI: `10.1021/ja029529h` (cit. on pp. 56, 76, 82, 103).

(153) Crivillers, N.; Furukawa, S.; Minoia, A.; Ver Heyen, A.; Mas-Torrent, M.; Sporer, C.; Linares, M.; Volodin, A.; Van Haesendonck, C.; Van der Auweraer, M.; Lazzaroni, R.; De Feyter, S.; Veciana, J.; Rovira, C. *J. Am. Chem. Soc.* **2009**, *131*, 6246–6252, DOI: `10.1021/ja900453n` (cit. on p. 57).

(154) Heimel, G.; Zojer, E.; Romaner, L.; Brédas, J.-L.; Stellacci, F. *Nano Lett.* **2009**, *9*, 2559–64, DOI: `10.1021/nl9006613` (cit. on p. 57).

(155) Simão, C.; Mas-Torrent, M.; Crivillers, N.; Lloveras, V.; Artés, J. M.; Gorostiza, P.; Veciana, J.; Rovira, C. *Nat. Chem.* **2011**, *3*, 359–364, DOI: `10.1038/nchem.1013` (cit. on pp. 57, 61, 62).

(156) Despotović, I.; Maksić, Z. B.; Vianello, R. *Eur. J. Org. Chem.* **2007**, *2007*, 3402–3413, DOI: `10.1002/ejoc.200700132` (cit. on p. 57).

(157) Yoshifuji, M.; Kawasaki, S. *Sci. Synth.* **2006**, *28*, 623–628 (cit. on p. 58).

(158) Dhirani, A.-A.; Zehner, R. W.; Hsung, R. P.; Guyot-Sionnest, P.; Sita, L. R. *J. Am. Chem. Soc.* **1996**, *118*, 3319–3320, DOI: `10.1021/ja953782i` (cit. on p. 58).

(159) Rissner, F.; Egger, D. A.; Natan, A.; Körzdörfer, T.; Kümmel, S.; Kronik, L.; Zojer, E. *J. Am. Chem. Soc.* **2011**, *133*, 18634–18645, DOI: `10.1021/ja203579c` (cit. on pp. 60, 64, 93, 94, 122–125).

(160) Tamura, M.; Nakazawa, Y.; Shiomi, D.; Nozawa, K.; Hosokoshi, Y.; Ishikawa, M.; Takahashi, M.; Kinoshita, M. *Chem. Phys. Lett.* **1991**, *186*, 401–404, DOI: `10.1016/0009-2614(91)90198-I` (cit. on p. 61).

(161) Alberola, A.; Less, R. J.; Pask, C. M.; Rawson, J. M.; Palacio, F.; Oliete, P.; Paulsen, C.; Yamaguchi, A.; Farley, R. D.; Murphy, D. *Angew. Chem.* **2003**, *115*, 4930–4933, DOI: `10.1002/ange.200352194` (cit. on p. 61).

(162) Crespo, P.; Litrán, R.; Rojas, T.; Multigner, M.; de la Fuente, J.; Sánchez-López, J.; García, M.; Hernando, A.; Penadés, S.; Fernández, A. *Phys. Rev. Lett.* **2004**, *93*, 087204, DOI: `10.1103/PhysRevLett.93.087204` (cit. on p. 61).

(163) Gonzalez, C.; Simón-Manso, Y.; Marquez, M.; Mujica, V. *J. Phys. Chem. B* **2006**, *110*, 687–691, DOI: `10.1021/jp054583g` (cit. on p. 61).

(164) Naaman, R.; Vager, Z. *MRS Bull.* **2010**, *35*, 429–434 (cit. on pp. 61, 95).

(165) Grimme, S. *J. Comput. Chem.* **2006**, *27*, 1787–1799, DOI: `10.1002/jcc.20495` (cit. on p. 63).

(166) Tkatchenko, A.; Scheffler, M. *Phys. Rev. Lett.* **2009**, *102*, 073005, DOI: `10.1103/PhysRevLett.102.073005` (cit. on p. 63).

(167) Garcia-Lastra, J.; Rostgaard, C.; Rubio, A.; Thygesen, K. *Phys. Rev. B* **2009**, *80*, 245427, DOI: `10.1103/PhysRevB.80.245427` (cit. on p. 65).

(168) Biller, A.; Tamblyn, I.; Neaton, J. B.; Kronik, L. *J. Chem. Phys.* **2011**, *135*, 164706, DOI: `10.1063/1.3655357` (cit. on pp. 65, 103).

(169) Nakayama, H.; Morita, T.; Kimura, S. *PCCP* **2009**, *11*, 3967–3976, DOI: `10.1039/b817685j` (cit. on pp. 69, 96, 106).

(170) Nakayama, H.; Morita, T.; Kimura, S. *J. Phys. Chem. C* **2010**, *114*, 4669–4674, DOI: `10.1021/jp101021d` (cit. on pp. 69, 96, 106).

(171) Staykov, A.; Nozaki, D.; Yoshizawa, K. *J. Phys. Chem. C* **2007**, *111*, 11699–11705, DOI: `10.1021/jp072600r` (cit. on pp. 69, 96, 106).

(172) Li, Y.; Zhao, J.; Yin, X.; Yin, G. *J. Phys. Chem. A* **2006**, *110*, 11130–11135, DOI: `10.1021/jp0557058` (cit. on pp. 69, 96, 106).

(173) Yin, X.; Li, Y.; Zhang, Y.; Li, P.; Zjao, J. *Chem. Phys. Lett.* **2006**, *422*, 111–116, DOI: `10.1016/j.cplett.2006.02.020` (cit. on pp. 69, 96, 106).

(174) Choi, Y. C.; Kim, W. Y.; Park, K.-S.; Tarakeshwar, P; Kim, K. S.; Kim, T.-S.; Lee, J. Y. *J. Chem. Phys.* **2005**, *122*, 094706, DOI: `10.1063/1.1858851` (cit. on pp. 69, 96, 106).

(175) Kim, W. Y.; Kim, K. S. *Acc. Chem. Res.* **2010**, *43*, 111–120, DOI: `10.1021/ar900156u` (cit. on pp. 69, 96).

(176) Rai, D.; Joshi, H.; Kulkarni, A. D.; Gejji, S. P.; Pathak, R. K. *J. Phys. Chem. A* **2007**, *111*, 9111–9121, DOI: `10.1021/jp074051v` (cit. on pp. 69, 96, 106).

(177) Tóbik, J.; Dal Corso, A.; Scandolob, S.; Tosatti, E. *Surf. Sci.* **2004**, *566-568*, 644–649, DOI: `10.1016/j.susc.2004.06.116` (cit. on pp. 69, 96, 106).

(178) Arnold, A; Weigend, F; Evers, F *J. Chem. Phys.* **2007**, *126*, 174101, DOI: `10.1063/1.2716664` (cit. on pp. 69, 96).

(179) Malicki, M.; Heimel, G.; Guan, Z.-L.; Ha, S. D.; Barlow, S.; Kahn, A.; Marder, S. R. *J. Phys. Chem. C* **2011**, *115*, 7487–7495, DOI: `10.1021/jp111900g` (cit. on p. 69).

(180) Winkler, S.; Käfer, D.; Wöll, C. In *talk: Correlation between the interface-energetics and thermal stability of SAMs on Gold. DPG Frühjahrstagung Dresden, Thins Films Division*, 2011 (cit. on p. 69).

(181) Rissner, F.; Egger, D. A.; Romaner, L.; Heimel, G.; Zojer, E. *ACS Nano* **2010**, *4*, 6735–6746, DOI: `10.1021/nn102360d` (cit. on pp. 71, 95, 103).

(182) Kind, M.; Wöll, C. *Prog. Surf. Sci.* **2009**, *84*, 230–278, DOI: 10.1016/j.progsurf.2009.06.001 (cit. on pp. 72, 95).

(183) Love, J. C.; Estroff, L. A.; Kriebel, J. K.; Nuzzo, R. G.; Whitesides, G. M. *Chem. Rev.* **2005**, *105*, 1103–1170, DOI: 10.1021/cr0300789 (cit. on pp. 72, 95).

(184) Gooding, J.; Mearns, F.; Yang, W.; Liu, J. *Electroanalysis* **2003**, *15*, 81–96, DOI: 10.1002/elan.200390017 (cit. on pp. 72, 95).

(185) Fontaine, P.; Goguenheim, D.; Deresmes, D.; Vuillaume, D.; Garet, M.; Rondelez, F. *Appl. Phys. Lett.* **1993**, *62*, 2256–2258, DOI: 10.1063/1.109433 (cit. on pp. 72, 95).

(186) Guo, X.; Myers, M.; Xiao, S.; Lefenfeld, M.; Steiner, R.; Tulevski, G. S.; Tang, J.; Baumert, J.; Leibfarth, F.; Yardley, J. T.; Steigerwald, M. L.; Kim, P.; Nuckolls, C. *Proc. Natl. Acad. Sci. U.S.A.* **2006**, *103*, 11452–11456, DOI: 10.1073/pnas.0601675103 (cit. on pp. 72, 95).

(187) Pacher, P.; Lex, A.; Proschek, V.; Etschmaier, H.; Tchernychova, E.; Sezen, M.; Scherf, U.; Grogger, W.; Trimmel, G.; Slugovc, C.; Zojer, E. *Adv. Mater.* **2008**, *20*, 3143–3148, DOI: 10.1002/adma.200800058 (cit. on pp. 72, 95).

(188) Koch, N. *J. Phys. Condens. Matter* **2008**, *20*, 184008, DOI: 10.1088/0953-8984/20/18/184008 (cit. on pp. 72, 95).

(189) Chen, J.; Reed, M.; Rawlett, A.; Tour, J. *Science* **1999**, *286*, 1550–1552, DOI: 10.1126/science.286.5444.1550 (cit. on pp. 72, 95).

(190) Kushmerick, J.; Holt, D.; Yang, J.; Naciri, J.; Moore, M.; Shashidhar, R. *Phys. Rev. Lett.* **2002**, *89*, 086802, DOI: 10.1103/PhysRevLett.89.086802 (cit. on pp. 72, 95).

(191) Bumm, L. A.; Arnold, J. J.; Cygan, M. T.; Dunbar, T. D.; Burgin, T. P.; Jones, L.; Allara, D. L.; Tour, J. M.; Weiss, P. S. *Science* **1996**, *271*, 1705–1707, DOI: 10.1126/science.271.5256.1705 (cit. on pp. 72, 95).

(192) Donhauser, Z.; Mantooth, B.; Kelly, K.; Bumm, L.; Monnell, J.; Stapleton, J.; Price Jr, D.; Rawlett, A.; Allara, D.; Tour, J.; Weiss, P. *Science* **2001**, *292*, 2303–2307, DOI: 10.1126/science.1060294 (cit. on pp. 72, 95).

(193) Park, J.; Pasupathy, A. N.; Goldsmith, J. I.; Chang, C.; Yaish, Y.; Petta, J. R.; Rinkoski, M.; Sethna, J. P.; Abruña, H. D.; McEuen, P. L.; Ralph, D. C. *Nature* **2002**, *417*, 722–725, DOI: 10.1038/nature00791 (cit. on pp. 72, 95).

(194) Nitzan, A.; Ratner, M. A. *Science* **2003**, *300*, 1384–1389, DOI: 10.1126/science.1081572 (cit. on pp. 72, 95).

(195) Lörtscher, E.; Ciszek, J. W.; Tour, J.; Riel, H. *Small* **2006**, *2*, 973–977, DOI: 10.1002/smll.200600101 (cit. on pp. 72, 95).

(196) Venkataraman, L.; Klare, J. E.; Nuckolls, C.; Hybertsen, M. S.; Steigerwald, M. L. *Nature* **2006**, *442*, 904–904, DOI: `10.1038/nature05037` (cit. on pp. 72, 95).

(197) De Renzi, V.; Rousseau, R.; Marchetto, D.; Biagi, R.; Scandolo, S.; del Pennino, U. *Phys. Rev. Lett.* **2005**, *95*, 046804, DOI: `10.1103/PhysRevLett.95.046804` (cit. on p. 73).

(198) Sun, Q.; Selloni, A.; Scoles, G. *J. Phys. Chem. B* **2006**, *110*, 3493–3498, DOI: `10.1021/jp053673i` (cit. on pp. 73, 74).

(199) De Renzi, V. *Surf. Sci.* **2009**, *603*, 1518–1525, DOI: `10.1016/j.susc.2008.10.063` (cit. on pp. 73, 95).

(200) Wang, J.-g.; Prodan, E.; Car, R.; Selloni, A. *Phys. Rev. B* **2008**, *77*, 245443, DOI: `10.1103/PhysRevB.77.245443` (cit. on pp. 73, 76, 97).

(201) Wang, L.; Rangger, G. M.; Romaner, L.; Heimel, G.; Bučko, T.; Ma, Z.; Li, Q.; Shuai, Z.; Zojer, E. *Adv. Funct. Mater.* **2009**, *19*, 3766–3775, DOI: `10.1002/adfm.200901152` (cit. on pp. 73, 75, 80, 82, 95, 96, 103, 139, 143, 144).

(202) Natan, A.; Zidon, Y.; Shapira, Y.; Kronik, L. *Phys. Rev. B* **2006**, *73*, 193310, DOI: `10.1103/PhysRevB.73.193310` (cit. on pp. 73, 74, 76, 82, 95, 96, 103).

(203) Cornil, D.; Olivier, Y.; Geskin, V.; Cornil, J. *Adv. Funct. Mater.* **2007**, *17*, 1143–1148, DOI: `10.1002/adfm.200601116` (cit. on pp. 73, 76, 82, 103).

(204) Bain, C. D.; Evall, J.; Whitesides, G. M. *J. Am. Chem. Soc.* **1989**, *111*, 7155–7164, DOI: `10.1021/ja00200a039` (cit. on p. 73).

(205) Bain, C. D.; Whitesides, G. M. *J. Am. Chem. Soc.* **1989**, *111*, 7164–7175, DOI: `10.1021/ja00200a040` (cit. on p. 73).

(206) Folkers, J. P.; Laibinis, P. E.; Whitesides, G. M. *Langmuir* **1992**, *8*, 1330–1341, DOI: `10.1021/la00041a015` (cit. on p. 73).

(207) Bertilsson, L.; Liedberg, B. *Langmuir* **1993**, *9*, 141–149, DOI: `10.1021/la00025a032` (cit. on p. 73).

(208) Ballav, N.; Terfort, A.; Zharnikov, M. *J. Phys. Chem. C* **2009**, *113*, 3697–3706, DOI: `10.1021/jp808303z` (cit. on p. 73).

(209) Silien, C.; Räisänen, M. T.; Buck, M. *Small* **2010**, *6*, 391–394, DOI: `10.1002/smll.200901909` (cit. on p. 73).

(210) Wu, K.-Y.; Yu, S.-Y.; Tao, Y.-T. *Langmuir* **2009**, *25*, 6232–6238, DOI: `10.1021/la900046b` (cit. on pp. 73, 88).

(211) Folkers, J. P.; Laibinis, P. E.; Whitesides, G. M.; Deutch, J. *J. Phys. Chem.* **1994**, *98*, 563–571, DOI: `10.1021/j100053a035` (cit. on p. 73).

(212) Chen, S.; Li, L.; Boozer, C. L.; Jiang, S. *Langmuir* **2000**, *16*, 9287–9293, DOI: `10.1021/la000417i` (cit. on p. 73).

(213) Chen, S.; Li, L.; Boozer, C. L.; Jiang, S. *J. Phys. Chem. B* **2001**, *105*, 2975–2980, DOI: `10.1021/jp0040650` (cit. on p. 73).

(214) Kang, J. F.; Ulman, A.; Liao, S.; Jordan, R. *Langmuir* **1999**, *15*, 2095–2098, DOI: `10.1021/la9813883` (cit. on pp. 73, 80).

(215) Ooi, Y.; Hobara, D.; Yamamoto, M.; Kakiuchi, T. *Langmuir* **2005**, *21*, 11185–11189, DOI: `10.1021/la051160x` (cit. on p. 73).

(216) Doneux, T.; De Decker, Y. *Langmuir* **2009**, *25*, 2199–2203, DOI: `10.1021/la8033066` (cit. on p. 73).

(217) Salaita, K.; Amarnath, A.; Maspoch, D.; Higgins, T. B.; Mirkin, C. A. *J. Am. Chem. Soc.* **2005**, *127*, 11283–11287, DOI: `10.1021/ja042393y` (cit. on p. 73).

(218) Ballav, N.; Weidner, T.; Rössler, K.; Lang, H.; Zharnikov, M. *ChemPhysChem* **2007**, *8*, 819–822, DOI: `10.1002/cphc.200700120` (cit. on p. 73).

(219) Ballav, N.; Shaporenko, A.; Krakert, S.; Terfort, A.; Zharnikov, M. *J. Phys. Chem. C* **2007**, *111*, 7772–7782, DOI: `10.1021/jp0700635` (cit. on p. 73).

(220) Troughton, E. B.; Bain, C. D.; Whitesides, G. M.; Nuzzo, R. G.; Allara, D. L.; Porter, M. D. *Langmuir* **1988**, *4*, 365–385, DOI: `10.1021/la00080a021` (cit. on p. 73).

(221) Shon, Y.-S.; Lee, S.; Perry, S. S.; Lee, T. R. *J. Am. Chem. Soc.* **2000**, *122*, 1278–1281, DOI: `10.1021/ja991987b` (cit. on p. 73).

(222) Shon, Y.-S.; Lee, S.; Colorado Jr., R.; Perry, S. S.; Lee, T. R. *J. Am. Chem. Soc.* **2000**, *122*, 7556–7563, DOI: `10.1021/ja000403z` (cit. on p. 73).

(223) Heister, K.; Allara, D.; Bahnck, K.; Frey, S.; Zharnikov, M.; Grunze, M. *Langmuir* **1999**, *15*, 5440–5443, DOI: `10.1021/la9902385` (cit. on p. 73).

(224) Madueno, R.; Räisänen, M. T.; Silien, C.; Buck, M. *Nature* **2008**, *454*, 618–621, DOI: `10.1038/nature07096` (cit. on p. 73).

(225) Pace, G.; Petitjean, A.; Lalloz-Vogel, M.-N.; Harrowfield, J.; Lehn, J.-M.; Samorì, P. *Angew. Chem. Int. Ed.* **2008**, *47*, 2484–2488, DOI: `10.1002/anie.200704731` (cit. on p. 73).

(226) Salzmann, I.; Duhm, S.; Heimel, G.; Oehzelt, M.; Kniprath, R.; Johnson, R. L.; Rabe, J. P.; Koch, N. *J. Am. Chem. Soc.* **2008**, *130*, 12870–12871, DOI: `10.1021/ja804793a` (cit. on p. 73).

(227) Nottbohm, C. T.; Turchanin, A.; Gölzhauser, A. *Z. Phys. Chem.* **2008**, *222*, 917–926, DOI: `10.1524/zpch.2008.6015` (cit. on p. 74).

(228) Al-Rawashdeh, N.; Azzam, W.; Wöll, C. *Z. Phys. Chem.* **2008**, *222*, 965–978, DOI: `10.1524/zpch.2008.6017` (cit. on p. 74).

(229) Weckenmann, U.; Mittler, S.; Naumann, K.; Fischer, R. A. *Langmuir* **2002**, *18*, 5479–5486, DOI: `10.1021/la011857s` (cit. on p. 74).

(230) Liu, H.; Bhushan, B.; Eck, W.; Stadler, V. *J. Vac. Sci. Technol., A* **2001**, *19*, 1234–1240, DOI: `10.1116/1.1353538` (cit. on p. 74).

(231) Kleineberg, U.; Brechling, A.; Sundermann, M.; Heinzmann, U. *Adv. Funct. Mater.* **2001**, *11*, 208–212, DOI: 10.1002/1616-3028(200106)11:3<208::AID-ADFM208>3.0.CO;2-X (cit. on p. 74).

(232) Leung, T.; Schwartz, P.; Scoles, G.; Schreiber, F.; Ulman, A. *Surf. Sci.* **2000**, *458*, 34–52, DOI: 10.1016/S0039-6028(00)00385-X (cit. on p. 74).

(233) Tao, Y.-T.; Wu, C.-C.; Eu, J.-Y.; Lin, W.-L. *Langmuir* **1997**, *13*, 4018–4023, DOI: 10.1021/la9700984 (cit. on p. 74).

(234) Baker, K. N.; Fratini, A. V.; Resch, T.; Knachel, H. C.; Adams, W.; Socci, E.; Farmer, B. *Polymer* **1993**, *34*, 1571–1587, DOI: 10.1016/0032-3861(93)90313-Y (cit. on pp. 74, 97).

(235) Fukagawa, H.; Yamane, H.; Kera, S.; Okudaira, K.; Ueno, N. *Phys. Rev. B* **2006**, *73*, 041302(R), DOI: 10.1103/PhysRevB.73.041302 (cit. on pp. 76, 82, 88, 103).

(236) Egger, D. A. Electronic structure of self-assembled monolayers with distributed dipole moments., MA thesis, Graz: University of Technology, 2010 (cit. on p. 94).

(237) Smits, E. C. et al. *Nature* **2008**, *455*, 956–959, DOI: 10.1038/nature07320 (cit. on p. 95).

(238) Selzer, Y.; Salomon, A.; Ghabboun, J.; Cahen, D. *Angew. Chem. Int. Ed.* **2002**, *41*, 827–830, DOI: 10.1002/1521-3773(20020301)41:5<827::AID-ANIE827>3.0.CO;2-N (cit. on p. 95).

(239) Hwang, J.; Wan, A.; Kahn, A. *Mater. Sci. Eng., R* **2009**, *64*, 1–31, DOI: 10.1016/j.mser.2008.12.001 (cit. on p. 95).

(240) Monti, O. L.; Steele, M. P. *PCCP* **2010**, *12*, 12390–12400, DOI: 10.1039/c0cp01039a (cit. on pp. 95, 96).

(241) Steele, M. P.; Kelly, L. L.; Ilyas, N.; Monti, O. L. *J Chem Phys* **2011**, *135*, 124702, DOI: 10.1063/1.3637051 (cit. on pp. 95, 96).

(242) Cahen, D.; Naaman, R.; Vager, Z. *Adv. Funct. Mater.* **2005**, *15*, 1571–1578, DOI: 10.1002/adfm.200500187 (cit. on p. 95).

(243) Piacenza, M.; D'Agostino, S.; Fabiano, E.; Della Sala, F. *Phys. Rev. B* **2009**, *80*, 153101, DOI: 10.1103/PhysRevB.80.153101 (cit. on p. 95).

(244) Kimura, S. *Org. Biomol. Chem.* **2008**, *6*, 1143–1148, DOI: 10.1039/b717898k (cit. on p. 95).

(245) Vilan, A.; Cahen, D. *Trends Biotechnol.* **2002**, *20*, 22–29, DOI: 10.1016/S0167-7799(01)01839-X (cit. on p. 95).

(246) Egger, D. A.; Rissner, F.; Rangger, G. M.; Hofmann, O. T.; Wittwer, L.; Heimel, G.; Zojer, E. *PCCP* **2010**, *12*, 4291–4294, DOI: 10.1039/b924238b (cit. on pp. 95–97, 103, 112, 116, 119, 121, 122, 124).

(247) Chaki, N. K.; Mandal, S.; Reber, A. C.; Qian, M.; Saavedra, H. M.; Weiss, P. S.; Khanna, S. N.; Sen, A. *ACS Nano* **2010**, *4*, 5813–5818, DOI: 10.1021/nn101640r (cit. on p. 96).

(248) Tóbik, J.; Dal Corso, A. *J. Chem. Phys.* **2004**, *120*, 9934–9941, DOI: `10.1063/1.1729853` (cit. on p. 96).

(249) Natan, A.; Kuritz, N.; Kronik, L. *Adv. Funct. Mater.* **2010**, *20*, 2077–2084, DOI: `10.1002/adfm.200902162` (cit. on pp. 96, 103).

(250) Yoshimoto, S. *Bull. Chem. Soc. Jpn.* **2006**, *79*, 1167–1190, DOI: `10.1246/bcsj.79.1167` (cit. on pp. 97, 122).

(251) Taniguchi, I.; Yoshimoto, S.; Sunatsuki, Y.; Nishiyama, K. *Electrochemistry (Tokyo, Jpn.)* **1999**, *67*, 1197–1199 (cit. on pp. 97, 122).

(252) Sek, S. *Langmuir* **2009**, *25*, 13488–13492, DOI: `10.1021/la901984v` (cit. on pp. 97, 122).

(253) Potts, A.; Holland, D.; Trofimov, A.; Schirmer, J.; Karlsson, L.; Siegbahn, K. *J. Phys. B: At. Mol. Opt. Phys.* **2003**, *36*, 3129–3143, DOI: `10.1088/0953-4075/36/14/314` (cit. on p. 99).

(254) Lottermoser, U.; Rademacher, P.; Mazik, M.; Kowski, K. *Eur. J. Org. Chem.* **2005**, *2005*, 522–531, DOI: `10.1002/ejoc.200400534` (cit. on p. 99).

(255) van den Ham, D.; van der Meer, D.; Feil, D. *J. Electron. Spectrosc. Relat. Phenom.* **1974**, *3*, 479–487, DOI: `10.1016/0368-2048(74)80035-6` (cit. on p. 99).

(256) Körzdörfer, T.; Kümmel, S.; Marom, N.; Kronik, L. *Physical Review B* **2010**, *82*, 129903, DOI: `10.1103/PhysRevB.82.129903` (cit. on pp. 99, 102).

(257) Stenuit, G.; Castellarin-Cudia, C.; Plekan, O.; Feyer, V.; Prince, K.; Goldoni, A.; Umari, P. *PCCP* **2010**, *12*, 10812–10817, DOI: `10.1039/c004332j` (cit. on p. 99).

(258) Blase, X.; Attaccalite, C.; Olevano, V. *Phys. Rev. B* **2011**, *83*, 115103, DOI: `10.1103/PhysRevB.83.115103` (cit. on p. 99).

(259) Arantes, J.; Lima, M.; Fazzio, A.; Xiang, H.; Wei, S.-H.; Dalpian, G. *J. Phys. Chem. B* **2009**, *113*, 5376–5380, DOI: `10.1021/jp8101018` (cit. on p. 99).

(260) Stradi, D.; Díaz, C.; Martín, F.; Alcamí, M. *Theor. Chem. Acc.* **2011**, *128*, 497–503, DOI: `10.1007/s00214-010-0852-1` (cit. on p. 99).

(261) Sánchez-Friera, P.; Godby, R. *Phys. Rev. Lett.* **2000**, *85*, 5611–5614, DOI: `10.1103/PhysRevLett.85.5611` (cit. on p. 102).

(262) Heyd, J.; Scuseria, G. E.; Ernzerhof, M. *J. Chem. Phys.* **2003**, *118*, 8207–8215, DOI: `10.1063/1.1564060` (cit. on p. 102).

(263) Heyd, J.; Scuseria, G. E. *J. Chem. Phys.* **2004**, *121*, 1187–1192, DOI: `10.1063/1.1760074` (cit. on p. 102).

(264) Heyd, J.; Scuseria, G. E.; Ernzerhof, M. *J. Chem. Phys.* **2006**, *124*, 219906, DOI: `10.1063/1.2204597` (cit. on p. 102).

(265) Stein, T.; Eisenberg, H.; Kronik, L.; Baer, R. *Phys. Rev. Lett.* **2010**, *105*, 266802, DOI: `10.1103/PhysRevLett.105.266802` (cit. on p. 103).

(266) Quek, S. Y.; Choi, H. J.; Louie, S. G.; Neaton, J. *Nano Lett.* **2009**, *9*, 3949–3953, DOI: 10.1021/nl9021336 (cit. on p. 103).

(267) Adam, N.; Danielli, J.; Harding, J. *Proc. R. Soc. Lond. A* **1934**, *147*, 491–499, DOI: 10.1098/rspa.1934.0231 (cit. on pp. 103, 124).

(268) Baldereschi, A.; Baroni, S.; Resta, R. *Phys. Rev. Lett.* **1988**, *61*, 734–737, DOI: 10.1088/0953-4075/36/14/314 (cit. on p. 104).

(269) Zhao, X.; Wei, C.; Yang, L.; Chou, M. *Phys. Rev. Lett.* **2004**, *92*, 236805, DOI: 10.1103/PhysRevLett.92.236805 (cit. on p. 104).

(270) Popovic, Z.; Satpathy, S. *Phys. Rev. Lett.* **2005**, *94*, 176805, DOI: 10.1103/PhysRevLett.94.176805 (cit. on p. 104).

(271) Wu, Z.; Neaton, J.; Grossman, J. C. *Phys. Rev. Lett.* **2008**, *100*, 246804, DOI: 10.1103/PhysRevLett.100.246804 (cit. on p. 104).

(272) Zharnikov, M. *J. Electron. Spectrosc. Relat. Phenom.* **2010**, *178-179*, 380–393, DOI: 10.1016/j.elspec.2009.05.008 (cit. on p. 104).

(273) Doron-Mor, I.; Hatzor, A.; Vaskevich, A.; van der Boom-Moav, T.; Shanzer, A.; Rubinstein, I.; Cohen, H. *Nature* **2000**, *406*, 382–385, DOI: 10.1038/35019025 (cit. on p. 104).

(274) Leroux, M.; Grandjean, N.; Laügt, M.; Massies, J.; Gil, B.; Lefebvre, P.; Bigenwald, P. *Phys. Rev. B* **1998**, *58*, R13371–R13374, DOI: 10.1103/PhysRevB.58.R13371 (cit. on p. 104).

(275) Miller, D.; Chemla, D.; Schmitt-Rink, S. *Phys. Rev. B* **1986**, *33*, 6976–6982, DOI: 10.1103/PhysRevB.33.6976 (cit. on pp. 104, 106, 110).

(276) Heilbronner, E.; Bock, H., *Das HMO-Modell und seine Anwendung Bd. 1. Grundlagen und Handhabung.* Verlag Chemie: Weinheim, 1968 (cit. on pp. 104, 110).

(277) Pellegrin, E.; Fink, J.; Drechsler, S. *Phys. Rev. Lett.* **1991**, *66*, 2022–2025, DOI: 10.1103/PhysRevLett.66.2022 (cit. on pp. 104, 110).

(278) Zojer, E.; Knupfer, M.; Resel, R.; Meghdadi, F.; Leising, G.; Fink, J. *Phys. Rev. B* **1997**, *56*, 10138–10144, DOI: 10.1103/PhysRevB.56.10138 (cit. on pp. 104, 110).

(279) Zojer, E.; Shuai, Z.; Leising, G.; Brédas, J.-L. *J. Chem. Phys.* **2011**, *111*, 1668–1675, DOI: 10.1063/1.479426 (cit. on pp. 104, 110).

(280) Seki, K.; Karlsson, U. O.; Engelhardt, R.; Koch, E.-E.; Schmidt, W. *Chem. Phys.* **1984**, *91*, 459–470, DOI: 10.1016/0301-0104(84)80078-6 (cit. on pp. 106, 110).

(281) Narioka, S.; Ishii, H.; Edamatsu, K.; Kamiya, K.; Hasegawa, S.; Ohta, T.; Ueno, N.; Seki, K. *Phys. Rev. B* **1995**, *52*, 2362–2373, DOI: 10.1103/PhysRevB.52.2362 (cit. on pp. 106, 110).

(282) Koller, G.; Berkebile, S.; Oehzelt, M.; Puschnig, P.; Ambrosch-Draxl, C.; Netzer, F.; Ramsey, M. *Science* **2007**, *317*, 351–355, DOI: 10.1126/science.1143239 (cit. on pp. 106, 110).

(283) Häming, M.; Ziroff, J.; Salomon, E.; Seitz, O.; Cahen, D.; Kahn, A.; Schöll, A.; Reinert, F.; Umbach, E. *Phys. Rev. B* **2009**, *79*, 155418, DOI: 10.1103/PhysRevB.79.155418 (cit. on pp. 106, 110).

(284) Miller, D., *Quantum Mechanics for Scientists and Engineers.* Cambridge University Press: New York, 2009 (cit. on pp. 106, 112).

(285) Nguyen, D.; Odagaki, T. *Am. J. Phys.* **1987**, *55*, 466–469, DOI: 10.1119/1.15132 (cit. on pp. 106, 112).

(286) Puri, A.; Sun, J.; Odagaki, T. *Solid State Commun.* **1989**, *70*, 907–910, DOI: 10.1016/0038-1098(89)90293-7 (cit. on pp. 106, 112).

(287) Miller, D.; Chemla, D.; Damen, T. *Phys. Rev. Lett.* **1984**, *53*, 2173–2176, DOI: 10.1103/PhysRevLett.53.2173 (cit. on p. 106).

(288) Blumenfeld, M. L.; Steele, M. P.; Monti, O. L. *J. Phys. Chem. Lett.* **2010**, *1*, 145–148, DOI: 10.1021/jz9000517 (cit. on p. 116).

(289) Jacquemin, D.; Adamo, C. *J. Chem. Theory Comput.* **2011**, *7*, 369–376, DOI: 10.1021/ct1006532 (cit. on p. 117).

(290) Frisch, M. et al. Gaussian 03, Revision C.02., Gaussian, Inc., Wallingford, CT, 2004 (cit. on pp. 118, 124).

(291) Chelikowsky, J.; Troullier, N.; Saad, Y. *Phys. Rev. Lett.* **1994**, *72*, 1240–1243, DOI: 10.1103/PhysRevLett.72.1240 (cit. on pp. 118, 124).

(292) Kronik, L.; Makmal, A.; Tiago, M. L.; Alemany, M.; Jain, M.; Huang, X.; Saad, Y.; Chelikowsky, J. R. *Phys. Status Solidi B* **2006**, *243*, 1063–1079, DOI: 10.1002/pssb.200541463 (cit. on pp. 118, 124).

(293) Troullier, N.; Martins, J. L. *Phys. Rev. B* **1991**, *43*, 1993–2006, DOI: 10.1103/PhysRevB.43.1993 (cit. on pp. 118, 124).

(294) Frisch, M. J. et al. Gaussian 09 Revision A.2., Gaussian Inc. Wallingford CT 2009 (cit. on p. 119).

(295) Morales, G. M.; Jiang, P.; Yuan, S.; Lee, Y.; Sanchez, A.; You, W.; Yu, L. *J. Am. Chem. Soc.* **2005**, *127*, 10456–10457, DOI: 10.1021/ja051332c (cit. on p. 122).

(296) Díez-Pérez, I.; Hihath, J.; Lee, Y.; Yu, L.; Adamska, L.; Kozhushner, M. A.; Oleynik, I. I.; Tao, N. *Nat. Chem.* **2009**, *1*, 635–641, DOI: 10.1038/nchem.392 (cit. on p. 122).

(297) Gierschner, J.; Cornil, J.; Egelhaaf, H.-J. *Adv. Mater.* **2007**, *19*, 173–191, DOI: 10.1002/adma.200600277 (cit. on pp. 124, 128).

(298) Noguera, C. *J. Phys. Condens. Matter* **2000**, *12*, R367–R410, DOI: 10.1088/0953-8984/12/31/201 (cit. on p. 126).

(299) Goniakowski, J.; Finocchi, F.; Noguera, C. *Rep. Prog. Phys.* **2008**, *71*, 016501, DOI: 10.1088/0034-4885/71/1/016501 (cit. on p. 126).

(300) Tasker, P. *J. Phys. C: Solid State Phys.* **1979**, *12*, 4977–4984, DOI: 10.1088/0022-3719/12/22/036 (cit. on p. 126).

(301) Goniakowski, J.; Noguera, C.; Giordano, L. *Phys. Rev. Lett.* **2007**, *98*, 205701, DOI: `10.1103/PhysRevLett.98.205701` (cit. on p. 126).

(302) Matsuzaki, K.; Hosono, H.; Susaki, T. *Phys. Rev. B* **2010**, *82*, 033408, DOI: `10.1103/PhysRevB.82.033408` (cit. on p. 126).

(303) Kiguchi, M.; Entani, S.; Saiki, K. *Phys. Rev. B* **2003**, *68*, 115402, DOI: `10.1103/PhysRevB.68.115402` (cit. on p. 126).

(304) Kantorovich, L.; Tupitsyn, I. *J. Phys. Condens. Matter* **1999**, *11*, 6159–6168, DOI: `10.1088/0953-8984/11/32/307` (cit. on p. 126).

(305) Sabatani, E.; Cohen-Boulakia, J.; Bruening, M.; Rubinstein, I. *Langmuir* **1993**, *9*, 2974–2981, DOI: `10.1021/la00035a040` (cit. on p. 136).

(306) Kim, Y.-H.; Jang, S. S.; Goddard, W. A. *J. Chem. Phys.* **2005**, *122*, 244703, DOI: `10.1063/1.1937391` (cit. on p. 136).

(307) Pulay, P.; Fogarasi, G.; Pang, F.; Boggs, J. E. *J. Am. Chem. Soc.* **1979**, *101*, 2550–2560, DOI: `10.1021/ja00504a009` (cit. on p. 136).

(308) Fogarasi, G.; Zhou, X.; Taylor, P. W.; Pulay, P. *J. Am. Chem. Soc.* **1992**, *114*, 8191–8201, DOI: `10.1021/ja00047a032` (cit. on p. 136).

(309) Pulay, P.; Fogarasi, G. *J. Chem. Phys.* **1992**, *96*, 2856–2860, DOI: `10.1063/1.462844` (cit. on p. 136).

(310) Baker, J.; Kessi, A.; Delley, B. *J. Chem. Phys.* **1996**, *105*, 192–212, DOI: `10.1063/1.471864` (cit. on p. 136).

(311) Baker, J.; Pulay, P. *J. Chem. Phys.* **1996**, *105*, 11100, DOI: `10.1063/1.472911` (cit. on pp. 136, 147).

(312) Schlegel, H. B. In *Advances in Chemical Physics: Ab Initio Methods in Quantum Chemistry Part I, Volume 67*, Lawley, K., Ed.; John Wiley & Sons Ltd.: 1987; Chapter Optimization of Equilibrium Geometries and Transition Structures, pp 249–285, DOI: `10.1002/9780470142936.ch4` (cit. on p. 136).

(313) Koslover, E. F.; Wales, D. J. *J. Chem. Phys.* **2007**, *127*, 234105, DOI: `10.1063/1.2807227` (cit. on p. 136).

(314) Kudin, K. N.; Scuseria, G. E.; Schlegel, H. B. *J. Phys. Chem.* **2001**, *114*, 2919–2923, DOI: `10.1063/1.1340578` (cit. on p. 136).

(315) Andzelm, J.; King-Smith, R.; Fitzgerald, G. *Chem. Phys. Lett.* **2001**, *335*, 321–326, DOI: `10.1063/1.1864932` (cit. on p. 136).

(316) Németh, K.; Challacombe, M. *J. Chem. Phys.* **2005**, *123*, 194112, DOI: `10.1063/1.2121569` (cit. on p. 136).

(317) Bashir, A.; Käfer, D.; Müller, J.; Wöll, C.; Terfort, A.; Witte, G. *Angew. Chem. Int. Ed.* **2008**, *47*, 5250–5252, DOI: `10.1002/anie.200800883` (cit. on pp. 137, 146, 147).

(318) Track, A. M.; Rissner, F.; Heimel, G.; Romaner, L.; Käfer, D.; Bashir, A.; Rangger, G. M.; Hofmann, O. T.; Bučko, T.; Gregor, W.; Zojer, E. *J. Phys. Chem. C* **2010**, *114*, 2677–2684, DOI: `10.1021/jp9102756` (cit. on pp. 137, 139, 144–147).

(319) Track, A. M.; Rissner, F.; Heimel, G.; Romaner, L.; Käfer, D.; Bashir, A.; Rangger, G. M.; Hofmann, O. T.; Bučko, T.; Gregor, W.; Zojer, E. *J. Phys. Chem. C* **2010**, *114*, 12838–12838, DOI: 10.1021/jp105593n (cit. on pp. 137, 139, 144–147).

(320) Tersoff, J.; Hamann, D. *Phys. Rev. Lett.* **1983**, *50*, 1998–2001, DOI: 10.1103/PhysRevLett.50.1998 (cit. on p. 137).

(321) Tersoff, J.; Hamann, D. *Phys. Rev. B* **1985**, *31*, 805–813, DOI: 10.1103/PhysRevB.31.805 (cit. on p. 137).

(322) Császár, P.; Pulay, P. *J. Mol. Struct.* **1984**, *114*, 31–34, DOI: 10.1016/S0022-2860(84)87198-7 (cit. on p. 138).

(323) Farkas, Ö.; Schlegel, H. B. *PCCP* **2002**, *4*, 11–15, DOI: 10.1039/b108658h (cit. on p. 138).

(324) Fischer, T. H.; Almlöf, J. *J. Phys. Chem.* **1992**, *96*, 9768–9774, DOI: 10.1021/j100203a036 (cit. on p. 138).